

BULGARIAN CHEMICAL COMMUNICATIONS

2020 Volume 52 / Number 2

*Journal of the Chemical Institutes
of the Bulgarian Academy of Sciences
and of the Union of Chemists in Bulgaria*

Solutions and thermodynamic properties of three pharmacologically important drugs in ethanol

K. Mehmood¹, M. Shakeel^{1*}, M. Siddiq²

¹Department of Chemistry, Hazara University 21300 Mansehra, KPK, Pakistan

²Department of Chemistry, Quaid-e-Azam University 45320 Islamabad, Pakistan

Received: April 24, 2015; Accepted: February 30, 2020

This manuscript reports the determination of critical micelle concentration of three pharmacologically important drugs at four temperatures within the range 288K-318K by using conductivity and refractive index measurements. These drugs included chlorpheniramine maleate, losartan potassium and sodium valporate. The effect of change in temperature on CMC of these drugs was also studied. The electrical conductivity measurements were used to find important thermodynamic parameters for the micellization process. These thermodynamic parameters include free energy of micellization, enthalpy of micellization and entropy of micellization. The results showed that the process of micellization is spontaneous, endothermic and leads to a decrease in entropy for all the drugs studied.

Keywords: Micellization, entropy of micellization, sodium valporate, conductometry.

INTRODUCTION

Most of the allopathic drugs are organic compounds and have amphiphilic character because they have both hydrophilic and hydrophobic parts in their molecules. These drugs also act as surfactants and have ability to form micelles in solution. The study of these drug micelles is important as these micelles may become accumulated in different parts of the body as a result of micellization when a drug is administered in a large amount in the body. The concentration of drug at which micelles just start to form is called critical micelle concentration (CMC). The size and shape of micelles depend on pH, temperature, concentration and ionic strength [1]. CMC of an amphiphile depends on temperature, pressure and presence and concentration of the added substance [1].

CMC can be determined by measuring specific physical properties as these properties undergo changes in different manner before and after CMC and so when these properties are plotted *versus* concentration straight lines of different slopes are obtained. The point of intersection of these straight lines gives the CMC of the drug. The micelles are structurally similar to biomembranes due to which they can be used as a model system to study drug membrane interaction *in vitro* [2-4].

In micelles the distribution of water molecules is anisotropic which results in solubilization of non-polar molecules in the micellar core and molecules of low polarity at intermediate position between core and surface of micelles so these micelles can increase the solubility of insoluble or less soluble

substances [5].

Our present work is related with the determination of CMC and definite thermodynamic parameters of micellization of three pharmacologically important drugs. These drugs are chlorpheniramine maleate (CPAM), sodium valporate (SV) and losartan potassium (LP). Most workers select drugs which either have similar structures or similar mode of action but here we have chosen different drugs so that the properties of different drugs can be compared.

CPAM is a first-generation alkylamine antihistamin and is used to treat hay fever or other respiratory allergies. It is used to prevent symptoms of allergic conditions like urticaria and rhinitis and is also found to have anti-anxiety and anti-depressant effects [6]. Due to relatively weaker sedative effects it is advantageous over other antihistamin drugs [6].

SV is one of the series of fatty acids or carboxylic acids with antiseizure activity and is used for the treatment of panic attack, epilepsy, anxiety disorder, anorexia nervosa, post-traumatic stress disorder, migraine and bipolar disorder and to treat other psychiatric problems [7].

LP is mainly used for the treatment of hypertension [8] and also delays the progression of diabetic nephropathy [9]. In patients having type 2 diabetes, hypertension and microalbuminuria, it is used for reducing renal disease progression [8]. By maintaining blood pressure, it also has a beneficial effect on mitochondria by reversing age-related dysfunctions in cellular energy usage [10].

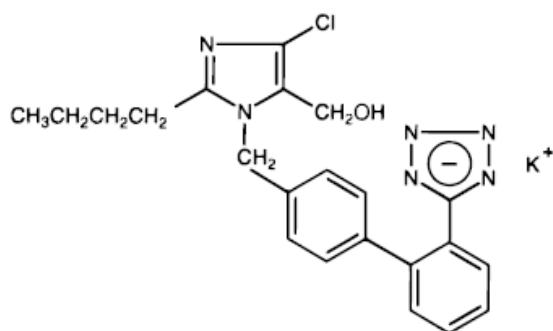
* To whom all correspondence should be sent:

E-mail: m_s313141@yahoo.com

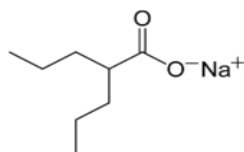
EXPERIMENTAL

Materials

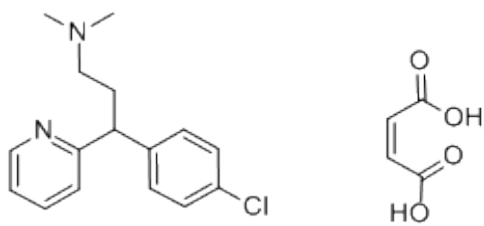
Sodium valporate ($\geq 98\%$ purity) was purchased from Sigma, CPAM ($\geq 98.5\%$ purity) from Fluka, LP (purity 99.5%) from TCI America and absolute ethanol from Merck. The structures of the drugs are shown in scheme 1. The solutions of drugs having different concentrations in terms of mol/kg were prepared at room temperature in dry absolute ethanol using a balance (Rice Lake TA-120) with precision of ± 0.0001 g.



Losartan potassium



Sodium valporate



Chlorpheniramine maleate

Scheme 1. Structures of drugs used

Apparatus and methods

Specific conductivities were measured with digital conductivity meter (Model No. 103 Manufacturer: Jinco Electronics Ltd.) having accuracy of $\pm 0.5\% \pm 2$ digits and temperature control accuracy of $\pm 0.5^\circ\text{C}$. The measurements of electrical conductivity were taken in the temperature range of 288K-318K at 10K intervals.

The temperature was controlled by using a water circulator (IRMECO I-1800 GmbH, Germany). The

conductivity meter was calibrated with a standard solution of KCl over the appropriate concentration range.

Refractive index measurements were taken at one temperature (room temperature) using Abbe's refractometer (Model: ABBE 2WAJ Manufacturer: PCE Instruments) with accuracy of ± 0.0002 . The instrument was calibrated with distilled water.

RESULTS AND DISCUSSION

Critical micelle concentration

CMC can rapidly and accurately be determined by electrical conductivity measurements. For this purpose, the electrical conductivity measurements for solutions of drugs with different concentrations were plotted *versus* concentration to get straight lines in pre- and post-micellar regions and the point of intersection of these lines gave CMC (Figs. 1, 2, 3). Similarly, refractive index measurements can be used to find CMC (Figs. 4, 5, 6).

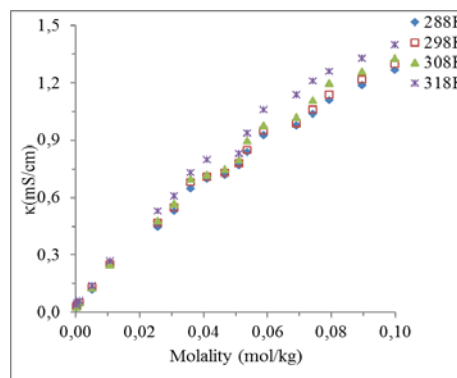


Figure 1. Electrical conductivity *versus* concentration plots for CPAM in ethanol at different temperatures.

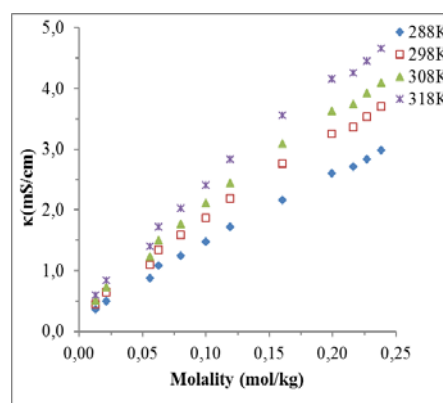


Figure 2. Electrical conductivity *versus* concentration plots for LP in ethanol at different temperatures.

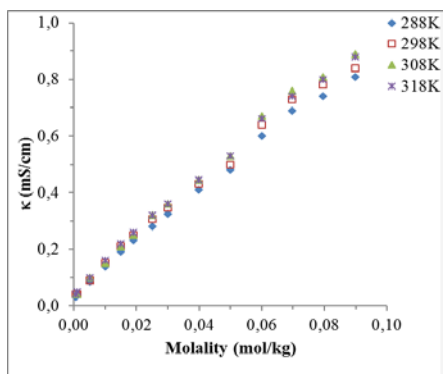


Figure 3. Electrical conductivity versus concentration plots for SV in ethanol at different temperatures.

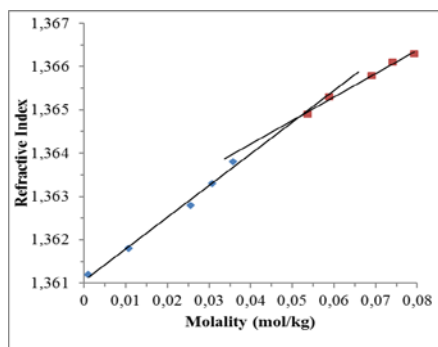


Figure 4. Refractive index versus concentration plots for CPAM in ethanol at 288K.

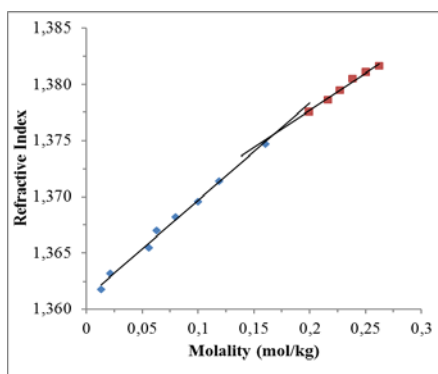


Figure 5. Refractive index versus concentration plot for LP in ethanol at 288K.

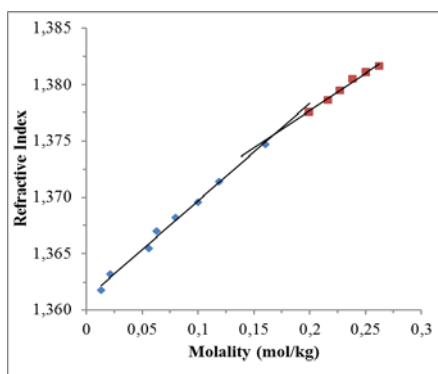


Figure 6. Refractive index versus concentration plot for SV in ethanol at 288K.

From the electrical conductivity measurements, we can also find some important parameters as follows:

The degree of ionization (β) of an electrolytic drug is the ratio of the slopes of post-micellar (S_2) to pre-micellar (S_1) regions of the conductivity-concentration plot and is calculated with the help of the following relation [11]:

$$\beta = \frac{S_2}{S_1} \quad (1)$$

Free energy of micellization (ΔG_m°) can be calculated by the following equation [1]:

$$\Delta G_m^\circ = (2 - \beta)RT \ln X_{CMC} \quad (2)$$

Here, R is gas constant, T is temperature in Kelvin scale and X_{CMC} is CMC in mole fraction.

Enthalpy of micellization can be calculated by using equation (3) while entropy of micellization - by equation (4) [1]:

$$\Delta H_m^\circ = -(2 - \beta)RT^2 \left[\frac{\partial(\ln X_{cmc})}{\partial T} \right]_P \quad (3)$$

$$\Delta S_m^\circ = \frac{\Delta H_m^\circ - \Delta G_m^\circ}{T} \quad (4)$$

As apparent from table 1 CMC of CPAM at 288K is $0.0550 \text{ mol kg}^{-1}$ as determined by the electrical conductivity method in ethanol, which is very close to that determined by refractive index measurements ($0.054 \text{ mol kg}^{-1}$). The value of CMC first decreases with increase in temperature till 298K and then increases with increase in temperature. In ethanol CMC of LP (table 2) is found to be $0.168 \text{ mol kg}^{-1}$ at 288K which is very close to that determined by refractive index measurements ($0.166 \text{ mol kg}^{-1}$). This value also first decreases up to 298K and then increases. CMC of SV in ethanol is found to be $0.0345 \text{ mol kg}^{-1}$ at 288K (table 3) as determined by a conductivity method which is very close to that determined by refractive index measurements ($0.033 \text{ mol kg}^{-1}$).

The reason for such variation in CMC is due to two opposing processes which directly affect CMC of amphiphiles with temperature changes. Firstly, the temperature rise decreases lyophobic solvation which decreases CMC by favoring micellization. Secondly, the increase in temperature decreases lyophilic solvation which disfavors micellization due to the increase in repulsion between ionic heads which increases CMC by making micellization unfavorable [12]. Relative magnitude of these opposing processes decides about the change in CMC. In case of CPAM and LP lyophobic desolvation is dominant over lyophilic desolvation up to 298K. The effect of lyophilic desolvation

becomes dominant above this temperature, as a result CMC decreases up to 298K and then increases [12]. However, in case of SV the CMC of the drug decreases with temperature rise due to the dominance of lyophobic desolvation over lyophilic desolvation.

ΔG_m° is found to be negative for all the drugs under study and this negative value further increases with temperature rise which shows that the process of micellization is spontaneous and becomes more spontaneous at elevated temperatures [1]. ΔH_m° is positive for all drugs in ethanol solvent and its values become higher at higher temperatures showing that micellization is endothermic and becomes more heat-absorbing at higher temperatures [1].

ΔS_m° is found to be positive representing that micellization results in a decrease in randomness [13,14]. The positive values of ΔS_m° point to a transfer of solvophobic chains of SV from the bulk solution phase to the micelle core, which results in an increase in disorder of the system [12,15,16]. There exists strong hydrogen bonding between molecules of solvent in the immediate vicinity of solvophobic chains, which is different from normal interaction of a solvent with solute particles. The neighboring solvent molecules around solvophobic groups are more strongly attracted by nearby solvent molecules as there exists no attractive force between solvophobic drug molecules and solvent, which causes tightening of solvent structure around solvophobic chains.

Table 1. Thermodynamic and micellar parameters for CPAM in ethanol at different temperatures.

Temperature (K)	CMC (mol/kg)	CMC ($X \times 10^4$)	β	α	ΔG_m° (kJ/mol)	ΔH_m° (kJ/mol)	ΔS_m° (J/K/mol)
288.0	0.0550	25.30	0.583	0.417	-20.29	10.01	105.20
298.0	0.0545	25.07	0.599	0.401	-20.79	10.75	105.84
308.0	0.0570	26.22	0.580	0.420	-21.61	11.36	107.07
318.0	0.0575	26.45	0.486	0.514	-23.76	11.97	112.36

Table 2. Thermodynamic and micellar parameters for LP in ethanol at different temperatures.

Temperature (K)	CMC (mol/kg)	CMC ($X \times 10^4$)	β	α	ΔG_m° (kJ/mol)	ΔH_m° (kJ/mol)	ΔS_m° (J/K/mol)
288.0	0.168	77.28	0.732	0.268	-14.76	16.81	109.63
298.0	0.164	75.44	0.678	0.322	-16.01	18.04	114.26
308.0	0.166	76.36	0.617	0.383	-17.26	19.17	118.28
318.0	0.168	77.28	0.575	0.425	-18.32	20.34	121.57

Table 3. Thermodynamic and micellar parameters for SV in ethanol at different temperatures.

Temperature (K)	CMC (mol/kg)	CMC ($X \times 10^4$)	β	α	ΔG_m° (kJ/mol)	ΔH_m° (kJ/mol)	ΔS_m° (J/K/mol)
288.0	0.0345	15.87	0.791	0.209	-18.67	5.86	85.14
298.0	0.0340	15.64	0.778	0.222	-19.56	6.29	86.77
308.0	0.0340	15.64	0.775	0.225	-20.27	6.73	87.65
318.0	0.0332	15.27	0.756	0.244	-21.33	7.22	89.76

As a result, internal torsional vibrations of chains of drug molecules become restricted in solution, leading to a decrease in entropy of the

system. When the solvophobic groups are transferred from the bulk ethanolic medium to the micelles then this order is destroyed and

randomness increases making the process of micellization entropically favorable [17,18].

CONCLUSIONS

The CMCs of CPAM and LP were found to first decrease and then increase with temperature rise while that of SV was found to decrease with temperature rise. The ΔG_m° was negative, becoming more negative at elevated temperature, showing that the spontaneous nature of the process becomes more spontaneous at elevated temperatures for all the drugs. Positive ΔH_m° represented the endothermic nature of micellization while positive ΔS_m° showed that the process of micellization took place with a rise in randomness of the system due to transfer of hydrophobic chains from the bulk solution to the micellar phase. This transfer of hydrophobic chains results in destruction of the ethanol structure because the presence of these chains results in hydrophobic solvation which results in an increase in structure of solvent.

REFERENCES

1. M. J. Rosen, Surfactants and Interfacial Phenomena, Wiley-Interscience Publications, New York, 1973.
2. D. Attwood, A. T. Florence, Surfactant systems, Chapman and Hall, London, 1985.
3. A. M. Khan, S. S. Shah, *J. Chem. Soc. Pak.*, **30**, 186 (2008).
4. P. Taboada, M. Ruso, M. Garcia, V. Mosquera, *Colloids Surf. A.*, **179**, 125 (2001).
5. C. O. Rehgel-Yagui, A. Pessoa Jr., L. C. Tavares *Pharm. Pharmaceut. Sci.*, **8**, 147 (2005).
6. A. Carlsson, M. Lindqvist, *J. Pharm. Pharmacol.*, **21**, 460 (1969).
7. M. Gelder, R. Mayou, J. Geddes, *Psychiatry*, 3rd edn., Oxford, Oxford University Press, 2006.
8. B. K. Katzung, Basic and clinical pharmacology, 8th edn., McGraw Hill Medical Publishing division, London, 2008.
9. C. Boersma, J. Atthobari, R. T. Gansevoort, L. T. de Jong-Van den Berg, P. E. de Jong, D. de Zeeuw, L. J. Annemans, M. J. Postma, *Pharmacoeconomics*, **24(6)**, 523 (2006).
10. P. M. Abadir, D. B. Foster, M. Crow, C. A. Cooke, J. J. Rucker, A. Jain, B. J. Smith, T. N. Burks, R. D. Cohn, N. S. Fedarko, R. M. Carey, B. O'Rourke, J. D. Walston, *Proceedings of the National Academy of Sciences*, **108 (36)**, 14849 (2011).
11. P. C. Hiemenz, R. Rajagopalan, Principles of Colloids and Surface Chemistry, 3rd edn., 1997.
12. F. Akhtar, M. A. Hoque, M. A. Khan, *J. Chem. Thermodyn.*, **40**, 1082 (2008).
13. S. S. Shah, K. Naem, S. W. H. Shah, *Colloids Surf. A.*, **148**, 299 (1999).
14. M. Sarkar, S. Poddar, *J. Colloid Interface Sci.*, **221**, 181 (2000).
15. D. C. Kabiraz, T. K. Biswas, M. N. Islam, M. E. Huque, *J. Sci. Res.*, **3 (2)**, 437 (2011).
16. K. S. Sharma, A. K. Rakshil, *Indian J. Chem.*, **43**, 265 (2004).
17. P. Taboada, D. Attwood, M. J. Ruso, M. Garcia, F. Sarmiento, V. Mosquera, *Langmuir*, **16**, 3175 (2000).
18. A. M. Khan, S. S. Shah, *J. Chem. Soc., Pak.* **30**, 186 (2008).

Microwave-assisted synthesis of 2,2'-(2-oxindoline-3,3'-diyl)-bis(1*H*-inden-1,3(2*H*)-dione) derivatives using SBA-Pr-SO₃H and their antibacterial activities study

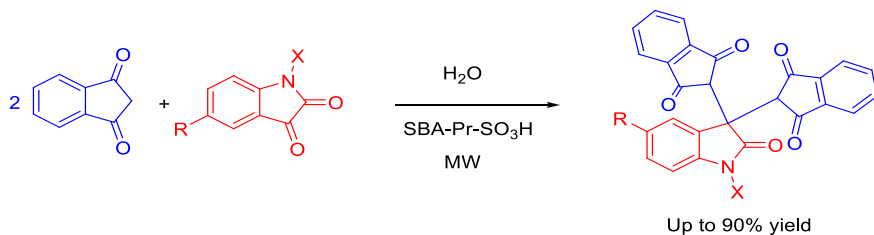
G. Mohammadi Ziarani^{1*}, Z. Hassanzadeh¹, A. Badiei², S. Asadi¹, A. Abolhassani Soorki³

¹ Department of Chemistry, Alzahra University, Vanak Square, Tehran, Iran. gmohammadi@alzahra.ac.ir

² School of Chemistry, College of Science, University of Tehran, Tehran, Iran

³ ACECR- Research Institute of Applied Sciences, Shahid Beheshti University, Tehran, Iran

Received July 22, 2015; Revised November 5, 2019



A microwave-assisted protocol for the synthesis of 2,2'-(2-oxindoline-3,3'-diyl)-bis(1*H*-inden-1,3(2*H*)-dione) derivatives was reported *via* condensation of isatin derivatives with 1,3-indandione in water as a solvent using SBA-Pr-SO₃H as a nanoporous catalyst. SBA-Pr-SO₃H has the property of being reusable and easily removed from the reaction mixture. Application of SBA-Pr-SO₃H as a nanocatalyst is an efficient strategy for the construction of the oxindole nucleus, because of very short reaction times, good yields and easy work-up. This method is also applicable when isatin is replaced by ninhydrin or acenaphthoquinone compounds.

Keywords: Spirooxindole; SBA-Pr-SO₃H; Nano catalyst; Microwave irradiation; Multi-component reaction.

INTRODUCTION

Multi-component reactions (MCRs) have received considerable attention in recent decades due to their atom-economy, flexibility and selectivity. In this method, there is no need to isolate the reaction intermediate, and the time and the raw materials are saved. MCRs are an excellent approach to develop heterocyclic scaffolds to enrich the chemical libraries of drug-like molecules [1-4].

Microwave irradiation as a source of heating shortens the reaction time and has the advantage of being reproducible, offers higher yields and affords an easy scale-up. Association of multi-component reactions and microwave-assisted chemistry effectively diminishes the reaction times and starting material consumption.

The oxindole nucleus has shown a wide range of interesting biological potencies and pharmacological activities such as progesterone receptors agonists, laxative agents, anti-inflammatory, antiprotozoal, antibacterial activities, and it has been used in cancer chemotherapy [5-10]. Isolated oxindoles from marine plants such as bryozoans *Amathia convoluta*

showed special activity in the differentiation of HI-60 human promyelocytic leukemia cells [11].

Mesoporous materials have attracted considerable interest in recent years. These materials showed efficient characteristics including large pore volume, high specific surface area and controllable pore size. These materials were described to have utilization in different fields such as chromatography [12], drug delivery [13], catalysis [14] and adsorption [15]. SBA-15-functionalized sulfonic acid (SBA-Pr-SO₃H) as one of the mesoporous materials shows an excellent catalytic property. In continuation of our works on the synthesis of heterocyclic compounds [16-22], SBA-Pr-SO₃H was used as a reusable and highly efficient heterogeneous catalyst. Wide spectrum of biological properties and efficiency of our nanocatalyst brought us to interest in a new approach to develop functionalized oxindoles under microwave irradiation. All above advantages led us to apply microwave irradiation as an efficient source of energy for the SBA-Pr-SO₃H-catalyzed one-pot synthesis of 2,2'-(2-oxindoline-3,3'-diyl)bis(1*H*-inden-1,3(2*H*)-dione).

* To whom all correspondence should be sent:

E-mail: gmohammadi@alzahra.ac.ir;

gmziarani@hotmail.com

EXPERIMENTAL

Materials and equipment

All chemicals were purchased from Merck and were used as received. Infrared spectra were recorded from KBr pellets with a FT-IR Bruker Tensor 27 instrument. Mass spectra data were obtained by using Network mass selective detector (Agilent) 6890/5973. Melting points were measured by using a Barnstead Electrothermal 9200 apparatus. ^1H NMR was run on a Bruker DPX, 400 MHz and ^{13}C NMR on Bruker DPX, 100 MHz in TMS as an internal standard and in DMSO- d_6 solvent. A Milestone MicroSYNTH (Microwave Synthesis Labstation) apparatus was used to irradiate the reaction mixture.

General procedure for the synthesis of catalyst

As maintained in our previous report, SBA-15 was synthesized and the interior surface was functionalized with propyl sulfonic acid groups. The result of this functionalization was verified with SEM and TEM images as illustrated in Figure 1. As seen in the SEM image (Figure 1), the morphology of functionalized SBA-15 is the same as of non functionalized SBA-15, which shows that functionalization has not considerably changed its morphology. The TEM image illustrates that during the surface modification of SBA-15, the parallel channels representing the presence of pore configuration of SBA-Pr-SO₃H were not collapsed.

General procedure for the synthesis of 2,2'-(2-oxindoline-3,3'-diyl)-bis(1H-inden-1,3(2H)-dione).

In this research, condensation of indandione (0.29 g, 2 mmol) **1** and isatin derivatives (1 mmol) **2** was reported in the presence of SBA-Pr-SO₃H (0.02 g) as an efficient nanoporous acid catalyst under microwave irradiation (500 W, 95 °C) in water for the synthesis of the oxindole compound. After completion and monitoring of the reaction by TLC, at first, the reaction mixture was filtered, and the crude product was dissolved in hot ethyl acetate in order to remove the SBA-Pr-SO₃H nanocatalyst. The

pure crystalline product was obtained by cooling the filtrate. As shown in Table 1, the recycled catalyst could be used in subsequent reactions without significant loss of activity.

The physical and spectral (IR, ^1H NMR, ^{13}C NMR and MS) data for the new compounds are given below:

2,2'-(5-Chloro-2-oxindoline-3,3'-diyl)-bis(1H-indene-1,3(2H)-dione) (**3c**): Mp = 248-252 °C. IR (KBr): ν_{max} = 3286, 2871, 2675, 1710, 1705, 1614, 1590, 1435, 1256 cm^{-1} . ^1H NMR (300 MHz, DMSO- d_6) δ_{H} (ppm) 4.83 (2H, s, CH), 6.75 (1H, d, $^3J_{\text{HH}} = 7.5$, H-Ar), 7.06 (1H, d, H-Ar), 7.60 (1H, s, H-Ar), 7.93 (8H, bs, H-Ar), 10.77 (1H, s, NH). ^{13}C NMR (75 MHz, DMSO- d_6): δ_{C} (ppm) 52.2, 53.0, 111.3, 122.8, 125.2, 128.8, 130.2, 136.1, 136.3, 141.8, 141.9, 142.1, 175.5, 196.7, 197.7; MS (m/z) = 455 (M^+), 341, 310, 256, 146, 109, 95, 69 and 43.

2,2'-(5-Iodo-2-oxindoline-3,3'-diyl)-bis(1H-indene-1,3(2H)-dione) (**3e**): Mp = 268-271 °C. IR (KBr): ν_{max} = 3315, 2872, 1707, 1591, 1470, 1262 cm^{-1} . ^1H NMR (300 MHz, DMSO- d_6) δ_{H} (ppm) 4.83 (2H, s, CH), 6.60 (1H, d, $^3J_{\text{HH}} = 8.2$, H-Ar), 7.0 (1H, s, H-Ar), 7.42 (1H, d, $^3J_{\text{HH}} = 8.2$, H-Ar), 7.94 (8H, bs, H-Ar), 10.77 (1H, s, NH). ^{13}C NMR (75 MHz, DMSO- d_6): δ_{C} (ppm) 52.0, 53.0, 84.0, 112.3, 122.7, 122.8, 130.8, 131.2, 136.0, 136.3, 137.4, 142.0, 142.1, 142.6, 175.2, 196.8, 197.6; MS (m/z) = 545 (M^+), 401, 290, 190, 146, 118, 107, 90, 76, 63 and 50.

Table 1. Synthesis of 2,2'-(2-oxindoline-3,3'-diyl)-bis(1H-inden-1,3(2H)-dione) **3a** with recycled SBA-Pr-SO₃H.

	1 st run	2 nd run	3 rd run	4 th run	5 th run
Time (min)	3	3	4	5	5
Yield* (%)	90	88	86	85	82

* Recycle experiments were carried out on reaction of indandione (2 mmol) and isatin (1 mmol) in the presence of SBA-Pr-SO₃H, under microwave irradiation. After each run, the regained catalyst can be reactivated by simple subsequent washing with the diluted acid solution, water and acetone.

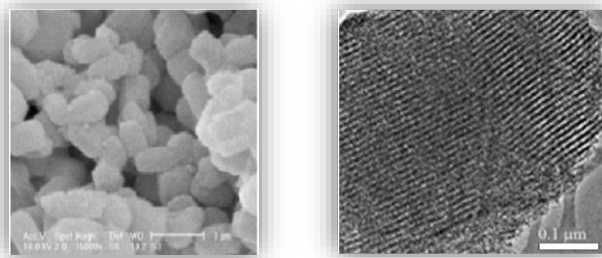


Figure 1. SEM image (left) and TEM (right)

RESULTS AND DISCUSSION

The multi component reaction of indandione (2 mmol) **1** and isatin (1 mmol) **2a** was reported using SBA-Pr-SO₃H as an efficient nanoporous acid catalyst under microwave irradiation (500 W, 95 °C) in water for the synthesis of oxindole compound **3a** (Scheme 1).

As shown in Table 2, this reaction was extended to various isatin derivatives in the same conditions. In all cases, the products were obtained in a brief reaction time (3 min) with good to excellent yields (75-90 %). To study the generality of this method, isatin was replaced by acenaphthoquinone and ninhydrin molecules, which showed acceptable results (Table 3).

A suggested mechanism for the synthesis of 2,2'-(2-oxindoline-3,3'-diyl)bis(1H-inden-1,3(2H)-dione) derivatives **3** is presented in Scheme 2. At first, a keto-enol tautomerism of indandione **1** is performed in the presence of SBA-Pr-SO₃H. Then, a nucleophilic attack of indandione enol form **1** to isatin **2** leads to intermediate **4** which reacts with the second molecule of indandione **1** to give the oxindole compound **3** through dehydration reaction.

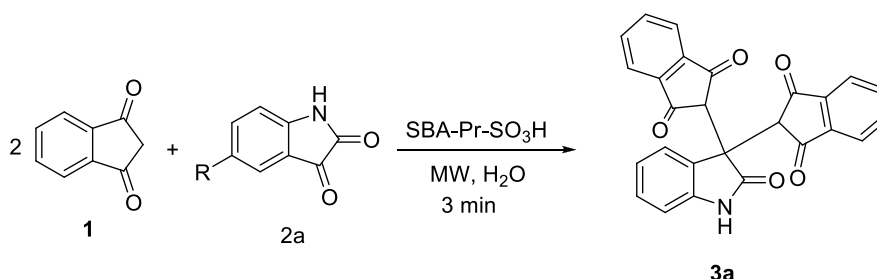
To the best of our knowledge, only one case was previously reported in the literature for the synthesis

of 2,2'-(2-oxindoline-3,3'-diyl)bis(1H-inden-1,3(2H)-dione) as mentioned in Table 4. The present method has the advantage of accelerating the reaction and leads to good yield of product.

Antimicrobial activity

The antimicrobial activity evaluation of the synthesized compounds was performed through the disk diffusion method (IZ) (Table 5) [23] and the minimum inhibitory concentration technique (MIC) (Table 6) [24]. Their activities were studied against gram positive bacteria *Bacillus subtilis* (ATCC 465) and *Staphylococcus aureus* (ATCC 25923), gram negative bacteria *Escherichia coli* (ATCC 25922) and *Pseudomonas aeruginosa* (ATCC 85327) and fungus *Candida albicans* (ATCC 10231).

Compound **5** displays the best results among other compounds against *B. subtilis*, *S. aureus* and *E. coli* with 24, 18 and 10 mm of inhibition zone, respectively. This result was compared to commercial antibiotics such as chloramphenicol, gentamicin and nystatin. Compounds **3b-f** showed poor activity against *B. subtilis* and *S. aureus*. All compounds showed activity against *P. aeruginosa* and *C. albicans*.



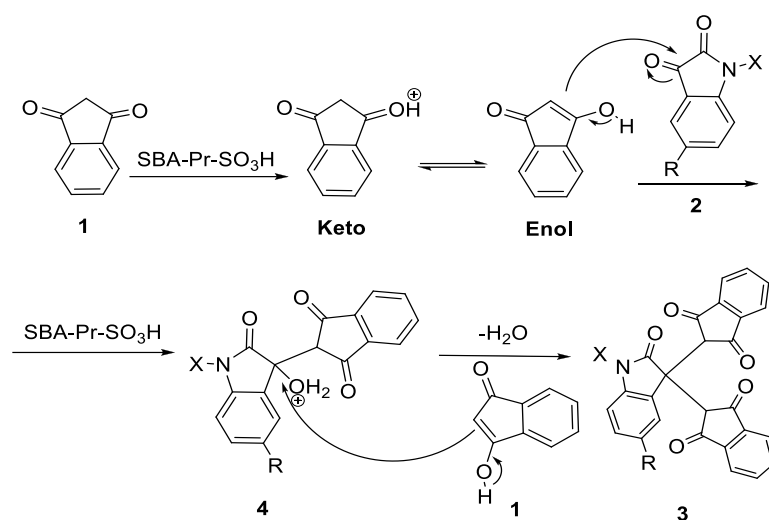
Scheme 1. Synthesis of 2,2'-(2-oxindoline-3,3'-diyl)-bis(1H-inden-1,3(2H) dione) **3a** using SBA-Pr-SO₃H under microwave irradiation

Table 2. Microwave-assisted synthesis of oxindole derivatives **3** using SBA-Pr-SO₃H in 3 min

Entry	Product	R	X	Yield (%)	Mp (°C)	Mp [Ref.]
1	3a	H	H	90	256-258	255-257 [25]
2	3b	Br	H	84	248-250	242 [25]
3	3c	Cl	H	80	248-252	New
4	3d	NO ₂	H	81	240-242	234-236 [25]
5	3e	I	H	75	268-271	New
6	3f	H	Bn	84	217-220	218-221 [25]

Table 3. The results for the replacement of isatin with ninhydrin and acenaphthoquinone

Entry	Product	Time (min)	Yield (%)	Mp (°C)	Mp [Ref.]
1		3	73	273	276 [25]
2		6	92	253	240-242 [25]

**Scheme 2.** Proposed mechanism for the synthesis of 2,2'-(2-oxindoline-3,3'-diyl)bis(1H-inden-1,3(2H)-dione) derivatives**Table 4.** Comparison of different conditions in synthesis of 2,2'-(2-oxindoline-3,3'-diyl)bis(1H-inden-1,3(2H)-dione).

Entry	Catalyst	Solvent	Reaction conditions	Time	Yield (%)	Year
1	<i>p</i> -TSA	EtOH/40 °C	US	2 h	81-94	2011 [25]
2	SBA-Pr-SO ₃ H	H ₂ O	MW	3-6 min	73-92	Present work

Table 5. Inhibition zone (mm) of the synthesized compounds against some gram positive bacteria, gram negative bacteria and fungi by the disc diffusion method.

Compound	<i>B. subtilis</i>	<i>S. aureus</i>	<i>E. coli</i>	<i>P. aeruginosa</i>	<i>C. albicans</i>
3a	0	0	0	0	0
3b	15	16	0	0	0
3c	15	16	0	0	0
3d	15	0	0	0	0
3e	15	16	0	0	0
3f	10	9	0	0	0
4	0	0	0	0	0
5	24	18	10	0	0
Chloramphenicol	26	22	24	8	-
Gentamicin	28	20	18	18	-
Nystatin	-	-	-	-	18

Table 6. Minimum inhibitory concentration ($\mu\text{g/ml}$) of synthesized compounds against some gram positive bacteria, gram negative bacteria and fungi.

Compound	<i>B. subtilis</i>	<i>S. aureus</i>	<i>E. coli</i>	<i>P. aeruginosa</i>	<i>C. albicans</i>
3a	-	-	-	-	-
3b	128	64	-	-	-
3c	128	64	-	-	-
3d	128	-	-	-	-
3e	128	64	-	-	-
3f	512	512	-	-	-
4	-	-	-	-	-
5	8	64	512	-	-
Chloramphenicol	4	8	4	256	-
Gentamicin	0.125	0.5	0.5	1	-
Nystatin	-	-	-	-	8

CONCLUSION

In this work, we have demonstrated an efficient one-pot reaction of isatin with indandione for the synthesis of oxindole derivatives using SBA-Pr-SO₃H as an eco-friendly heterogeneous acid nanocatalyst under microwave irradiation. The advantages of this method are: use of an easily removed catalyst, benign solvent, very fast reaction and high yield. Compounds **3b-f** display antimicrobial activities against some gram positive bacteria, and compound **5** shows the best result among other compounds against *B. subtilis*, *S. aureus* and *E. coli*.

Acknowledgements: We sincerely acknowledge the financial support provided by the Research Council of Alzahra University, and University of Tehran.

REFERENCES

- D. J. Ramón, M. Yus, *Angew. Chem. Int. Ed.*, **44**, 1602 (2005).
- C. Simon, T. Constantieux, J. Rodriguez, *Eur. J. Org. Chem.*, **24**, 4957 (2004).
- J. Zhu, *Eur. J. Org. Chem.*, **7**, 1133 (2003).
- J. Zhu, H. Bienaymé, *Multicomponent reactions*, John Wiley & Sons, 2006.
- V. V. Bolotov, V. V. Drugovina, S. M. Drogovoz, L.V. Yakovleva, A. I. Bereznyakova, *Pharm. Chem. J.*, **16**, 48 (1982).
- F. Garrido, J. Ibanez, E. Gonalons, A. Giraldez, *Eur. J. Med. Chem.*, **10**, 143 (1975).
- H. Pajouhesh, R. Parsons, F.D. Popp, *J. Pharm. Sci.*, **72**, 318 (1983).
- F. D. Popp, *J. Heterocycl. Chem.*, **21**, 1367 (1984).
- T. Tokunaga, W. E. Hume, J. Nagamine, T. Kawamura, M. Taiji, R. Nagata, *Bioorg. Med. Chem. Lett.*, **15**, 1789 (2005).
- S. R. Yong, A. T. Ung, S. G. Pyne, B. W. Skelton, A. H. White, *Tetrahedron*, **63**, 5579 (2007).
- Y. Kamano, H.-p. Zhang, Y. Ichihara, H. Kizu, K. Komiyama, G.R. Pettit, *Tetrahedron Lett.*, **36**, 2783 (1995).
- T. Yasmin, K. Müller, *J. Chromatogr. A*, **1218**, 6464 (2011).
- S.-W. Song, K. Hidajat, S. Kawi, *Langmuir*, **21**, 9568 (2005).
- A. Badiei, H. Goldooz, G. Mohammadi Ziarani, *Appl. Surf. Sci.*, **257**, 4912 (2011).
- T. Tang, Y. Zhao, Y. Xu, D. Wu, J. Xu, F. Deng, *Appl. Surf. Sci.*, **257**, 6004 (2011).
- G. Mohammadi Ziarani, S. Asadi, A. Badiei, A. Sharifi, M. Amanlou, *Iranian Journal of Pharmaceutical Research, IJPR*, **15**, 55 (2016).
- G. Mohammadi Ziarani, S. Asadi, A. Badiei, S. Mousavi, P. Gholamzadeh, *Res. Chem. Intermed.*, **41**, 637 (2015).
- G. Mohammadi Ziarani, S. Faramarzi, S. Asadi, A. Badiei, R. Bazl, M. Amanlou, *DARU*, **21**, 3 (2013).
- G. Mohammadi Ziarani, M. Rahimifard, F. Nouri, A. Badiei, *J. Serb. Chem. Soc.*, **80**, 1265 (2015).
- G. Mohammadi Ziarani, A. Badiei, Z. Aslani, N. Lashgari, *Arab. J. Chem.*, **8**, 54 (2015).
- G. Mohammadi Ziarani, A. Badiei, N. Lashgari, T. Pourjafar, Z. Farahani, *Bulg. Chem. Commun.*, **46**, 719 (2014).
- G. Mohammadi Ziarani, M.S. Nahad, N. Lashgari, *Bulg. Chem. Commun.*, **47**, 55 (2015).
- P. NCCLS. Performance Standards for Antimicrobial Disk Susceptibility Tests, National Committee for Clinical Laboratory Standards, Villanova, 1990, Approved Standard M2-A4.
- w.G.A. NCCLS. Methods for Dilution Antimicrobial Susceptibility Tests for Bacteria, 5th edn., NCCLS: Villanova, PA, 2000, Approved Standard M7-A5.
- R. Ghahremanzadeh, F. Fereshtehnejad, P. Mirzaei, A. Bazgir, *Ultrason. Sonochem.*, **18**, 415 (2011).

Process optimization for copper sorption onto synthetic zeolite NaX

S. Svilović*, D. Rušić, R. Stipišić, N. Kuzmanić

*Department of Chemical Engineering, Faculty of Chemistry and Technology, University of Split,
Ruđera Bošković 35, 21000 Split, Croatia*

Received: July 18, 2017; Accepted: February 10, 2020

Taguchi's approach to experimental design was applied to determine the effect of some process parameters on the sorption of copper ions onto zeolite NaX. The impact of solute concentration (c), temperature (T), contact time (t), impeller speed (n) and anion type (A) on the amount of copper retained on the zeolite, in a batch stirred reactor, was investigated. Optimum experimental conditions and influence of controllable factors were determined using larger-the-better approach. The applied method showed that the optimal copper removal is achieved at the lowest solute concentration, when sulphate anions were used, at the highest impeller speed and temperature used and after 45 min. The influence of controllable factors in descending order is $c > n > A > T > t$. Also, the impact of anion type, solute concentration and temperature on the process equilibrium was examined. The experimental data were modelled using Langmuir, Freundlich and Sips isotherms and their goodness-of-fit was analysed. Thermodynamic parameters such as ΔG^0 , ΔH^0 , and ΔS^0 were also determined. According to the thermodynamic parameters copper sorption on zeolite NaX was a spontaneous and endothermic process for all anions used.

Keywords: Taguchi method; zeolite NaX; isotherms; equilibrium; thermodynamic

INTRODUCTION

Zeolites are an appropriate material for removing heavy metal ions from wastewater and a very promising support for design and preparation of environmentally friendly catalysts. Copper-exchanged zeolites are also used as catalysts and, among others, are applied to selective ammonia oxidation, carbon monoxide oxidation at low temperatures, toluene removal, and wet peroxide oxidation of phenol [1–4]. Zeolite NaX after copper sorption also could be used as a catalyst [3, 4]. Cu-NaX zeolite can be prepared by sorption of copper ions on zeolite NaX from various copper solutions. In previous studies impact of a few parameters on copper sorption from nitrate solutions was studied [5–7]. Also the equilibrium of copper sorption from chloride and sulphate solution on NaX, synthesized from fly ash, was investigated [8]. In most studies all parameters but one are fixed at a certain level in order to determine the optimum conditions. This procedure requires a large number of experiments and that is why Taguchi method arises as an important tool for optimisation.

The Taguchi method uses a specifically designed orthogonal array consisting of controllable parameters and their variation levels in order to optimise experimental conditions. The advantage of Taguchi method is the assessment of optimal experimental conditions with the least number of experiments. This method has already been used for process optimization for heavy metal sorption [9-

13].

In this paper, along with process optimization using Taguchi method, equilibrium data for copper sorption on synthetic zeolite NaX using $\text{CuSO}_4 \times 5\text{H}_2\text{O}$, $\text{CuCl}_2 \times 2\text{H}_2\text{O}$ and $\text{C}_4\text{H}_6\text{CuO}_4 \times \text{H}_2\text{O}$ solutions were obtained.

The goals of this work were to: a) obtain optimum operating conditions to effectively use zeolite NaX for maximum copper removal; b) make a comparison of different adsorption models that can describe the sorption of Cu on zeolite NaX by using nonlinear regression analysis; c) find thermodynamic parameters such as ΔG^0 , ΔH^0 , and ΔS^0 ; d) compare obtained data to previous research in which copper nitrate solution was used.

MATERIALS AND METHODS

Materials

Zeolite NaX (Sigma-Aldrich) with $r\text{Si}/\text{Al} = 1.23$ was crushed and sieved to obtain particles smaller than 0.09 mm. Solutions containing Cu^{2+} were prepared by dissolving appropriate weights of $\text{Cu}(\text{NO}_3)_2 \times 3\text{H}_2\text{O}$; $\text{CuSO}_4 \times 5\text{H}_2\text{O}$, $\text{CuCl}_2 \times 2\text{H}_2\text{O}$ and $\text{C}_4\text{H}_6\text{CuO}_4 \times \text{H}_2\text{O}$ (Kemika), respectively, in distilled water. The initial concentrations were checked using a Perkin Elmer Lambda 25 UV/VIS spectrophotometer.

Taguchi's methodology

The Taguchi method applies an orthogonal array for experimental design and the signal to noise (S/N)

* To whom all correspondence should be sent:
E-mail: sandra@ktf-split.hr

ratio for quality assessment [9].

In this study experiments were planned according to Taguchi's L16 orthogonal array, which has 16 rows corresponding to the number of experiments and five columns corresponding to the controllable factors, Table 1. Anion type, concentration, impeller speed, time and temperature were chosen as controllable factors and their impact on the amount of copper retained into the zeolite phase was studied. As it can be seen from Table 2, each factor used had four testing conditions – represented by levels 1, 2, 3 and 4.

In this work larger-the-better quality characteristic was used [9]:

$$S / N_{LB} = -10 \log \frac{\sum_{i=1}^n \frac{1}{(y)_i}}{n} \quad (1)$$

Table 1. Design of the experiments.

Test	Factor				
	A	C	n	t	T
1	1	1	1	1	1
2	1	2	2	2	2
3	1	3	3	3	3
4	1	4	4	4	4
5	2	1	2	3	4
6	2	2	1	4	3
7	2	3	4	1	2
8	2	4	3	2	1
9	3	1	3	4	2
10	3	2	4	3	1
11	3	3	1	2	4
12	3	4	2	1	3
13	4	1	4	2	3
14	4	2	3	1	4
15	4	3	2	4	1
16	4	4	1	3	2

where S/N_{LB} represents signal-to-noise ratio; subscript LB represents larger-the-better; n is the number of repetitions (four) under the same experimental conditions and y is a measurement result, i.e. sorption efficiency.

The sorption efficiency is presented as $R\%$ and it was calculated by eq. (2):

$$R\% = \frac{(c_0 - c_e)}{c_0} \cdot 100 \quad (2)$$

The next step in Taguchi method is the calculation of the average S/N_{LB} ratio of each controllable factor at level i , denoted as S/N_{FL} , to determine the optimal conditions:

$$S / N_{FL} = \frac{\sum_{j=1}^{n_{Fi}} [(S / N_{LB})_i^F]_j}{n_{Fi}} \quad (3)$$

where S/N_{FL} represents S/N_{LB} ratio for factor F on the level i , the superscript j is the j -th appearance of the i -th level [9]. For the 16 tests, each level for every factor appears 4 times.

Experimental procedure – Taguchi

Experiments for Taguchi method were carried out in stirred batch reactors. Each batch reactor was filled with $V = 0.2 \text{ dm}^3$ of metal solution and $m = 1 \text{ g}$ of zeolite NaX. The mixture was agitated with a turbine impeller. After a defined time, Table 2, samples were taken from the suspensions. Prior to the analysis with the UV/Vis spectrophotometer, all samples were centrifuged and filtrated.

Isotherms and thermodynamic parameters

The purpose of the sorption isotherms is to reveal the relation between equilibrium concentration of the heavy metal in the bulk and on the zeolite [14]. Their application is very useful for understanding the sorption mechanisms and the surface properties and affinities of the sorbent [12].

Table 2. Controllable factors and associated levels.

Factor	Level 1	Level 2	Level 3	Level 4
Anion; A	Cl^-	SO_4^{2-}	CH_3COO^-	NO_3^-
Concentration; C (mmol dm^{-3})	3	6	9	12
Impeller speed; n (rpm)	0	60	120	180
Time; t (min)	15	30	45	60
Temperature (K)	300	302	304	306

A number of isotherm models can be found in the literature but three more frequently used, Langmuir, Freundlich and Sips isotherm (Table 3), were chosen in this study [15–17]. The amount of copper retained in the zeolite phase, q_e , was calculated by eq (4) as the difference between the amount present in the initial copper solution and that remaining in the solution after equilibrium [5]:

$$q_e = \frac{(c_0 - c_e) V}{m} \quad (4)$$

where c_0 and c_e are the initial and equilibrium concentrations of metal in solutions, V is the volume of solution, and m is the mass of the zeolite NaX.

Table 3. Isotherm models [15–17]

	Isotherm models	
Langmuir	$q_e = \frac{K c_e q_{max}}{(1 + K c_e)}$	(5)
Freundlich	$q_e = K c_e^\beta$	(6)
Sips	$q_e = \frac{K^\beta c_e^\beta q_{max}}{1 + K^\beta c_e^\beta}$	(7)

* q_{max} is maximum sorption capacity (mmol g⁻¹), K is constant, β is constant.

The amount of copper ions exchanged for all equilibrium experiments was used to obtain the thermodynamic parameters. These parameters were calculated using the following equations [5, 18]:

$$K_d = \frac{q_e}{c_e} \quad (8)$$

$$\ln K_d = \frac{\Delta S^0}{R} - \frac{\Delta H^0}{R T} \quad (9)$$

$$\Delta G^0 = \Delta H^0 - T\Delta S^0 \quad (10)$$

where K_d is the distribution coefficient, T is temperature (K), R is gas constant (J mol⁻¹ K⁻¹), ΔH^0 is the molar enthalpy change (J mol⁻¹), ΔS^0 is the molar entropy change (J mol⁻¹ K⁻¹) and ΔG^0 is Gibbs free energy of change (J mol⁻¹).

Experimental procedure – Equilibrium

Equilibrium studies were performed in the same batch reactors as experiments for Taguchi analysis. The reactors were filled with $V = 0.2$ dm³ of metal solution and $m = 1$ g of zeolite NaX. The impeller speed for this investigation was fixed at 180 rpm and the time at 24 hours. The pH value was not buffered in order to compare results with previous research [5].

Prior to the analysis with the UV/Vis spectrophotometer, all samples were centrifuged and filtrated.

RESULTS AND DISCUSSION

Process optimization

One of the goals of this investigation was to find the optimum experimental conditions which provide the highest copper removal using larger-the-better quality characteristic. The results for S/N_{LB} ratios, calculated by Eq. (1), along with the sorption efficiency i.e. removal (%), the average removal (average of four repeated experiments denoted as R1, R2, R3 and R4) and standard deviation are shown in the Table 4. The results show that average removal is in the range from 32.081% to 100% and S/N_{LB} ratio in the range from 30.125 to 40.000 depending of the controllable factors.

Along with S/N_{FL} ratios of each controllable factor, range for every controllable factor was calculated (Table 5). Range was used to determine the impact of the controllable factors on the amount of copper removed from solution. It was calculated as the difference between highest and lowest signal-to-noise ratio of the factor. The largest range implied the most effective factor. In this study, according to range, concentration was found to be the most effective factor and it is followed by impeller speed and anion type whereas temperature and contact time were less effective.

From these S/N_{LB} ratios related S/N_{FL} (Eq. 3) ratios of each controllable factor were calculated and shown in Fig. 1 and Table 5. It could be seen that within increase of the concentration there are a significant decrease in efficiency of removal which may be explained by the saturation of available sorption sites [19].

The impact of impeller speed could be explained through the effect of film diffusion on the sorption, i.e. sorption kinetics since it is known that agitation speed affects the thickness of film around the particle, but, also, it could be that complete suspension is achieved only at maximum impeller speed used. The effect of anion, in the presence of acetate solution, might be explained by loss of sorption sites. It is found that in the presence of acetate ions dealumination and desilication of zeolite X occur and the increase in initial copper acetate concentration leads toward mild increase of Si/Al ratio [20]. When nitrate solution is used the Si/Al ratio remains unchanged and in the presence of chloride ions the Si/Al ratio after ion exchange is lower in comparison with pure NaX [21, 22].

It could be also observed that, for temperature, the difference for the S/N_{LB} ratios for the first three levels was only 0.154. Slightly larger impact of the temperature on the process was observed only for the highest temperature used. For the experimental

conditions used the final range for contact time was 0.193. This value indicates that the larger part of the copper is exchanged up to the first contact time level regardless of the slowest process, meaning that for high impeller speed equilibrium is reached fast and that for slower impeller speed, when the film diffusion affects the process, the differences between exchanges after 15 and 60 min are not significant.

Also, an evaluation of factor importance was made in statistical sense using sum of squares (SS), mean squares (MS) and percentage of contribution (pC), Table 5. Comparing these results with the range results it could be seen that the previously obtained order of significance is confirmed. So, every controllable factor, considering the obtained range, SS, MS and PC, was associated with rank. The factor which has a rank 1 should be utilized first and so on. From Table 5 the optimum operating

conditions could be evaluated and for the present study these conditions are: A2; C1; n4; t3; T4; that is solution of $\text{CuSO}_4 \times 5\text{H}_2\text{O}$, concentration 3 mmol dm^{-3} , 180 rpm impeller speed, 45 min contact time and temperature of 306 K.

Effect of process parameters on equilibrium

The effect of anion type was studied using chloride, sulphate and acetate solutions (Fig. 2). Data obtained in this work were also compared with data from a previous study and it is evident that the changes in the sorption capacity due to anion type are noticeable on the synthetic zeolite NaX while the sorption on NaX zeolite synthesized from coal fly ash showed negligible capacity differences for chloride and sulphate solutions (around 1%) [5, 8].

Table 4. Results of experimental part of Taguchi design, S/ N_{LB} ratios and standard deviation

Test	Removal (%)				Average removal (%)	STD	S/N _{LB} ratio
	R1	R2	R3	R4			
1	76.212	77.080	76.416	76.212	76.480	0.356	37.671
2	74.251	74.118	74.188	73.378	73.966	0.344	37.380
3	70.562	71.431	70.562	72.300	71.214	0.720	37.050
4	61.652	61.720	61.720	61.533	61.656	0.077	35.800
5	91.999	91.754	91.509	91.754	91.754	0.173	39.252
6	73.523	73.262	73.138	73.400	73.331	0.145	37.306
7	78.420	78.508	78.409	77.950	78.322	0.218	37.878
8	58.081	58.016	58.147	57.680	57.981	0.180	35.266
9	91.682	92.090	92.090	91.810	91.918	0.178	39.268
10	90.129	90.223	90.129	90.050	90.133	0.061	39.098
11	41.146	41.304	41.191	41.225	41.217	0.057	32.301
12	32.020	32.079	32.112	32.112	32.081	0.038	30.125
13	100.00	100.00	100.00	100.00	100.00	0.000	40.000
14	96.848	97.135	96.991	96.562	96.884	0.212	39.725
15	44.919	45.014	44.919	45.109	44.991	0.079	33.062
16	32.861	32.790	32.790	32.790	32.808	0.031	30.320

Table 5. S/N_{FL} ratios and contribution of each controllable factor.

Factor	A	C	N	t	T
Level 1	36.975	39.048	34.399	36.350	36.274
Level 2	37.425	38.377	34.955	36.237	36.211
Level 3	35.198	35.073	37.827	36.430	36.120
Level 4	35.777	32.877	38.194	36.359	36.770
Range	2.288	6.171	3.795	0.193	0.650
SS	12.813	100.308	45.330	0.077	1.014
MS	4.2711	33.4359	15.1099	0.0255	0.3381
pC (%)	8.03	62.87	24.41	0.050	0.64
Rank	3	1	2	5	4

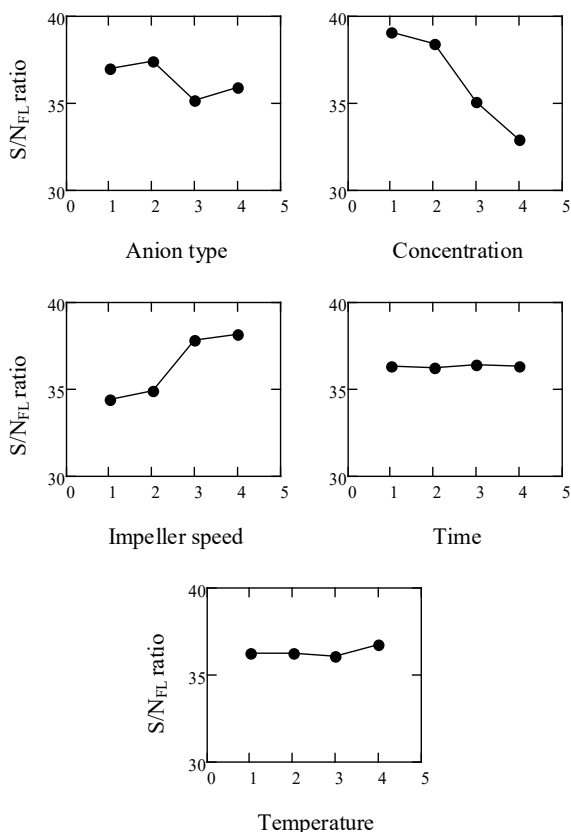


Figure 1. Response distribution of S/N_{FL} ratios.

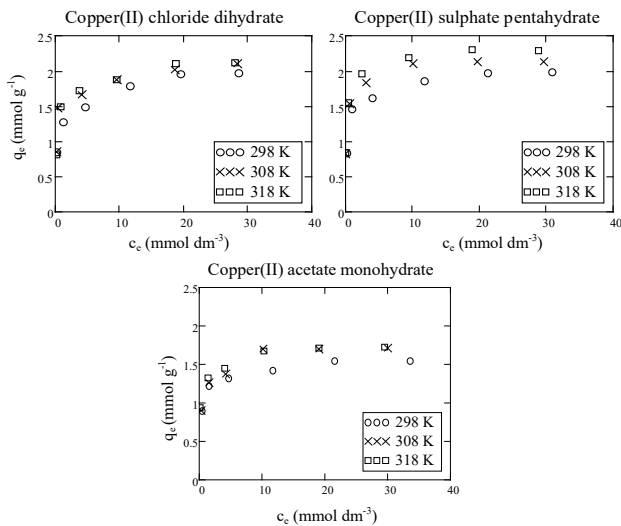


Figure 2. Experimental equilibrium data

Following sorption capacities were achieved for 298 K: for acetate solution 1.555 mmol g⁻¹, for nitrate solution 1.668 mmol g⁻¹, for chloride solution 1.975 mmol g⁻¹ and for sulphate solution 1.986 mmol g⁻¹. Kyziol-Komosińska *et al.* also found that the maximum sorption capacity was achieved for a sulphate solution [8]. These results are in correlation with the observation in the Process optimisation

chapter of this work.

Also it can be seen that for all anions used the copper sorption was favoured by an increase in temperature. This is probably a consequence of the reduced effective size of ions caused by a decrease of the ion hydration shell, which allows ions to diffuse in the inner part of the pore system of the zeolite [5]. This increase indicates the endothermic nature of the process.

Comparison of the isotherms

Values for experimental maximum sorption capacity, q_{max} , statistical comparison values, and the other parameters of all isotherms are shown in Table 6. For all the equilibrium experiments Freundlich or/and Sips isotherms work better than Langmuir isotherm. Like in the previous study [5] the isotherm models that take into account some sort of heterogeneity, seem to have an advantage over the Langmuir isotherm in explaining the equilibrium relations. Also, the β values calculated from the Freundlich and Sips isotherm were less than 1, confirming this statement.

In the study of sorption equilibrium from copper nitrate solution on zeolite NaX all isotherms showed the same trend in the changes of the parameter values [5]. In this study q_{max} , increases with increased temperature for all isotherms. For other parameters, in few calculations, there was a deviation from the trend. In the presence of chloride and sulphate ions β decreases as temperature increases while in acetate solution this trend for Freundlich isotherm was not observed. For the K constant in the presence of the sulphate ions for Langmuir isotherm and in the presence of acetate ions for Sips isotherm the trend was not observed. For all other calculations K increases with the temperature, like q_{max} , this indicates that the sorption was more favourable at the higher temperature.

Thermodynamic parameters

Calculated thermodynamic parameters along with the coefficient of determination are presented in Table 7. According to the obtained results the sorption process is endothermic ($\Delta H^0 > 0$) and spontaneous ($\Delta G^0 < 0$) regardless of anion type and temperature used. ΔG^0 becomes more negative with increasing temperature and less negative with increasing initial concentration. This shows that spontaneity grows with an increase in temperature and reduces with an increase in initial concentration, the same was observed for the sorption from a nitrate solution [5].

Table 6. Adsorption isotherm parameters and statistical comparison values.

Isotherm parameters for copper (II) chloride dihydrate				
Isotherm	Parameter	Temperature		
		298 K	308 K	318 K
	q_{\max} experimental (mmol g ⁻¹)	1.975	2.107	2.113
Langmuir	K	5.067	5.550	5.944
	q_{\max}	1.799	1.934	1.972
	r^2	0.790	0.905	0.915
	RMSE	0.228	0.167	0.164
	χ^2	0.144	0.072	0.068
Freundlich	K	1.214	1.335	1.373
	β	0.153	0.144	0.140
	r^2	0.991	0.953	0.940
	RMSE	0.047	0.117	0.132
	χ^2	5.58×10 ⁻³	0.047	0.058
Sips	K	1.757	2.212	2.861
	q_{\max}	2.003	2.249	2.380
	β	0.659	0.570	0.454
	r^2	0.938	0.979	0.991
	RMSE	0.189	0.110	0.074
	χ^2	0.209	0.047	0.014
Isotherm parameters for copper (II) sulphate pentahydrate				
Isotherm	Parameter	Temperature		
		298 K	308 K	318 K
	q_{\max} experimental (mmol g ⁻¹)	1.986	2.131	2.295
Langmuir	K	7.892	7.676	31.375
	q_{\max}	1.858	2.054	2.103
	r^2	0.892	0.935	0.794
	RMSE	0.164	0.152	0.271
	χ^2	0.067	0.065	0.156
Freundlich	K	1.334	1.478	1.622
	β	0.128	0.127	0.120
	r^2	0.951	0.913	0.965
	RMSE	0.109	0.17	0.136
	χ^2	0.039	0.083	0.049
Sips	K	4.921	5.100	55.247
	q_{\max}	2.037	2.304	2.328
	β	0.694	0.535	0.490
	r^2	0.964	0.997	0.924
	RMSE	0.117	0.032	0.268
	χ^2	0.042	2.04×10 ⁻³	0.180

Isotherm parameters for copper (II) acetate monohydrate				
Isotherm	Parameter	Temperature		
		298 K	308 K	318 K
	q_{\max} experimental (mmol g ⁻¹)	1.555	1.707	1.720
Langmuir	K	3.019	3.929	4.721
	q_{\max}	1.511	1.646	1.660
	r^2	0.944	0.849	0.839
	RMSE	0.066	0.143	0.110
	χ^2	0.013	0.059	0.034
Freundlich	K	1.085	1.161	1.213
	β	0.122	0.129	0.118
	r^2	0.932	0.938	0.967
	RMSE	0.072	0.091	0.075
	χ^2	0.019	0.022	0.002
Sips	K	3.157	3.878	3.112
	q_{\max}	1.673	1.822	2.014
	β	0.542	0.513	0.417
	r^2	0.982	0.953	0.981
	RMSE	0.038	0.086	0.034
	χ^2	4.29×10 ⁻³	0.019	2.99×10 ⁻³

Table 7. Thermodynamic parameters for the sorption of copper ions on zeolite NaX.

Thermodynamic parameters for copper (II) chloride dihydrate						
Concentration mmol dm ⁻³	ΔS^0 kJ mol ⁻¹ K ⁻¹	ΔH^0 kJ mol ⁻¹	ΔG^0_{298} kJ mol ⁻¹	ΔG^0_{308} kJ mol ⁻¹	ΔG^0_{318} kJ mol ⁻¹	R ²
4.121	0.127	16.385	-21.598	-22.872	-24.147	0.823
8.121	0.133	22.267	-17.508	-18.843	-20.178	0.835
12.299	0.094	13.521	-14.372	15.307	16.244	0.975
18.933	0.074	9.581	-12.567	-13.309	-14.052	0.777
29.381	0.052	3.924	-11.443	-11.959	-12.474	0.953
38.843	0.047	3.352	-10.519	-10.984	-11.450	0.860

Thermodynamic parameters for copper (II) sulphate pentahydrate						
Concentration mmol dm ⁻³	ΔS^0 kJ mol ⁻¹ K ⁻¹	ΔH^0 kJ mol ⁻¹	ΔG^0_{298} kJ mol ⁻¹	ΔG^0_{308} kJ mol ⁻¹	ΔG^0_{318} kJ mol ⁻¹	R ²
4.210	0.185	32.464	-22.620	-24.468	-26.317	0.924
8.311	0.150	26.532	-18.219	-19.721	-21.222	0.995
12.262	0.141	27.032	-14.888	-16.294	-17.770	0.996
20.500	0.092	14.890	-12.605	-13.527	-14.450	0.931
30.344	0.073	10.04	-11.241	-11.971	-12.700	0.997
38.843	0.062	8.209	-10.321	-10.943	-11.564	1.000

Thermodynamic parameters for copper (II) acetate monohydrate						
Concentration mmol dm ⁻³	ΔS^0 kJ mol ⁻¹ K ⁻¹	ΔH^0 kJ mol ⁻¹	ΔG^0_{298} kJ mol ⁻¹	ΔG^0_{308} kJ mol ⁻¹	ΔG^0_{318} kJ mol ⁻¹	R ²
4.275	0.155	27.024	-19.057	-20.604	-22.149	0.858
7.888	0.081	7.643	-16.414	-17.220	-18.028	1
11.168	0.079	9.339	-13.994	-14.776	-15.559	1
18.733	0.078	11.296	-12.026	-12.809	-13.591	0.769
29.256	0.066	9.078	-10.669	-11.331	-11.994	0.814
38.537	0.063	9.088	-9.569	-10.195	-10.821	0.840

CONCLUSION

The objectives of this study were to investigate the optimum process parameters and equilibrium data of copper ions sorption on zeolite NaX in an agitated and temperature-controlled batch reactor. Impact of five process parameters was investigated in this study. The parameters were combined using Taguchi's design of experiments which led to 16 experiments. As a result, it could be concluded that concentration has a very significant role, followed by impeller speed and anion type while other process parameters are less significant.

All isotherms used can be fitted to the experimental equilibrium data but isotherms that took surface heterogeneity into account, Freundlich and Sips isotherm, showed better agreement with the experimental data.

Thermodynamic parameters indicate that copper sorption on zeolite NaX from all solutions used was a spontaneous and endothermic process.

Acknowledgement: This work has been fully supported by the Croatian Science Foundation under the project HETMIX (IP-11-2013-8959).

REFERENCES

1. M. Jabłońska, R. Palkovits, *Appl. Catal. B Environ.*, **181**, 332 (2016).
2. O. P. Tkachenko, A. A. Greish, A. V. Kucherov, K. C. Weston, A. M. Tsybulevski, L. M. Kustov, *Appl. Catal. B Environ.*, **179**, 521 (2015).
3. D. Romero, D. Chlala, M. Labaki, S. Royer, J-P. Bellat, I. Bezverkhyy, J-M. Giraudon, J-F. Lamonier, *Catal.*, **5**, 1479 (2015).
4. K. Maduna Valkaj, A. Katović, S. Zrnčević, *Industrial & Eng.Chem. Res.*, **50**, 4390 (2011).
5. S. Svilović, D. Rušić, R. Žanetić, *C,hem. Biochem. Eng. Q.*, **22**, 299 (2008).
6. S. Svilović, D. Rušić, R. Stipišić, *J. Hazard. Mater.*, **170**, 941 (2009).
7. S. Svilović, D. Rušić, A. Bašić, *Des.*, **259**, 71 (2010).
8. J. Kyziol-Komosińska, C. Rosik-Dulewska, M. Franus, P. Antoszczyszyn-Szpicka, J. Czupiol, I. Krzyżewska, *Pol. J. Environ. Stud.*, **24**, 1111 (2015).
9. H. Y. Yen, J. Y. Li, *Environ. Manage.*, **161**, 344 (2016).
10. H. Y. Yen, C. P. Lin, *Desalin. Water Treat.*, **57**, 11154 (2016).
11. Ö. U. Özdemir, B. Özbay, I. Özbay, S. Veli, *Ecotoxicol. Environ. Saf.*, **107**, 229 (2014).
12. G. Nagpal, A. Bhattacharya, N. B. Singh, *Asian J. Chem.*, **28**, 814 (2016).
13. R. Salahandish, A. Ghaffarinejad, R. Norouzbeigi, *Anal. Methods.*, **8**, 2515 (2016).
14. H. Zheng, D. Liu, Y. Zheng, S. Liang, Z. Liu, *J. Hazard. Mater.*, **167**, 141 (2009).
15. S. Dubey, D. Gusain, Y. C. Sharma, *J. Mol. Liq.*, **219**, 1 (2016).
16. K. Y. Foo, B. H. Hameed, *Chem. Eng. J.*, **156**, 2 (2010).
17. A. M. M. Vargas, A. L. Cazetta, M. H. Kunita, T. L. Silva, V. C. Almeida, *Chem. Eng. J.*, **168**, 722 (2011).
18. S. Hojati, A. Landi, *J. Environ. Stud.*, **40**, 15 (2015).
19. A. Günay, E. Arslankaya, I. Tosun, *J. Hazard. Mater.*, **146**, 362 (2007).
20. B. M. Abu-Zied, *Microporous Mesoporous Mater.*, **139**, 59 (2011).
21. H. Hammoudi, S. Bendenia, K. Marouf-Khelifa, R. Marouf, J. Schott, A. Khelifa, *Microporous Mesoporous Mater.*, **113**, 343 (2008).
22. F. Benaliouche, Y. Boucheffa, P. Ayrault, S. Mignard, P. Magnoux, *Microporous Mesoporous Mater.*, **111**, 80 (2008).

Comparative analysis of phenolic and mineral composition of traditionally used wild medicinal plants from Southeast Serbia

J. M. Velicković*, E. J. Kostić

¹Department of Chemistry, Faculty of Sciences and Mathematics, University of Nish, Višegradska 33,
Faculty of Medicine, University of Nish, Bulevar dr Zorana Đinđića 81,
18000 Nish, Serbia

Received: October 15, 2018; Accepted: January 24, 2020

In this study a comparative analysis was carried out of the contents of total phenols, flavonoids and metals in different extracts of wild winter savory (*Satureja montana* L.) and herb peter (*Primula vulgaris* L.) plants.

The results showed that the content of total phenols in the investigated extracts is very high. The difference in the total content of phenolic compounds depends on the extraction solution. The content of the metal is higher in the extracts of the *Primula vulgaris* L. plant compared to the extracts of the plant *Satureja montana* L. There is a high correlation coefficient between total phenols and flavonoids in both plants. Also, there is a high correlation coefficient between total content of phenol and flavonoids and the contents of Mn and Cu in the plant extracts of *Satureja montana* L., and the content of Mn in the plant extracts of *Primula vulgaris* L. The two cultivars studied: wild winter savory and herb peter plant from Southeast Serbia are suitable for the preparation of teas and herbal extracts because they are an excellent source of polyphenol compounds and a good source of the minerals Fe, Cu, Zn and Mn.

Keywords: total phenols, flavonoids, metals, *Satureja montana* L., *Primula vulgaris* L.

INTRODUCTION

The potency of different medicinal plants is related to their individual mechanisms of action in different disorders. Humans consume and use a variety of medicinal plants in the form of teas, extracts, tinctures and other. Although medicinal plants are widely considered to be of lower risk compared with synthetic drugs, they are not completely free from the possibility of toxicity or other adverse effects [1], therefore, analysis of the plants used in the treatment is necessary. Phenolic compounds from plants belong to a class of bioactive components with antioxidant activities [2, 3]. Flavonoids represent one of the most studied classes of phenolic compounds containing carbohydrate units important for their biological activities [4]. Flavonoids exhibit a wide range of biological effects (antibacterial, antiviral, anti-inflammatory and anti-allergic) by reducing low-density lipoproteins in plasma, inhibiting platelet aggregation, scavenging free radicals, and preventing cell proliferation [5]. However, there is considerable interest in identifying natural antioxidants from plants that protect against free radical damage as an alternative to synthetic medicines.

Winter savory (*Satureja montana* L.) belongs to the *Lamiaceae* family native to the Mediterranean regions. It is a perennial herb (20–30 cm tall) with

white flowers and small rough leaves[6]. Winter savory is a well-known aromatic and medicinal plant which contains various biologically active constituents such as essential oil, triterpenes [7], flavonoids [8], and rosmarinic acid [9]. The whole herb is mildly antiseptic, aromatic, carminative, digestive, mildly expectorant and stomachic, while its essential oil is used in the food industry, liqueurs and in perfumery. The positive effects of savory on human health are attributed to its active constituents which show a high antioxidant effect [10]. The typical phenolic compound of *Satureja montana* L. is carvacrol, and the prevailing carvacrol chemotype occurs also in Italy and the former Yugoslavia [11].

Herb peter (*Primula vulgaris* L.), *Primula* is a plant genus including about 400 species. Some of them are popular garden plants because of their colourful blossoms. Efficacy of primrose extracts, which are rich in saponins, has been demonstrated in a number of pharmacological studies, as potent anti-asthmatic, anti-inflammatory and antiviral properties. Phenolic glycosides and saponins are characteristic compounds for the genus *Primula* [12]. Flavonoids may have existed in nature for over one billion years. Methoxyflavones have important effects in plant biochemistry and physiology, acting as antioxidants, enzyme inhibitors, precursors of toxic substances and have long been recognized to possess anti-allergic, anti-inflammatory, antiviral, anti-proliferative and anti-carcinogenic activities,

* To whom all correspondence should be sent:
E-mail: jasmina@frad.rs

as well as to affect some aspects of mammalian metabolism [13]. Ten lipophilic flavones were isolated from *Primula veris* L. *in vitro* cultures. Two new flavonol glycosides have been identified and isolated from Italian *Primula* species [14]. *Primula* species can also contain allergens and some species are used traditionally to treat epilepsy and convulsions.

Although the effectiveness of medicinal plants is mainly associated with their constituents such as essential oils, vitamins, glycosides, etc., it was found that prolonged intake can cause health problems due to the possible presence of heavy metals [15]. Plants can easily be contaminated by heavy metals in the course of cultivation or later during the processing stage and, therefore, determining the content of the accumulated heavy metals is of high importance. The content of heavy metals is one of the criteria for the use of plant material in the production of traditional medicines and herbal infusions. Therefore, control of heavy metals in medicinal plants and their products should be made such to ensure safety and efficacy of herbal products [16].

However, there is no information about comparative analysis of contents of total phenols, flavonoids, and metals in the different extracts of the herbs peter plant (*Primula vulgaris* L.) and winter savory (*Satureja montana* L.).

The present study investigated the contents of total phenols, flavonoids, and heavy metals of herb peter and winter savory in order to evaluate their medicinal value and to point to an easily accessible source of natural antioxidants that could be used as a possible food supplement or in the pharmaceutical industry. Therefore, this work represents the first report on phenolic content and contents of heavy metals in different extracts of two plant cultivars of wild winter savory and herb peter plant from Southeast Serbia.

Statistical analysis was used to evaluate possible correlations among metal ions amount, and the amounts of phenolic compounds and flavonoids in the investigated extracts.

EXPERIMENTAL

Preparation of materials

Fully dry samples of winter savory (*Satureja montana* L.) and herb peter (*Primula vulgaris* L.), collected throughout the months of April and May 2017, were used for the investigation. This region of Serbia (Soko Banja) at the foothills of the Rtanj mountain is said to be free of negative environmental influences, as it is largely devoid of industries and major highways.

Determination of selected metals

The standard procedure for the determination of selected metals described by the Association of Official Analytical Chemists (AOAC) was followed for the preparation of samples for the analysis of heavy metals [17]. Accurately weighed (2 g) sample was transferred into a silica crucible and kept in a muffle furnace for ashing at 450°C for 3 h and then 5 ml of 6 M HCl was added to the crucible. Care was taken to ensure that all ash came into contact with the acid. Further, the crucible containing acid solution was kept on a hot plate and digested to obtain a clear solution. The final residue was dissolved in 0.1 M HNO₃ solution and made up to 50 ml. Working standard solutions were prepared by diluting the stock solution with 0.1 M nitric acid in order to check the linearity.

Preparation of herbal extracts

The dry samples of winter savory (*Satureja montana* L.) and herb peter (*Primula vulgaris* L.) were ground in a blender, and 2 g samples were extracted by either of the following solvents: ethanol and ethanol-water (50/50, v/v%). Extraction was carried out in an ultrasonic bath for 15 min three times in succession with 30, 20, and 20 ml of the solvent, respectively. The extract was filtered through a Büchner funnel and filter paper (blue collar) (CHEMLAB, Spain), transferred into a 100 ml flask and made up to the mark with the same solvent.

Chemicals and reagents

Quercetin and AlCl₃ were purchased from Sigma Chemical Co. (St. Louis, MO, USA). Folin-Ciocalteu's phenol reagent and sodium carbonate were purchased from Merck Chemical Suppliers (Darmstadt, Germany). Sodium chlorate buffer (pH 1.0) and acetate buffer (pH 4.5) were purchased from the same producer. All other chemicals used, including solvents, were of analytical grade Sigma-Aldrich (GmbH, Steinheim, Germany). The working solutions were prepared immediately before the analysis from the basic solution (concentration 1000 mg l⁻¹ for all metals). For the preparation of standard solutions high-purity Milli-Q water was used. The glassware and polyethylene containers used for analysis were washed with tap water, then soaked overnight in 6 M HNO₃ solution and rinsed several times with ultra-pure water to eliminate absorbance due to detergent.

Determination of the total phenolics

Total phenol contents in the extracts were determined by the modified Folin-Ciocalteu method

[18]. An aliquot of the extracts (1 ml) was mixed with 0.5 ml of Folin-Ciocalteu reagent and 1.5 ml of sodium carbonate solution (20 %). Tubes were vortexed for 15 s and allowed to stand at 40°C for 30 min in order to develop color. Absorbance was then measured at 765 nm using Hewlett Packard UV-VIS spectrophotometer. Total phenol content was expressed as mg g⁻¹ of gallic acid equivalent (GAE). The result of each assay was obtained from three parallel determinations.

Determination of total flavonoid content

Total flavonoid contents were determined using the spectrophotometric method based on the formation of flavonoid complex with aluminum [19]. A volume of 0.5 ml of 2 % AlCl₃ methanol solution was added to 0.5 ml of sample solution. After one hour-standing at room temperature, the absorbance was measured at 420 nm. The yellow color indicated that the extracts contained flavonoids. Total flavonoid content was calculated as concentration of quercetin (mg g⁻¹) using the equation based on the calibration curve.

Statistical analysis

The experimental results were expressed as mean value ± standard error of the mean value of three replicates. In order to estimate statistically any significant differences among mean values, where applicable, the data were subjected to a one-way analysis of variance (ANOVA) test [20].

RESULTS AND DISCUSSION

In our work the content of total phenols was determined in the investigated extracts of dry samples of the plants winter savory (*Satureja montana* L.) and herb peter (*Primula vulgaris* L.) from the region of Southeast Serbia. The content of total phenols in the extracts of the investigated dry samples was determined using Folin-Ciocalteu method and was expressed as GAE g⁻¹ of the dry sample (Fig. 1).

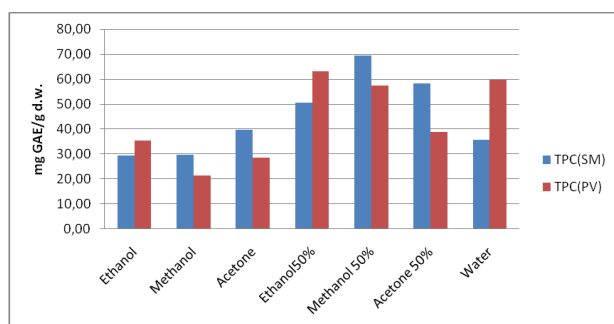


Fig. 1. Comparative study of total phenols content (mg GAE/g d.w.) in the investigated extracts of *Satureja montana* L. and *Primula vulgaris* L.

The results showed that the content of total phenols in the investigated extracts is very high. The highest content of total phenols was in methanol-water (50/50, v/v (%)) extract of winter savory (69.5 mg GAE g⁻¹ d.w.) and in ethanol-water (50/50, v/v (%)) extract of peter herb (63.1 mg GAE g⁻¹ d.w.). The difference in the total content of phenolic compounds depends on the extraction solution. Ethanol-water (50/50, v/v (%)) and (methanol-water (50/50, v/v (%)) extracts of winter savory have a higher content of total phenolics in relation to the water extract. Ethanol, methanol and acetone extracts of herb peter have a lower content of total phenolics in relation to the corresponding extracts which contain 50% of water.

The content of phenols represents a pharmacological characteristic of the plant. On the basis of numerous studies it is known that the content of polyphenol compounds depends on genotype, soil conditions and difference in plant ripening [21-23]. Also, outdoor conditions, like altitude, light, temperature, content of feeding material in the soil can have an effect on the phenylpropanoid metabolism [24]. Study allowed evidencing that *S. montana* L. growing in Egypt has a high content of phenolic and flavonoid compounds which could be responsible for the remarkable radical scavenging and antioxidant properties observed. This promising efficacy suggests its possible role as antioxidant agent, in order to improve antioxidant status and counteract the risk of diseases associated with oxidative stress [25]. It has been reported that the content of total phenols in the water extract of winter savory is 27.1 mg GAE g⁻¹ d.w. [26]. The results of this study agree with those of our work with respect to total phenols. The differences in total phenol compounds content depended on the extraction medium used and are a consequence of the different polarity of the organic solvents used and their mixtures, which selectively extract individual phenol compounds.

On the basis of the experimental results shown in Fig. 2, the content of total flavonoids in the extracts of the investigated plants is much lower than the phenol content. The content of total flavonoids is expressed in mg of quercetin equivalent (QE g⁻¹ d.w.).

The content of total flavonoids is very low and ranges from 2.3 to 8.5 mg QE g⁻¹ d.w. (ethanol and ethanol-water (50/50, v/v (%)) extract of winter savory and from 5.7 to 21.2 mg QE g⁻¹ d.w. extract of peter herb. The highest content of total flavonoids has the water extract of herb peter. On the basis of the experimental results the content of flavonoids in

the extracts of the investigated herb peter is almost uniform.

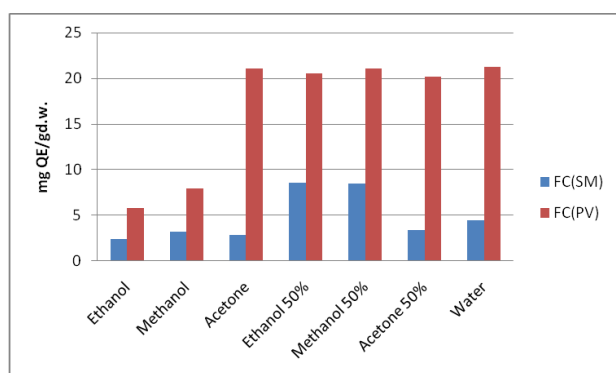


Fig. 2. Comparative study of flavonoids content (mg QE/g d.w.) in the investigated extracts of *Satureja montana* L. and *Primula vulgaris* L.

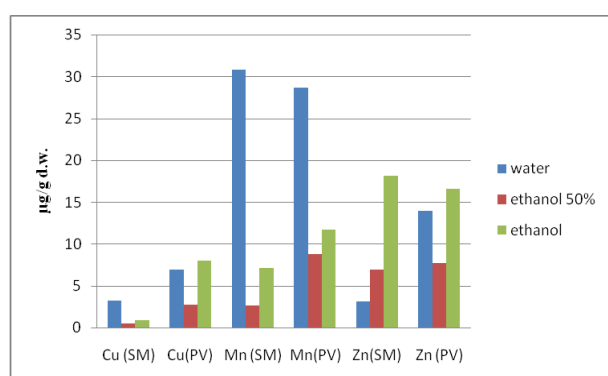


Fig. 3. Comparative survey of metal content in the extracts of *Satureja montana* L. and *Primula vulgaris* L.

In their study, Nayan *et al.* investigated the phenolic composition, antioxidant and radical scavenging activities of *Primrose (Primula vulgaris L.)* [27]. Comparing our results for the total content of phenol and flavonoids of the investigated extracts of plants from the Southeast area of Serbia with the results of other authors, we can see a firm agreement.

The presence of heavy metals in the extracts can be explained by possible complex formation that occurs between metal and organic compounds in the plants. The presence of metals in plants is a result of the transfer of metals from the soil, water and atmospheric precipitation during growing. Content of metals in the investigated plants *Satureja montana* L. and *Primula vulgaris* L. is presented in Table 1.

Table 1. Content of metals in the investigated plants *Satureja montana* L. and *Primula vulgaris* L.

Plant	Fe (µg/g)	Cu (µg/g)	Zn (µg/g)	Mn (µg/g)
<i>Satureja montana</i> L.	265.24 ±4.70	28.75±0.57	31.00±0.62	40.65 ±0.85
<i>Primula vulgaris</i> L.	303.61±3.16	35.70±0.71	22.90±0.45	38.20±1.15

Ions of Cd, Pb, and Cr were not detected in the plants. Contents of other metals are generally low in the extracts using different solvents. Iron content is the highest in all plant extracts. The content of the metal is higher in the extracts of the *Primula vulgaris* L. plant compared to the extracts of the plant *Satureja Montana* L. (Fig. 3).

The highest content of Fe is in water (160.0<182.0 µg/g), 50% ethanol (110.28>65.33 µg/g) and ethanolic (12.40>8.40 µg/g) extract of both plants.

The content of the metal is higher in the extracts of the *Primula vulgaris* L. plant compared to the extracts of the plant *Satureja montana* L. The content of Cu and Zn is higher in ethanolic than in ethanol-water extracts of both plants. Water extracts have a higher content of Cu and Mn than ethanolic and ethanol-water extracts of both plants.

Minerals are inorganic substances present in all body tissues and fluids and their presence is necessary for the maintenance of certain physicochemical processes which are essential to life [15,28, 29]. These include calcification of bone, blood coagulation, neuromuscular activity, acid-base equilibrium, enzyme activity, osmotic regulation.

Analyzed was the correlation between the contents of total phenols, flavonoid compounds, and heavy metals of the investigated extracts, which is presented in Table 2. This work represents the first report on the correlation between the contents of total phenols, flavonoid compounds, and heavy metals of the investigated extracts of selected medicinal plants from Southeast Serbia.

There is a high correlation coefficient between total phenols and flavonoids in both plants. Also, there is a high correlation coefficient between total content of phenol and flavonoids and the content of Mn and Cu in the plant extracts of *Satureja montana* L., and the content of Mn in the plant extracts of *Primula vulgaris* L. There is a high correlation coefficient between the contents of Fe and Zn, Cu and Mn in the extracts of *Satureja montana* L., and between Fe and Mn, Zn and Cu in the extracts of *Primula vulgaris* L.

These differences are a result of phylogenetic characterization of plants since they originate from the same field and the use of different extraction solvents.

Our study confirms the results of many authors who have established that the selected medicinal plants are an excellent source of polyphenol compounds, which together with other biologically active compounds as vitamin C, vitamin E and carotenoids can be regarded as a source of natural antioxidants. They may also be a good source of the minerals Fe, Cu, Zn and Mn. Based on these results we recommend the use of the investigated extracts because they are an excellent source of polyphenol

compounds and a good source of minerals Fe, Cu, Zn and Mn, as presented in Table 3.

Extraction coefficient, *EC*, is defined by Eq. (1):

$$EC = \frac{CM(\text{extract}) \times 100}{CM(\text{plant})} \quad (1)$$

The extraction coefficients *EC* obtained in this study varied markedly. Based on the results, the analyzed elements can be classified into three groups: elements with a low extraction coefficient (less than 10%); elements with a medium extraction coefficient (10–30%), and elements with a high extraction coefficient (more than 30%).

Table 2. Correlation coefficients of total phenolic, flavonoids contents, and metal content in the investigated extracts *Satureja montana* L. and *Primula vulgaris* L.

Plant	-	Total phenols content ^a	Flavonoid content ^b	Fe mg/kg	Cu mg/kg	Zn mg/kg	Mn mg/kg
<i>Satureja montana</i> L.	Total phenols content ^a	1.0	0.97	0.01	0.90	0.03	0.80
	Flavonoid content ^b		1.0	0.08	0.89	0.05	0.94
	Fe (mg/kg)			1.0	0.4	0.98	0.25
	Cu (mg/kg)				1.0	0.16	0.98
	Zn (mg/kg)					1.0	0.15
	Mn (mg/kg)						1.0
<i>Primula vulgaris</i> L.	Total phenols content ^a	1.0	0.97	0.83	0.12	0.04	0.98
	Flavonoid content ^b		1.0	0.94	0.01	0.00	0.91
	Fe (mg/kg)			1.0	0.02	0.04	0.78
	Cu (mg/kg)				1.0	0.98	0.18
	Zn (mg/kg)					1.0	0.05
	Mn (mg/kg)						1.0

^aExpressed as mg GAE/g d.w.

^bExpressed as mg QE/g d.w.

Table 3. Coefficients of extraction of metals with different solvents

Plant	Extract	<i>EC</i> (%)			
		Fe	Cu	Zn	Mn
<i>Satureja montana</i> L.	Water	60.32	11.02	10.10	75.76
	Ethanol 50%	41.57	0.76	22.25	6.39
	Ethanol	4.67	3.90	58.38	17.46
<i>Primula vulgaris</i> L.	Water	59.94	19.32	60.69	75.13
	Ethanol 50%	21.51	7.65	33.62	22.98
	Ethanol	2.76	22.4	72.48	30.62

The extraction coefficient mostly depends on the extraction medium. The highest transfer of heavy metals is in the aqueous extract. The extraction coefficient also depends on the plant species that is being extracted. In aqueous extracts of the investigated plants certain metals were detected while the concentration of other metals remained below the detection limits of the apparatus. The aqueous and aqueous/ethanolic extracts had a low efficiency of Fe extraction; medium efficiency of Mn and Cu extraction, and high efficiency of Zn extraction. The ethanolic extracts of all plants had medium and high efficiencies of extraction of the investigated elements. Based on these results, we recommend the use of aqueous extracts of lower abundance for the heavy metals extraction.

CONCLUSIONS

All investigated extracts of the selected medicinal plants, winter savory (*Satureja montana* L.) and herb peter (*Primula vulgaris* L.) contain high polyphenol concentration. The contents of heavy metals in their extracts are low. The investigated plants from Southeastern Serbia are suitable for the preparation of teas and herbal extracts due to the low content of toxic metals (Zn, Fe, Cu, Mn) and the high content of phenolic compounds.

REFERENCES

1. P. A. G. M. De Smet, *Clin. Pharmacol. Ther.*, **76**, 1 (2004).
2. E. G. Kovatcheva-Apostolova, M. I. Georgiev, M. P. Ilieva, L. H. Skibsted, A. Rodtjer, M. L. Andersen, *Eur. Food Res. Technol.*, **227**, 1243 (2008).
3. A. Kirca, E. Arslan, *J. Food Sci. Technol.*, **43**, 2038 (2008).
4. X. Yang, Y. Sun, Q. Xu, Z. Guo, *Org. Biomol. Chem.*, **4**, 2483 (2006).
5. E. Middleton, C. Kandaswami, T. C. Theoharides, *Pharm. Rev.*, **52**, 673 (2000).
6. N. Bezic, M. Skocibusic, V. Dunkic, *Acta Bot. Croatica*, **64** (2), 313 (2005).
7. J. Escudero, J. C. Lopez, R. M. Rabanal, S. Valverde, *J. Natur. Products*, **48**, 128 (1985).
8. F. A. Thomas-Barberan, S. Z. Huisain, M. J. Gil, *J. Biochem. System. and Ecology*, **16**, 43 (1987).
9. A. Reschke, *Z. Lebensmitt. Unters. Forsch.*, **176**, 116 (1983).
10. H. L. Madsen, B. R. R. Nielsen, G. Bertelsen, L. H. Skibsted, *J. Food. Chem.*, **57**, 331 (1996).
11. E. Stahl-Biskup, Springer, Berlin, 1998, p. 522.
12. A. Muller, M. Ganýera, H. Stuppner, *J. Chromat. A*, **1112**, 218 (2006).
13. C. W. Huck, C. G. Huber, K. H. Onganyá, G. K. Bonn, *J. Chromat. A*, **870**, 453 (2000).
14. G. Fýco, G. Rodondý, G. Flamýný, D. Passarella, F. Tome, *Phytochem.*, **68**, 1683 (2007).
15. S. Jabeen, M. Tahir Shah, S. Khan, M. Qasim Hayat, *J. Med. Plants Res.*, **4**, 559 (2010).
16. S. Nookabkaew, N. Rangkadilok, J. Satayavivad, *J. Agr. Food Chem.*, **54**, 6939 (2006).
17. Official Methods of Analysis, Association of Official Analyt. Chem. EUA (2000).
18. V. L. Singleton, J. A. Rossi, *J. American Enol. Viticult.*, **16**, 144 (1965).
19. A. A. L. Ordon Ez, J. D. Gomez, M. A. Attuone, M. I. Isla, *J. Food Chem.*, **97**, 452 (2006).
20. Statistical Analysis and Reporting System, ser. Guide, Version 1.0, IBM (1999).
21. D. D. Orhan, A. Hartevioğlu, E. Küpeli, E. Yesilada, *J. Ethnopharm.*, **112**, 394 (2007).
22. N. Gougoulías, N. Mashev, *Oxid. Communic.*, **1**, 25 (2015).
23. N. Gougoulías, *Oxid. Communic.*, **1**, 35 (2015).
24. R. A. Dixon, N. L. Paiva, *J. Plant Cell.*, **7**, 1085 (1995).
25. H. D. Hassanein, H. A. H. Said-Al Ahl, M. M. Abdelmohsen, *J. Pharm. Pharm. Sci.*, **6**(4), 975 (2014).
26. D. Chrpova, L. Kouřimska, M. H. Gordon, V. Heřmanova, I. Roubičkova, J. Panek, *J. Food Sci.*, **28**, 317 (2010).
27. D. Nazan, A. G. Azize, N. Hayrunnisa, D. Yaşar, *J. Experiment. Biol.*, **4**(2), 395 (2014).
28. S. A. Khan, L. Khan, I. Hussain, K. B. Marwat, N. Akhtar, *J. Weed Sci. Res.*, **14**, 101 (2008).
29. M. N. Mitic, D. A. Kostic, A. N. Pavlovic, S. B. Tosic, B. T. Stojanovic, D. D. Paunovic, *Oxid. Communic.*, **37**(4), 1074 (2014).

Comparison of selenium determination in bone tissue samples from lambs, piglets and calves by spectrophotometry and inductively coupled plasma – tandem mass spectrometry

L. Dospatliev^{1*}, M. Ivanova²

¹Department of Pharmacology, Animal Physiology and Physiological Chemistry, Trakia University, 6000 Stara Zagora, Bulgaria

²Department of Informatics and Mathematics, Trakia University, 6000 Stara Zagora, Bulgaria

Received: January 30, 2019; Revised: February 25, 2020

Selenium measurement in bone tissue or liver is the most accurate way to assess Se status for diagnostic purposes. This study was conducted in order to develop a methodology for the mineralization of bone tissue samples using acid mixture of HNO₃+HCl+HF and also to compare the spectrophotometric method with that using inductively coupled plasma – tandem mass spectrometry (ICP-MS/MS) for detection and quantification of Se. Detection by ICP-MS/MS was optimized by yttrium for Se⁷⁸, used as an internal standard. Selenium was determined quantitatively by both methods in samples taken from different organs from lambs, piglets and calves: shoulder blade (scapula), large shin bone (tibia) and spine (vertebral column). The results showed that ICP-MS/MS can be reliably used in place of a spectrophotometric method to quantify Se in bone tissue using an acid mixture of HNO₃+HCl+HF for sample mineralization.

Keywords: Se, Bone tissue, Acid mixture of HNO₃+HCl+HF, UV-Vis spectrophotometry, ICP-MS/MS

Abbreviations: AOAC – Association of Official Analytical Chemists; ICP-OES – inductively coupled plasma-optical emission spectrometry; ICP-MS – inductively coupled plasma-mass spectrometry; ETAAS – electrothermal atomic absorption spectrometry; FL – fluorometry; HG-AAS – hydride generation atomic absorption spectroscopy; ICP-MS/MS – inductively coupled plasma-tandem mass spectrometry.

INTRODUCTION

Today it is universally known that most diseases have a chemical origin and develop because of a surplus, deficit or imbalance of micro- and macroelements in the body [1]. Chemical elements are active centers of all enzymes, hormones, antibodies, etc. [2]. We have recently observed increased interest in the thorough investigation of trace element exchange in the human organism, as well as in animals under normal and pathological conditions. A new trend called microelementology develops in biomedical research [3, 4]. A Se deficit may occur in a variety of diseases, and its restoration can lead to normalizing the impaired functions of the body. Selenium has a specific therapeutic value. Se imbalance is associated with the pathogenesis of diseases going under the name of "Free radical diseases". Se is an essential trace component of body's antioxidant defenses against free radicals [1, 5]. Se is important for the normal activity of glutathione peroxidase. A trace element deficiency may affect the balance of pro- / antioxidant system, leading to weakening of antioxidant status and anti-cancer protection. The importance of Se for the normal development and functioning of the tissues of the human body is considered nowadays to be scientifically proven.

One of the selenium deficiency manifestations is its influence on the articular cartilage and bone tissue (Kashin-Beck disease). The incidence of Se deficiency is significantly greater than that of Se intoxication, so that veterinary laboratories are often concerned about the detection of low levels of Se in diagnostic assays. Se is an essential cofactor for sulfotransferase that performs the transfer of sulfur residue to glycosaminoglycan molecules. That is why Se participates in cartilage tissue metabolism and its components [6, 7]. Selenium status was assessed as an alleged factor in the etiology of certain cancers. Research has shown that there is a reverse correlation between cancer mortality and selenium status. In this context, the aim of our study is to develop a methodology for simultaneous determination of Se and bone tissue macro- and micronutrients by ICP-MS/MS, as well as to compare Se concentrations acquired by ICP-MS/MS with the values obtained for the same samples using UV-Vis spectrophotometry.

EXPERIMENTAL

Facilities

Selenium was determined in the samples using an ICP-MS/MS instrument equipped with an octopole reaction system positioned in-between two quadrupole mass analyzers and a JEOL JNM

* To whom all correspondence should be sent:
E-mail: lkd@abv.bg

DELTA 500 spectrophotometer at a Se wavelength of 378.5 nm.

Table 1. ICP-MS/MS parameters used

Plasma and gas conditions	Value
RF power	1500 W
Plasma gas flow rate	15 L min ⁻¹
Auxiliary gas flow rate	0.86 L min ⁻¹
Carrier gas flow rate	0.9 L min ⁻¹
Sampling depth	8.0 mm
Reaction or collision gas	hydrogen or helium
Reaction or collision gas flow rate	4.6 mL min ⁻¹
Data acquisition	Se (78)
Monitored isotopes (m/z)	
Data point	3 points/peak
Integration time	0.3 s/isotope
Repetition	5 times

Reagents

Reagents were qualified as pure (Merck and Fluka). The standard solutions for ICP-MS/MS determination of Se with a concentration of 1000 mg kg⁻¹ were supplied by Merck, Darmstadt Germany. Water was deionized in a Milli Q system (Millipore, Bedford, MA, USA) to a resistivity of 18.2 MΩ cm. All plastic and glassware were cleaned by soaking in dilute HNO₃ (1/9, v/v) and were rinsed with distilled water prior to use.

Samples

The samples of organ meat were bought in local supermarkets and butchers' shops of Stara Zagora (a city in Bulgaria). They were then transported to the laboratory of the Department of Chemistry, where they were dried in a fan oven at 60 °C for 48 h, their edible parts having been previously separated. Finally, samples were homogenized and kept in dark plastic polyethylene bottles at - 18 °C until analyzed.

Mineralization of samples

Part 1: We weighed 3.0 g of air-dried bone tissue to the nearest 0.01 g in a round-bottomed 100 mL flask and added 22.5 mL of HCl and 7.5 mL of HNO₃. We connected the flask to a reflux condenser and let it stand for no less than 16 h at room temperature, then gently heated to boiling for 2 h. After cooling and flushing the condenser with 25 mL of 12.5% nitric acid the sample was filtered and 100 mL of 12.5% nitric acid was added to the part of it in liquid phase.

Part 2: The undissolved component after the first phase was dried at 105 °C and quantitatively transferred into a 50 mL teflon vessel with a well-

fitting lid. We added 5 mL of hydrofluoric acid and heated for 30 min at 140 – 150 °C. After cooling, we added 50 mL of saturated boric acid solution and transferred it to a 100-mL volumetric flask after which distilled water was added to the mark.

Microwave acid digestion method used for sample preparation

An amount of 0.2 g of samples was taken into digestion tubes and 5 mL of HNO₃ (65%), 1 mL of HCl (37%) and 3 mL of H₂O₂ (30%) were added. The samples were digested in a microwave closed system Multiwave 3000 (Anton Paar, Germany) according to the following heating program: (1) 15 min ramp to 120 °C, (2) 20 min ramp to 200 °C, and (3) 20 min hold at 200 °C. After digestion, the samples were diluted up to 25 mL with 2 mL L⁻¹ HNO₃. Duplicate analysis was performed on the samples. Blank digestion was carried out in the same way.

Statistical analysis

All statistical computing, tests and graphics were performed with the statistical software R version 3.5.1 (2018-07-02). The data were presented as mean value and standard deviation (SD). The results were analyzed through one-way analysis of variance (ANOVA) followed by Duncan's test with p<0.05. Multiple pair-wise comparisons of means among species were obtained by the Tukey HSD test with p<0.05 and box and whisker plots.

RESULTS AND DISCUSSION

It is well known that in making ICP-MS/MS quantitative measurements, the most commonly used is the method of line calibration (MLC). It is based on solutions obtained by diluting a mono or multi standard with 1% or 2% acid solution used in sample mineralization (Fig. 1).

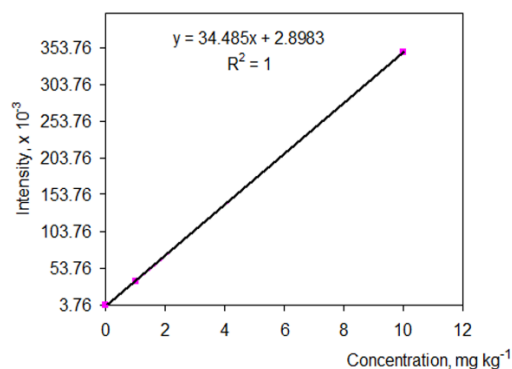


Fig. 1. Se calibration at 0.1, 1 and 10 mg kg⁻¹.

C_K unknown concentration was determined by the equation $I = M_2 \cdot C_K + B_2$, where I is the sample intensity.

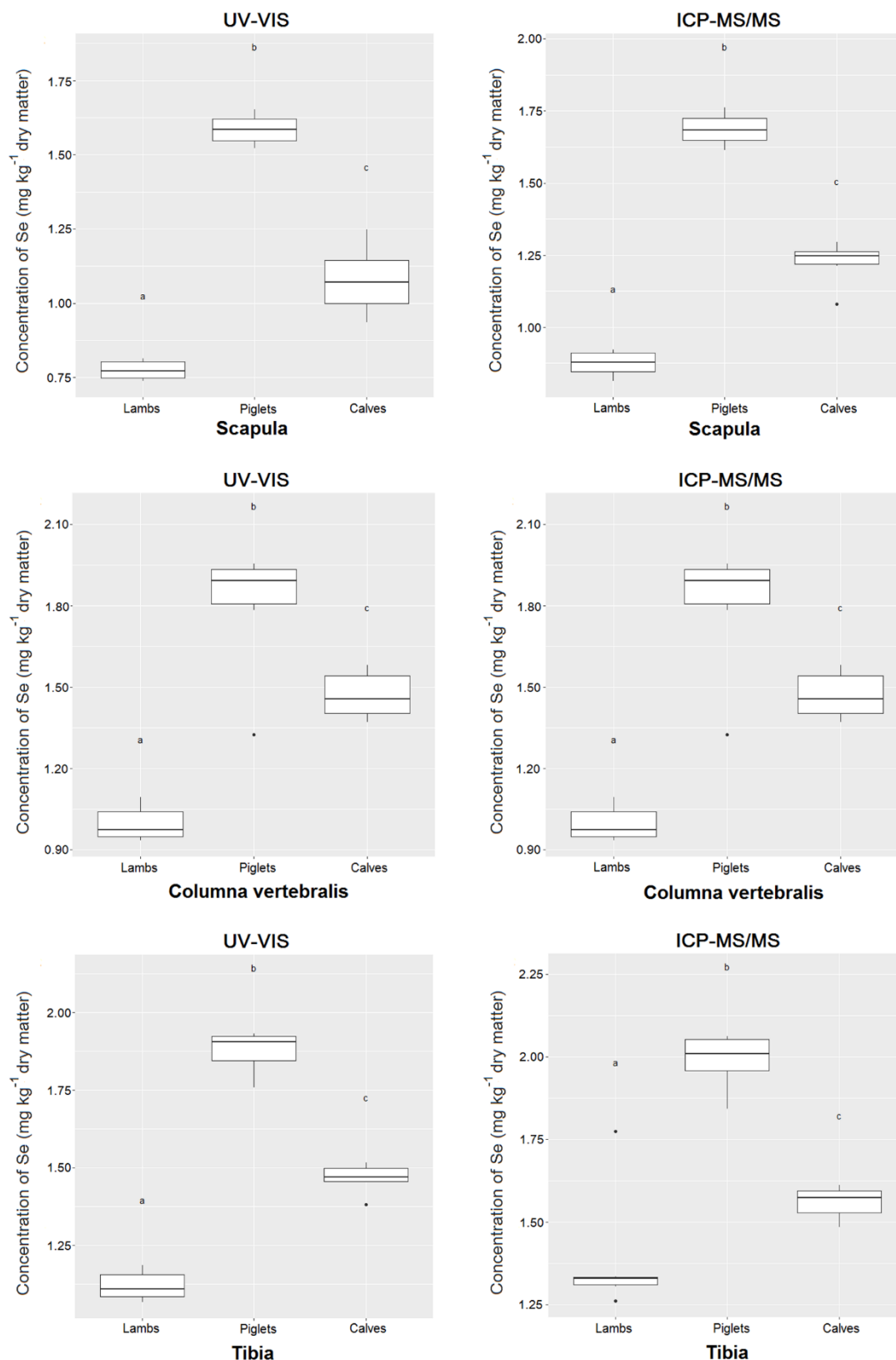


Fig. 2. Box and whisker plots representing the distribution of Se content in bone tissue as determined by UV-Vis spectrophotometry and ICP-MS/MS (n=6). The box represents the interquartile range, solid line within the box represents the median, and the whiskers represent the extremes of the distribution. Letters represent the results of Tukey's post hoc comparisons of mean values among the species (p<0.05).

Ideally, analytical methods must be able to accurately determine selenium in various matrix samples at low concentrations from micrograms per kilogram to several hundred micrograms per gram. The methods approved by the AOAC are the best specific analysis procedures under controlled conditions [8-10]. Overall, the most widely used trace elements determination techniques in bone samples are FL [11], HG-AAS, UV-Vis spectrophotometry, ETAAS [12], X-ray fluorescence, ICP-OES [13-15] and ICP-MS [14-20]. Some of these methods can give good selectivity and sensitivity, but require very expensive reagents, as well as time-consuming and complicated procedures. In recent years there has been a trend of displacing the classical colorimetric method for determining selenium in biological materials by the modern ICP-MS/MS method [21-25]. The main advantages of the ICP-MS/MS method are associated with the measurement speed and the possibility for simultaneous determination of the mass of bone macro- and micronutrients. The application of this method is not easy because of the conflicting results when comparing it with the established in practice colorimetric one. This requires expanding the volume of research in this area and accumulation of more experimental results in terms of sample preparation methods of biological samples.

As seen from the results presented in Fig. 2, both methods (spectrophotometric and ICP-MS/MS) for selenium measurement in samples give comparable results. In samples from lambs, the UV-Vis spectrophotometry yielded 0.775 mg kg⁻¹ in the scapula; 0.896 mg kg⁻¹ in the vertebral column and 1.120 mg kg⁻¹ in the tibia. Through ICP-MS/MS, the same samples gave Se amounts as follows: 0.874 mg kg⁻¹ in the scapula; 0.997 mg kg⁻¹ in the vertebral column and 1.388 mg kg⁻¹ in the tibia. In samples from piglets, the UV-Vis spectrophotometry yielded 1.585 mg kg⁻¹ in the scapula; 1.739 mg kg⁻¹ in the vertebral column and 1.876 mg kg⁻¹ in the tibia. Through ICP-MS/MS, the same samples gave Se amounts as follows: 1.686 mg kg⁻¹ in the scapula; 1.792 mg kg⁻¹ in the vertebral column and 1.985 mg kg⁻¹ in the tibia. In samples from calves, the UV-Vis spectrophotometry yielded 1.028 mg kg⁻¹ in the scapula; 1.328 mg kg⁻¹ in the vertebral column and 1.466 mg kg⁻¹ in the tibia. Through ICP-MS/MS, the same samples gave Se amounts as follows: 1.275 mg kg⁻¹ in the scapula; 1.471 mg kg⁻¹ in the vertebral column and 1.559 mg kg⁻¹ in the tibia.

The published scientific information leads to the conclusion that the ICP-MS/MS method gives better results for the total selenium content in bones than

the spectrophotometric method [26-29]. However, there are a lot of exceptions and conflicting results, so that no definite answer can be given. It should be borne in mind that in none of the sample mineralization studies hydrofluoric acid was used, i.e. the matrix did not pass into the solution, being necessary to use a mixture of HNO₃+HCl+HF. The use of a mixture of HNO₃+HCl+HF ensures total bone sample digestion while the methods described in literature use different acid mixtures without the participation of hydrofluoric acid in surveyed element extraction.

CONCLUSIONS

It can be concluded that:

- Sample mineralization for analysis is a critical step in obtaining accurate data about Se content. This is particularly important in the studies on biological materials, because most often they are not sufficiently homogeneous and usually contain variable matrices;
- Although there is some matrix interference, the correction factor introduction to the calibration curve results requires more experimental results and mathematical processing.

The ICP-MS/MS advantages over alternative methods include: application on various types of samples, high sensitivity, need for minimal sample preparation, small sample sizes, as well as both multi-element analysis and high performance.

REFERENCES

1. A. Avtsyn, A. Lark, M. Roche, L. Strochkova, Human microelementoses: etiology, classification, organopathology, Medicine, KMK, Moscow, 1991.
2. L. Anikin, L. Nikitina, Selenium: ecology, pathology, correction, Chita, 2002.
3. M. Abdelrahman, R. Kincaid, *J. Dairy Sci.*, **78**, 625 (1995).
4. V. Tutelian, V. Prince, S. Khotimchenko, N. Golubkina, N. Sokolov, Selenium in the human body. Metabolism, antioxidant properties, role in carcinogenesis, Moscow Academy of Medical Sciences, Moscow, 2002.
5. W. Brumbaugh, M. Walther, *J. Assoc. Off. Anal. Chem.*, **74**(3), 570 (1991).
6. J. Aaseth, H. Frey, E. Glattre, *Biol. Trace Elem. Res.*, **24**, 147 (1990).
7. R. Olivas, O. Donard, C. Camara, P. Quevauviller, *Anal. Chim. Acta*, **286**, 357 (1994).
8. AOAC, Official methods of analysis, 20th edn., Washington, DC, 2016.
9. J. Bellanger, *J. AOAC Int.*, **78**(2) 477 (1995).
10. R. Isaac, M. Ihnat, in: Official methods of analysis of AOAC international, 16th edn., P. Cunniff (ed.), 1995, Chapter 3, p. 20.
11. M. Rose, M. Knaggs, L. Owen, M. Baxter, *J. Anal. Atom. Spectrom.*, **16**, 1101 (2001).

12. I. C. Chuang, Y. L. Huang, T. H. Lin, *Anal. Sci.*, **15**(11), 1133 (1999).
13. J. Bland, D. Altman, *Stat. Methods Med. Res.*, **8**, 135 (1999).
14. G. M. Farias, R. G. Wuilloud, S. Moyano, J. A. Gasquez, R. A. Olsina, L. D. Martinez, *J. Anal. Toxicol.*, **26**(6), 360 (2002).
15. L. Dospatliev, G. Mihaylova, M. Varbanov, *Ecology and Future*, **10**(1-2), 29 (2011).
16. R. Forrer, K. Gautschi, A. Stroh, H. Lutz, *J. Trace Elem. Med. Biol.*, **12**, 240 (1999).
17. R. Forrer, C. Wenker, K. Gautschi, H. Lutz, *Biol. Trace Elem. Res.*, **81**, 47 (2001).
18. H. Matsuura, A. Hokura, F. Katsuki, A. Itoh, H. Haraguchi, *Anal. Sci.*, **17**, 391 (2001).
19. R. E. Gosslim, R. P. Smith, H. C. Hodge, L. E. Braddock, *Food. Chem. Toxicol.*, **45**, 1060 (2007).
20. I. Boevski, M. Milanova, N. Velitchkova, I. Havezov, S. Velitchkov, N. Daskalova, *Eurasian J. Anal. Chem.*, **3**(1), 19 (2008).
21. X. N. Lin, Q. Dai, W. D. He, X. L. Wei, H. Y. Zhang, X. C. Zeng, Y. Q. *Journal of Food Safety and Quality*, **8**, 1572 (2017).
22. G. Papadomichelakis, E. Zoidis, A. C. Pappas, K. C. Mountzouris, K. Fegeros, *Meat Sci.*, **131**, 132 (2017).
23. S. Meyer, M. Markova, G. Pohl, T. A. Marschall, O. Pivovarova, A. F. H. Pfeiffer, T. Schwerdtle, *J. Trace Elem. Med. Biol.*, **49**, 157 (2018).
24. A. L. Vieira, K. Miranda, A. Virgilio, E. C. Ferreira, J. A. G. Neto, *J. Anal. Atom. Spectrom.*, **33**, 1354 (2018).
25. C. B. Williams, G. L. Donati, *J. Anal. Atom. Spectrom.*, **33**, 762 (2018).
26. B. Sun, M. Xing, *Biol. Trace Elem. Res.*, **169**, 359 (2016).
27. K. D. Cashman, A. Hayes, *Meat Sci.*, **132**, 196 (2017).
28. M. Malhi, N. Bhatti, A. H. Shah, S. A. Soomro, M. N. Sanjrani, *PJAAEVS*, **33**(2), 254 (2017).
29. O. Miedico, M. Iammarino, M. Tarallo, A. E. Chiaravalle, *Int. J. Food Prop.*, **20**(12), 2888 (2017).

Development of a novel agitated vessel for gas-induction to improve the gas-liquid mass transfer

G. Chinnasamy^{1*}, S. Kaliannan¹, P. M. Jeganathan²

¹Department of Chemical Engineering, Kongu Engineering College, Perundurai, Erode-638060, Tamilnadu, India

²Department of Food Science and Nutrition, Periyar University, Salem-636011, Tamilnadu, India

Received: February 06, 2019; Revised: February 20, 2020

A novel agitated vessel was developed for improving the gas-liquid mass transfer by a self-inducing mechanism. The effects of aeration time, orifice submergence depth (0.10 - 0.30 m), total gas-free liquid level (0.20 - 0.40 m) and impeller speed on the dissolved oxygen content of water and the volumetric mass transfer coefficient were investigated. The results indicated that the dissolved oxygen content of water increased with increase in aeration time and reached an equilibrium value. It was also noticed that the time required for attaining the equilibrium value of dissolved oxygen content increased with increase in orifice submergence depth and hence with increase in total gas-free liquid level. The volumetric mass transfer coefficient was found to increase with increase in rotational speed of the impeller but decreased with increase in liquid level to tank diameter ratio (H/T) at all the impeller speeds chosen for the present work.

Keywords: air-inducing reactor, critical speed, gas holdup, dissolved oxygen, mass transfer coefficient.

Nomenclature: C – Dissolved oxygen concentration in water at time t , mg/L; C_0 – Initial dissolved oxygen concentration in water, mg/L; C^* – Equilibrium dissolved oxygen concentration in water, mg/L; D – Diameter of the impeller, m; h – Orifice submergence depth, m; H – Total gas-free liquid height, m; ID – Inner diameter, m; k_{La} – Volumetric mass transfer coefficient, min^{-1} ; N – Rotational speed of the impeller, rpm (revolutions per minute); OD – Outer diameter, m; P – Shaft power, kW; P/V – Power consumption per unit volume of the gas-free liquid, W/m^3 ; t – Time, min; T – Tank diameter, m; V – Volume of the gas-free liquid, m^3 ; ε_G – Fractional gas holdup.

INTRODUCTION

Hydrogenation of a variety of substances, ozonolysis, oxidation, alkylation, hydrochlorination and hydrobromination, halogenation, ammonolysis, etc. are industrially important unit processes, which necessitate the complete utilization of the solute gas to a practically possible extent. In a conventional agitated vessel used for gas-liquid operation, the gas is sparged at the bottom of the tank in the form of bubbles and the gas-liquid system is well agitated in order to improve the effective utilization of the gas. But in most of the gas-liquid operations/processes carried out in a conventional agitated vessel, the utilization of gas in a single pass is considerably low due to the low residence time of the gas in the liquid. The utilization of the gas phase in such systems could be improved by external recycling of the unused/unreacted gas, which requires additional energy. Surface aeration is one of the options for internal recycling of the gas in an agitated vessel; but involves some limitations such as high maintenance requirement, inefficient aeration, limited mixing performance, inefficiency at higher liquid depths, etc. Self-inducing type of agitated vessels could provide better contact between gas and liquid at relatively lower power consumption when compared

with surface aerators [1–8]. Moreover, by using self-inducing reactors, the solid particles could be kept in suspension at relatively lower impeller speeds than that required by a surface aerator [9, 10].

The gas-inducing reactors found in the literature have a hollow shaft and a hollow impeller. The acceleration of the fluid caused by the rotation of the impeller leads to a reduction in the static pressure. When the area of the low pressure is connected to the gas space, and the reduction in pressure is higher enough to overcome the resistances in the path of the gas, induction of the gas takes place [9–11]. Apart from the hollow-impeller and hollow-shaft combination for gas-induction, stator-rotor (draft-tube) type of gas-induction is also found in the literature [12, 13]. There have been continuous modifications in the design and fabrication of air-inducing reactors over the past three decades [14]. However, all the air-inducing reactors reported so far in the literature could be classified into any one of the three types, namely, stator-rotor type, hollow-impeller and hollow-shaft type and surface aerator type, respectively. Of the three types of air-inducing reactors, the hollow-impeller and hollow-shaft types were investigated by the majority of the researchers. There are many complications in the design and fabrication of hollow-impeller and hollow-shaft type

* To whom all correspondence should be sent:
E-mail: cgomadurai@gmail.com

of the air-inducing reactors due to their complicated geometry. Moreover, the mechanisms of air-induction reported in the literature necessitate the complete fabrication of an air-inducing impeller system, and cannot convert a conventional agitated vessel into an air-inducing reactor.

In the present study, a novel method was developed for self-induction of air in order to improve the gas-liquid mass transfer performance of a self-inducing agitated vessel. A self-inducing tube set was designed, fabricated and attached to the impeller shaft for converting a conventional agitated vessel into a self-inducing reactor. The gas-liquid mass transfer performance of the newly developed self-inducing reactor was analyzed by taking water as the working fluid and measuring the dissolved oxygen content of water upon induced aeration under various operating conditions.

EXPERIMENTAL

In order to study the performance of the novel air-inducing impeller, a conventional baffled agitated vessel retrofitted with a specially designed air-inducing tube-bundle was fabricated. The schematic diagram of the experimental setup is shown in Fig. 1.

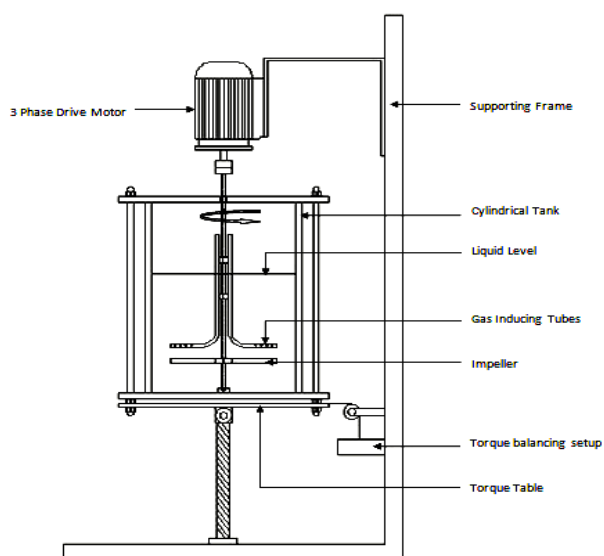


Figure 1. Experimental setup of the gas inducing mechanically agitated contactor.

Agitated vessel

A flat-bottomed cylindrical agitated vessel of 0.455 m inner diameter, 0.012 m wall thickness, and 0.570 m height, made up of acrylic material, was mounted on a torque-table fixed to the floor. Four vertical baffles were fitted to seize the vortex formation and ensure effective mixing of the working fluid. The impeller diameter and the baffle width were 1/3 and 1/10 of the inner diameter of

tank, respectively. The impeller, mounted on a vertical solid shaft, was driven by a 2 hp, 3-phase AC induction motor (Monark, Stark Motors, India). The rotational speed (N) of the impeller was regulated by a speed control drive (Commander SK, Emerson, India) and the power consumed by the motor was measured using two single phase digital wattmeters (Ampere, India). The shaft power (P) was calculated from the counter weight on a load cell which was connected to the torque table. The impeller speed was measured using a digital tachometer (Systems, India). The vessel was covered to avoid surface aeration.

Tube bundle

The tube bundles used for inducing air into the vessel were fabricated using stainless steel tubes (SS306, 10 mm OD, 7 mm ID) bent to 'L' shape (height of vertical section: 345 mm; length of horizontal section: 140 mm) and welded vertically to two hub rings (10 mm ID, 25 mm OD) at an equiangular radial array with the horizontal ends facing outwards. The tube bundle was fabricated using 6 tubes. The tube ends at the horizontal section of the tube bundle were closed and those of the vertical section were left open. There were eight 2-mm orifices arranged in two opposite rows in the horizontal section of each tube in the tube bundle.

The tube bundle was attached to the impeller shaft by means of scrub screws in order to make the tube bundle run along with the impeller shaft. For all experimental runs, the horizontal section of the tube bundle was immersed in the liquid and the tube ends at the vertical section were above the liquid level in the reactor. In addition to the impeller assemblies, the bottom clearance and the submersion depth of the horizontal section of the primary impeller (i.e., the submersion depth of the orifices) were varied by sliding and fixing the hub-rings on to the shaft. The schematic diagrams of the air-inducing tube set and the six-bladed straight-blade turbine are shown in Fig. 2.

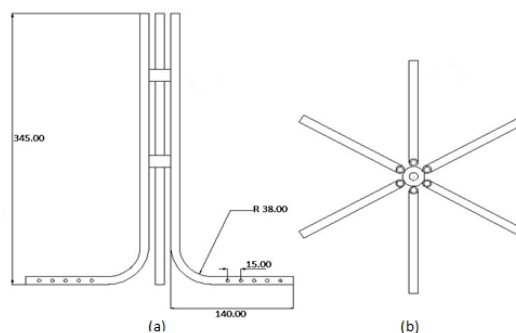


Figure 2. Air-inducing tube bundle (a) front view, (b) top view.

In order to study the performance of the self-inducing agitated vessel for gas-liquid mass transfer, tap water was used as the working fluid and the dissolved oxygen content of water was measured using dissolved oxygen meter (Hanna HI-9142, India). Initially sodium sulphite was gradually added to water to expel the residual dissolved oxygen content from water. The rotational speed of the impeller was maintained at various levels from 3.33 s^{-1} (200 rpm) to 10 s^{-1} (600 rpm) with an increment of 1.67 s^{-1} (100 rpm) using the speed control drive. At each impeller speed maintained, the dissolved oxygen content of the water was recorded against time until the equilibrium dissolved oxygen content

was reached. The total gas-free liquid level in the tank was varied from 20 cm to 40 cm. The impeller speed was measured by a tachometer, the fractional gas holdup was determined by measuring the levels of the working fluids before and after the induction of air [13, 14] and the power consumption was measured using torque table and load cell. The effects of impeller speed, initial gas-free liquid level in the tank and orifice submergence depth on fractional gas holdup, dissolved oxygen content, mass transfer coefficient and power consumption were determined. The details of the initial conditions maintained for the measurement of dissolved oxygen content in water are presented in Table 1.

Table 1. Initial conditions for mass transfer studies by dissolved oxygen measurement.

Impeller speed (rpm)	Tube set clearance (m)	Impeller clearance (m)	Orifice submergence depth (m)	Total liquid level (m)
200	0.10	0.10	0.10	0.20
			0.15	0.25
			0.20	0.30
			0.25	0.35
			0.30	0.40
300	0.10	0.10	0.10	0.20
			0.15	0.25
			0.20	0.30
			0.25	0.35
			0.30	0.40
400	0.10	0.10	0.10	0.20
			0.15	0.25
			0.20	0.30
			0.25	0.35
			0.30	0.40
500	0.10	0.10	0.10	0.20
			0.15	0.25
			0.20	0.30
			0.25	0.35
			0.30	0.40
600	0.10	0.10	0.10	0.20
			0.15	0.25
			0.20	0.30
			0.25	0.35
			0.30	0.40

The volumetric mass transfer coefficient $k_L a$ was determined by:

$$k_L a = \frac{\ln\left(\frac{C^* - C_0}{C^* - C}\right)}{t} \quad (1)$$

where, C^* = equilibrium dissolved oxygen concentration in water, mg/L, C_0 = initial dissolved oxygen concentration in water, mg/L and C = dissolved oxygen concentration in water at time t .

RESULTS AND DISCUSSION

Effect of rotational speed of the impeller on fractional gas holdup in water

The variations of fractional gas holdup in water with variations in rotational speed of the impeller for an air-inducing tube set with 6 tubes along with a six-bladed straight-blade turbine impeller for bottom clearance of 0.10 m for straight blade turbine impeller and 0.10 m for air inducing tube set are presented in Fig. 3. For a given liquid level in the tank, the increase in impeller speed increased the rate of induction of air into the vessel and hence there was a corresponding increase in the fractional gas holdup in the liquid for all five liquid levels, viz., 0.20, 0.25, 0.30, 0.35 and 0.40 m in the vessel. Inclusion of this new type of air-inducing tube bundle to the agitated vessel provides results similar to those observed by previous researchers who used several different methods for the induction of air [15, 17–19].

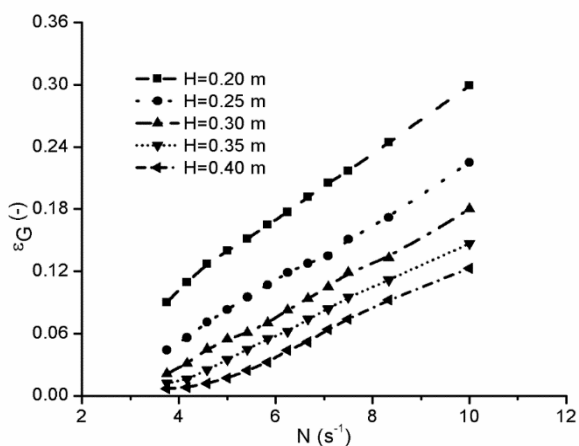


Figure 3. Effect of the rotational speed of the impeller on fractional gas holdup in water for an air-inducing tube set with 6 tubes along with a six-bladed straight-blade turbine impeller for bottom clearance of 0.10 m for a straight-blade turbine impeller and 0.10 m for an air-inducing tube set.

Effect of rotational speed of the impeller on the dissolved oxygen concentration of water

The effect of rotational speed of the impeller on the dissolved oxygen concentration of water for an orifice submergence depth of 0.20 m and a gas-free liquid level of 0.30 m is presented in Fig. 4. It was observed that for a given time of aeration, the dissolved oxygen content of water increased with increase in rotational speed of the impeller until the equilibrium dissolved oxygen concentration was reached. It was also noticed that the time required for attaining the equilibrium value of dissolved oxygen content in water increased with an increase in orifice submergence depth and an increase in total gas-free liquid level. The reason for this effect is that both the rate of air-induction and the fractional gas holdup decrease with an increase in orifice submergence depth. Since the time required for attaining the equilibrium value of the dissolved oxygen content in water is inversely proportional to the rate of air induction and the fractional gas holdup, the time required for attaining the equilibrium decreases with an increase in orifice submergence depth. Moreover, for a given orifice submergence depth the time required for attaining the equilibrium value of the dissolved oxygen content in water is inversely proportional to the rotational speed of the impeller as the rate of air induction and fractional gas holdup increase with an increase in rotational speed of the impeller [20–22]. The gas holdup observed in this study was higher than the gas holdup level reported in the literature [7–9, 22].

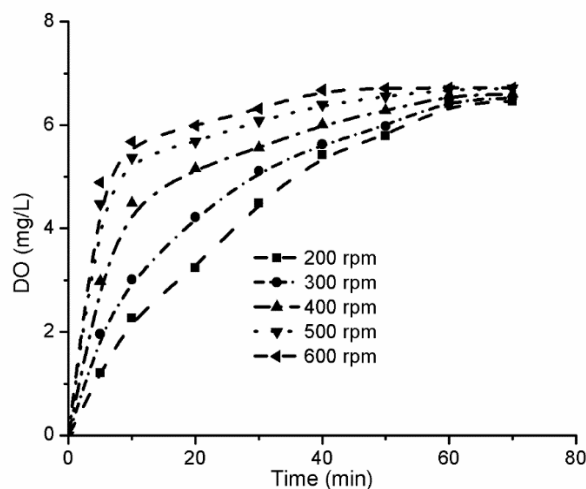


Figure 4. Effect of the rotational speed of the impeller on the dissolved oxygen concentration of water for orifice submergence depth of 0.20 m and gas-free liquid level of 0.30 m for different impeller speeds.

Effect of the rotational speed of the impeller on the volumetric mass transfer coefficient

The variations in volumetric mass transfer coefficient with variations in rotational speed of the impeller are presented in Fig. 5 for orifice submergence depth of 0.25 m and gas-free liquid level of 0.35 m. The volumetric mass transfer coefficient was found to increase with an increase in rotational speed of the impeller for all orifice submergence levels. This behavior was attributed to the fact that the volumetric mass transfer coefficient increases with an increase in the interfacial area between water and the induced air bubbles. Since the increase in rotational speed of the impeller leads to an increase in air induction rate, gas holdup and hence the increase in mass transfer area, the volumetric mass transfer coefficient increases with an increase in rotational speed of the impeller for all orifice submergence depths.

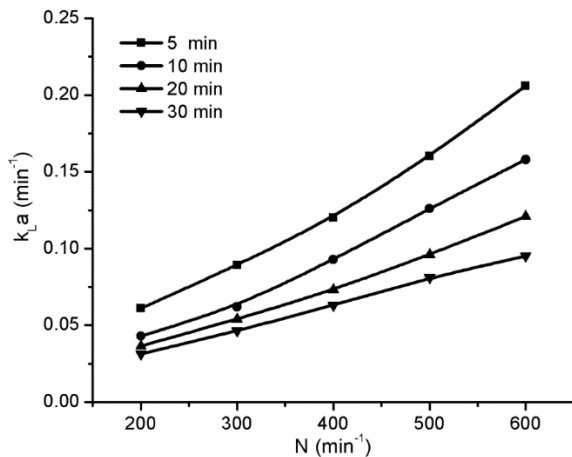


Figure 5. Effect of the rotational speed of the impeller on the volumetric mass transfer coefficient for orifice submergence depth of 0.25 m and gas-free liquid level of 0.35 m.

It was noticed that for a given orifice submergence depth and a given rotational speed of the impeller, the volumetric mass transfer coefficient decreased with an increase in the time of induced aeration [8, 20]. This is due to the fact that the rate of oxygen transfer from the induced air to the water is inversely proportional to the dissolved oxygen concentration in water. Initially the dissolved oxygen content of water is brought to zero by expelling the residual dissolved oxygen content of water by using sodium sulphite, but during the induced aeration of water, the dissolved oxygen concentration of water starts to continuously increase until reaching the equilibrium value. Since the difference between the equilibrium value of dissolved oxygen content of water and the actual

oxygen content of water, which is the driving force for the transfer of oxygen from induced air to the water, decreases continuously during induced aeration, the volumetric mass transfer coefficient decreases with an increase in time of induced aeration.

Effect of liquid level to tank diameter ratio on volumetric mass transfer coefficient

Fig. 6 shows the effect of liquid level to diameter ratio on the volumetric mass transfer coefficient for 30 min of induced aeration time for impeller speeds of 200, 300, 400, 500 and 600 rpm. It was observed that the volumetric mass transfer coefficient decreased with an increase in liquid level to tank diameter ratio (H/T) at all impeller speeds higher than the critical speed. The increase in liquid level to tank diameter ratio indicates an increase in liquid level in the tank. Therefore, when the liquid level in the tank increases, the orifice submergence depth also increases. Since the increase in orifice submergence decreases the rate of air-induction, the fractional gas holdup and hence the mass transfer area, the volumetric mass transfer coefficient decreases with an increase in H/T ratio. It was noticed that for a given H/T ratio and a given time of induced aeration, the volumetric mass transfer coefficient increased with an increase in rotational speed of the impeller. The reason for this effect is that the volumetric mass transfer coefficient increases with an increase in gas holdup and interface mass transfer area between water and induced air which increase due to the increase in rotational speed of the impeller.

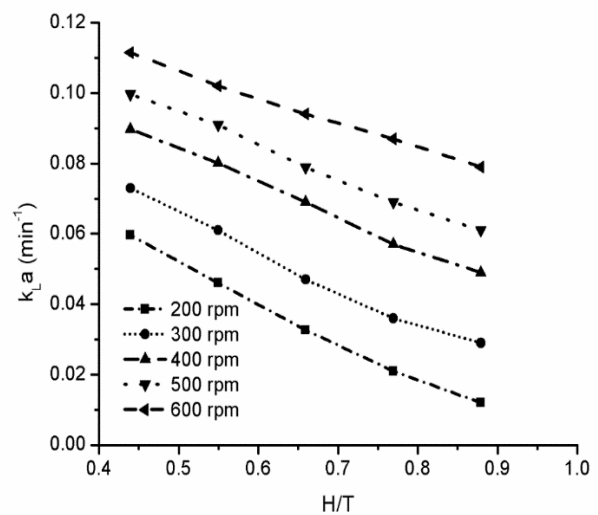


Figure 6. Effect of liquid level to tank diameter ratio on the volumetric mass transfer coefficient for induced aeration time of 30 min.

Effect of power consumption per unit volume of the liquid on the volumetric mass transfer coefficient

The effect of power consumption per unit volume of the liquid on the volumetric mass transfer coefficient is shown in Fig. 7 for orifice submergence depth of 0.20 m and a gas-free liquid level of 0.30 m. It was observed that the volumetric mass transfer coefficient increased with an increase in power consumption per unit volume of the liquid [6, 7]. This behavior of the system was attributed to the fact that the increase in power consumption per unit volume of the liquid indicates an increase in rotational speed of the impeller.

The rate of air-induction, gas holdup and interface mass transfer area increase with the rotational speed of the impeller. Therefore, the volumetric mass transfer coefficient increases with an increase in power consumption per unit volume of the liquid. Moreover, it was noticed that for a given value of power consumption per unit volume of the liquid for a given liquid level, the volumetric mass transfer coefficient decreased with an increase in time of induced aeration.

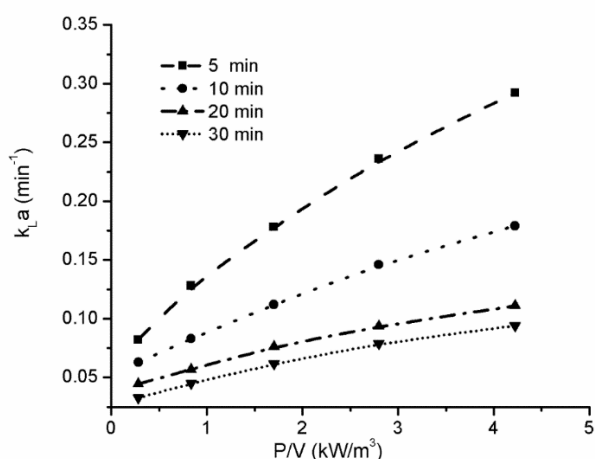


Figure 7. Effect of power consumption per unit volume of the liquid on the volumetric mass transfer coefficient for orifice submergence depth of 0.20 m and gas-free liquid level of 0.30 m.

CONCLUSION

In order to improve the gas-liquid mass transfer in a self-inducing agitated vessel, a novel method was developed and tested. The influence of parameters such as orifice submergence depth (0.10–0.30 m), total gas-free liquid level (0.20–0.40 m) and impeller speed on the dissolved oxygen content of water and the volumetric mass transfer coefficient were studied. The relationship of dissolved content in water versus aeration time at various rotational speeds was revealed. When compared with the design and fabrication of the air-inducing reactors

found in the literature, the novel method employed for self-induction of air in this study is the one that requires the simplest modification for converting a conventional agitated vessel into an air-inducing reactor. The analysis of the results indicated that for impeller speeds less than 10 rps, the gas holdup and the volumetric mass transfer coefficient of the novel air-inducing reactor used in the present work are significantly higher than the gas holdup and the volumetric mass transfer coefficient reported in the literature [7–9, 22]. Hence, it is clear that the novel air-inducing reactor developed in this study can be an alternative wherever a higher gas holdup is required for gas-liquid operations/processes.

REFERENCES

1. M. Jafari, J. S. S Mohammadzadeh, *Chem. Eng. J.*, **103**, 1 (2004).
2. S. S. Patil, V. D. Mundale, J. B. Joshi, *Ind. Eng. Chem. Res.*, **44**, 1322 (2005).
3. N. A. Deshmukh, S. S. Patil, J. B. Joshi, *Chem. Eng. Res. Des.*, **84** (A2), 124 (2006).
4. F. Scargiali, R. Russo, F. Grisafi, A. Brucato, *Chem. Eng. Sci.*, **62**, 1376 (2007).
5. Z. Wang, P. Xu, X. Li, S. Wang, Z. Cheng, F. Ju, *Chem. Eng. Process.*, **69**, 63 (2013).
6. J. H. Chen, Y. C. Hsu, Y. F. Chen, C. C. Lin, *Water Res.*, **37**, 2919 (2003).
7. R. B. Kasundra, A. V. Kulkarni, J. B. Joshi, *Ind. Eng. Chem. Res.*, **47**, 2829 (2008).
8. S. Poncin, C. Nguyen, N. Midoux, J. Breyse, *Chem. Eng. Sci.*, **57**, 3299 (2002).
9. J. B. Joshi, M. M. Sharma, *Can. J. Chem. Eng.*, **55**, 683 (1977).
10. S.B. Sawant, J.B. Joshi, *Chem. Eng. J.*, **18**, 87 (1979).
11. A. D. Raidoo, K. S. M. S. R. Rao, S. B. Sawant, J. B. Joshi, *Chem. Eng. Commun.*, **54**, 241 (1987).
12. D. A. White, J. U. De Villiers, *Chem. Eng. J.*, **14**, 113 (1977).
13. M. Major-Godlewska, D. Radecki, *Pol. J. Chem. Technol.*, **20** (1), 7 (2018).
14. V. Sivakumar, K. Senthilkumar, T. Kannadasan, *Pol. J. Chem. Technol.*, **12** (4), 64 (2010).
15. F. Ju, Z. M Cheng, J. H. Chen, X. H. Chu, (2009). *Chem. Eng. Res. Des.*, **87**, 1069 (2009).
16. C. Gomadurai, K. Saravanan, E. Abraham, N. Deepa, *N. Korean J. Chem. Eng.*, **33** (4), 1181 (2016).
17. R. Fakuda, M. Tokumura, H. T. Zand, Y. Kawase, *Chem. Eng. Res. Des.*, **87**, 452 (2009).
18. A. Kielbus-Rapala, J. Karcz, *Chemical Papers*, **64** (2), 154 (2010).
19. F. Yang, S. Zhou, X. An, *Chinese J. Chem. Eng.*, **23**, 1746 (2015).
20. K. Souidi, A. Mardaru, M. Roudet, A. Marcati, D. D. Valle, G. Djelveh, *Chem. Eng. Sci.*, **74**, 287 (2012).
21. D. H. Song, H. D. Kim, K. C. Kim, K. C., *Opt. Laser Eng.*, **50**, 74 (2012).
22. R. Achouri, S. B. Hamza, H. Dhaouadi, H. Mhiri, P. Bournot, *Energ. Convers. Manage.*, **71**, 69 (2013).

Optimization of an organic waste biogas reactor

A. Ullah¹, A. Mushtaq^{2*}, R. Ahmed Qamar¹, Z. Uddin Ali¹

¹Chemical Engineering Department, ²Polymer and Petrochemical Engineering Department,
NED University of Engineering & Technology, Karachi, Sindh, Pakistan

Received: February 13, 2019; Revised: February 22, 2020

Pakistan is a country that has the potential to compete with any country in the world, but due to some reasons it is not able to utilize its full potential. One of the reasons for its slow progress is the shortage of energy. This problem can be reduced to a certain extent by utilizing the resources that are available in Pakistan that is moving towards renewable sources of energy such as biofuels. The production of biogas from organic waste can be done in many ways, but the most efficient and applicable process is the production of biogas through anaerobic treatment of organic waste. Pakistan has livestock of around 56.9 million of cows, buffalos and bullocks. The animal dung produced is around 854 million per day. If half of this quantity is used for biogas production almost 21.35 million m³ of biogas can be produced, which also means that 450 million tons of biofertilizer are also produced per day. Dung containing bedding can produce about 100 m³ of biogas from 1 ton. Also, 5700 GWh of electricity can be annually produced from bagasse (the fibrous residue of sugarcane after its processing). The scope of this study is to convert organic waste into biogas. Biogas can be used as domestic and vehicle fuel. The results obtained in bioreactors with and without agitation is that gas is produced in both cases but the time required to produce is different, in 15 days with continuous agitation and in 25 days without agitation.

Keywords: Biogas; Organic waste; Aerobic digestion; Anaerobic digestion; Bioreactor; Agitation.

INTRODUCTION

Generating and using a sustainable power source, both in a worldwide and a national setting are required by the impact of environmental change and consistent value ascent of fossil fuels. The primary explanations behind the spread of sustainable power sources are to expand the security of the energy supply and to acknowledge add up to energy autonomy. So, as to save the decreasing reserves of fossil fuel based energy sources and to end the environmental change, it is important to change the renewable energy sources and their utilization step by step over the next coming years. Renewable sources of energy offer the highest preservation and advancement choice for the future at affordable prices; many developed, as well as underdeveloped countries working on the use of biogas [1, 2].

Biogas is formed by the decomposition of organic matter in the absence of oxygen. Biogas is a clean and renewable fuel which can be harnessed by man. It can be produced from raw materials like agricultural waste, kitchen waste, human waste, plant waste or sewage. Biogas comprises mainly methane (the cause of energy inside the fuel) and carbon dioxide, as appears in Figure 1. It may also contain hydrogen or nitrogen in little amounts. Contaminants in the biogas can incorporate sulfur or siloxanes [3, 4].

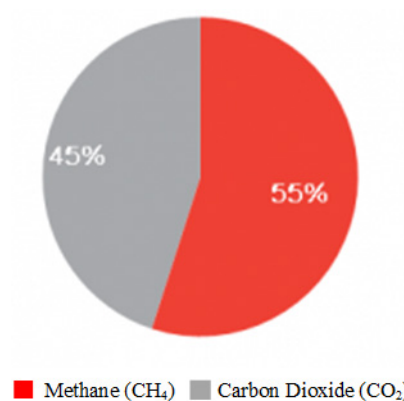


Fig. 1. Biogas composition from agricultural residue

The contents of methane and carbon dioxide in the biogas are impacted by various aspects including the proportion of starches, proteins, fats in the feedstock and the weakening element in the digester. The produced biogas can supplant conventional energy sources like firewood and animal dung, in this manner adding to battle deforestation and soil exhaustion. Biogas can add to supplant petroleum products, in this manner dwindling the emanation of ozone-harming substances and other destructive outflows, and changing natural waste into high-quality fertilizer [4, 5].

* To whom all correspondence should be sent:
E-mail: engrasimmushtaq@yahoo.com

Different components impacting achievement have been nearby natural directions and different strategies overseeing land use and waste transfer. In light of these ecological weights, numerous countries have executed or are thinking about strategies to lessen the natural effects of waste transfer. Many countries utilize anaerobic absorption as a pretreatment step that brings down slop transfer costs, controls scents, and decreases the expenses of conclusive treatment. Pakistan produces almost 1 billion tons of animal waste and 225000 tons of agricultural waste. Our goal is to utilize this waste and convert this waste into useful products. This will benefit society and will be helpful for keeping the environment clean. The objective is to optimize the bioreactor parameters and to keep the environment clean.

Sustainable power sources assume as essential to meet ambitious climate policy targets. Worldwide, around two million individuals need perfect and safe cooking fuel. They depend on traditional fuels like agricultural, farming waste and dried compost. In many countries, the biogas plants are very well able to provide livestock farmers with sustainable cooking fuel and potent organic fertilizer; this energy resource must be environmentally friendly. Anaerobic digestion is the most encouraging technology to accommodate this requirement due to the advantage of producing fuel gas and also producing smell-free remains-rich supplements, which can be utilized as fertilizers [6, 7]. Inside the scope of accessible sustainable power sources, bioenergy is likely to deliver the major share of future renewable generation. Already today bioenergy delivers about a third of all primary energy production from renewable sources. It is important to note that the primary product of interest for this study is the generated biogas and consequently energy production. Biogas can act as a fuel source to produce electricity and heat. It consists primarily of methane (50-60%), carbon dioxide (40-50%), and small traces of other gases such as hydrogen sulfide. The biogas can be fed directly into a modified engine-generator set that normally runs on fossil fuels such as natural gas and diesel fuel [8]. Biogas combustion results in the production of heat by the engine, which can be used to maintain the specific temperature range (mesophilic or thermophilic) of the anaerobic digester. Additionally, biogas combustion allows for the production of electricity used to provide electricity directly on-site or be sold to the local energy grid as a source of revenue [9, 10].

Biogas as a renewable energy source could be a substitute method of solving the issues of the

energy crisis. Agriculture has a key significance in the Pakistan economy. Agriculture has remained the premise of Pakistan's economy as it offers employment to 45 percent of the populace and gives contribution to agro based industry. In Pakistan, relatively 20% of foreign exchange is spent on furnace oil import. Realization of the significance of biogas innovation will enhance the ordinary vitality sources in the rustic regions of Pakistan. An association did an examination on the possibility of a family unit biogas program in mid-2007. The result of the investigation revealed that Pakistan has one of the biggest unexploited biogas assets in the district and dependent on the accessibility of domesticated animals and reasonable climatic conditions, the specialized potential was assessed to be more than 5 million family unit biogas digesters in the nation. The aim of this study was to conduct a specialized survey of existing biogas plants developed crosswise over Pakistan over the previous years to encourage the arrangement of an execution plan for the proposed National Domestic Biogas Program. Data on the accompanying perspectives were gathered and examined by financial qualities of tested biogas families (populace design, family measure, occupations, arrive possessions, agrarian creation, domesticated animals proprietorship and instructive status), development, activity and upkeep of biogas plant. Effects of biogas on users and evaluation of best appropriate model(s) are to be dispersed under the structure of the proposed biogas program. Biomass is the most easily accessible and the least expensive energy resource. By the economic overview of Pakistan the biomass assets of Pakistan are shown in Table 1 [11, 12].

Table 1. Livestock population in Pakistan

Species	Livestock Population (Million)
Cattle	35.6
Buffalo	31.7
Sheep	28.1
Goat	61.5
Camel	1.0
Horses	0.4
Asses	7.0
Mules	0.2

Raw materials and products

In biogas plants, biogas can be delivered by utilizing various distinctive input substrates.

Natural materials are basic substrates for creating biogas and the key beginning stage for the generation procedure. There are seven groups of organic materials which are appropriate substrates. The domestic organic waste means separate gathered vegetable and fruit wastes, flowers, flower soil, eggshells, tea and coffee filters and other organic remains [13, 14]. The level of dry issue differs somewhere in the range of 10 - 30 %. The green and plant squanders hacking and scraps from cutting greenhouses or parks which do not contain wood make a difference (lignin). The public sewage slop extra from shared waste water treatment is ooze, which must be disinfected to be utilized for biogas generation. This sewage slop can contain phosphorus, nitrates and overwhelming metals. Experience demonstrates that slime from waste water treatment is appropriate in biogas plants, is, however, not considered as an amazing substrate. It is unlawful to utilize slop from non-open sources on account of the higher content of substantial metals or hereditarily adjusted living beings or hormones. The level of dry issue shifts somewhere in the range of 20 - 30 % [15].

The liquid or solid manure from animal cultivating is one of the basic substrates for the digestion process. Cow manure is best, while chicken fertilizer for instance has a high yield, yet may contain sand [16, 17]. Chicken compost can likewise be utilized for biogas creation. Chicken dung produces biogas quicker than some other substrates. The dry matter of a solid fertilizer changes somewhere in the range of 15 - 30% and of fluid excrement somewhere in the range of 5 - 7 % [18]. The energy crops are fundamentally developed on generally neglected fields, for example, corn, sudan grass, millet, white sweet-clover. The modern nourishment squander originates from sustenance and meat creation locales or procedures, for example, whey, potato squash, vegetable leftovers, brewer grains, apple marc. These sorts of substrates are typically entirely reasonable and do not contain unsafe substances. Substrates from meat generation, such as slaughterhouse squander, are useful natural materials yet require exceptional treatment to decrease wellbeing dangers and smell. The products are biogas, high-quality fertilizer and a potential source of energy like heat, light and electricity [15, 19].

Cow dung of generally dark magenta in colour is utilized as agricultural fertilizer. If not recycled into the soil by some species like earthworms and dung beetles, cow dung can dry out and stay on the field, making a territory of munching land which is

unpalatable to domesticated animals. Nowadays dung may also be collected and used to produce biogas to generate heat and electricity. The gas is used in rural areas of Pakistan and elsewhere to provide a stable and renewable source of electricity [4].

The past several years have witnessed some energizing improvements that present a chance to give natural waste streams something to do in a lot bigger route towards giving a source of renewable energy to meet power, warmth and transportation energy needs. In light of the fact that when a fertilizer is joined with a higher-carbon source, for example, fats, oils or sustenance handling waste, ventures can significantly offer large biogas generation, and this can positively affect venture financial matters. There have additionally been undertakings that have spearheaded the capacity to evacuate carbon dioxide and other follow gases or contaminations to deliver an item that is identical to flammable gas and can be infused into the petroleum gas pipeline to meet warmth needs, or supply a source of fuel for the gaseous petrol vehicle use. These advancements distinctly exhibit the capacity of biogas energy frameworks to additional successful management of natural waste streams while providing a dependable and adaptable source of renewable energy source [16, 20].

Biogas production in Sweden

Sweden is on the top of the mountains in the production of biogas. It has almost 230 facilities for the production of biogas. Half of the production of biogas is from wastewater treatment plants. Since the ban on landfilling in 2005, the biogas production in landfills has reduced. However, new plants, mainly co-digestion plants, are being established. Sweden produces 1.4 TWh (terawatt hours) annually from its 230 facilities. Table 2 shows the type and number of plants in Sweden and the energy produced from biogas [21]. Sweden has the theoretical potential of producing biogas of more than 15 TWh/year, which is approximately 10 times than its production at this time. Many substrates are still considered residue or waste, so research is being done to use this substrate or waste to increase the production of biogas. Agriculture residue is showing great potential for the production of biogas. 7 TWh of biogas can be annually produced if Sweden uses 10% of their agricultural land. Table 3 shows the potential for biogas production [21].

The biogas production depends upon the substrate. If substrates have good nutrients and good

potential, then production of biogas can be increased. Table 4 shows the production of biogas from different substrates, as tested in the laboratory, so these results are higher, and in the actual process, the production will be low [22, 23].

Biogas production can be greatly increased by using crops as a substrate. Table 5 shows the potential of some crops for producing biogas [8, 13].

Table 2. Number of different biogas plants in Sweden

Biogas Plant	Number	Energy in Biogas (GWh/year)
Waste water treatment plants	135	614
Co-digestion plant	18	344
Farm plants	14	16
Industrial wastewater	5	114
Landfills	57	298
Sum	229	1387

Table 3. Different substrates and their potential for producing energy

Substrate	Potential Biogas Production with Limitations* [TWh]	Total Biogas Potential [TWh]
Food wastes	0.76	1.35
Wastes from parks and gardens	0	0.40
Industrial waste and residue (including food industry)	1.06	1.96
Sludge from wastewater treatment plant	0.7	0.73
Agriculture residue and manure**	8.10	10.78
Total	10.62	15.22

*Taking into account limitations in today's technical and economic situation.

** 5.8 TWh of this potential origin from straw which requires pretreatment before digestion

Table 4. Production of biogas from different substrates and methane concentration

Substrate	TS [%]	Biogas Production		Methane Concentration [%]
		[m ³ .ton ⁻¹ TS]	[m ³ .ton ⁻¹ wet weight]	
Sludge from waste water treatment plants	5	300	15	65
Fish waste	42	1279	537	71
Straw	78	265	207	70
Sorted food waste	33	618	204	63
Liquid cattle manure	9	244	22	65
Potato helum	15	453	68	56
Slaughter house waste	16	575	92	63
Liquid pig slurry	8	325	26	65

Table 5. Different agricultural wastes and their methane production

Substrate	Harvest ¹ [Ton/hand year]	TS [% of wet weight]	Methane Yield [Nm ³ methane/Ton wet weight]	Substrate Need [Ton/GWh]	Land Requirement [Ha/GWh]
Jerusalem artichoke ²	60	22	48	1500	25
Maize	43	30	95	1070	25
Potato	26	25	100	1020	39
Sugar beet ³	50	24	94	1090	22
Grass	22	35	95	1100	50
Wheat grain	5.2	86	370	300	58

¹Harvest quantities are valid for the area of Malardalen.

²Data are valid for harvest of stem.

³Harvest quantities are valid for the area of Skane

Table 6. Difference between aerobic and anaerobic digestion

Aerobic Digestion	Anaerobic Digestion
It occurs in the presence of oxygen	It occurs in the absence of oxygen
It always releases CO ₂ and H ₂ O	Its end product may vary, depending on the feed
High production of biological sludge	Less production of biological sludge
It yields at 36 ATPs	It yields at 2 ATPs

The potential of biogas in Pakistan

Pakistan's main source of income is through agriculture. An agricultural country must have a huge number of livestock and farms to fulfil its requirement and made a profit. Due to this huge amount of waste is produced in agricultural countries. Pakistan also produces a huge quantity of animal waste and agricultural residue. Pakistan produces daily almost 55000 tons of solid waste, 225000 tons of crop residue and almost 1 billion tons of animal manure. According to a survey done in 2016, Pakistan has livestock of around 56.9 million of cows, buffalos and bullocks. On average, 15 kg of dung are dropped daily by an animal. So the total amount of animal dung produced is around 854 million per day. If half of this quantity is used for biogas production almost 21.35 million m³ of biogas can be produced, which also means that 450 million tons of bio-fertilizer are also produced per day. Also in 2016, 15 million layer-chicken and 528 million broiler chicken birds were bred in Pakistan. Chicken dung can also be used for biogas production. Chicken dung produces biogas faster than some other substrates. One ton of layer-chicken and broiler chicken fresh dung can produce 170-200 m³ of biogas. Dung containing bedding can produce about 100 m³ of biogas from 1 ton.

Pakistan has the potential of producing 8.8 to 17.2 billion m³ of biogas per year (equivalent to 55 to 106 TWh of energy) from livestock residue. Also, 5700 GWh of electricity can be annually produced from bagasse (the fibrous residue of sugarcane after its processing) [24, 25].

Aerobic digestion process

This is a process carried out in the presence of oxygen. The oxygen comes directly from the surrounding. Generally, by doing aerobic digestion, the end product is carbon dioxide and water. The carbon dioxide produces a greenhouse effect in the environment and for preventing this carbon dioxide is collected in a gas collecting system. If the feed contains nitrogen, phosphorus and sulfur, so the end products will be nitrates, phosphates and sulfates. The advantage of aerobic digestion process from start to end is that it takes only 5 days. The end product of the aerobic digestion is safe for the environment and the personnel. The time and the effort required to convert any food to waste for aerobic digestion is on the top. The limitations of aerobic digestion process are due to the oxygen supplying cost and the generally poor dewatering characteristics of the sludge produced by aerobic digestion [26].

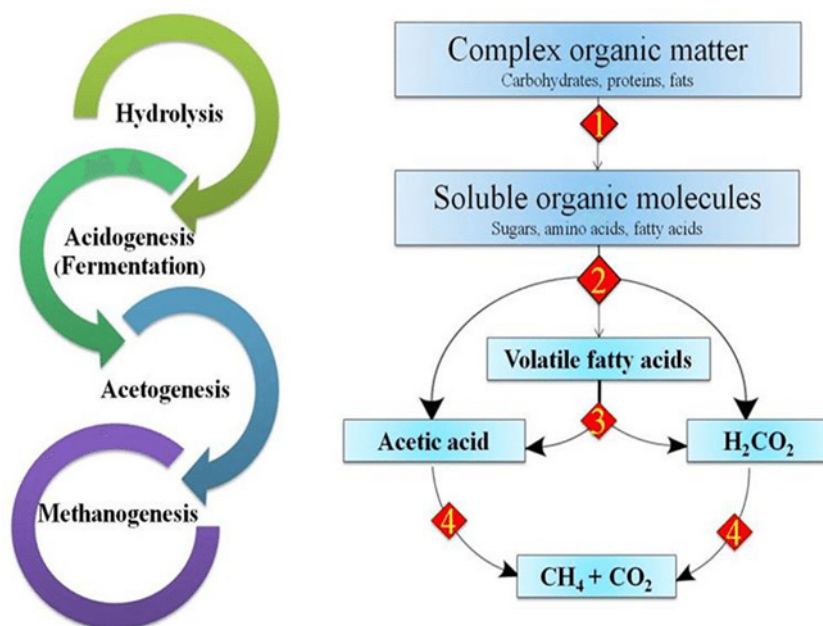


Fig. 2. Process of anaerobic digestion

Anaerobic digestion processes

This is a process carried out in the absence of oxygen. The basic purpose of the anaerobic digestion is to convert the waste to a useful product such as biogas that can be used as a fuel. The anaerobic digestion process is shown in Figure 2. The steps included in the formation of biogas through anaerobic digestion are: hydrolysis, acidogenesis, acetogenesis and methanogenesis [25, 27]. The steps are interlinked. The biogas formed by anaerobic digestion is high in percentage (50-75%). The end products of anaerobic digestion are carbon dioxide and methane. The quantity of gas produced depend on the amount of feed entered in the digester. The advantages of anaerobic digestion are that the wastewater pollutant is converted into methane, carbon dioxide and traces of biosolids, the biomass growth is much lower and low nutrients are required. The limitations of anaerobic digestion are that the exhaust gas coming from the gas engines requires treatment and cleaning of biogas to avoid corrosion [27]. The differences between aerobic and anaerobic digestion are shown in Table 6.

By considering the advantages and the limitations of both the processes, anaerobic digestion was selected, because there is no requirement of oxygen, fewer requirements of nutrients, a potential source of fuel, less production of biological sludge because the growth of the cell is slow. Anaerobic digestion is very cheap as compared to the aerobic digestion. It also has high treatment efficiency for the biodegradable sludge.

The methane production in anaerobic digestion is in larger percentage as compared to the aerobic digestion. The residual sludge is also used as a soil conditioner [27, 28]. The series of biological processes in which the complex compounds can be broken down into the simplest compounds is shown in Figure 2. Anaerobic digestion works in the absence of oxygen. The end product is biogas that has very vast use: it is used to generate electricity, as a fuel, it is converted into renewable natural gas. Generally, the anaerobic digestion takes place in a sealed vessel that has an inlet valve for feed and a discharge valve; it also has a gas outlet point, it provides the agitator and the heater in the cold season (weather) to set the desired temperature in the vessel.

Hydrolysis is the first step in the production of biogas. In this process, complex polymers such as carbohydrates, fats and proteins are converted into simpler monomers such as amino acids, fatty acids and glycerol. This is a very important step determining the rate if the process of decomposing of the complex polymer is slow so the next three steps will be affected, that results in increasing the retention time. By hydrolysis carbohydrates are converted into sugars; fats are converted into fatty acids and proteins are converted into amino acids [28, 29].



After hydrolysis, the next step is acidogenesis; this is the continuation step in which the amino acids, sugars and fatty acids that are the product of

hydrolysis are converted into acetates, hydrogen, carbon dioxide, traces of volatile fatty acids (VFA) and alcohols. The main products of acidogenesis are propionic acid (CH_3CH_2COOH), butyric acid ($CH_3CH_2CH_2COOH$), acetic acid (CH_3COOH) and others.



After acidogenesis, the products of previous steps: hydrogen, carbon dioxide, formic acid, propionic acid and other simple acids are converted into acetic acid. This is an important acid as it directly produces methane. The acetogenesis process is done in the presence of acetogenesis bacteria used to produce acetic acid, hydrogen and carbon dioxide. It makes sure that the hydrogen produced in this step has partially low pressure which helps for the conversion of all acids. This type of low pressure is carried out by hydrogen scavenging bacteria [25].



As the most important step in the production of methane in this stage the methanogenic bacteria convert the products of acetogenesis (acetic acid, hydrogen and carbon dioxide) into methane as shown in Figure 2. The following reactions take place:



There are two conventional operational levels of temperature for the anaerobic digestions, to find species of methanogens in the digester. Mesophilic digestion is the type of anaerobic digestion taking place optimally around 30 - 38°C, or at ambient temperature between 20°C and 45°C where the mesophiles are the primary microorganisms present. Thermophilic type of anaerobic digestion takes place optimally around 49 - 57°C, or at elevated temperature to 70°C, where thermophiles are the primary microorganisms present [25].

There are many parameters that have to be set in order to achieve maximum production of biogas. The parameters must be controlled in the desired range in order to obtain the complete and effectively breakdown by microorganisms. The temperature must be controlled in the desired range because the microorganisms need a suitable temperature environment to work; the methanogenesis phase is very sensitive to temperature as it affects the methanogens that

produce methane. It also depends on the seasons. In the winter season, the digester is facing the sun, daytime is the time the measures are quickly be taken, because at the night time the temperature of the atmosphere is decreasing, so to prevent this the digester is covered with some clothes and the gas holder is covered with transparent polyethylene during the sunshine hours and insulating it in the off-shine hours, the temperature must be maintained at 30-40°C. In anaerobic digestion, the temperature is divided into two types of conditions. In mesophilic conditions the operating temperature is between 30-38°C, the mesophilic conditions require less input energy and are also less sensitive to shock load or toxic substances. The temperature which is favourable for this condition is 37°C. The bacteria present in this condition are called mesophiles. The mesophiles are more efficient than thermophiles because most of the methanogens belong to mesophiles. The retention time for the mesophilic condition is 25 to 30 days. In thermophilic condition, the operating temperature is between 50-60°C. The thermophiles are more efficient compared to the mesophiles because they take less retention time, but on the other hand, they require high energy input and are highly sensitive to a shock load. The yield of thermophilic condition is high compared to mesophilic one, the retention time for the mesophilic condition is 15-20 days [11, 25, 27].

Agitation plays an important role in the anaerobic process. By agitation, the feed and microbes that are present in digester mix well and also the temperature is uniformly distributed throughout the feed in the vessel. Mixing increases the contact area and provides a uniform concentration of products and prevents scum formation. The pH has a very high impact on the stability of anaerobic digestion. The pH is a measure of acidity and alkalinity of a solution; if pH is 7.0 the solution is neutral, if pH is less than 7.0 it is acidic. The pH range where a digester performs well is from 6.8 to 7.4. If the pH is less than 6.8 so the production rate is decreased and if pH is greater than 7.4 the same results. To stabilize the alkalinity we use potassium bicarbonate or calcium carbonate (lime). The formation of carbon dioxide and fatty acids affects the pH of the digester. Most of the research papers show that the effective pH for digestion is in-between 6.8-7.2. It was found that above pH 5.0 the efficiency of production of methane is increased by 75% [30].

The effect of total solid content in the anaerobic digester is low: solid systems have less than 10% total solids, medium solid systems have less than

15-20% total solid and high solid systems have 22-40% total solid content. The carbon-to-nitrogen ratio plays an important role in the production of biogas. For optimal growth of bacteria, it should be noticed that the nutrients are provided with desirable concentration. Nitrogen is the building structure of the cell; the low C/N ratio means formation of ammonia and inhibits the formation of methane. C/N ratio depends on the feed composition. The optimal C/N ratio was found to be 15:1 in case of a cattle dung and 25:1 to 30:1 in general, as shown in Table 7. A very high C/N ratio means shortage of nitrogen [31].

Light has a very important effect on the production of methane. It inhibits the production of methane, that is why all digestion reactors are placed in darkness and sprayed in black color to prevent the light.

METHODOLOGY

The concept of bioreaction or “fermentation” was initially not known to humanity, but humans were taking the advantages of its results. Bread, cheese, wine and beer were all made by a process traditionally known as fermentation (a little-understood process successful more by chance than design) — the failure and frustration of the French vintners who found that they often produce vinegar, not wine. This led the famous French chemist and microbiologist Louis Pasteur to study the fermentation at their request. Pasteur discovered that the biological activity of a microscopic plant called yeast causes the fermentation and its results. When unwanted microbes infiltrated the wine and fed on alcohol produced by the yeast, the microbes

left behind distasteful and harmful wastes. Thus, flavour of the wine is ruined. Pasteur’s work revolutionized the bioreaction industry because once the process is identified and understood, it can be controlled [30]. The scope of bioengineering has grown to the industrialization of wine, cheese, beer and milk to biotechnology’s newer products like antibiotics, enzymes, steroidal hormones, vitamins, sugars and organic acids. A system in which biological conversion is affected is called a bioreactor. The bioreactors referred here include only mechanical vessels in which organisms are cultivated in a controlled manner and products are formed through specific reactions. Bioreactors are different from chemical reactors because they are specially designed to influence metabolic pathways. Chemical reactors whose design and models can be used as bioreactors include continuous stirred-tank reactor, continuous flow stirred-tank reactor, plug flow reactor and fluidized bed-reactor [30]. More severe consequences are posed by deactivation of biomass than chemical upset. An incubation period is required by all bioreactions for the establishment of the environment which favours the bioreactor for production of microbes. The bio-reaction can take 10-20 days for completion. Most of the bioreactions are done in batch reactors. The first phase is usually sterilization; after that enzyme culture is developed for the production of microbes. During the reaction time enzyme, substrate and product concentration can vary. This can be avoided by proper mixing and proper temperature maintaining. For aerobic reaction, a continuous supply of oxygen is provided.

Table 7. Carbon-to-nitrogen ratios of organic materials

Average carbon-to-nitrogen (C:N) ratios for organic materials			
Greens/ Nitrogen	C:N Ratio	Browns/ Carbon	C:N Ratio
Pig manure	5-7:1	Leaves	30-80:1
Poultry manure (fresh)	10:1	Cornstalks	60:1
Alfalfa or sweet clover hay	12:1	Straw	40-100:1
Vegetable scraps	12-20:1	Bark	100-130:1
Poultry manure with litter	13-18:1	Paper	150-200:1
Coffee grounds	20:1	Sawdust	400:1
Grass clippings	12-25:1	Wood chips	800:1
Cow manure	20:1		
Horse manure	25:1		
Horse manure with litter	30-60:1		

The advantages of the batch reactor are: contamination of reactor is minimized due to the long growth period, low capital investment, higher flexibility with products and high conversion. The disadvantage of the batch reactor is the time-consumption due to filling, heating, sterilization, emptying and cleaning, the greater expense for establishing a new environment for new products and industrial hygiene risk. In the continuous reactor, the environment for the production of microbes is continuously fed to the bioreactor to maintain the steady state and product is continuously drawn. The advantages of the continuous reactor are: potential for automating the process, low labour cost, lower time consumption and constant product quality. The disadvantages of the continuous reactor are: lower flexibility, uniform supply of reactors and substrates required, high capital cost [33].

Designing of a bioreactor

The most important task is to control and have a positive influence on the bioreaction in the effective bioreactor. The key points which are to be focused during the designing of a bioreactor are: controlled temperature, maintained pH, appropriate amount of substrate, availability of water, salts, vitamins, oxygen (for the aerobic process), gas outlet and collection, products and side products collection and separation [33]. The reactor was made up of stainless steel because bioreaction required acid or base for control of pH and also produced acidic gases, due to which metal oxides were formed in the bioreactor, and it became corroded. Also, it had many leakages, due to which biogas cannot be contained in the reactor nor collected.

Considering the design of a pervious batch a simple first pilot plant was fabricated. The bioreactor was made of plastic so that contamination may not happen. In this reactor, only inlet and outlet for biomass is provided and also a gas outlet for its collection. No agitation was provided, temperature was not controlled, and no constant pH was maintained. As a result, the desired results were not obtained. Due to the absence of key factors in designing the bioreactor, the first pilot plant was not successful. Therefore, a second pilot plant was fabricated and was provided with key factors like temperature control, pH control and proper agitation.

Reactor designing on software NX 8.0 and specification

NX Unigraphics (U-G) is an advanced high-end CAD/CAM/CAE software package initially

developed by Unigraphics, but since 2007 by Siemens PLM Software. It is used for designing (parametric and direct solid modelling), engineering analysis (dynamic, static, electro-magnetic, thermal, using the finite element technique, and fluid using the finite volume technique) and manufacturing a finished design by using involved machining modules. The 3D-diagrams are shown in Figure 3. Figures 4 to 6 show the top, side and front views of the bioreactor, agitator and cup. The reactor specification is given in Table 8.

Table 8. Equipment with specifications

Equipment	Specification
Reactor vessel	19.0 liters
Electric heater	500 watts
Slurry inlet pipe	2.0 inches
Slurry outlet pipe	1.25 inches
Gas outlet pipe	0.5 inches
Acid or base inlet pipe	0.5 inches
Slurry inlet valve	2.0 inches ball valve
Slurry outlet valve	1.25 inches ball valve
Gas outlet valve	0.5 inches ball valve
Length of agitator fan	23.3 inches
Plastic tub (for water bath)	33 liters
Thermocouple	T-type

Calculations for heating coil for bioreactor by the last batch

For the calculation of the heating coil Eq. (8) was used:

$$h_b \frac{dv}{k} \times \left(\frac{\mu_s}{\mu}\right)^{0.14} = 0.55 \left(\frac{L^2 N}{\rho \mu}\right)^{0.67} \times \left(\frac{Cp}{\mu k}\right)^{0.25} \quad (8)$$

Since the agitator used in that bioreactor was of paddle type, the constant will be 0.36 and the index will be 0.67, if Reynold number condition is satisfied [1, 33].

$$\text{Stainless steel 304} = K = 14 \text{ W. m}^{-1} \text{K}^{-1}$$

$$\mu_{50^\circ\text{C}} = 0.000547 \text{ Pa. s}$$

$$Cp_{50^\circ\text{C}} = 4.182 \text{ KJ. kg}^{-1} \text{K}^{-1}$$

$$\rho_{50^\circ\text{C}} = 988 \text{ kg. m}^{-3}$$

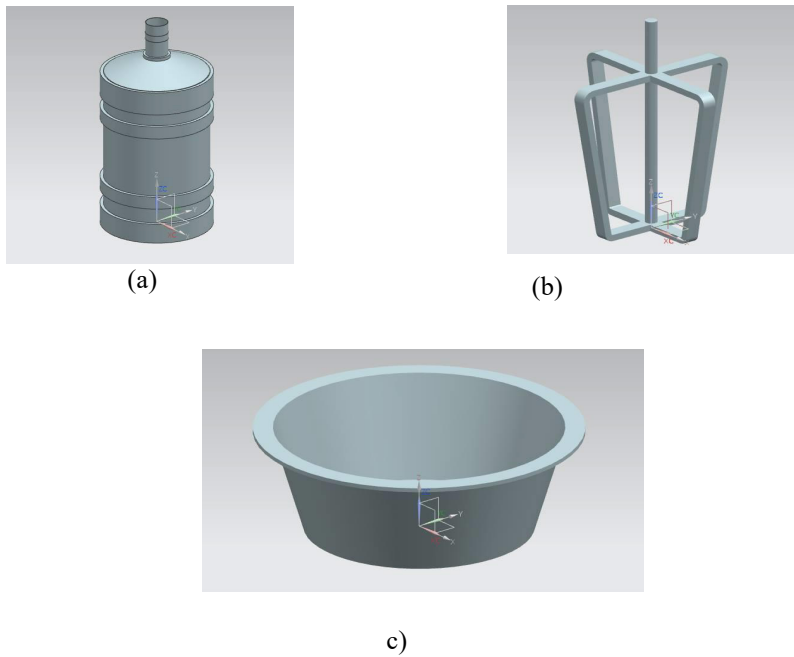


Fig. 3. 3D-diagram: (a) Bioreactor (b) Agitator (c) Moving cups

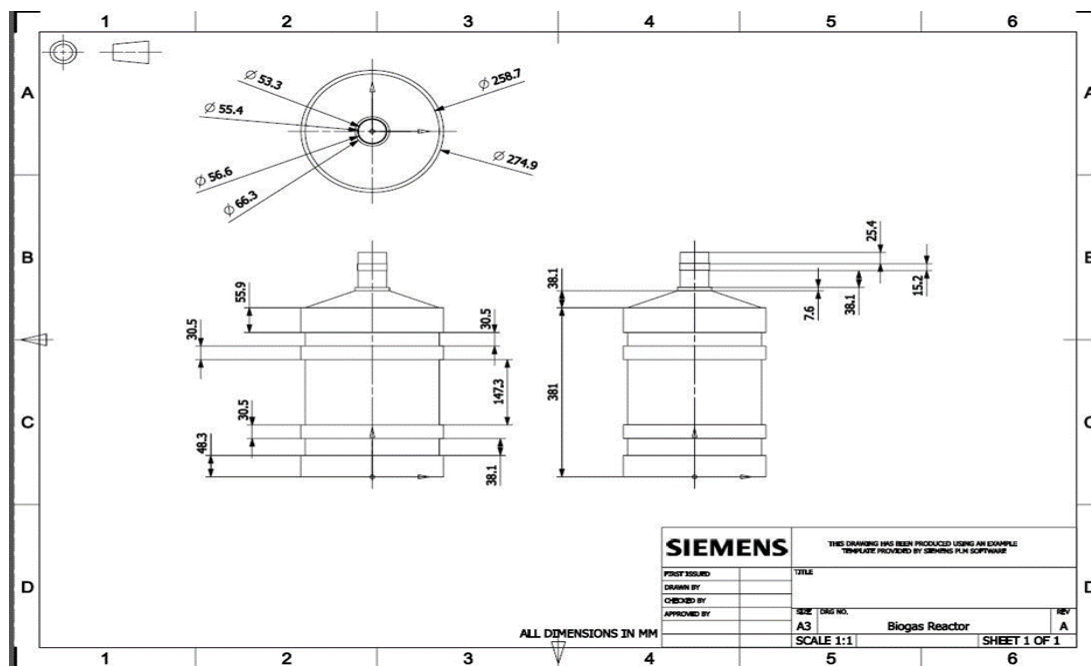


Fig. 4. The top, side and front view of the bioreactor

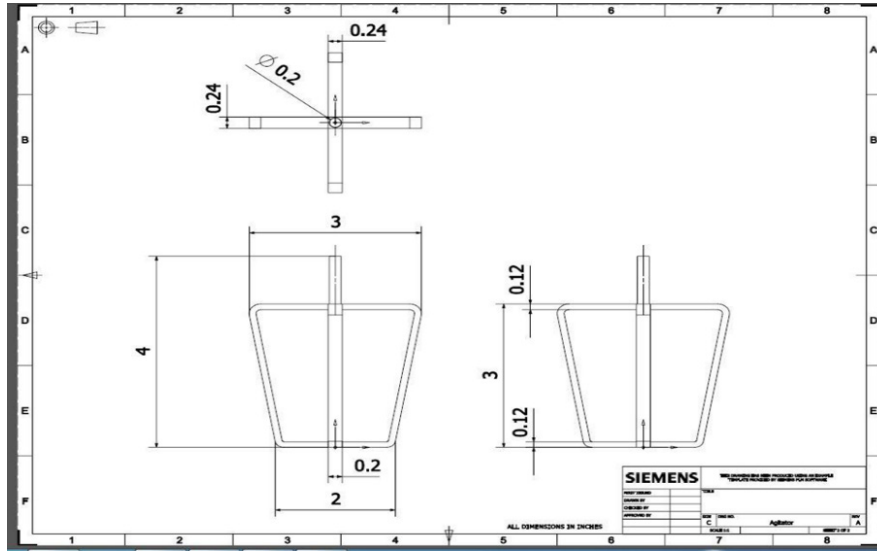


Fig. 5. The top, side and front view of the agitator

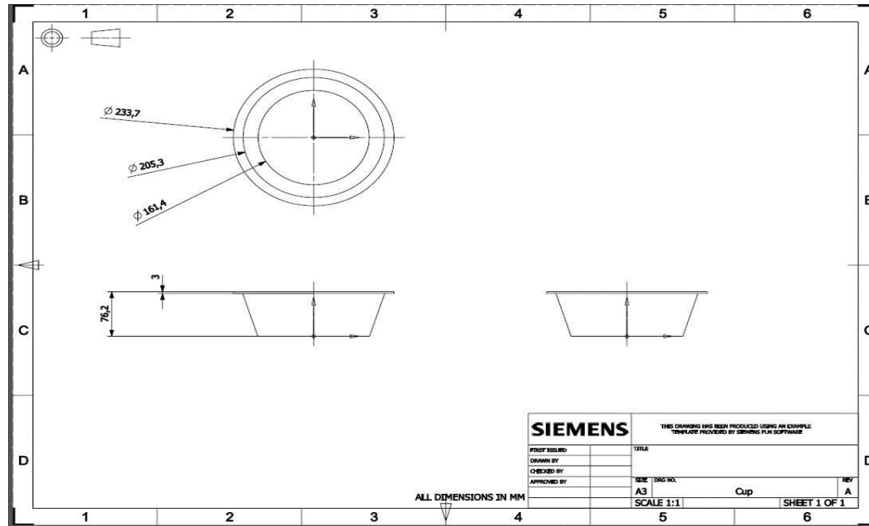


Fig. 6. The top, side and front view of cups

$$D_t = \text{Diameter of coil} = 0.0187 \text{ m}$$

$$Q = \text{Volumetric flowrate of water in coil} \\ = 2L \cdot \text{min}^{-1} \\ = 3.333 \\ \times 10^{-5} \text{ m}^3 \cdot \text{sec}^{-1} \quad (\text{assumed})$$

$$V = \frac{\text{Volumetric Flowrate}}{\text{Area of Coil}} \\ = \frac{3.333 \times 10^{-5}}{3.124 (0.0187)^2} 0.12134 \text{ m} \cdot \text{s}^{-1} \quad (9)$$

$$Re = \frac{\rho V D t}{\mu} = \left(\frac{988 \times 0.12134 \times 0.0187}{0.000547} \right) \quad (10)$$

$$Re = 4098.40823$$

Since Reynold number is greater than 4000 the above equation can be used.

L = Length of agitator = 0.304 m, N = Revolutions per second = 0.1 rps (assumed), d_v = Diameter of reactor = 0.776 m and h_b = Heat transfer coefficient of coil.

$$h_b \frac{d_v}{k} \times \left(\frac{\mu S}{\mu} \right)^{0.14} 0.36 \left(\frac{L^2 N \rho}{\mu} \right)^{0.67} \\ \times \left(\frac{C_p \mu}{k} \right)^{0.25} \left(\frac{0.0929 \times 0.1 \times 9.88}{0.000547} \right)^{0.67} \\ \times \left(\frac{4.182 \times 0.000547 \times 1000}{14} \right)^{0.25}$$

$$h_b = 6.494 \times (677.0213) \times (0.6358) \quad (11)$$

$$h_b = 2795.793127 \text{ W} \cdot \text{m}^{-2} \text{K}^{-1}$$

Calculations for agitation

The diameter of the impellor is 14 cm that is run by wind as shown in Figure 7. The calculation shows the force required by agitator to rotate [1].

The distance cover by the bowl to rotate the agitator is given by:

$$\begin{aligned}
 S &= R\theta & (12) \\
 R &= 60 \text{ cm or } 0.6 \text{ m} \\
 \theta &= 120^\circ \text{ or } \frac{2\pi}{3} \\
 \text{So,} \\
 S &= 0.6 \times \frac{2\pi}{3} = 1.256 \text{ m}
 \end{aligned}$$

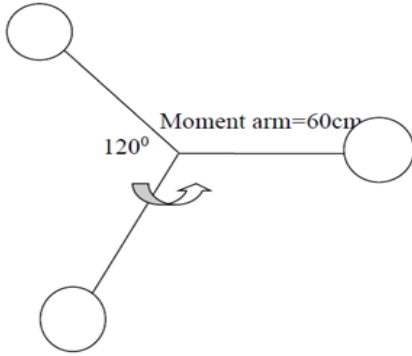


Fig. 7. Wind turbine for agitation

Density of slurry = 1047 kg.m^{-3} at 50°C , Density of air = 1.225 kg.m^{-3} at 50°C , Tank diameter = 0.226 m , Diameter of agitator = 0.14 m and Diameter of bowl = 16 cm . In this study, use two bowl of diameter 16 cm so the volume to trap the air is:

$$\begin{aligned}
 V' &= 3 \times \frac{4\pi r^3}{3} & (13) \\
 V' &= 3 \times \frac{4\pi(0.08)^3}{3} \\
 V' &= 6.434816 \times 10^{-3} \text{ m}^3
 \end{aligned}$$

The volume of half of the sphere is:

$$\begin{aligned}
 V_b &= \frac{V'}{2} & (14) \\
 V_b &= \frac{6.434816 \times 10^{-3}}{2} \\
 V_b &= 3.217408 \times 10^{-3}
 \end{aligned}$$

Mass of air = Density of air \times Volume of bowls (15)

$$M_a = 1.22 \times 3.217408 \times 10^{-3}$$

$$M_a = 3.92523776 \times 10^{-3} \text{ kg}$$

$$\begin{aligned}
 &\text{Mass of slurry} \\
 &= \text{Density of slurry} \\
 &\times \text{Volume displace by agitator in tank} & (16)
 \end{aligned}$$

$$\begin{aligned}
 \text{Volume displace by agitator} &= v \\
 &= \pi r^2 \times \text{width of agitator} & (17)
 \end{aligned}$$

$$M_f = 1047\pi\left(\frac{0.0762}{2}\right)^2 \times 0.02$$

$$M_f = 0.0955 \text{ kg}$$

Velocity after the collision of air with bowls, according to the law of conservation of momentum [1, 33]:

$$V_f = M_a \left(\frac{\text{Avg velocity of wind}}{M_a + M_f} \right) \quad (18)$$

$$V_f = 8 \left(\frac{3.92523776 \times 10^{-3}}{3.92523776 \times 10^{-3} + 0.0955} \right)$$

$$V_f = 0.0394 \text{ m.s}^{-1}$$

Acceleration due to change in velocity:

$$A = \frac{V_f^2 - V_i^2}{2S} \quad (19)$$

$$A = \frac{0.0394^2 - 8^2}{2 \times 1.256}$$

$$A = -25.47 \text{ m.s}^{-2}$$

Acceleration is decreasing that why it is negative.

Force on bowls to rotate

$$F = M_f A \quad (20)$$

$$F = 0.0955 \times 25.47$$

$$F = 2.432385 \text{ N}$$

Number of rotations per minute:

$$V = \pi D N \quad (21)$$

$$0.0394 \times 60 = \pi \times 0.0762 \times N$$

$$N = 10 \text{ rpm}$$

The force and number of rotations shown above can be changed by changing bowl diameter and agitator diameter.

RESULTS AND DISCUSSION

In this research, fish waste was used along with sewage water in a ratio of 1:1. The experiment was performed in 1.5 litre- bottles placed in a dark area.

The fish waste has great ability to produce biogas as compared to others. Co-digestion of manure with fish can give an optimum C/N ratio that helps in biogas production [19, 31]. The important characteristics of fish wastes, found in the study are given in Table 9.

Table 9. Characteristics of different fish wastes

Names	C.O.D. (ml.l ⁻¹)	B.O.D. (ml.l ⁻¹)	T.S. (ml.l ⁻¹)
Shrimp	3300	2000	900
Crab	6300	4460	620
Oysters	500-2000	250-800	200-2000
Tuna	1600	200	500
Salmon	300-550	250-2600	120-1400
Catfish	700	340	400

When using the liver of pink salmon, the moisture contents, lipids fats and proteins are 77%, 3.3% and 16%, respectively. When using the head of trout fish the moisture lipids, fats and proteins fractions are 70%, 12% and 14% respectively. When using intestines of trout fish, we have 56%, 35% and 8% respectively. Some factors are most important to control, such as pH, temperature, mixing, and ammonia inhibition [19]. There are lots of problems related to the first experiment. The most important problem was the fluctuation of temperature that was not controlled throughout the experiment. The temperature range to be maintained was 28-34°C. There was no pH controlling device neither. In this experiment no agitation was provided. The results obtained were that gas was produced, however, it had not enough methane content to burn.

Then, a new experiment was started which is known as co-digestion. Co-digestion of cow dung and banana skin with water was done. The ratio of cow dung, banana skin and waster was 60:25:15. The main purpose of co-digestion was to maintain the C/N ratio at the optimum point. Co-digestion is important when we have a waste of low C/N ratio so another waste was added to enhance the C/N ratio. The increase in C/N ratio reduces the effect of ammonia and maximizes the methane potential [19, 34]. The time period of this experiment was 25 days. The feed for the co-digestion experiment was: mass of banana skin 2.5 kg, mass of cow dung 6 kg and 1.5 l of sewage water. The temperature was ambient (fluctuation was observed), pH of water was 7.6, and overall pH was 8 (needed to be adjusted). This experiment was also started with the experiment above. Similarly, continuous agitation was not provided and temperature and pH were not

controlled. Similar results were obtained on gas production with no enough methane content to burn.

Cow dung and sewage water

In this experiment cow dung and sewage water were used. Water was 2.22607 l, and cow dung was 4.34921 kg. Water content plays a vital role in bacteria activities and growth. Bacteria movement and activity are determined by the water content in the digester. As the feed entered the reactor oxygen was removed by purging with nitrogen gas that is inert and anaerobic digestion was carried out. No particular temperature was maintained during this experiment. It was performed at variable temperatures. The hydraulic retention time of this experiment was 25 days. The average characteristics of cow dung are shown in Table 10.

The first stage was the pretreatment of organic waste to remove the impurities with a view to enhance bacterial growth. The second stage was the mixing of solids with water and homogenizaion of the slurry. The third stage was the batch digestion in the absence of oxygen. The fourth stage was the purging of nitrogen to displace remaining oxygen in the sealed reactor.

Table 10. Average properties of cow dung

Parameters	Composition
TS (mg.l ⁻¹)	156
VS (mg.l ⁻¹)	32.5
COD (mg.l ⁻¹)	2200
NH ₃ -N (mg.l ⁻¹)	680
pH	7.1-7.4
Moisture (%)	41.4

This experiment was conducted for 25 days. Although continuous agitation was not provided, high ambient temperature was maintained because at that time the temperature in Karachi was around 45-50°C. The results obtained showed a high methane content to produce the flame, as shown in Figure 8. So this proves that for production of biogas temperature plays an important role.

The pH decreased during the hydrolysis process in the reactor. The sudden decrease in pH created toxicity for the methanogenic bacteria that caused failure of the experiment. As the organic matter is reduced to volatile fatty acids and accumulated during digestion, so pH tends to decrease. If pH is below 6.5 the methane production decreases. As volatile fatty acids consume methane and thus acids are destroyed, pH of the digester increases.



Fig. 8. Flame test of cow dung and sewage water

There is a variation in temperature and control is not easy. It was observed that in the mesophilic temperature experiment a small tolerance (-3 to +3) may create 30% decrease in biogas production. Especially in thermophilic temperature conditions the system is very sensitive, and tolerance of about (-1 to +1) was observed. At 45 to 47°C the rate of reaction is low due to mesophilic and thermophilic microorganisms collision [10, 27]. Limits of temperature and pH for mesophilic digestion are shown in Table 11.

Table 11. Limits of temperature and pH for mesophilic digestion

Parameter	Hydrolysis/ Acidogenesis	Methanogenesis
Temperature	25-35°C	Mesophilic 30-40°C
pH value	5.2-6.3	6.7-7.5

Another problem is the agitation of the slurry at proper rpm. Because a slurry in a reactor needs to be continuously agitated to homogenize the bacteria with the substrate and prevent from partials settlement. Ammonium inhibition must be considered. Ammonium is toxic to mesophilic methanogenic bacteria at a concentration over 300 mg/l. The thermophilic process is more sensitive to ammonium. For the thermophilic process, ammonium shows the inhibitory concentration to be over 4900 mg/l when using fat substrate. From organic nitrogen, the ammonium is created during proteins degradation. Quality of cow dung was not constant place to place. Some of it contains poisonous contaminants; metals, inorganic substances, and non-degradable waste [10, 27]. No such nutrients were detected that was meaningful for biogas production. The material of the reactor created a hazard for bacteria, and microorganism performance decreased. The decrease in the activity of organisms decreased the gas production. The extra time that is above the experiment duration

time may degrade the methane gas and increase the carbon dioxide gas.

Waste solids such as food, silage, sewage waste that contain unique properties like volatile solids, optimum C/N ratios, pH range (6 to 7) better BOD, are good for biogas production. Protein-rich substrate is good because the optimally pH is maintained in the process stages. The substrate that contains fats increases the hydrolysis rate, but acetogenesis in limited thermophilic conditions is required. To control the pH, a separate device was introduced. If the pH increases or decreases, dilute hydrochloric acid for lower pH and sodium hydroxide for higher pH, respectively, was added. A pilot reactor of 19 l water cane was introduced that prevents methane gas from poisoning and minimizes the external impurities. To homogenize the feed slurry in the reactor to enhance the microorganisms activities, the reactor was equipped with anchor type agitator. This agitator does not run by an electric motor, but by the wind. Gearbox may be used to give power to the agitator. To control the temperature in the reactor, the latter was equipped with an electric heater with a bathtub that maintains the temperature in the range of 45 to 55°C, thermophilic conditions. Thermophilic digestion is about 10-15 days. Artificial nutrients and chemicals were introduced to enhance the activities of microorganisms. Yoghurt water and animal blood can increase the growth of bacteria because these materials have high BODs to degrade into methane producing substances. Regeneration time for microorganisms in the bioreactor is shown in Table 12. For gas collection, the motorbike tubes should be replaced with cylinders or glass bottles for gas because the polymer tubes may create impurities and react to forming non-favourable gases.

Table 12. Duration of different processes in the bioreactor

Process	Duration
Acidogenesis	Less than 36 h
Acitogenesis	80 - 90 h
Methanogenesis	5-16 days

In this experiment cow dung and sewage water were used with continuous agitation. Also, the temperature was being controlled, and constant pH was being maintained. 5.5448 kg of cow dung and 4 l of water were used. This experiment was done in the 2nd reactor with continuous agitation. The results obtained were quite remarkable: biogas was produced in 15 days. In cow dung and sewage water it took 25 days to produce biogas. So, by

continuous agitation, the production time of methane production can be reduced. So this is also an optimizing parameter.

Another experiment was done with cow dung and water using 6.9899 kg of cow dung and 4.2708 l of water. In this experiment water displacement technique was used to find out the flow rate. This experiment was also conducted at the same conditions as the above experiment, however, this time the production rate of biogas was measured. For this, the water displacement method or the volume displacement method was used. The gas produced contained methane, carbon dioxide and hydrogen sulfide. The data for the production of biogas for 5 days are shown in Figure 9.

The result obtained from cow dung and sewage water in bioreactors with and without agitation showed that biogas was produced in both cases but the time required to produce is different.

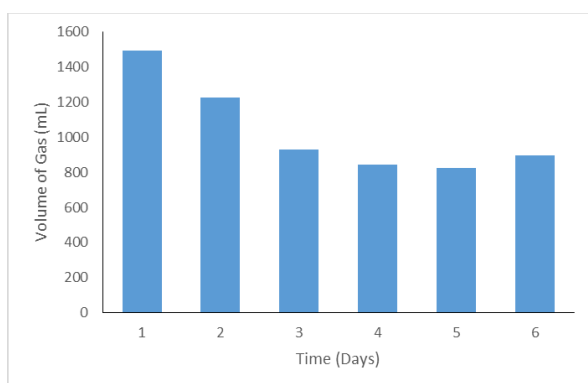


Fig. 9. Production of biogas with time

CONCLUSION

Pakistan has the potential of producing 8.8 to 17.2 billion m³ (55 to 106 TWh of energy) of biogas per year from just livestock residue. In this study cow dung and sewage water was used with continuous agitation for the production of biogas. The results obtained were quite remarkable and the product had high methane content to produce a flame. The results obtained showed that from cow dung and sewage water in bioreactors with and without agitation, biogas was produced in both cases but the production time was different. In the mesophilic temperature experiment a 30% decrease in biogas production was observed, especially in thermophilic temperature conditions, the system is very sensitive and tolerable. The biogas was measured by the water displacement method or the volume displacement method. The gas produced contains methane, carbon dioxide and hydrogen sulfide. The future recommendation is to fabricate a proper digester with an agitator, heating mechanism

and pH controlling device. Amine solvent should be used for absorption of carbon dioxide formed during the process.

Acknowledgement: The authors would like to acknowledge the Department of Chemical Engineering and the Department of Polymer and Petrochemical Engineering, NED University of Engineering & Technology, Karachi, Pakistan for supporting this research work.

REFERENCES

1. Y. A. Hilal, F. S. Atalay, *Energ. Source. Part A.*, **25**, 1063 (2010).
2. D. Divya, L. R. Gopinath, P. Merlin Christy, *Renew. Sustain. Energ. Rev.*, **42**, 690 (2015).
3. V. Kirubakaran, V. Sivaramakrishnan, S. Shanmugapriya, M. Premalatha, P. Subramanian, *Energ. Source. Part A*, **31**, 1700 (2009).
4. P. A. Ukpai, M. N. Nnabuchi, *Adv. Appl. Sci. Res.*, **3**, 1864 (2012).
5. O. Yaldiz, S. Sozer, N. Caglayan, C. Ertekin, D. Kaya, *Energ. Source. Part A.*, **33**, 1802 (2011).
6. K. Mokobia, E. U. Ikhuoria, D. Olugbemide, *Int. J. Basic Appl. Sci.*, **1**, 258 (2012).
7. Y. Singhal, S. K. Bansal, R. Singh, *Int. J. Emerg. Sci.*, **2**, 405 (2012).
8. C. Zhang, H. Su, J. Baeyens, T. Tan, *Renew. Sustain. Energ. Rev.*, **38**, 383 (2014).
9. A. Effuggi, D. Gelosa, M. Derudi, R. Rota, *Combust. Sci. Tech.*, **103**, 481 (2008).
10. P. Vindis, B. Mursec, M. Janzekovic, F. Cus, *J. Achiev. Mater. Manuf. Eng.*, **36**, 192 (2009).
11. F. Oliveira, K. Doelle, *J. Food Process. Technol.*, **6**, 1 (2015).
12. Y. Lee, S.-W. Oa, *J. Mater. Cycles Waste Manag.*, **18**, 201 (2015).
13. Z. Yong, Y. Dong, X. Zhang, T. Tan, *Renew. Energ.*, **78**, 527 (2015).
14. S. Pavi, L. E. Kramer, L. P. Gomes, L. A. S. Miranda, *Bioresour. Technol.*, **228**, 362 (2017).
15. I. R. Ilaboya, F. F. Asekhome, M. O. Ezugwu, A. A. Erameh, F. E. Omofuma, *World Appl. Sci. J.*, **9**, 537 (2010).
16. P. Abdesahian, J. S. Lim, W.S. Ho, H. Hashim, C.T. Lee, *Renew. Sustain. Energ. Rev.*, **60**, 714 (2016).
17. H. Afazeli, A. Jafari, S. Rafiee, M. Nosrati, *Renew. Sustain. Energ. Rev.*, **34**, 380 (2014).
18. A. N. Matheri, S. N. Ndiweni, M. Belaid, E. Muzenda, R. Hubert, *Renew. Sustain. Energ. Rev.*, **80**, 756 (2017).
19. X. Wang, G. Yang, Y. Feng, G. Ren, X. Han, *Bioresour. Technol.*, **120**, 78 (2012).
20. P. Merlin Christy, L. R. Gopinath, D. Divya, *Renew. Sustain. Energ. Rev.*, **34**, 167 (2014).
21. B. Zhu, P. Gikas, R. Zhang, J. Lord, B. Jenkins, X. Li, *Bioresour. Technol.*, **100**, 1122 (2009).
22. K. Hagos, J. Zong, D. Li, C. Liu, X. Lu, *Renew. Sustain. Energ. Rev.*, **76**, 1485 (2017).

23. R. Campuzano, S. Gonzalez-Martinez, *Waste Manag.*, **54**, 3 (2016).
24. X. Wang, G. Yang, F. Li, Y. Feng, G. Ren, *Waste Manag. Res.*, **31**, 60 (2013).
25. H. W. Yen, D. E. Brune, *Bioresour. Technol.*, **98**, 130 (2007).
26. P. Intanoo, P. Rangsanvigit, P. Malakul, S. Chavadej, *Bioresour. Technol.*, **173**, 256 (2014).
27. B.S.U.I. Abubakar, N. Ismail, *ARPN J. Eng. Appl. Sci.*, **7**, 169 (2012).
28. I. M. Nasir, T. I. M. Ghazi, R. Omar, A. Idris, *Energ. Source Part A.*, **36**, 1476 (2014).
29. I. Muhammad Nasir, T. I. Mohd Ghazi, R. Omar, *Appl. Microbiol. Biotechnol.*, **95**, 321 (2012).
30. C. M. Ajila, S. K. Brar, M. Verma, R. D. Tyagi, S. Godbout, J. R. Valero, *Crit. Rev. Biotechnol.*, **32**, 382 (2012).
31. L. Alejo-Alvarez, V. Guzman-Fierro, K. Fernandez, M. Roedel, *Environ. Technol.*, **37**, 2865 (2016).
32. B. Wu, *Comput. Electron. Agr.*, **93**, 195 (2013).
33. O. A. Aworanti, S. E. Agarry, O. A. Arinkoola, V. Adeniyi, *Int. J. Eng. Sci. Tech.*, **3**, 573 (2011).
34. A. Shilton, N. Powell, A. Broughton, C. Pratt, S. Pratt, C. Pepper, *Environ. Technol.*, **34**, 2491 (2013).

Estimation of mineral, trace element and fatty acid profile of Anatolian water buffalo milk

O. Ağyar³, A. S. Ertürk^{2*}, A. Özkaya^{1*}, M. G. Sucak³, Y. Şahin¹

¹Department of Chemistry, Faculty of Arts and Sciences, Adıyaman University, Adıyaman, Turkey

²Department of Analytical Chemistry, Faculty of Pharmacy, 02040, Adıyaman, Turkey

³Department of Veterinary, Kahta Vocational School of Adıyaman University, Adıyaman, Turkey

Received: February 14, 2019; Revised: February 15, 2020

Buffaloes are the second-most milk-producing animals in the world and Turkey is the tenth among the top buffalo milk (BM) producers. Although the buffalo population has increased through the world since 1980, a dramatic decrease was observed in the number of Anatolian water buffaloes (AWB) until 2008 (91.8% fall). Thus, there is a growing interest by the Turkish government to encourage production of AWB, BM and output products of BM. However, the nutrient profile of AWB milk (AWBM) has not been determined in details and the data about the biochemical composition of the AWBM are still limited. In this study, chemical, elemental, and fatty acid (FA) compositions of AWBM were determined by FT-120 milk analyzer, ICP-OES, and GC, respectively. Gross chemical composition of AWBM was found as total solids 17.15%, protein 4.67%, and fat 7.66%. Major elements in AWBM were determined as Ca (3,043.00 mg/L), P (1,831.33 mg/L), K (1,797.5 mg/L), and Na (675.66 mg/L) while minor elements were observed as Mg (243.91 mg/L), Zn (9.30 mg/L), Si (3.08 mg/L), Fe (1.59 mg/L), and Mn (0.6 mg/L). Proportions of total FAs were found as saturated FAs (Σ SFA) 66.16%, monounsaturated FAs (Σ MUFA) 29.68%, polyunsaturated FAs (Σ PUFA) 4.16%. In conclusion, the results of this study indicate that the potential nutrient profile of AWBM is of great significance to human nutrition. Furthermore, the results will be useful for the future studies concerning buffalo breeding and dairy processing.

Keywords: Anatolian water buffalo; buffalo milk; minerals; major elements; trace elements; fatty acids

INTRODUCTION

Milk is one of the most important parts of human diet. Buffalo, which is almost universally considered to be an Asian animal, is the second most milk producing animal in the world. The domestic water buffalo (*Bubalus bubalis*) has a great contribution to global milk production as a major milk providing animal in several countries. Food and Agriculture Organization (FAO) reported that there are about 168 million heads of water buffalo (WB) in the world, and more than 95% are found in Asia [1]. Turkey ranked tenth among the top buffalo milk (BM) producers with 54,803 tonnes in 2014 [2]. Turkish WB are commonly known as the Anatolian water buffaloes (AWB) and classified as Mediterranean buffaloes belonging to the River group involving Syrian, Egyptian and Southeast European animals [3, 4]. The AWB has been raised for more than 1,000 years as an antique part of Turkey's livestock resources and there was over 1 million heads just a few decades ago. Although the buffalo population has increased through the world since 1980, a dramatic decrease was observed in the number of the AWB from 1,040,000 heads in 1980 to the observed lowest values of 84,705 heads in

Thus, the fall in the AWB population was 91.8%. Among a number of reasons, intensification of the dairy activities, agricultural mechanization, consumer preferences, and less market demand to buffalo products [5] are shown as main responsibilities for this decrease. By 2011, the AWB population remained in steady state at around 84,726 heads [6]. With the first attempts on the conservation of animal genetics resources and diversities in 2008 and the foundation of the Water Buffalo Breeders Union in 2011, the buffalo number exceeded 100,000 heads and reached to 107,435 heads in 2012 [5, 7]. Notwithstanding the existing discrepancy between the FAO and Turkish Statistical Institute (TUIK) statistics in terms of the buffalo numbers by years, the recent accessible data for the number of AWB were reported by TUIK in 2016 as 133,776 heads in 2015 corresponding to 0.96% of 13,994,071 cattle [8]. From 2008 to 2015, a total of 57.9% increase in the AWB population can be seen as an obvious evidence of the positive impact of the recent legislations and conservation programs arranged by the government to prevent extinction of the AWB in Turkey [5]. Nevertheless, more efforts and promotions by the government are needed to encourage buffalo production and consumption of buffalo dairy products.

* To whom all correspondence should be sent:
E-mail: aozkaya01@gmail.com (A. Özkaya)
aserturk@gmail.com (Ali S. Ertürk)

In Turkey, not only AWBs have been bred for milk production, but also they are used as household livelihoods with their meat and draught power. In particular, BM outputs are a semi-hard cheese called "peyaz peyneri", ayran [9], buffalo cream from high-fat milk which is favorable as an additive to the traditional Turkish desserts [3]. Efforts on improving milk yields and lactation periods of the AWB from different provinces of Turkey are still continuing. Top three main distribution areas of the AWB are in the West Black Sea (39,738 heads), Central East Anatolia (14,337 heads), Central Anatolia (14,045 heads). Regarding the buffalo production numbers, focal points of the production of Turkish buffaloes are found in the provinces of Afyon (5,183 heads), Bitlis (7,594 heads), Diyarbakır (11,510 heads), Istanbul (11,518 heads), Kayseri (5,313 heads), Mus (6,087 heads), Samsun (17,043 heads), and Tokat (8,839 heads). The Aegean (2,091 heads) and the West Anatolia (1626 heads) have the lowest number of AWB [10]. In comparison to cow milk, it was reported in a comprehensive recent review that BM is richer in almost all main milk nutrients such as fatty acids, proteins, crude protein, calcium, fat, phosphorus and lactose [11]. Considering the high level of nutrients presents in BM and the added economic potential value of the output products of BM such as mozzarella, sweets, cream, it is necessary to better understand the nutrient profiles and composition of BM samples in Turkey. However, little attention has been paid to the detailed characterization of the chemical composition of AWB milk (AWBM). Thus, it is important to enlighten the composition of the AWBM to encourage AWB husbandry, buffalo products, and to conserve this national heritage.

The aim of this study is, therefore, to analyze the milk quality of AWB in terms of chemical, elemental and fatty acid compositions, to create awareness on the potential use of the AWBM, and strengthen its use in dairy production and demand in the market. Total solids, fat, protein, solids-non-fat, lactose, casein, density, urea, total acidity, free fatty acid, citric acid and freezing point depression, elemental levels, and fatty acid composition of AWBM were examined. The results will be useful for the future studies concerning buffalo breeding and dairy processing.

EXPERIMENTAL

Sampling (milk samples)

Milk products used in this study, within General Directorate of Agricultural Research and Policies, were obtained from the incorporated materials in National Community Based Anatolian Water

Buffalo Breeding Program (TAGEM/49 MANDA 2012-01). Muş is located in Eastern Anatolia region of Turkey with the latitudes of 38° 44'41" N, 41° 39'14" E and elevation 1,400 meters above sea level (m.a.s.l.). All AWB were multiparous (para 2, lactation stage: 2, body weight, 450-550 kg; milk yield 6.5 ± 2.5 kg/d), and fed on natural pastures of Muş Plain of Turkey. 50 mL milk samples (n=35) were collected directly in sterilized plastic containers in the morning milking session, brought to the laboratory with cold chains, and immediately stored at -20 °C until required for analysis. No other pretreatments or preservatives were used for the milk samples.

Analytical procedures

Determination of chemical composition. FOSS MilkoScan™ FT-120 (Foss Electric, Denmark), calibrated with appropriate buffalo standards, was used to analyze total solids (%), protein (%), fat (%), casein (%), lactose (%), citric acid (%), density (g/cm^3), urea (mg/dL), total acidity (°SH), free fatty acids (mmol/10L), and freezing point depression (FPD) (°C) in raw BM samples. FTIR analytical technology utilized in MilkoScan™ FT-120 is compatible with IDF (International Dairy Federation) principles and AOAC (Association of Official Analytical Chemists) formal procedures [12].

Determination of elements. Milk samples (2 mL) were transferred to DAP60-K PTFE vessels of a microwave digestion system, and 4 mL of HNO_3 (65% w/v) and 1 mL of HClO_4 (60% w/v) were added. After digestion, the digested samples were transferred to 20 mL volumetric flasks and made up to final volume with 0.1 M HNO_3 . Also, blank samples were prepared and digested in the same way. Final sample solutions were analyzed by inductively coupled plasma optical emission spectrometry (ICP-OES) [13].

Determination of fatty acid composition. Milk fat extraction [14] and transformation of the fatty acids to methyl esters [15] were carried out according to literature and are briefly summarized hereafter. 1 mL of BM samples were taken, and homogenized in a hexane/ isopropanol (3:2 v/v) mixture. Lipid extracts were centrifuged at 10,000 rpm for 5 min. Then, solvents were removed at 40 °C. The fat extracts were stored at -25°C before fatty acid analysis. Three replicate measurements were taken for each sample. Fatty acids in the lipid extract were treated with 2% sulfuric acid (v/v) in methanol and transformed into methyl esters. Fatty acid methyl esters were extracted with hexane. After transforming the fatty

acids in the lipid extracts to methyl esters the latter were analyzed by gas chromatography (SHIMADZU GC 2025 with a flame ionization detector) using TR-CN 100 capillary column (60 m × 0.20 mm i. d. with 25 µm film thickness) (Teknokroma, Spain). Calculations were performed using GC Solution program (V.2.42).

Statistical analysis

Descriptive statistics were performed with SPSS statistic software. (SPSS 20.00, Chicago). The data were presented as mean ± standard deviation.

RESULTS AND DISCUSSION

Chemical composition of AWBM

Descriptive statistics of the variables studied for the chemical composition of the AWBM are presented in Table 1. Total milk solids 17.15 ± 1.35%, protein 4.67 ± 0.47%, and fat 7.66 ± 1.12% were in good agreement with the findings of a previous study (total solids: 16.6 ± 1.6%, protein: 4.40 ± 0.51%, and fat: 7.1 ± 1.4%) [16]. In the same way, the solid-non-fat value 10.04 ± 0.51% was aligned with the value of 9.6 ± 0.8% of the same study. While the observed lactose value was 4.94 ± 0.18% of the AWB, the casein value of 3.50 ± 0.48% was similar to the previously reported value of 4.40 ± 0.51 [16]. On the other hand, a good agreement was also observed between the density, urea, total acidity, free fatty acid, citric acid, and FPD values of the AWBM and those presented in a recent study [17] as in the minimum and maximum range of 1.028 to 1.033 g/cm³, 0.036 to 0.057 mg/dL, 5.96 to 9.94 °SH, 3.22-6.35 mmol/10L, 0.11 to 0.15%, -0.46 to -0.66°C, respectively. Taken all in consideration,

it is noteworthy that the obtained values of the milk chemical composition variables of the AWBM in this study were not only correlated with the reported values in former local studies [16, 17] but also were in the accepted range of composition and properties of BM [11].

Table 2 presents detailed information about the comparison of the elemental levels of BMs from different locations of the world. Major elements in AWB milk were found as Ca (3,043.00 mg/L), P (1,831.33 mg/L), K (1,797.5 mg/L), and Na (675.66 mg/L) while minor elements were observed as Mg (243.91 mg/L), Zn (9.30 mg/L), Si (3.08 mg/L), Fe (1.59 mg/L), and Mn (0.6 mg/L). Five macro elements such as Ca, Mg, K, Na and P were determined in all of our samples. The observed individual mean concentrations of Ca (3,043 mg/L), Mg (243.91 mg/L), K (1,797.5 mg/L), Na (675.66 mg/L), and P (1,831.33 mg/L) in BM samples were the highest compared to the results obtained in earlier studies from Bangladesh [18], Italy [19], Argentina [21], Pakistan [22], and India [25] (Table 3). There are many benefits and crucial roles of Ca in human body such as hormone secretion, enzymatic reaction and relaxation of muscles [26]. Likewise, Mg not only takes role as a cofactor in more than 300 enzymes in the human body but also regulates many diverse biochemical reactions. Moreover, P in milk is found in many derivatives such as ester or inorganic phosphorous and converted into active biological forms thorough intestinal adsorption [27].

Investigation of the obtained results revealed that three essential trace elements were determined in all of our AWBM samples, which were Fe, Mn and Zn (Table 3).

Table 1. AWBM chemical composition (n=35)

Variable	Mean	SD	Minimum	Maximum
Total solids (%)	17.15	1.35	14.59	19.70
Fat (%)	7.66	1.12	6.22	9.48
Protein (%)	4.67	0.47	3.62	5.33
Solids-non-fat (%)	10.04	0.51	9.45	10.96
Lactose (%)	4.94	0.18	4.68	5.31
Casein (%)	3.50	0.48	2.87	4.61
Density (g/cm ³)	1.036	2.36	1.032	1.042
Urea (mg/dL)	0.043	0.013	0.004	0.059
Total acidity (°SH)	8.63	1.27	7.04	10.53
Free fatty acids (mmol/10L)	4.43	0.97	3.25	6.37
Citric acid (%)	0.18	0.03	0.12	0.22
Freezing point depression (°C)	-0.63	0.04	-0.55	-0.70

Elemental composition of AWBM

Table 2. Descriptive statistics of data in raw WB milk samples (mg/L)

Elements	Mean	SD	Range	
			Min.	Max.
Ca	3,043.00	329.05	2,929.98	3,156.02
P	1,831.33	404.76	1,692.55	1,970.11
K	1,797.5	315.67	1,688.79	1,905.21
Na	675.66	177.50	614.20	735.8
Mg	243.91	62.00	222.61	265.21
Zn	9.30	2.51	8.44	10.16
Si	3.08	0.75	2.82	3.34
Fe	1.59	0.47	1.43	1.75
Mn	0.60	0.05	0.58	0.62

Table 3. Comparison of the elemental levels of BM samples in this work with previous works^a

Element	Turkey This work (mg/L) (n=35)	Bangladesh [18] (mg/kg) (n=9)	Italy [19] (mg/kg) (n=6)	Campania, Italy [20] (mg/kg) (n=68)	Argentina [21] (mg/kg) (n=105)	Pakistan [22] (mg/L) ^b	West Bengal [23] (mg/kg) (n=10)	Egypt [24] (mg/kg) (n=60)	India [25] (mg/kg) n=496
Ca	3,043	1.480	1.740		1.120	702			
Fe	1.59		0.3		1.61		3.50	0.980	3.05
K	1,797.5	860	641		920	145			
Mg	243.91	140			80	193			
Mn	0.60	0.07	0.0024	0.0493	0.27		1.74	0.076	0.56
Na	675.66	370			350	16			
P	1,831.33	1.070	1.190		990				
Zn	9.30	4.58	6.49	5.74	4.1		3.75	4.37	3.57

^aData are reported as mean values^bNumber of samples is not available

In particular, Zn was the most abundant of the trace elements (9.30 mg/L) which was followed by Fe (1.59 mg/L) and Mn (0.60 mg/L). Zn content was above the values obtained in all of the similar studies given in Table 3. The mean Fe content of our AWBM samples was more or less different from those reported in the literature. It was higher than for Egypt (0.980 mg/kg) [24], and Italy (0.3 mg/kg) [19] while lower than for Argentina (1.61 mg/kg) [21], West Bengal (3.50 mg/kg) [23] and India (3.05 mg/kg) [25]. The mean concentration of Mn was observed as 0.60 mg/mL, which was very close to the reported value for India (0.56 mg/kg) [25] and the second highest value after West Bengal (1.74 mg/kg) [23]. In contrast, the level of Mn was much higher than the reported values for Bangladesh (0.07 mg/kg) [18], Italy (0.024 mg/kg) [19], Campania, Italy (0.0493 mg/kg) [20], Argentina (0.27 mg/kg) [21] and Egypt (0.076 mg/kg) [24]. On the other

hand, the mean concentration of Si was found as 3.08 mg/L which is very close to the value of 3.26 mg/L for BM reported in the study of Nirgude *et al.* [28] and lower than in goat milk (10.59 mg/mL) of local goat breeds collected from Üzümdallı village in Hatay province of Turkey [29]. Si plays a role in the normal metabolism of higher animals as connective tissue, especially in bone and cartilage and forms important relations with other elements [28].

The fatty acid content of AWBM

Chemical composition of milk can be influenced by several factors such as animal species, genetics, environmental conditions, lactation stage, and nutritional status [30-35]. Among these factors, significant differences were found in BM fat composition due to variations in animal nutrition related with the buffaloes' feeding management with different herds [30]. On the other hand, the milk fatty

acid quality was reported as better in younger buffaloes at early lactation stage depending on the effect of age and lactation on milk fatty acid profile in dairy buffaloes [32]. Apart from these factors, it was found that WB milk has lots of biochemical materials such as amino acids, fatty acids, minerals, enzymes and vitamins, which are very important for human metabolism, especially for the skeletal system [36]. No information is available for the fatty acid composition of milk samples from buffalo in Turkey. Milk fatty acid (FA) compositions of the AWBMs are presented in Table 4. Σ SFA fraction rate was found to be 66.16%. The major FAs in all AWBM samples were palmitic acid (C16:0)

33.90%, myristic acid (C14:0) 10.09%, stearic acid (C18:0) 12.82%. Σ UFA accounted for 33.84% while the percentage of monounsaturated fatty acids (Σ MUFA) and total polyunsaturated fatty acids (Σ PUFA) constituted 29.68% and 4.16%, respectively. On the other hand, the levels of important PUFAs were linoleic acid (C18:2n6c) 1.76%, linolelaidic acid (C18:2n6t) 0.25%, gamma linolenic acid (C18:3n6) 1.01%, and docosahexaenoic acid (C22:6n3) 0.28%. The largest MUFA was oleic acid (C18:1n9c) 22.33%, and the others were myristoleic acid (C14:1) 1.07% and elaidic acid (C18:1n9t) 1.59%.

Table 4. Fatty acid content of Turkish WB milk (%)^a

SFA	Mean ± SD	PUFA	Mean ± SD	MUFA	Mean ± SD
C4:0	0.26 ± 0.05	18:2n6c	1.76 ± 0.22	C14:1	1.07 ± 0.25
C6:0	1.04 ± 0.16	18:2n6t	0.24 ± 0.04	C15:1	0.57 ± 0.09
C8:0	0.59 ± 0.09	18:3n6	1.02 ± 0.18	C16:1	2.21 ± 0.32
C10:0	1.12 ± 0.16	18:3n3	0.17 ± 0.03	C17:1	0.46 ± 0.11
C11:0	0.06 ± 0.02	20:3n6	0.21 ± 0.09	C18:1n9t	1.60 ± 0.25
C12:0	1.68 ± 0.18	C20:2	0.07 ± 0.01	C18:1n9c	22.34 ± 2.93
C13:0	0.09 ± 0.01	20:3n3	0.04 ± 0.01	C20:1	1.00 ± 0.14
C14:0	10.09 ± 1.50	20:4n6	0.17 ± 0.04	C22:1n9	0.24 ± 0.05
C15:0	1.95 ± 0.28	C22:2	0.13 ± 0.02	C24:1	0.22 ± 0.06
C16:0	33.90 ± 2.47	C20:5	0.07 ± 0.01	Σ MUFA	29.68 ± 2.37
C17:0	1.37 ± 0.17	C22:6	0.28 ± 0.04	Σ UFA	33.84 ± 2.70
C18:0	12.82 ± 1.77	Σ PUFA	4.16 ± 0.52		
C20:0	0.40 ± 0.14				
C21:0	0.08 ± 0.02				
C22:0	0.38 ± 0.09				
C24:0	0.34 ± 0.08				
Σ SFA	66.16 ± 4.62				

^aSFA, saturated fatty acids, MUFA, monounsaturated fatty acids; PUFA, polyunsaturated fatty acids; UFA, unsaturated fatty acids. Results are presented as means of 35 different samples with three replicate measurements ± standard deviation (SD).

Taken into consideration the results of our study, similar levels of Σ FAs in milk fat have been reported in the literature. Mihaylova *et al.* [37] found the ratio of FAs in BM as 72.15% (Σ SFA), 24.70% (Σ MUFA), 3.15% (Σ PUFA) while Fernandes *et al.* [38] reported these ratios as 65.04%, 31.68% and 3.28%, respectively. In another study, Talpur *et al.* [39] compared milk FA levels of Nili-Ravi and Kundi. Results of their study revealed that Σ SFA, Σ MUFA, Σ PUFA values of Nili-Ravi were 69.09%, 25.20%, and 2.76% while those of Kundi were 66.96%, 27.62%, and 2.77, respectively. It is well known that long-chain PUFAs have an important role in many aspects of children's health, notably in

neuro developmental and psychiatric conditions [40]. Moreover, it was reported that diets with high amounts of MUFAs and PUFAs decrease the risk for coronary artery disease [41]. Considering the results of the above mentioned studies, it is noteworthy that Σ PUFA levels were found in our study (4.16%, Table 4). PUFAs consist of many long-chain FAs. Some of the members of long-chain omega-3 FAs are eicosapentaenoic acid (C20:5n3) and docosahexaenoic acid (C22:6n3). They diminish the risks of cardiovascular incidence [42]. In the study on the long-chain FA profiles in BMs we found linolelaidic acid (C18:2n6t), gamma-linolenic acid (C18:3n6), cis-8,11,14-eicosatrienoic acid

(C20:3n6), cis-11,14-icosadienoic acid (20:2n3), cis-11,14,17-eicosatrienoic acid (C20:3n3), erucic acid (C22:1n9) and nervonic acid (C24:1). Furthermore, linoleic (C18:2n6c), linolenic (C18:3n3) and oleic (C18:1n9c) acids are known as to be cardio protective fatty acids [43]. In our study, the total of these FAs were 24.27% of total FAs whereas Qureshi *et al.* [44] and Mihaylova *et al.* [37] reported them as 34.38% and 20.81%, respectively. On the other hand, the total fraction of lauric acid (C12:0), myristic acid (C14:0) and palmitic acid (C16:0) is called hypercholesterolemic FAs (HCFA), over intake of which from diet causes cardiovascular diseases [45]. In our study, the HCFA ratio was determined as 45.67% similar to Pakistan buffalo breed Nili-Ravi buffaloes having 43.33% [44] and Bulgarian Murrah buffaloes having 43.62 % [37]. Moreover, Talpur *et al.* found HCFA ratios of BM as 45.48% (Kundi) and 46.54% (Nili-Ravi) [39]. BM has a high level of nutrients and therefore an economic potential value. Production of yogurt, cheese, ice cream, and sweets from Water BMs is not common in Turkey as in Italy that has its own brand like mozzarella cheese and wide WB milk products. In summary, AWBM deserves much more attention in diets of children and older people in Turkey.

CONCLUSION

In this study, chemical, elemental and fatty acid compositions of milk samples from AWB were extensively analyzed. The results obtained from these biochemical parameters showed that the AWBM is rich in terms of various elements, PUFA and MUFA FAs. This study is important since it reveals the potential nutrient profile of AWBM for human nutrition and creates awareness on the output products of AWBM. Additionally, the results will be useful for the future studies concerning buffalo breeding and dairy processing.

Acknowledgements: This research has been supported by Adiyaman University Scientific Research Projects Coordination Department. Project Numbers: FEFLAP/2014-003. Milk products used in this study, within General Directorate of Agricultural Research and Policies was obtained from the incorporated materials in National Community Based Anatolian Water Buffalo Breeding Program TAGEM/49MANDA2012-01. Authors declare that there is no conflict of interests.

REFERENCES

1. <http://www.fao.org/agriculture/dairy-gateway/milk-production/dairy-animals/water-buffaloes/en/#.VxSeJ49OLmI>

2. FAOSTAT. Livestock database 2014. Available from: <http://www.fao.org/faostat/en/#data/QL>.
3. *Buffalo Livestock and Products*. A. Borghese (ed.), Euroformazione KFT, Pecs, Hungary, 2012.
4. I. L. Mason, *A World Dictionary of Livestock Breeds, Types and Varieties*. CAB International, 1996.
5. O. Yilmaz, M. Ertugrul, R. T. Wilson, *Tropical Animal Health and Production*, **44** (4), 707 (2012).
6. FAOSTAT. Livestock database 2011. Available from: <http://www.fao.org/faostat/en/#data/QL>.
7. TurkStat (2013) Turkey's Statistical Yearbook 2013.
8. http://www.turkstat.gov.tr/VeriBilgi.do?alt_id=1002
9. A. Borghese, M. Mazzi, *Buffalo Production and Research*, **67**, 1 (2005).
10. <https://biruni.tuik.gov.tr/bolgeselistatistik/anaSayfa.do?dil=en>
11. M. H. Abd El-Salam, S. El-Shibiny, *Dairy Science & Technology*, **91** (6), 663 (2011).
12. W. Horwitz, *Official Methods of AOAC International*, 17th edn. (Association of Official Analytical Chemists: Gaithersburg, MD), 2000.
13. Ciftci, A. Ozkaya, E. Kariptas, *J Food, Agriculture and Environment*, **7** (3-4), 72 (2009).
14. A. Hara, N. S. Radin, *Analytical Biochemistry*, **90** (1), 420 (1978).
15. W. W. Christie, *Gas chromatography and lipids: a practical guide*. The Oily Press, Matreya, 1989.
16. Ö. Şekerden, H. Erdem, B. Kankurdan, B. Özlü, *Turkish J Veterinary and Animal Sciences*, **23** (6), 505 (1999).
17. A. Sahin, A. Yildirim, Z. Ulutas, *Italian J. Food Science*, **26** (4):398 (2014)
18. M. A. Islam, M. K. Alam, M. N. Islam, M. A. S. Khan, D. Ekeberg, E. O. Rukke, G. E. Vegarud, *Asian-Australasian J. Animal Sciences*, **27** (6), 886 (2014).
19. C. Benincasa, J. Lewis, G. Sindona, A. Tagarelli, *Food Chemistry*, **110** (1), 257 (2008)
20. M. Esposito, O. Miedico, S. Cavallo, R. Pellicano, G. Rosato, L. Baldi, A. E. Chiaravalle, *Food Chemistry*, **233** (Supplement C), 378 (2017).
21. E. Patino, D. Pochon, E. Faisal, J. Cedres, F. Mendez, C. Stefani, G. Crudeli, *Italian J. Animal Science*, **6** (suppl. 2), 1046 (2007).
22. M. Imran, H. Khan, S. S. Hassan, R. Khan, *J. Zhejiang University Science B*, **9** (7) 546 (2008).
23. M. Mondal, S. Pyne, G. Samanta, R. Roy, *Int. J. Biores. Env. Agril. Sci.*, **1** (1), 36 (2015).
24. A. Enb, M. A. Donia, N. Abd-Rabou, A. Abou-Arab, M. El-Senaity, *Global Veterinaria*, **3** (3), 268 (2009).
25. A. Guha, S. Gera, A. Sharma, *Asian-Australasian J. Anim. Sci.*, **25** (3), 353 (2012).
26. G. D. Miller, J. K. Jarvis, N. D. Council, L. D McBean. *Handbook of Dairy Foods and Nutrition*, second edn., CRC Press, (2002).
27. M. Ahmed, A. Khaleeq, R. Huma, M.A. Qadir, M. I. Shafiq, A. Israr, A. Ali, S. Shahzad, *Food Analytical Methods*, **9** (10), 2933 (2016).
28. N. T. Nirgude, G. R. Bhagure, *American Int. J Contemporary Scientific Research*, **2** (5), 70 (2015).

29. Z. Güler, *Small Ruminant Research*, **71** (1):130 (2007).
30. M. L. Varricchio, A. Di Francia, F. Masucci, R. Romano, V. Proto, *Italian J. Animal Science*, **6** (suppl.1), 509. (2007).
31. L. Caldeira, S. Ferrão, S. de A Fernandes, T. Santos, A. Magnavita, *Revista Veterinaria* **21** (1), 564 (2010).
32. M. S. Qureshi, M. Anila, J. Shaista, R. Inyat ur, *Buffalo Bulletin*, **34** (3), 275 (2015).
33. P. Kalac, E. Samkova, *Czech Journal of Animal Science*, **55** (12), 521 (2010).
34. A. B. Shori, *J. Food and Drug Analysis*, **23** (4), 609 (2015).
35. S. Miglani, R. R. Patyar, S. Patyar, M. R. Reshi, *Journal of Food and Drug Analysis*, **24** (4), 716 (2016).
36. S. Ahmad, F. Anjum, N. Huma, A. Sameen, T. Zahoor, *J. Anim. Plant Sci.*, **23**, 62 (2013).
37. G. Mihaylova, T. Peeva, *Italian J. Animal Science*, **6** (suppl. 2), 1056 (2007).
38. S. Fernandes, W. Mattos, S. Matarazzo, H. Tonhati, M. Gama, D. Lanna, *Italian J. Animal Science*, 1063 (2007).
39. F. Talpur, N. Memon, M. Bhangar, *Pakistan J. Analyt. and Environm. Chem.*, **8** (1-2), 15 (2007).
40. A. H. Cao, L. Yu, Y. W. Wang, G. J. Wang, G. F. Lei, *Brain Research*, **1528**, 49 (2013).
41. R.P. Mensink, P.L. Zock, A.D. Kester, M.B. Katan, *The American J Clinical Nutrition*, **77** (5):1146 (2003).
42. W. S. Harris, P. M. Kris-Etherton, K. A. Harris, *Current Atherosclerosis Reports*, **10** (6):503 (2008).
43. W. J. Bemelmans, J. Broer, E. J. Feskens, A. J. Smit, F. A. Muskiet, J. D. Lefrandt, V. J. Bom, J. F. May, B. Meyboom-de Jong, *The American J. Clinical Nutrition*, **75** (2), 221 (2002).
44. M. S. Qureshi, A. Mushtaq, S. Khan, G. Habib, Z. A. Swati, *Asian-Australasian J. Anim. Sci.*, **23**, 340 (2010).
45. C. M. Williams, *Annales de Zootechnie*, **49**, 165 (2000).

4-Methyl-7-alkynyl coumarin derivatives as potent antimicrobials and antioxidants

M. N. Joy^{1,2*}, Y. D. Bodke^{2,3}, S. Telkar⁴

¹Innovation Center for Chemical and Pharmaceutical Technologies, Institute of Chemical Technology, Ural Federal University, 19 Mira Street, 620002 Yekaterinburg, Russia

²Department of P.G. Studies and Research in Industrial Chemistry, Kuvempu University, Jnana Sahyadri, Shankaraghatta, Shimoga, 577451 Karnataka, India

³Department of P. G. Studies and Research in Chemistry, Kuvempu University, Jnana Sahyadri, Shankaraghatta, Shimoga, 577451 Karnataka, India

⁴Department of P. G. Studies and Research in Biotechnology, Kuvempu University, Jnana Sahyadri, Shankaraghatta, Shimoga, 577451 Karnataka, India

Received: February 26, 2019; Revised: August 03, 2019

An assortment of previously synthesized 4-methyl-7-alkynyl coumarins **4a-p** was screened for their antimicrobial and antioxidant properties. Some of the compounds exhibited promising antibacterial activities (MIC ranging from 5 to 150 µg/mL) and moderate antifungal activities when compared to the respective standards. The compound **4p** showed comparable antibacterial activity with the standard (ciprofloxacin), whereas the compounds **4b** and **4p** displayed better antifungal activity when compared to the other synthesized compounds. The *in silico* docking studies of the active compound were carried out against the gyrase enzyme and it was acknowledged that **4p** demonstrates ability for considerable hydrogen bonding and hydrophobic interactions which could be the possible reason for its superior activity as compared to the other compounds. The compounds **4f** and **4g** showed comparable antioxidant activity with the standard (butylated hydroxytoluene), which could be ascribed to the presence of electron-donating substituents.

Keywords: Coumarin; Antimicrobial; Antioxidant.

INTRODUCTION

The discovery of different types of microorganisms has explained the major reasons for a variety of infectious diseases responsible for the most complex health issues of this era. Different microorganisms like bacteria, fungi and viruses are identified to cause serious global health hazards [1]. Even if a lot of drugs have been identified as potent antimicrobial agents until now, the rise of multi drug resistance in microorganisms remains as a major global concern [2]. Therefore, the discovery of new drugs with good anti-microbial potency, particularly against the resistant strains, is highly essential for addressing this issue [3]. On the other hand, reactive free radicals and oxygen species present in the biological systems can abstract hydrogen atom from membrane, lipid, protein, DNA etc. and eventually lead to damages of several biological species thereby initiating numerous degenerative diseases [4]. The supply of antioxidants (free radical scavengers) is believed to be beneficial for liquidating this hazard as they possess the specific ability to trap the free radical species. Coumarins belong to an important class of benzopyrones found in green plants and display a broad spectrum of pharmacological activities [5]. The isolation and synthesis of various novel coumarins from natural sources and synthetic

laboratories has gained considerable attention nowadays. Several coumarin derivatives are accounted to be potent antibacterial [6], anti-inflammatory [7] and antiviral agents [8] and the various therapeutic applications of coumarin compounds include photo chemotherapy, anti-tumor therapy and anti-HIV therapy [9]. Some of the marketed drugs that contain coumarin core include warfarin, acenocoumarol, carbocromen, etc., and antibiotics such as novobiocin, clorobiocin and coumermycin A1 [10]. Owing to these interesting biological properties, the exploration of natural or synthetic coumarin derivatives for their applicability as drugs has attracted medicinal chemists for decades. On the other hand, alkynes linked with heterocyclic compounds are reported to possess various biological potencies such as neuroprotective, antibacterial and antifungal activities [11,12]. These observations of coumarins and alkynes stimulated us to synthesize a variety of coumarins coupled with terminal alkynes and to examine their pharmacological potential. The synthetic methodology for the palladium-catalyzed copper, amine and ligand-free Sonogashira cross-coupling reaction of 4-methyl-7-nonafluorobutylsulfonyloxy coumarins with different terminal alkynes was previously reported by us [13].

* To whom all correspondence should be sent:
E-mail: mnibinjoy@gmail.com

As a continuation of our ongoing research in the biological evaluation of the previously synthesized molecules [14,15], it has been planned to examine the antimicrobial and antioxidant properties of the formerly prepared 4-methyl-7-alkynyl coumarins. In this paper, we report our results of the evaluation of antimicrobial and antioxidant activity along with the *in silico* docking studies of the aforementioned compounds.

RESULTS AND DISCUSSION

Chemistry

As mentioned earlier, the synthesis of various 4-methyl-7-alkynyl coumarins **4a-p** was achieved by the method previously reported by us [13]. The typical synthetic methodology started from the synthesis of the parent coumarin compound **2** by using the modified Pechmann cyclization reaction (Scheme 1) of resorcinol **1** with ethyl acetoacetate in 1-butyl-3-methylimidazolium chloroaluminate [16]. The obtained hydroxy coumarin **2** was then converted to the corresponding nonaflate **3** by treating it with nonafluorobutane sulfonic anhydride in the presence of pyridine as base at -10 °C. The intermediate **3** was then subjected to Sonogashira coupling with various terminal acetylenes by using PdCl₂(PCy₃)₂ as catalyst and TBAF·3H₂O as base in DMA at 100 °C under microwave irradiation to pursue a series of 4-methyl-7-alkynyl coumarins **4a-p** of significant pharmacological relevance.

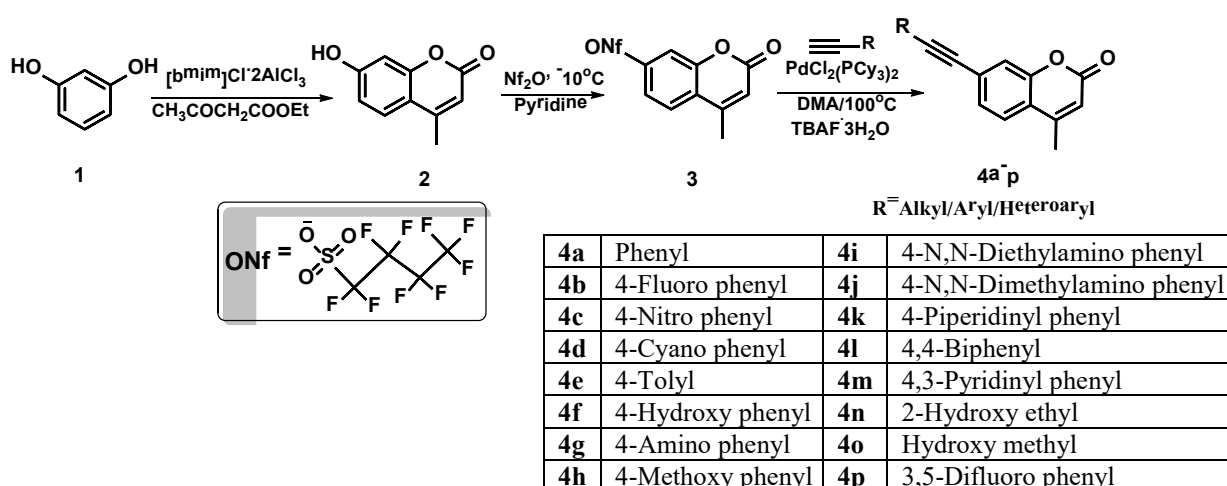
Biology: Antimicrobial activity

The analysis of antibacterial (Table 1) and antifungal activities (Table 3) of the compounds **4a-**

p was carried out against two Gram-positive bacteria (*Staphylococcus aureus* ATCC 25923 and *Bacillus subtilis* ATCC 6633), two Gram-negative bacteria (*Pseudomonas aeruginosa* ATCC 27853 and *Escherichia coli* ATCC 25922) and three fungi (*Aspergillus flavus* ATCC 9643, *Chrysosporium keratinophilum* ATCC90272 and *Candida albicans* MTCC 227). As apparent from Table 1, some of the compounds exhibited promising antibacterial activity as compared to the standard drug ciprofloxacin. The compounds **4b**, **4c**, **4d**, **4k**, **4m** and **4p** showed good and comparable activity with the standard whilst the compounds **4i**, **4j**, **4n** and **4o** failed to show any activity towards the tested strains. All the other compounds showed moderate to poor antibacterial activity.

The minimum inhibitory concentration (MIC) of the more active compounds was determined by the broth dilution method using nutrient broth (Table 2). The compound **4p** was found to be highly active against all the bacterial strains. The compounds **4k** and **4m** were found to possess superior activity when compared to the compounds **4b**, **4c** and **4d**.

The antifungal activity of the synthesized compounds was studied by taking fluconazole as the standard. Unfortunately, only a few compounds inhibited the growth of most of the tested fungi (Table 3). The compounds **4b** and **4p** showed good activity when compared to the other remaining compounds. Alternatively, all the other compounds failed to show good and comparable activity to that of the standard.



Scheme 1. Synthesis of 4-methyl-7-nonafluorobutylsulfonyloxy coumarin intermediate and its Sonogashira coupling with various terminal acetylenes

Table 1. Determination of antibacterial activity of the synthesized organic compounds

Compounds	<i>Escherichia coli</i>		<i>Staphylococcus aureus</i>		<i>Pseudomonas aeruginosa</i>		<i>Bacillus subtilis</i>	
	1	0.5	1	0.5	1	0.5	1	0.5
Conc. in mg/mL								
Control	00	00	00	00	00	00	00	00
Ciprofloxacin	22±0.1	17±0.1	21±0.1	18±0.1	21±0.1	18±0.1	23.8±0.1	14.2±0.1
4a	07±0.1	05±0.1	08±0.1	06±0.1	05±0.1	03±0.1	10±0.1	08±0.1
4b	14±0.1	11±0.1	13±0.1	09±0.1	14±0.1	10±0.1	13±0.1	09±0.1
4c	13±0.1	10±0.1	13±0.1	09±0.1	15±0.1	10±0.1	14±0.1	08±0.1
4d	13±0.2	10±0.2	12±0.1	07±0.1	13±0.2	08±0.2	12±0.2	08±0.2
4e	05±0.2	03±0.2	04±0.2	02±0.2	07±0.2	04±0.2	06±0.2	03±0.2
4f	06±0.1	02±0.1	08±0.1	05±0.1	08±0.1	04±0.1	07±0.1	03±0.1
4g	08±0.2	04±0.2	09±0.2	05±0.2	07±0.2	03±0.2	07±0.2	04±0.2
4h	07±0.1	03±0.1	08±0.1	04±0.1	06±0.1	03±0.1	07±0.1	04±0.1
4i	00	00	00	00	00	00	00	00
4j	00	00	00	00	00	00	00	00
4k	15±0.1	11±0.1	12±0.1	09±0.1	14±0.1	10±0.1	13±0.1	08±0.1
4l	06±0.1	03±0.1	08±0.1	05±0.1	07±0.1	04±0.1	06±0.1	03±0.1
4m	13±0.2	11±0.2	11±0.2	07±0.2	14±0.2	10±0.2	14±0.2	09±0.2
4n	00	00	00	00	00	00	00	00
4o	00	00	00	00	00	00	00	00
4p	18±0.1	14±0.1	16±0.1	13±0.1	18±0.1	14±0.1	18±0.1	11±0.1

^a The experiment was performed in triplicate and the values are expressed as mean ±SD

Table 2. Minimum inhibitory concentration of active compounds^a

Compounds in µg/mL	<i>Escherichia coli</i>	<i>Staphylococcus aureus</i>	<i>Pseudomonas aeruginosa</i>	<i>Bacillus subtilis</i>
4b	50	100	100	50
4c	50	50	100	50
4d	50	100	100	50
4k	10	10	10	25
4m	10	10	10	10
4p	5	10	5	5
Ciprofloxacin	0.6	0.2	0.5	0.4

^a The experiment was performed in triplicate and the values are expressed as mean ±SD

Table 3. Determination of antifungal activity of the synthesized compounds^a

Compounds	<i>Aspergillus flavus</i>		<i>Chrysosporium keratinophilum</i>		<i>Candida albicans</i>	
	1	0.5	1	0.5	1	0.5
Concn. in mg/mL						
Control	00		00		00	
Fluconazole	13±0.1	10±0.1	17±0.1	15±0.1	22±0.1	20±0.1
4a	05±0.2	03±0.2	04±0.2	02±0.2	05±0.2	03±0.2
4b	09±0.1	06±0.1	10±0.1	07±0.1	11±0.1	08±0.1
4c	00	00	00	00	00	00
4d	00	00	00	00	00	00
4e	00	00	00	00	00	00
4f	06±0.2	03±0.2	05±0.1	02±0.1	05±0.1	02±0.1
4g	04±0.1	03±0.1	05±0.1	03±0.1	06±0.2	03±0.1
4h	00	00	00	00	00	00
4i	03±0.1	00	02±0.1	00	03±0.1	01±0.1
4j	00	00	00	00	00	00
4k	02±0.1	00	03±0.1	00	02±0.1	00
4l	05±0.1	03±0.1	04±0.2	02±0.1	06±0.2	04±0.1
4m	05±0.2	02±0.1	03±0.2	01±0.1	04±0.2	02±0.1
4n	06±0.1	02±0.1	05±0.1	02±0.1	04±0.1	01±0.1
4o	00	00	00	00	00	00
4p	10±0.3	07±0.3	08±0.3	06±0.3	12±0.2	07±0.2

^a The experiment was performed in triplicate and the values are expressed as mean ±SD

Biology: Antimicrobial activity.

Structure-activity relationships

The presence of electron withdrawing fluoro groups in **4p** and **4b** is presumed to be the reason for the comparable antimicrobial activity of that compound. The presence of heterocyclic ring having a nitrogen atom was assumed to be beneficial for the superior activity of compounds **4k** and **4m**. The existence of electron withdrawing groups is expected to increase the lipophilicity and thereby enhance the cell permeability of the molecule [17]. In general, it can be summarized that in the present study, the presence of an electron withdrawing group

and a heterocyclic group with nitrogen atom in 4-methyl-7-alkynyl coumarins is an essential feature for the antimicrobial potency of the synthesized compounds.

Biology: Antioxidant activity

The DPPH procedure is one of the most common methods for analyzing the concentration of radical scavenging materials as it does not have to be generated prior to analysis [18]. DPPH radical scavenging activity evaluation is a rapid and convenient assay for screening the antioxidant activities of newly synthesized compounds. These observations prompted us to evaluate the radical

scavenging activity (Fig. 1) of the synthesized 4-methyl-7-alkynyl coumarin derivatives as they possess an extended p-conjugated system [19]. The synthesized compounds **4a-p** were evaluated for antioxidant activities by taking butylated hydroxytoluene (BHT) as the standard (Fig. 1). In this assay, the standard BHT showed a strong scavenging activity whereas the compounds **4f** (74.2 %), **4g** (70.8 %), **4h** (61.8 %), **4e** (61.8 %) and **4o** (63.3 %) showed comparable activity (Fig. 1). All the other compounds also exhibited substantial scavenging activity, but demanded higher concentrations of the compounds.

*Biology: Antioxidant activity:
Structure-activity relationships*

The results of antioxidant screening revealed that the presence of electron-donating ring systems attached to the phenyl ring of 4-methyl-7-alkynyl coumarins is an essential characteristic for their radical scavenging activity. The hydrophilic

electron-donating groups are expected to assist the stabilization of the oxygen-centered radical and reduce the O–H bond dissociation enthalpy (BDE) thus increasing the radical scavenging activity by hydrogen abstraction [20]. This could be the probable reason for the better activity of compounds **4f**, **4g**, **4h**, **4e** and **4o** to that of the other synthesized molecules.

Biology: Molecular docking studies

Encouraged by the comparable antibacterial activity of some of the synthesized compounds as per the *in vivo* results, it was thought worthy to substantiate those results by performing molecular docking studies or *in silico* studies. The molecular docking study of the most active compound **4p** was carried out against gyrase as it is an essential enzyme in all bacteria but is absent in higher eukaryotes and hence makes it a beautiful antibacterial target [21,22].

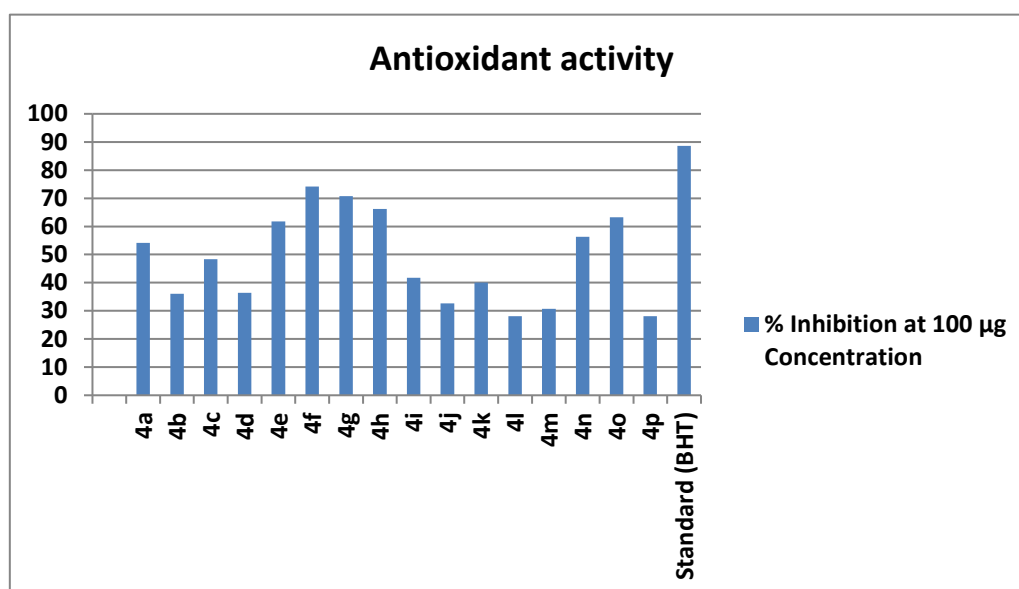


Figure 1. Antioxidant activity of 4-methyl-7-alkynyl coumarins.

Moreover, the mode of antibacterial action of ciprofloxacin is by significantly inhibiting the gyrase enzyme. The comparative docking of receptor gyrase with **4p** and ciprofloxacin exhibited good affinity. The 2D representation of **4p** and the standard ciprofloxacin is depicted in Fig. 2. The compound **4p** demonstrated ability for hydrogen bonding with three amino acids in the receptor active pocket and hydrophobic interactions with four amino acid residues (Fig. 2A). The standard ciprofloxacin (Fig. 2B) represents the hydrophobic contacts with five different residues, later a total of two H-bonds were formed with various amino acids. In all the cases of the 2D representation, ligands are

highlighted in blue colour. The set of conserved residues that are commonly involved in interaction with the ligands and ciprofloxacin are encircled with red colour. Furthermore, the extrapolation of binding conformation of **4p** and ciprofloxacin was carried out by 3D protein-ligand interaction analysis. Fig. 2 (C and D) represents the 3D interaction of **4p** and ciprofloxacin, respectively, with gyrase by using the educational version of PyMol. The ligands are represented in green colour, H-bonds with their respective distances are represented in yellow colour and the interacting residues are presented with ball and stick model representation. In the present study, **4p** was identified to be the best antibacterial agent

among all the synthesized compounds which could be attributed to the electron-withdrawing character of fluorine atoms, as well as to the ability of the molecule for considerable hydrogen bonding and hydrophobic interactions.

Experimental: Antibacterial activity

The antibacterial potency of compounds **4a-p** was determined by the well plate method in nutrient agar medium [23]. The compounds, along with the standard ciprofloxacin, were tested against a panel of pathogenic microorganisms like *E. coli*, *S. aureus*, *B. subtilis* and *P. aeruginosa*. The strains of microorganisms were maintained on nutrient agar medium at 37 °C and the cultures were inoculated in fresh 10-mL nutrient broth to get an initial suspension of approximately 10-100 cfu/mL. All the broths were then statically incubated at the

forementioned temperatures for 18-24 h so that all cells arrive at a stationary phase. Susceptibility of the organisms to the compounds was determined by employing the well plate technique. The bacterial suspensions were diluted tenfold in sterilized distilled water and 0.1 mL from the appropriate dilution was spread plated on nutrient agar in order to give a population of about 10⁶ cfu/plate. A 6 mm diameter well was then carefully punched using a sterile cork borer and 30 µL of test solutions of different concentrations were added into each labeled well. The same procedure was replicated for different microorganisms and each experiment was carried out in triplicate. After the incubation, the inhibition zone was measured and the values for control were deduced to get the actual values.

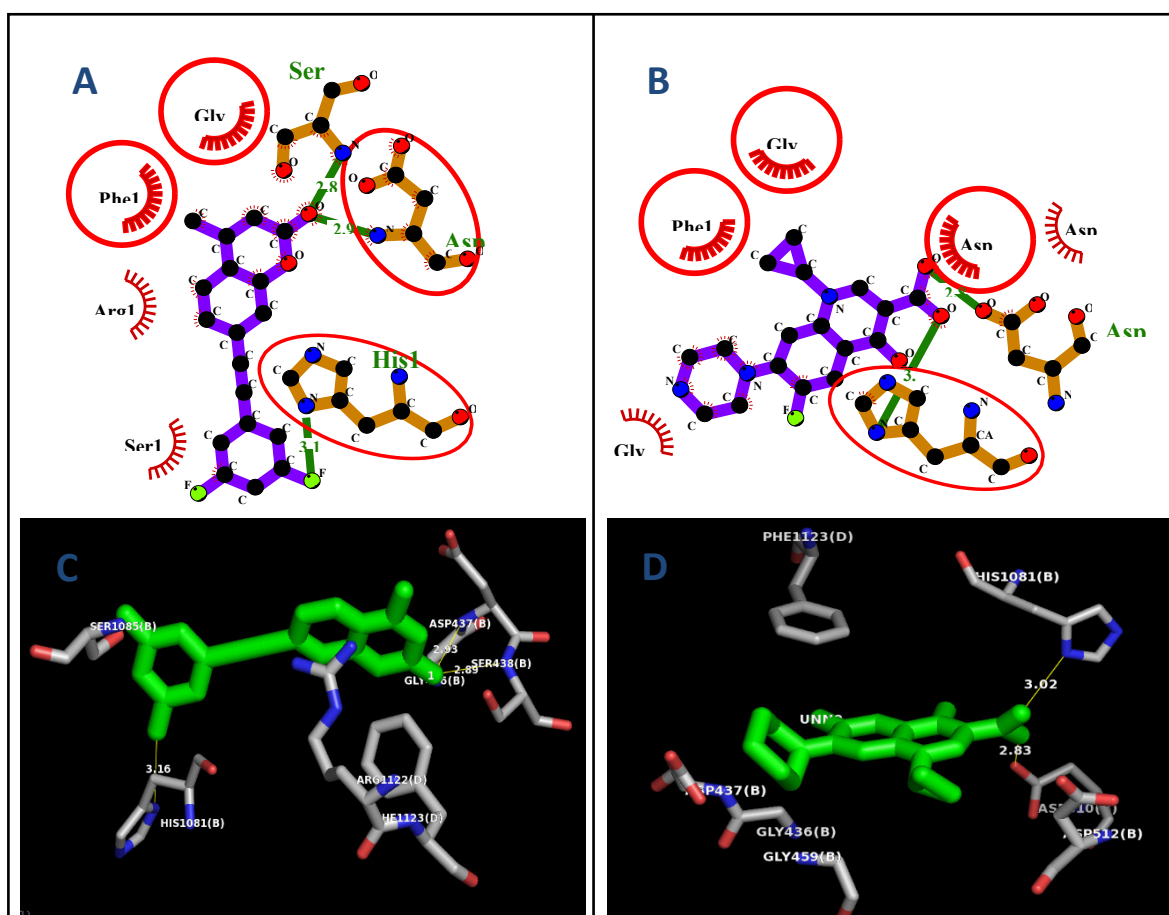


Figure 2. 2D and 3D representation of the interaction of **4p** and ciprofloxacin with 2XCT (gyrase)

Determination of Minimum Inhibitory Concentration

The minimum inhibitory concentration (MIC) of the active compounds was determined by the broth dilution method using nutrient broth. The MIC value, representing the lowest concentration that

completely inhibited the formation of visible growth, was estimated after 18 h of incubation at 37 °C.

Antifungal activity

Antifungal studies of the synthesized compounds **4a-p** were performed by the well plate method against *A. flavus*, *C. keratinophilum* and *C. albicans*.

Normal saline was taken to make a suspension of spores of fungal strains for lawning [24] and a loopful of a particular fungal strain was transferred to 3 mL of saline to get a suspension of the corresponding species. 20 mL of agar medium was poured into each Petri dish, excess of suspension was decanted and plates were dried in an incubator at 37 °C for 1 h. The borer was punched carefully using sterile cork. The wells were made on these seeded agar plates and various concentrations of the test compounds in DMSO were added to each labeled well. A control in DMSO was also prepared for the plates in the same way. The Petri dishes were prepared in triplicate and maintained at 25 °C for 72 h and antifungal activity was evaluated by measuring the diameter of the inhibition zone. The activity of each compound was compared along with fluconazole as the standard.

Antioxidant activity

The usual colorimetric DPPH• scavenging capacity assay was performed according to a previously described laboratory protocol [25]. 100 µL (100 µg concentration) samples of the compounds in methanol were added to 3 mL of 0.004 % w/v DPPH• solution and each test tube was made up to a final volume of 4 mL. BHT was used as a reference standard and was dissolved in methanol to get the same concentration as that of the remaining extracts. Each mixture was vortexed for some time and left to stand in the dark for 10 min at ambient temperature. The absorbance of each reaction mixture at 517 nm was measured against a blank of methanol by using a UV-visible spectrometer (Shimadzu UV-1800). The level of DPPH• remaining in each reaction was calculated as:

$$\% \text{ Scavenging activity} = \frac{\text{Absorbance of the control} - \text{Absorbance of the test sample}}{\text{Absorbance of the control}} \times 100$$

The inhibition curve was plotted for triplicate experiments and represented as percentage of mean inhibition ± standard deviation.

In silico studies

An entirely in-house extended drug discovery informatics system OSIRIS was used to perform ADMET based calculations. It is a Java based library layer that provides reusable cheminformatics functionality and was used to calculate the toxicity risks and overall drug score *in silico* [26]. The structures of the synthesized molecules and of the standards were drawn in ChemBioDraw tool (ChemBioOffice Ultra 14.0 suite) assigned with proper 2D orientation and the structure of each was checked for drawing error. Energy of each molecule was reduced using ChemBio3D (ChemBioOffice Ultra 14.0 suite). The energy-minimized ligand molecules were then utilized as input for AutoDockVina, to carry out the docking simulation [27]. The protein databank (PDB) coordinate file entitled '2XCT.pdb' was employed as receptor (protein) molecule which is a structure of *S. aureus* gyrase in complex with ciprofloxacin and DNA [28]. All the water molecules were removed from the receptor and SPDBV DeepView was used to automatically rebuild the missing side chains in the receptor. The Graphical User Interface program 'MGL Tools' was used to set the grid box for docking simulations and the grid was set in such a way that it surrounded the region of interest (active site) in the macromolecule. In the present study, the

active site was chosen based on the amino acid residues of 2XCT, which are involved in binding with ciprofloxacin. Therefore, the grid was centered at the region including the two amino acid residues (Arg 458 and Gly 459) and the four nitrogenous bases from DNA. that is guanine (G), adenine (A), thymine (T) or cytosine (C), as evidenced by Bax *et al.* in 2010 [29]. This surrounded the active site. The grid box volume was set to 8, 14 and 14 Å for x, y and z dimensions, respectively, and the grid center was set to 3.194, 43.143 and 69.977 for x, y and z center respectively, that covered the two amino acid residues and four nitrogenous bases in the considered active pocket. The AutoGrid 4.0 Program was used to produce grid maps. The docking algorithm provided with AutoDockVina was used to search for the best docked conformation between the ligand and the protein. During the docking procedure, a maximum of 10 conformers was considered for each ligand. All the AutoDock docking runs were carried out in Core i7 Intel processor CPU with 8 GB DDR31 RAM. AutoDockVina was compiled and run under Windows 8.0 professional operating system and LigPlot+ [30] and PyMol [31] were used to deduce the pictorial representation of the interaction between ligands and target protein.

CONCLUSION

In summary, we have evaluated the antimicrobial and antioxidant activity of an array of previously synthesized 4-methyl-7-alkynyl coumarins by the

well plate method. The compound **4p** exhibited comparable antibacterial activity with ciprofloxacin against all the tested bacteria. The *in silico* docking studies of the more active antibacterial agents were carried out against the gyrase enzyme and revealed that **4p** demonstrates ability for significant hydrogen bonding and hydrophobic interactions, which could be a plausible reason for its improved potency along with the presence of electron-withdrawing fluoro groups. The antifungal activity of the compounds was found to be moderate. Nevertheless, the compounds **4b** and **4p** showed better antifungal activity when compared to the other remaining compounds. The compounds **4f** and **4g** showed comparable antioxidant activity with the standard BHT, presumably due to the presence of electron-donating substituents. The present study paved the way for understanding of the biological profile of 4-methyl-7-alkynyl coumarin analogues and further derivatization and lead optimization are currently in progress in our laboratory.

Acknowledgement: We are thankful to the Department of Industrial Chemistry, Kuvempu University for providing the facilities to carry out the experiments.

REFERENCES

1. R. C. Moellering, *Am. J. Med.*, **99**, 11S (1995).
2. P. Singh, A. Anand, V. Kumar, *Eur. J. Med. Chem.*, **85**, 758 (2014).
3. N. P. Peet, *Drug. Discov. Today*, **15**, 583 (2010).
4. J. K. Sugamura, J. F. Keaney, *Free Radical Biol. Med.*, **51**, 978 (2011).
5. F. Borges, F. Roleira, N. Milhazes, L. Santana, E. Uriarte, *Curr. Med. Chem.*, **12**, 887 (2005).
6. M. A. Al-Haiza, M. S. Mostafa, *Molecules*, **8**, 275 (2003).
7. K. C. Fylaktakidou, D. H. Litina, *J. Curr. Pharm. Des.*, **10**, 3813 (2004).
8. N. Lall, A. A. Hussein, J. J. M. Meyer, *Fitoterapia*, **77**, 230 (2006).
9. I. Kostova, S. Raleva, P. Genova, R. Argirova, *Bioinorg. Chem. Appl.*, (2006).
10. J. W. Hinman, H. Hoeksema, E. L. Caron, W. G. Jackson, *J. Am. Chem. Soc.*, **78**, 1072 (1956).
11. S. Triloknadh, C. V. Rao, K. Nagaraju, N. H. Krishna, C. V. Ramaiah, W. Rajendra, D. Trinath, Y. Suneetha, *Bioorg. Med. Chem. Lett.*, **28**, 1663 (2018).
12. J. R. Komsani, S. Koppireddi, S. Avula, P. K. Koochana, R. Yadla, *Eur. J. Med. Chem.*, **68**, 132 (2013).
13. M. N. Joy, Y. D. Bodke, K. K. A. Khader, A. M. Sajith, *Tetrahedron Lett.*, **55**, 2355 (2014).
14. A. M. Sajith, K. K. A. Khader, N. Joshi, M. N. Reddy, M. S. A. Padusha, H. P. Nagaswarupa, M. N. Joy, Y. D. Bodke, R. P. Karuvalam, R. Banerjee, A. Muralidharan, P. Rajendra, *Eur. J. Med. Chem.*, **89**, 21 (2015).
15. C. Aswathanarayanappa, E. Bheemappa, Y. D. Bodke, P. S. Krishnegowda, S. P. Venkata, R. Ningegowda, *Arch. Pharm. Chem. Life. Sci.*, **346**, 922 (2013).
16. M. K. Potdar, S. S. Mohile, M. M. Salunkhe, *Tetrahedron Lett.*, **42**, 9285 (2001).
17. M. A. Parker, D. M. Kurrasch, D. E. Nichols, *Bioorg. Med. Chem.*, **16**, 4661 (2008).
18. E. Niki, *Chem. Phys. Lipids*, **44**, 227 (1987).
19. M. J. Matos, F. P. Cruz, S. V. Rodriguez, E. Uriarte, L. Santana, F. Borges, C. O. Azar, *Bioorg. Med. Chem.*, **21**, 3900 (2013).
20. C. Yamagami, M. Akamatsu, N. Motohashi, S. Hamada, T. Tanahashi, *Bioorg. Med. Chem. Lett.*, **15**, 2845 (2005).
21. B. J. Bradbury, M. J. Pucci, *Curr. Opin. Pharmacol.*, **8**, 574 (2008).
22. Y. C. Tse-Dinh, *Infect. Disord. Drug Targets*, **7**, 3 (2007).
23. B. A. A. Skaggs, D. W. Warnock, C. J. Morrison, *J. Antimicrob. Chemother.*, **44**, 2081 (2000).
24. D. J. M. Lowry, M. J. Jaqua, S. T. Selepak, *Appl. Microbiol.*, **20**, 46 (1970).
25. A. Braca, N. D. Tommasi, L. D. Bari, C. Pizza, M. Politi, I. Morelli, *J. Nat. Prod.*, **64**, 892 (2001).
26. T. Sander, J. Freyss, M. V. Korff, J. R. Reich, C. Rufener, *J. Chem. Inf. Model.*, **49**, 232 (2009).
27. O. Trott, A. J. Olson, *J. Comput. Chem.*, **31**, 455 (2010).
28. B. D. Bax, P. F. Chan, D. S. Eggleston, A. Fosberry, D. R. Gentry, F. Gorrec, *Nature*, **466**, 935 (2010).
29. G. M. Morris, D. S. Goodsell, R. S. Halliday, R. Huey, W. E. Hart, R. K. Belew, *J. Comput. Chem.*, **19**, 1639 (1998).
30. R. A. Laskowski, M. B. Swindells, *J. Chem. Inf. Model.*, **51**, 2778 (2011).
31. W. DeLano, The PyMOL molecular graphics system, (2002).
32. <http://www.citeulike.org/group/340/article/240061> (accessed October 21, 2014).

Optimization of the bi-functional oxygen electrode (BOE) structure for application in a Zn-air accumulator

B. Abrashev^{1*}, D. Uzun¹, A. Kube², N. Wagner², K. Petrov¹

¹Acad. Evgeni Budevski Institute of Electrochemistry and Energy Systems, Bulgarian Academy of Sciences, Acad. G. Bonchev Str., Bl. 10, 1113, Bulgaria

²German Aerospace Center, Pfaffenwaldring 38-40, 70569 Stuttgart, Germany

Received: March 13, 2019; Revised: March 09, 2020

A novel structure of a bi-functional oxygen electrode (BOE) was developed, which is based on a new technological process of teflonization. The electrochemical oxygen evolution reaction (OER) and oxygen reduction reaction (ORR) were studied in a half-cell configuration, to investigate its charge/discharge characteristics. Both the gas-diffusion layer (GDL) and active layers (AL) of the electrodes were optimized. Preliminary studies of GDLs with different carbon blacks and for different ratios between the PTFE and carbon blacks have shown, that the most stable GDL is produced from Vulcan XC-72 teflonized with 60 % PTFE – TV-60. The innovation regarding the GDL is in the way it is prepared using high-energy mixing, which assures an equal dispersion and intimate contact between the carbon black and Teflon particles. With this GDL an optimization of the AL was performed with respect to both the thickness (amount of catalytic mass – catalyst + PTFE) and the ratio between the catalyst and the binding agent (PTFE). The volt-ampere characteristics and the charge/discharge tests showed that the most suitable catalyst with respect to the stability of the GDE is a mix of Ag and Co₃O₄. The GDE with the above composition reaches more than 700 cycles without a decrease in performance.

Keywords: Me – air accumulator, GDL, electrochemical cell design.

INTRODUCTION

The necessity for energy storage systems is growing due to the fact that today's society is in transition from fossil fuel to clean energy sources. The use of renewable energy sources such as wind and photovoltaic systems requires the availability of cheap and efficient electrochemical systems to store the produced energy for a time when renewable energy production is greater than the energy consumption. Such systems may be metal/air-batteries. This gradual but inevitable process is accelerated by the latest active research on a global scale for the collection, transformation and storage of sustainable energy. Electrochemical systems (batteries, accumulators, etc.) have long been utilized in the conversion and storage of electrical energy [1].

Among the different metal/air systems, the zinc/air system is a relatively mature technology and has the required capacity for energy applications. Its primary batteries have been known to the scientific community since the late nineteenth century. Commercial products began to appear in the 1930s [2]. Both now and in the past because of their use in alkaline fuel cells, the concept of gas diffusion electrodes is important. The optimization and improvement of GDE has been explored since the 1960s. Intensive experimental research has been

carried out to improve the design and construction of the gas-diffusion and active-layer electrodes.

Electrically rechargeable metal/air-batteries are very attractive as candidates for an energy storage material, due to their low cost and high stability in an aqueous solution; they are environmentally benign and have a high specific energy density. Concentrated potassium hydroxide solution is the electrolyte of choice for rechargeable metal-air batteries such as the zinc-air and iron-air batteries, because of its high conductivity. Zinc-air batteries, to be more specific, yield an extremely high potential and therefore can be used in alternative energy storage devices. In an alkaline solution Al can corrode more easily than Zn, although Al-air cells have a much greater energy density than zinc-air cells [3, 4]. In addition, Zn has various advantages such as a low cost, is quite abundant, has a low equilibrium potential, is environmentally benign and has a protracted exploitation lifetime [5, 6]. A principal advantage of the alkaline zinc-air batteries is that non-noble metal catalysts can be used for the ORR and OER reactions, as calculated, the specific energy density of Zn-air batteries is 1084 W h kg⁻¹. In order to properly operate these metal-air systems, a bi-functional air electrode is required. Recent advances in bi-functional electrocatalysts for both the ORR and OER provide strong support for the use and development of bifunctional air electrodes (BAE) for metal air batteries [7–12].

* To whom all correspondence should be sent:

E-mail: babrashev@iecs.bas.bg

Recently many authors have improved the bi-functional air electrodes applied in Zn/air systems [13–16].

The current work describes our achievements in the development of bi-functional air electrodes. The oxygen reduction reaction occurs at the triple-phase interface, whereas the OER occurs at the two-phase interface [17]. The air electrode is composed of a porous hydrophobic membrane, a catalytic layer and a current collector. These electrodes are leak-proof and conductive, while remaining active and stable at high charge-discharge current densities and have a porous structure to ensure the supply of oxygen. The air electrodes usually contain a catalyst dispersed on a carbon substrate. This mixture is PTFE-bonded and forms the active part of the porous gas-diffusion electrode [18, 19].

EXPERIMENTAL

Air electrode design

The new design of the BOE is comprised of metal oxide-based catalysts. The electrochemical OER and ORR were studied in half-cell configurations to investigate the charge/discharge characteristics. By using a new process of high energy mixing teflonization, an even distribution of the carbon particles was obtained. The BAE is a double-layered structure (Fig. 1) comprised of two layers: a porous hydrophobic carbon black GDL and a semi-hydrophobic AL. The electrode was made using a matrix of a size corresponding to the electrodes produced (1, 10, 25 cm²). First the GDL is deposited followed by the catalytic layer onto the GDL and then the Ag based current collector is manually placed on top. After that the matrix is closed and hot-pressed at 300 kg cm⁻² for 1 min at 300°C. The GDL is produced from Vulcan XC-72 (Cabot corp.) which is modified by PTFE (Teflon emulsion, Sigma Aldrich) through a novel technology. The BAE is optimized with respect to both the GDL and the AL. The catalysts used were: (i) a mixture of Ag (Ferro AG, Ag 311), Co₃O₄ (Sigma Aldrich, < 50 nm) and PTFE (3M Dyneon, TF9207Z), (ii) only Ag (Ferro AG, Ag 311) and (iii) only Co₃O₄ (Sigma Aldrich, < 50 nm). The following parameters were studied: (i) catalyst amount, (ii) pressure during production, (iii) electrode thickness, (iv) PTFE amount.

Based on previous experience a catalyst mixed of Ag + Co₃O₄ was used for the AL [20]. The suggested composition of the AL was 70 wt.% Ag + 20 wt.% Co₃O₄ + 10 wt.% PTFE [21].

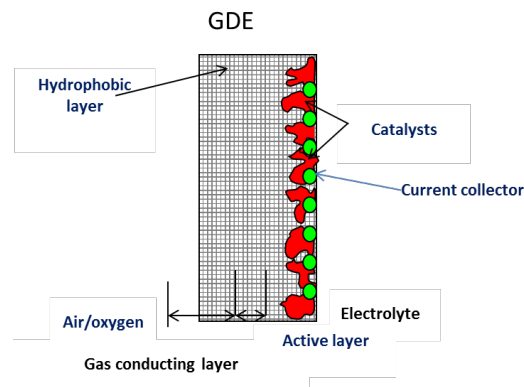


Figure 1. Schematic cross-section of the air gas diffusion electrode.

The amount of catalytic mass was optimized in a three electrode half-cell setup, whereas the Ag/Co₃O₄/PTFE was mixed with a double-knife mill and pressed on a stainless steel gauze (Haver&Boecker, W 0.5 mm, D 0.125 mm, SS type: 1.4306) as the current collector. After pressing at 2.5 bar, a heat treatment was applied at 340°C for 1 hour. The Ag/Co₃O₄ mixture is shown in Fig. 2, the big white particles are the Ag, and the smaller darker particles covering the Ag surface are the Co₃O₄ particles.

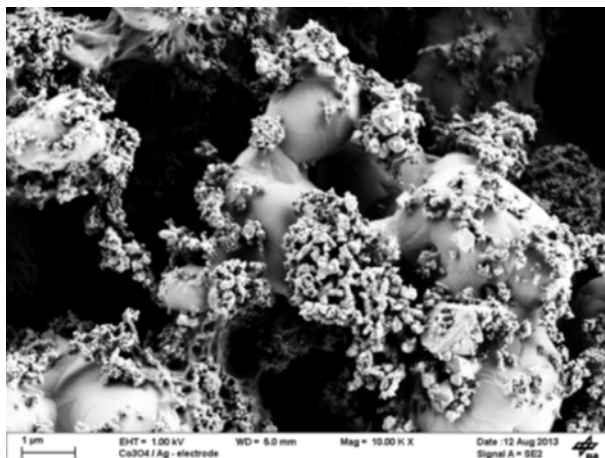


Figure 2. SEM picture of an Ag /Co₃O₄ mixture.

Due to this good coverage of conducting Ag particles with non-conducting Co₃O₄ particles, the performance of the mixture increases the electrochemical performance of the electrode. The thickness of these electrodes is in the order of 400 μm. The current density increased with an increase of Co₃O₄ amount up to 20 wt.%, above 20 wt.% the electric resistivity of the electrode increased by an order of several magnitudes. This is due to blocking of the conducting paths by the Co₃O₄ catalyst particles. This increase in electrical resistivity leads to a decrease in current density. The loading of the optimized electrode is a conductive additive

consisting of: 105 mg cm⁻² Ag, 30 mg cm⁻² Co₃O₄ and 15 mg cm⁻² PTFE.

The catalytic properties of the cathode electrodes were determined with the aid of 1, 10 and 25 cm² three-electrode cells as described in [22]. The process of ORR and OER was studied in 6M KOH. The counter-electrode was a stainless steel mesh. The reference electrode was a “Gaskatel” reversible hydrogen electrode (RHE). A Solartron 1286 Electrochemical Interface, was used for the galvanostatic measurements.

A minimum of four measurements were made for each result to achieve better reproducibility. Arithmetic averages are presented in the graphs.

The GDE (BOE) were optimized with respect to the catalyst used, electrode thickness and mass ratio between catalysts and binder, varying one parameter at a time and keeping the others constant.

RESULTS AND DISCUSSION

The working electrode (cathode) potential at a fixed current density ($i=10 \text{ mA cm}^{-2}$) was selected as a criterion for the quality of the electrode. With this criterion, electrodes with different amounts, resp. ratios of the components were compared to find the optimum composition.

Fig. 3 shows the optimization curves relative to 60% teflonized Vulcan XC-72 in mg cm⁻² at E ($i = 10 \text{ mA cm}^{-2}$), mV versus a RHE. From the data obtained, it can be seen that the electrodes containing 50 mg cm⁻² of 60% teflonized Vulcan XC-72 show the lowest overvoltage for both OER and ORR.

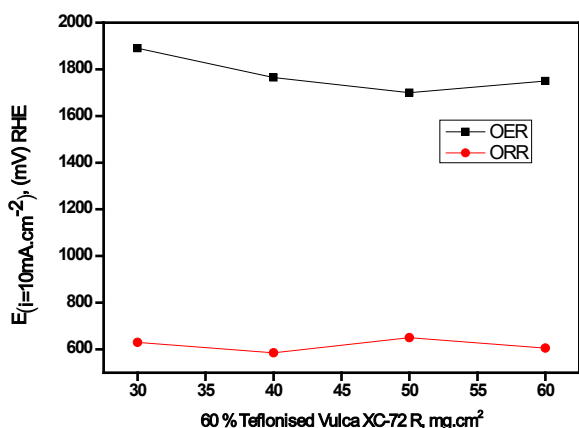


Figure 3. Optimization curve for a quantity of 60 % Teflonized Vulcan XC-72 in mg cm⁻² at E ($i = 10 \text{ mA cm}^{-2}$), mV versus RHE.

The newly developed technological process allowed a high teflonization (up to 60 wt.%) and homogenization of the GDL. By utilizing this process, the diffusion limitation is increased. Hence, the developed GDE is expected to be more

stable in alkaline solutions. Nevertheless, in comparison with previous research [20, 23] when using 35 wt.% teflonization the obtained current density was very low, about 30 mA cm⁻² for the ORR.

The AL catalytic mass in the electrodes is a mixture of the catalyst materials (Ag + Co₃O₄), which was used to fabricate the BOE. The active layers were optimized with respect to both the thickness (amount of catalytic mass – catalyst + PTFE, Fig. 4) and the ratio between the catalyst and the binding agent (PTFE, Fig. 6). Preliminary studies of the GDL with different ratios between the PTFE and carbon black content have shown that the most stable GDL is produced from Vulcan XC-72 teflonized with 60 % PTFE – TV-60. The total amount of TV-60 is 50 mg cm⁻². With this GDL as the backbone, an optimization of the AL was performed.

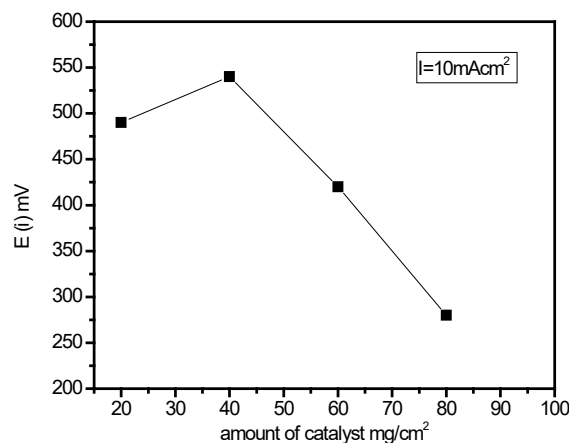


Figure 4. Optimization curve of the catalytic mass amount at a constant ratio for the ORR (catalyst: PTFE) = 80:20.

Shown in Fig. 4 is an optimization curve with respect to the catalytic mass for oxygen reduction at a constant current density $i = 10 \text{ mA cm}^{-2}$. From the data obtained it is seen that the electrodes containing 40 mg cm⁻² have the lowest overvoltage at ORR. The optimization towards OER of the catalytic mass was done following the same procedure. A similar optimal value of AL thickness 40 mg cm⁻² could be obtained.

Fig. 5 shows an optimization curve in terms of the quantity of Teflon in percent for oxygen reduction at a constant current density of 10 mA cm⁻². From the data obtained it can be seen that the electrodes containing 20 wt.% PTFE have the lowest ORR overvoltage. For the OER similar results were observed.

Cobalt oxide and silver were used as catalysts for optimization of the active layer. The dependence of the potential, with respect to the

current density, of the OER for Co_3O_4 is shown in Fig. 6. The electrode performs very well for OER, but for the ORR a very low current density (5 mA cm^{-2}) was achieved and the overpotential yield was not good.

The electrode with Ag powder catalyst performed well for the ORR. The anode curve had two characteristic domains with different slopes. The results presented in Fig. 6 are similar to those obtained by Amin *et al.* (2015) [24], where oxidation of Ag to AgO_2 was carried out.

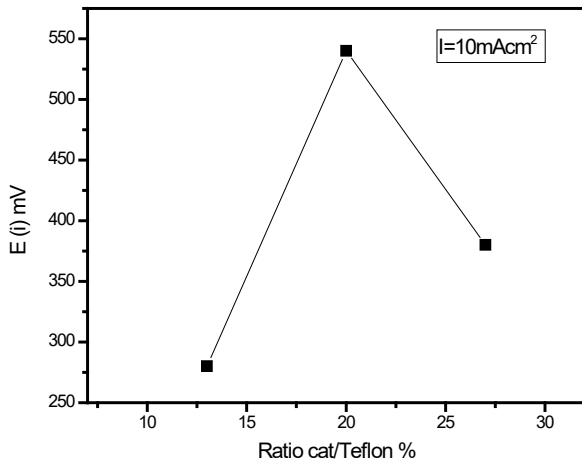


Figure 5. Optimization curve of the ratio for ORR (catalyst – PTFE at a constant catalytic mass amount = 40 mg/cm^2).

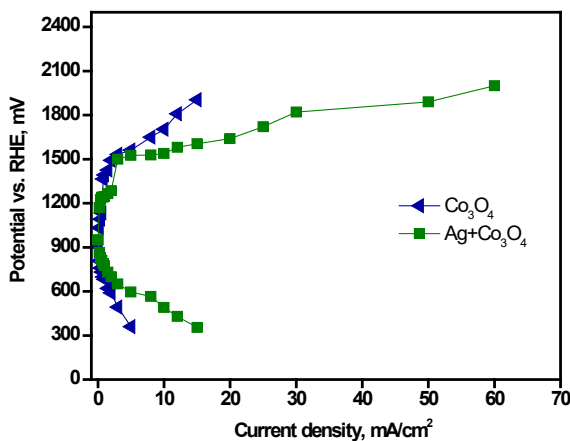


Figure 6. Polarization curves of the electrodes for ORR and OER for catalysts: ■ Ag + Co_3O_4 ; ▼ Co_3O_4 . The electrolyte was 6 M KOH at room temperature. The geometrical area of the electrode was 25 cm^2 .

Charge/Discharge tests

The behavior of the BOE improves with the addition of Co_3O_4 to the contained Ag catalyst reaching more than 700 charge/discharge cycles. Shown in Fig. 7 are the charge/discharge tests of the electrode containing a GDL – 60% teflonized Vulcan XC-72 – 50 mg cm^{-2} and an AL consisting

of 70% Ag + 20% Co_3O_4 + 10% PTFE – 40 mg cm^{-2} . The tests were carried out in a full cell. The area of the working electrode was 25 cm^2 . The charge/discharge time was 45/30 min, respectively. The counter electrode in the full cell was a stainless steel mesh.

The electrolyte was 6 M KOH at room temperature. The potential obtained at the OER reached between 1550–1600 mV vs. RHE and the ORR potential was 520–600 mV vs. RHE.

The results obtained for the volt-ampere characteristics and the charge/discharge tests showed that the most suitable catalyst with respect to the GDE is a mix of Ag and Co_3O_4 which ensures more than 700 cycles.

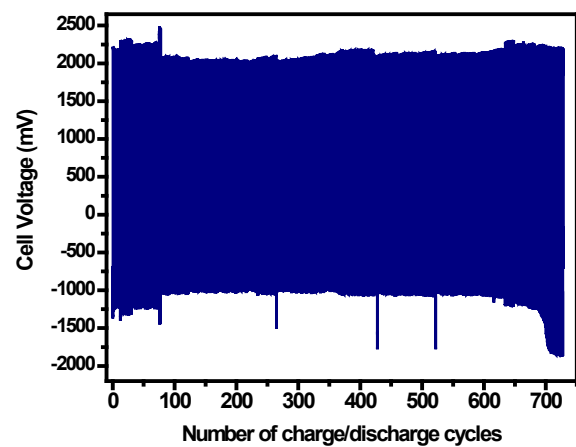


Figure 7. The electrode is comprised of a GDL – 60% teflonized Vulcan XC-72 – 50 mg cm^{-2} and an AL consisting of 70% Ag + 20% Co_3O_4 + 10% PTFE – 40 mg cm^{-2} . The electrode is with a work area of 25 cm^2 . The electrode is pressed at $P = 300 \text{ atm}$ and $T = 300^\circ\text{C}$.

CONCLUSIONS

From the volt-ampere characteristics obtained and the charge/discharge tests carried out it can be concluded that the most suitable catalysts with respect to the GDE are pure Ag and a mix of Ag and Co_3O_4 .

By applying this new technological method for the teflonization of carbon blacks from GDL of the electrodes a mix of Ag and Co_3O_4 reached more than 700 charge-discharge cycles, which can be regarded as one of the best reported results. The applied technological approach ensures extremely homogeneous distribution of the basic components for the gas diffusion layer of Teflon on to carbon particles.

Acknowledgement: We acknowledge the financial support by the EU commission (Horizon 2020 framework NMP program) through the project ZAS – zinc-air secondary batteries based on innovative

nanotechnology for efficient energy storage (Grant Agreement 646186).

REFERENCES

1. Y. Li, H. Dai, *Chem. Soc. Rev.*, **43**, 5257 (2014).
2. T. Danner, S. Eswara, V. P. Schulz, A. Latz, *J. Power Sources*, **324**, 646 (2016).
3. F. Zhan, L. J. Jiang, B. R. Wu, Z. H. Xia, X. Y. Wei, G. R. Qin, *J. Alloys Compd.*, **293**, 804 (1999).
4. P. Sapkota, H. Kim, *J. Ind. Eng. Chem.*, **15**, 445 (2009).
5. F. R. McLarnon, E. J. Cairns, *J. Electrochem. Soc.*, **138** (2), 645 (1991).
6. P. Arora, Z. J. Zhang, *Chem. Rev.*, **104**, 4419 (2004).
7. G. Du, X. Liu, Y. Zong, T.S.A. Hor, A. Yu, Z. Liu, *Nanoscale*, **5**, 4657 (2013).
8. Y. Li, M. Gong, Y. Liang, J. Feng, J. E. Kim, H. Wang, G. Hong, B. Zhang, H. Dai, *Nat. Commun.*, **4**, 1 (2013) doi: 10.1038/ncomms2812.
9. Z. Chen, A. Yu, R. Ahmed, H. Wang, H. Li, Z. Chen, *Electrochim. Acta*, **69**, 295 (2012).
10. D. J. Yang, L. J. Zhang, X. C. Yan, X. D. Yao, *Small Methods*, **1**, 1700209 (2017).
11. P. Gu, M. Zheng, Q. Zhao, X. Xiao, H. Xue, H. Pang, *J. Materials Chemistry A*, **5**, 7651 (2017). DOI: [10.1039/C7TA01693J](https://doi.org/10.1039/C7TA01693J)
12. K. Zhu, T. Wu, M. Li, R. Lu, X. Zhu, W. Yang, *J. Mater. Chem. A*, **5**, 19836 (2017). DOI: [10.1039/C7TA05404A](https://doi.org/10.1039/C7TA05404A)
13. B. Pichler, S. Weinberger, L. Rešćec, I. Grimmer, F. Gebetsroither, B. Bitschnau, V. Hacker, *Electrochimica Acta*, **251**, 488 (2017). DOI: [10.1016/j.electacta.2017.08.128](https://doi.org/10.1016/j.electacta.2017.08.128)
14. C. Alegre, E. Modica, A.S. Aricò, V. Baglio, *J. Electroanalytical Chem.*, **808**, 412 (2018). DOI: [10.1016/j.jelechem.2017.06.023](https://doi.org/10.1016/j.jelechem.2017.06.023)
15. Y. Li, H. Dai, *Chem. Soc. Rev.*, **43**, 5257 (2014).
16. Sh. Zeng, X. Tong, S. Zhou, B. Lv, J. Qiao, Y. Song, M. Chen, J. Di, Q. Li, *Small*, **14** (48), e1803409 (2018). DOI: [10.1002/smll.201803409](https://doi.org/10.1002/smll.201803409)
17. P. Pei, K. Wang, Z. Ma, *Applied Energy*, **128**, 315 (2014).
18. S. Muller, F. Holzer, O. Haas, *Electrochim. Acta*, **39**, 1661 (1994).
19. K. A. Striebel, F. R. McLarnon, E. J. Cairns, *J. Power Sources*, **47**, 1 (1994).
20. S. Gamburgzev, K. Petrov, A. J. Appleby, *J. Appl. Electrochem.*, **32**, 805 (2002).
21. D. Wittmaier, N. Wagner, K. A. Friedrich, H. M. A. Amin, H. Baltruschat, *J. Power Sources*, **265**, 299 (2014).
22. B. Abrashev, D. Uzun, H. Hristov, D. Nicheva, K. Petrov, *Advances in Natural Science: Theory & Applications*, **4** (2), 65 (2015).
23. V. Nikolova, P. Iliev, K. Petrov, T. Vitanov, E. Zhecheva, R. Stoyanova, I. Valov, D. Stoychev, *J. Power Sources*, **185** (2), 727 (2008).
24. H. M. A. Amin, H. Baltruschat, D. Wittmaier, K. A. Friedrich, *Electrochimica Acta*, **151**, 332 (2015).

Clerodane diterpenoids isolated from Bulgarian species of genus *Teucrium* (Lamiaceae)

P. I. Bozov

Department of Biochemistry and Microbiology, Plovdiv University, 24 Tzar Asen St., 4000, Plovdiv, Bulgaria

Received May 15, 2019; Revised March, 4, 2020

Neo-clerodane diterpenoids have attracted interest in a variety of skeletons owing to the many stereochemical problems arising during their identification and structural characterization and to the wide range of biological activity, especially their operation as insect-antifeedant agents. The present review reports on the clerodane diterpenoids isolated from Bulgarian *Teucrium* species (Lamiaceae), and the systematization of their characteristic structural features. The changes in the antifeedant activity due to chemical transformations of the compounds and some significant aspects of the structure-activity relationship are discussed.

Keywords: Lamiaceae, *Teucrium*, *T. botrys* L., *T. lamiifolium* D'Urv., *T. polium* L., *T. montanum* L., *T. scordium* L., *T. chamaedris* L., neo-clerodane diterpenes, antifeedant activity, hemisynthetic derivatives.

INTRODUCTION

The Lamiaceae genus *Teucrium* covers about 360 species spread in different climatic zones.

In Bulgaria the genus is represented by six species [1]. Since 1906 the species *T. botrys* L. is not confirmed in Bulgaria and it is probably extinct species for the country. Three of the species of genus *Teucrium* are represented by two subspecies. Common types of *T. polium* L. are the subspecies *capitatum* (L.) Arcangeli and subspecies *vincentinum* (Rouy) D. Wood; of *T. scordium* L. – subspecies *scordium* and subspecies *scordioides* (Schreb.) Maire et Petitmengin; of *T. montanum* L. – subspecies *montanum* and subspecies *skorpilii* (vel.) D. Peev.

The *Teucrium* species are honey-bearing with medical use. For thousands of years, paws and infusions of the plants are applied in open-wound healing, treatment of gastrointestinal pains, diabetes, inflammations, rheumatism and other disorders. They are also used as diuretic, antipyretic, tonic, diaphoretic, analgesic agents [2].

The species of the genus *Teucrium* are a rich source of biologically active compounds as diterpenes, flavonoids, phenols, iridoids. Clerodane diterpenoids are the main chemical constituents of the genus. For clarity and in order to classify all clerodane diterpenoids, their bicyclic basic skeleton is divided in two substructures: combined C-1–C-10 atoms into a decalin ring and a C-11–C-16 (with C-16 attached at C-13, i.e., 3-methylpentyl) six-carbon side chain at C-9. The rest four carbons (C-17–C-20) are linked up with C-8, C-4, C-5, and C-9, respectively, on the decalin core as it is illustrated on Fig. 1 [3, 4].

Approximately 25% of clerodanes have a 5:10 cis ring fusion as presented in columbin (Fig. 1). The rest 75% of clerodanes have a 5:10 trans ring fusion as demonstrated in clerodin.

Depending on the relative configuration of C-8 and C-9, in the molecule four substructures of the clerodane skeleton are defined as shown in Fig. 2: *trans*–*cis* (TC), *trans*–*trans* (TT), *cis*–*cis* (CC) and *cis*–*trans* (CT).

Merritt and Ley [5] have revised the absolute stereochemistry of clerodin, the first member of the clerodane series of the diterpenes, and offer a new nomenclature for the clerodane diterpenoids: *neo*-clerodanes (formerly *ent*-clerodanes) have the same absolute stereochemistry as clerodin, while *ent*-*neo*-clerodanes are enantiomeric to clerodin (Fig. 3).

The major compounds, isolated from the genus *Teucrium*, are *furo*-*neo*-clerodane diterpenes with 5:10 trans ring fusion, as more than 90 % of them are of the TC type.

The intensive study of *Teucrium* species for presence of *neo*-clerodane diterpenoids has started in the sixties of the twentieth century. First received *neo*-clerodanes from this genus in Bulgaria are montanins A (1) and B (2), isolated in 1978 from *T. montanum* by Malakov *et al.* (Table 1) [6].

This review summarizes more than 40 years of scientific studies of clerodane diterpenoid content in Bulgarian *Teucrium* species, systematizing their skeletons and the change of the antifeedant activity of the clerodanes in chemically modified hemisynthetic derivatives. The activity of the natural clerodane diterpenoids was compared with that of non-natural hemisynthetic derivatives and of the potent *neo*-clerodane antifeedant ajugarin I (Fig. 3) isolated by Kubo *et al.* from *Ajuga remota* [7].

* To whom all correspondence should be sent:
E-mail: bozov@uniplovdiv.bg

ISOLATED DITERPENOIDS

The first paper on the *neo*-clerodane diterpenoids from the Bulgarian genus *Teucrium*, which appeared in 1987, concerned *T. montanum* L. The group of Malakov [6] have isolated the *nor*-clerodane furanoid diterpenoids – montanines A (**1**) and B (**2**). The absolute configuration of **2** has been proved by correlation with teucvin (Fig. 3), a *nor*-clerodane diterpenoid isolated by Fujita *et al.* from *T. viacidum* var. *miquelianum* [8], whose construction had been determined by X-ray crystallographic analysis of the bromo-derivative and by some of its reactions. Later that year, the same team [9, 10] reported obtaining of

two more constituents of this species, the *neo*-clerodane diterpenes montanine C (**4**) and D (**7**).

In the next year five furanoid clerodane diterpenes, the known teucrin P₁ (**9**), teucrin H₃ (**10**, = 19-acetylgnafalin) montanine B (**2**) and the new teupolin I (**5**) and teupolin II (**12**), have been isolated for the first time from the bitter fraction of the aerial parts of *Teucrium polium* L. from Bulgaria by the same team [11]. Compound **9** has been found in Moldovian *T. polium* L. by Popa *et al.* [12] and compound **10** - in *T. hyrcanicum* by Gacs-Baitz *et al.* [13]. Only montanine B is a *nor*-clerodane diterpenoid, the other four terpenes are *neo*-clerodanes.

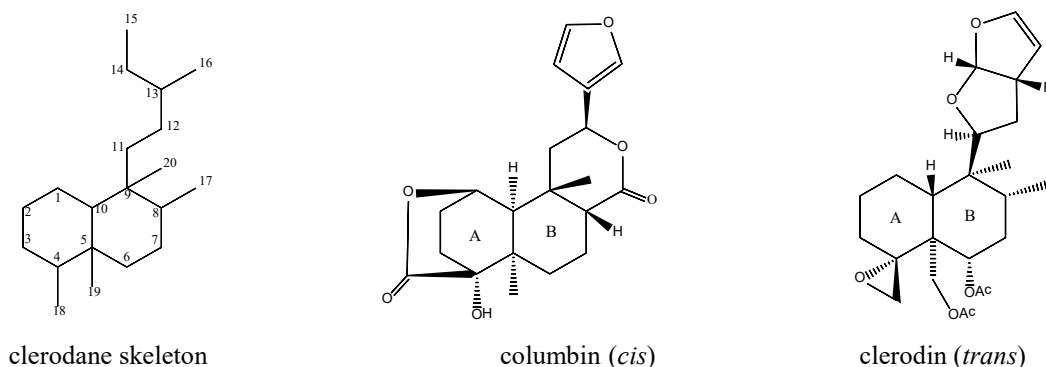
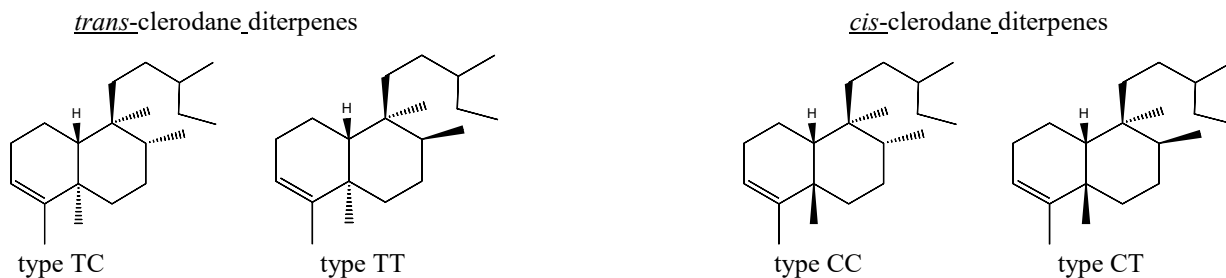


Figure 1. Basic clerodane skeleton and compounds with 5:10 *cis*- and *trans*- fusion of rings A and B.



Note: in the figure *neo*-absolute configurations are given, *ent*-*neo*-forms possess reversed configurations for all asymmetric carbon atoms.

Figure 2. Absolute configurations at C-8 and C-9 of the clerodane skeleton.

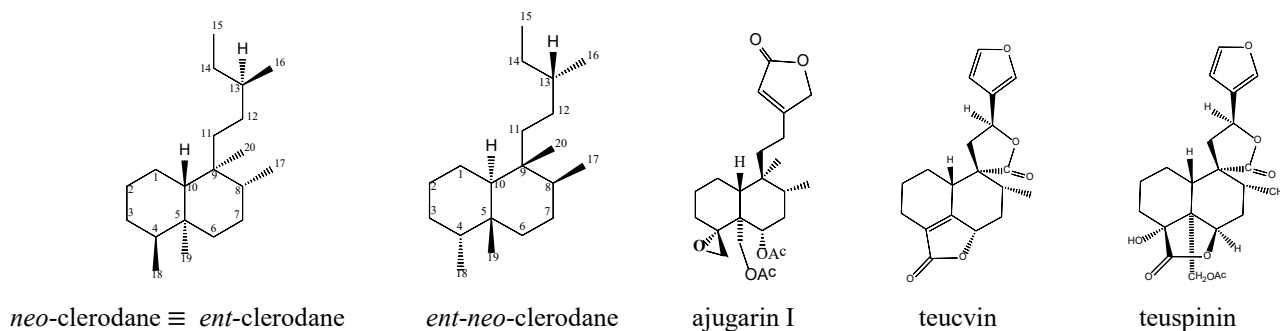
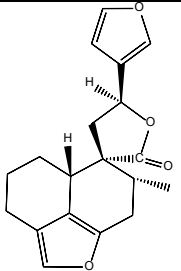
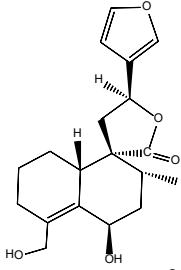
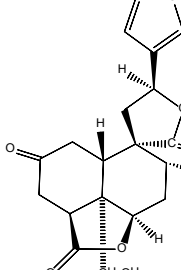
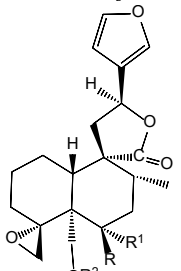
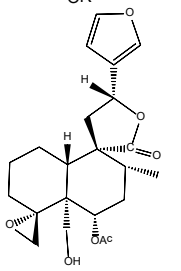
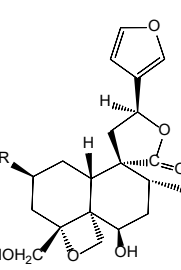
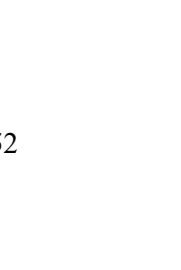
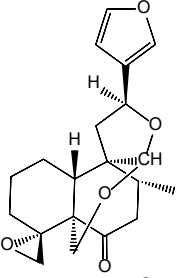
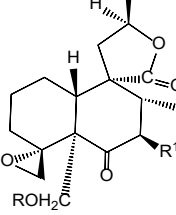
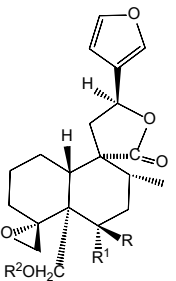
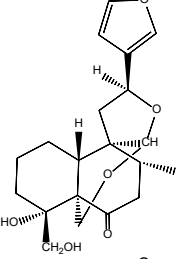
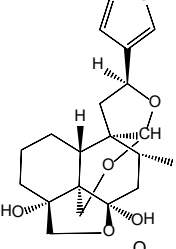
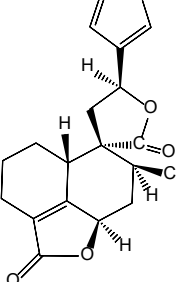


Figure 3. *Neo*-absolute configurations of clerodanes and structures of the compounds used in the discussion.

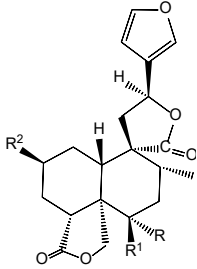
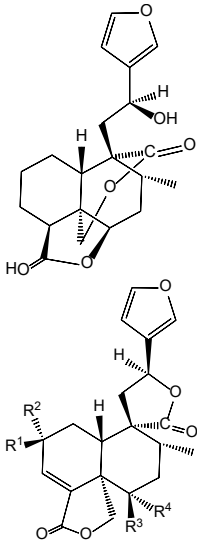
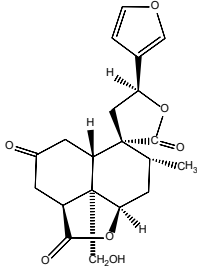
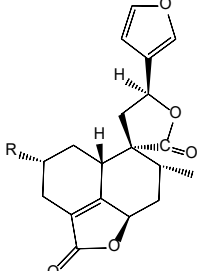
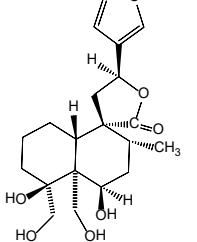
Table 1. Natural *neo*-clerodane diterpenoids isolated from Bulgarian *Teucrium* species.

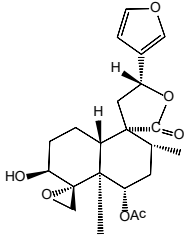
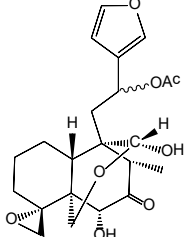
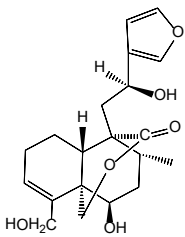
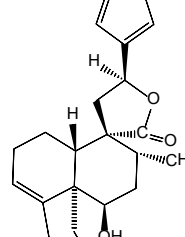
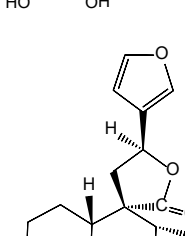
Compounds	Name	Source	Ref.
 <p>1</p>	Montanine A	<i>T. montanum</i> L.	6
 <p>2</p>	Montanine B	<i>T. montanum</i> L.	6
 <p>3</p>	Teucrin A	<i>T. chamaedrys</i> L. <i>T. chamaedrys</i> L.	16 18*
 <p>4 R = OAc R¹ = H</p>	Montanine C	<i>T. montanum</i> L.	9
 <p>5 R = OH R¹ = H</p>	Teupolin I	<i>T. polium</i> L.	38 11 38
 <p>6 R = H R¹ = Ac</p>	12-епитеуполин II	<i>T. lamifolium</i> D'Urv	33
 <p>7 R = H</p>	Montanine D	<i>T. montanum</i> L.	10
 <p>8 R = OH</p>	Teucroxide	<i>T. polium</i> subsp. <i>polium</i> <i>T. chamaedrys</i> L.	30 32

P. Bozov: Clerodane diterpenoids isolated from Bulgarian species of genus *Teucrium* (Lamiaceae)

	9			Teucrin P ₁	<i>T. polium</i> L.	11	
					<i>T. polium</i> L.	12	
	10	R = Ac	R ¹ = H	19-acetylnaphalin (= Teucrin H ₃)	<i>T. polium</i> L.	11	
					<i>T. hyrcaicum</i>	13	
	11	R = H	R ¹ = OAc	Teupolin IV	<i>T. polium</i> subsp. <i>polium</i>	15	
	12	R = H	R ¹ = OAc	R ² = H	Teupolin II	<i>T. polium</i> L.	11
	13	R = OH	R ¹ = H	R ² = Ac	Montanine F (teucjaponin A)	<i>T. montanum</i> subsp. <i>skorpilii</i> (vel.) D. Peev	25
						<i>Teucrium japonicum</i>	28
						<i>Hov TT</i>	
	14			Teupolin III	<i>T. polium</i> subsp. <i>polium</i>	14	
	15			Teupolin V	<i>T. polium</i> subsp. <i>polium</i>	15	
						<i>T. japonicum</i> Hov	28
					<i>T* T</i>		
	16			Teuchamaedryn A	<i>T. chamaedrys</i> L.	16	

P. Bozov: Clerodane diterpenoids isolated from Bulgarian species of genus *Teucrium* (Lamiaceae)

	17 R = H	R ¹ = OH	R ² = H	Teuchamaedryn B	<i>T. chamaedrys</i> L.	16
	18 R = OH	R ¹ = H	R ² = H	Teucrin E	<i>T. chamaedrys</i> L.	16
	19 R = H	R ¹ = OH	R ² = OH	Dihyroteugin	<i>T. chamaedrys</i> L.	19
	20 R = R ¹ = O	R ² = H		6-Ketoteuscordin	<i>T. chamaedrys</i> L.	17
					<i>T. chamaedrys</i> L.	20
					<i>T. scordium</i> subsp. <i>scordium</i>	22
	21			Teuchamaedryn C	<i>T. chamaedrys</i> L.	17
	22 R ¹ = R ² = H	R ³ = R ⁴ = O		Teuscordinon		
	23 R ¹ = R ² = H	R ³ = H	R ⁴ = OH	6 α -Hydroxyteuscordin	<i>T. scordium</i> subsp. <i>scordium</i>	21
	24 R ¹ = R ² = H	R ³ = OH	R ⁴ = H	6 β -Hydroxyteuscordin	<i>T. scordium</i> subsp. <i>scordium</i>	22
	25 R ¹ = OH	R ² = H, R ³ = OH	R ⁴ = H	2 β ,6 β -Dihydroxyteuscordin	<i>T. scordium</i> subsp. <i>scordium</i>	23
					<i>T. scordium</i> subsp. <i>scordium</i>	23
					<i>T. scordium</i> subsp. <i>scordium</i>	23
	26 R + R ¹ = O	R ² = H	R ³ = H	2-Keto-19-hydroxyteuscordin	<i>T. scordium</i> subsp. <i>scordium</i>	24
	27 R = OH			Teucrin H ₄	<i>T. scordium</i> subsp. <i>scordium</i>	24
	28 R = H			Teuflin	<i>T. hyrcanicum</i>	13
					<i>T. lamiifolium</i> D'Urv	31
				<i>Teucrium flavurn</i>	32	
	29			Montanine E	<i>T. montanum</i> subsp. <i>skorpilii</i> (vel.) D. Peev	25

 <p>30</p>	Montanine G	<i>T. montanum</i> subsp. <i>skorpilii</i> (vel.) D. Peev	26
 <p>31</p>	Montanine H	<i>T. montanum</i> subsp. <i>skorpilii</i> (vel.) D. Peev	27
 <p>32</p>	Teulamifin B (= teubotrin)	<i>T. polium</i> subsp. <i>polium</i> <i>T. lamifolium</i> <i>T. botrys</i>	29 30 31
 <p>33</p>	19- Deacetylteuscorodol	<i>T. lamifolium</i> <i>T. botrys</i>	29 31
 <p>34</p>	Teulamoside	<i>T. lamifolium</i>	36

* Bold-italic: species from which the compound has been isolated for the first time, when it is not new.

From 1982 to 1987 Malakov published in various collectives the data of three more new furo-*neo-clerodane* diterpenoids isolated from *T. polium* subsp. *polium*: teupolin III (**14**) [14], teupolins IV (**11**) and V (**15**) [15]. Their structures were established by spectroscopic and chemical means and for teupolin V by partial synthesis from teucrin P₁ (**9**).

From the aerial parts of *T. chamaedrys* six *neo-clerodanes* have been obtained by Malakov and Papanov. Three of them, Teuchamaedryns A (**16**), B

(**17**) [16] and C (**21**) [17] are new compounds; the rest three diterpenoids were previously isolated: teucrin A (**3**) and teucrin E (**18**) from Moldavian *T. chamaedrys* [18, 19], while dihydroteugin (**19**) has been found in Spanish *T. chamaedrys* [20]. Teuchamaedryn A (**16**) is with *nor-clerodane* skeleton and the only diterpene, isolated from Bulgarian *Teucrium* species, with clerodane skeleton of the TT type. Teuchamaedrin C (**21**) is the first diterpenoid, isolated from a *Teucrium* species, which possesses a C-18 – C-6 β hemiacetalic function.

The research of the species *T. scordium* subsp. *scordium* was conducted by Papanov and Malakov through the period 1981–1985. Six new furanoid *neo*-clerodane diterpenoids were described: teuscordinon (**22**) [21], 6-ketoteuscordin (**20**) and 6 α -hydroxyteuscordin (**23**) [22], 6 β -hydroxyteuscordin (**24**) and 2 β ,6 β -dihydroxyteuscordin (**25**) [23], 2-keto-19-hydroxyteuscordin (**26**) [24], besides the previously known diterpenoids teucrin E (**18**) [24] and teucrin H₄ (**27**) [24]. The structures of the compounds and their stereochemistry were determined on the basis of chemical reactions and spectroscopic evidence.

The study of the aerial parts of *T. lamiifolium* and *T. polium* subsp. *polium* [30] resulted in simultaneous isolation from both species of a *neo*-clerodane diterpenoid teulamifin B (**32**), besides the known diterpenoids 19-deacetyl-teuscorodol (**33**) previously isolated from *T. botrys* [31] and teucroxide (**8**) for the first time found in *T. chamaedrys* [32]. The structure of teulamifin B was established by chemical and spectroscopic means and by correlation with 19-deacetylteuscorodol. Later it was found that teulamifin B was identical to teubotrin previously isolated from *T. botrys*.

Three new *neo*-clerodane diterpenoids – montanines E (**29**) [25], G (**30**) [26] and H (**31**) [27], have been isolated from the aerial parts of *T. montanum* subsp. *skorpilii* (vel.) by D. Peev. In addition, two more previously known diterpenoids, montanine F (**13**) (which was identical to teucjaponin A [25, 28]) and teubotrin (**32**) (which was identical to teulamifin B [30, 31]) were obtained.

A new *neo*-clerodane diterpenoid, 12-epiteupolin II (**6**), was obtained from *T. lamiifolium* D'Urv by Boneva *et al.* [33], together with the previously known diterpenes teuscordinon (**22**) [21], teuflin (**28**) [34], montanine C (**4**) [9] and 19-acetylnaphalin (= teucrin H₃, **10**) [35]. The structure of 12-epiteupolin II was established by chemical and spectroscopic means and by correlation with montanine C. Five years later Boneva, in another team [36], isolated a new *neo*-clerodane glucoside teulamioside (**34**), in addition to the previously known diterpenes montanine E (**29**) [25] and teuspinin (Fig. 3) previously isolated by Savona *et al.* from *T. spinosum* L. [37].

Fayos *et al.* [38] proposed the reported stereochemistry of montanine C (**4**) and teupolin I (**5**) structures with C-12S configuration to be corrected to C-12R configuration. Three years later,

Gacs-Baitz *et al.* [39] established that the absolute stereochemistry of the C-12 chiral center must be maintained in an S configuration. This statement was based on chemical correlations with compounds of known C-12(S) absolute stereochemistry proven by X-ray analysis and studies using a variety of ¹H NOE experiments.

From the Bulgarian *Teucrium* species thirty-four furoclerodane diterpenoids were isolated. Five of them, **1**, **2**, **16**, **27** and **28**, had a *nor*-clerodane skeleton and the rest were *neo*-clerodanes. All compounds were of the TC type except **16** which was of the TT type.

ANTIFEEDANT ACTIVITY

In 1994 Malakov *et al.* [40] have subjected the *neo*-clerodane diterpenes montanine C (**4**), teucrin P₁ (**9**) and teupolin III (**14**) to a series of chemical transformations to obtain α,β -unsaturated 15,16-(**Aa**) and 16,15- γ -lactones (**Ab**), 13,14,15,16-tetranor-*neo*-clerodanes (**B**), chlorohydrins (**C**), vinyl chlorides (**D**), amine (**Ea**), 1-pyrroline (**Eb**) and 2-pyridazoline (**Ec**) derivatives (Fig. 4). These non-natural hemisynthetic derivatives have been assayed as insect antifeedants against larvae of the lepidopteran *Spodoptera littoralis* (Boisduval) in order to investigate how the changes in the structure influence the antifeedant activity. The results of the bioassays have been compared with the activity of the potent antifeedant ajugarin I.

Bioassay data showed that ajugarin I was the most potent agent among the 17 tested diterpenes (3 natural and 14 hemi-synthetic). Modification of the functional groups present in the ajugarin I molecule resulted in a decrease of antifeedant activity. For example, a comparison of the activity of ajugarin I with that of montanine C (**4**) and its chemical derivatives having an identical decalin core, bearing 4 α ,18-oxirane ring and two acetoxy groups at 6 α and 19 position, indicates that the functional groups on the C-9 side-chain influence the antifeedant activity of the compound. The results of the biological tests indicate that the presence of a lactone instead of the furan ring in the C-1 – C-16 substructure increases the activity of the compounds and that the regiochemistry of the lactone is important. Compounds having identical 15,16- γ -lactone (**Aa**, Fig. 4) moiety as that occurring in ajugarin I showed more potent antifeedant activity than the compounds having 16,15- γ -lactone (**Ab**, Fig. 4).

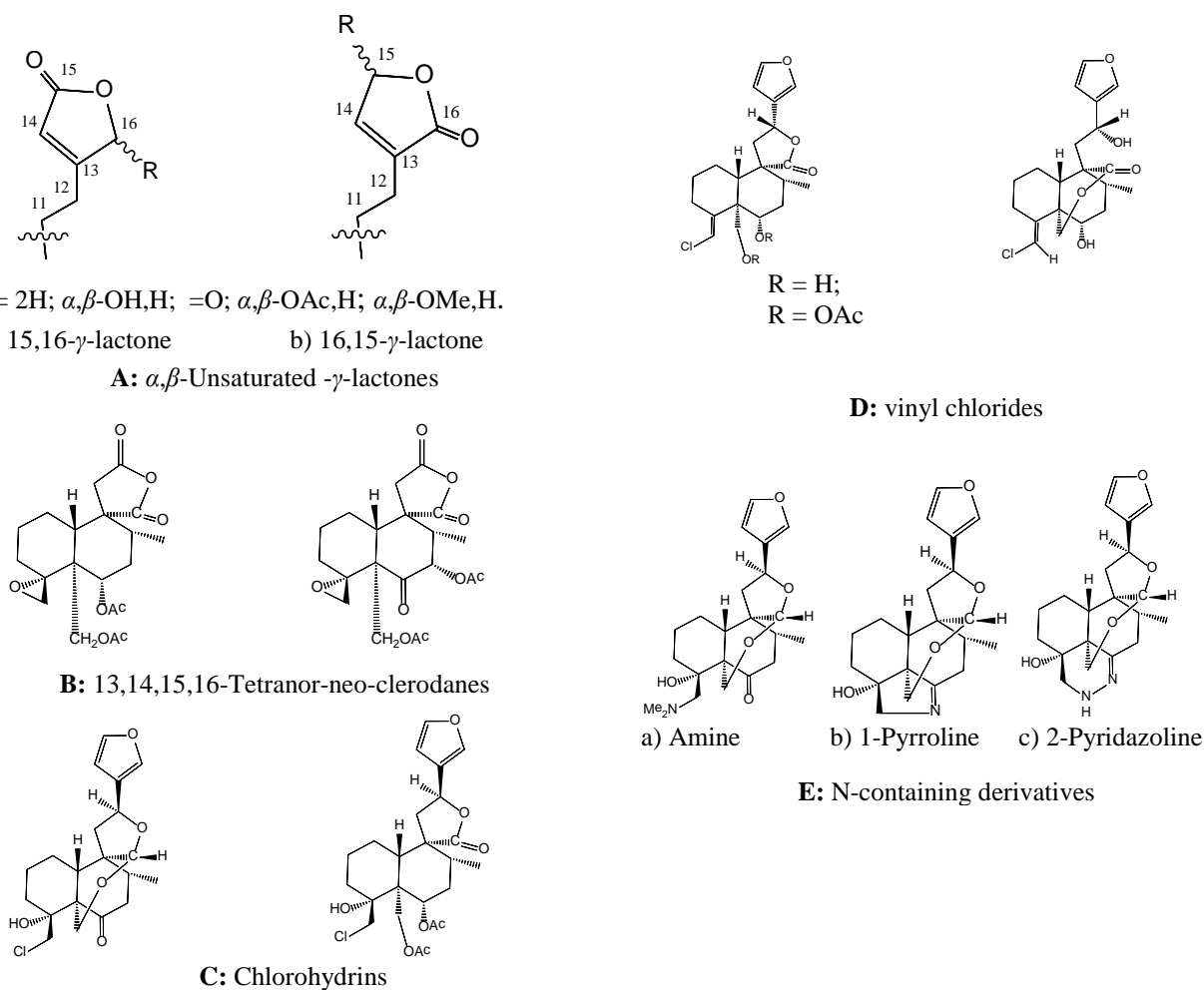


Fig. 4. Hemi-synthetic derivatives of the *neo*-clerodane diterpenes montanine C (7), teucin P₁ (12) and teupolin III (17).

The chemical reactions leading to the opening of the 4 α ,18-oxirane ring result in an antifeedant index with a negative value. Diterpenoids that are bridged by an oxygen atom between C-19 and C-20 either stimulate feeding or are inactive. Activity of all 13,14,15,16-tetranor-*neo*-clerodanes was drastically decreased.

Consequently, in order to optimize the antifeedant activity of natural *neo*-clerodanes from *Teucrium* by chemical transformations, the 4 α ,18-oxirane needs to be maintained and the furan ring should be oxidized.

REFERENCES

1. B. Kuzmanov, Flora Reipublicae Popularis Bulgariae, **IX**, 241 (1989).
2. A. Ulubelen, G. Topgu, U. Sonmez, *Studies in Natural Products Chemistry*, **23**, 591, (2000).
3. M. Bruno, Piozzi F., Rosselli S., *Nat. Prod. Rep.*, **19**, 357 (2002).
4. R. Li, S. L. Morris-Natschke, Kuo-Hsiung Lee, *Nat. Prod. Rep.*, **33**, 1166, (2016).
5. A. T. Merritt, S. V. Ley, *Nat. Prod. Rep.*, **9**, 243 (1992).
6. P. Y. Malakov, G. Y. Papanov, N. M. Mollov. *Tetrahedron *Lett.*, **23**, 2025 (1978).
7. I. Kubo, Y. W. Lee, V. Balogh-Nair, K. Nakanishi, A. Chapia, *J. Chem. Soc. Chem. Commun.*, **22**, 949 (1976).
8. E. Fujita, I. Uchida, T. Fujita, N. Masaki, K. Osaki, *J. Chem. Soc. Chem. Commun.*, **0** (20), 793 (1973).
9. P. Y. Malakov, G. Y. Papanov, N. M. Mollov, S. L. Spassov, *Z. Naturforsch.*, **33b**, 789 (1978).
10. P. Y. Malakov, G. Y. Papanov, N. M. Mollov, S. L. Spassov. *Z. Naturforsch.*, **33b**, 1142 (1978).
11. P. Y. Malakov, G. Y. Papanov., N. M. Mollov, *Z. Naturforsch.*, **34b**, 1370 (1979).
12. D. P. Popa, A. F. Tkhuik, *Chem. Nat. Compd.*, **13** (1), 42 (1977).
13. E. Gacs-Baitz, L. Radics, G. B. Oganessian, V. A. Mnatsakanian, *Phytochemistry*, **17**, 1967 (1978).

P. Bozov: Clerodane diterpenoids isolated from Bulgarian species of genus Teucrium (Lamiaceae)

16. G. Y. Papanov, P. Y. Malakov, *Z. Naturforsch.*, **35b**, 764 (1980).
17. P. Y. Malakov, G. Y. Papanov, *Phytochemistry*, **24** (2), 301 (1985).
18. D. P. Popa, A. M. Reinbol'd, *Khim. Prirodn. Soedin.*, **67**, 27 (1972).
19. A. M. Reinbol'd, D. P. Popa, *Khim. Prirodn. Soedin.*, **10**, 589 (1974).
20. G. Savona, M. C. Garcia-Alvarez, B. Rodriguez. *Phytochemistry*, **21** (3), 721 (1982).
21. G. Y. Papanov, P. Y. Malakov, F. Bohlmann, *Phytochemistry*, **20**, 170 (1981).
22. G. Y. Papanov, P. Y. Malakov, *Z. Naturforsch.*, **36b**, 112 (1981)
23. G. Y. Papanov, P. Y. Malakov, *Z. Naturforsch.*, **37b**, 519 (1982)
24. P. Y. Malakov, G. Y. Papanov, *Phytochemistry*, **24** (2), 297 (1985).
25. G. Y. Papanov, P. Y. Malakov, *Phytochemistry*, **22** (12), 2787 (1983).
26. P. Y. Malakov, G. Y. Papanov, *Z. Naturforsch.*, **42b**, 1000 (1987).
27. P. Y. Malakov, G. Y. Papanov, I. M. Boneva, *Phytochemistry*, **31** (11), 4029 (1992).
28. T. Miyase, H. Kawasaki, T. Noro, A. Ueno, S. Fukushima, T. Takemoto, *Chem. Pharm. Bull.*, **29** (12), 3561 (1981).
29. A. Fiorentino, B. D'Abrosca, S. Pacifico, M. Scognamiglio, G. D'Angelo, M. Gallicchio, A. Chambery, P. Monaco, *Phytochemistry*, **72**, 2037 (2011).
30. P. Y. Malakov, I. M. Boneva, G. Y. Papanov, S. L. Spasov, *Phytochemistry*, **27**, 1141 (1988).
31. M. C. De La Torre, F. Fernandez-Gadea, A. Michavila, B. Rodriguez, F. Piozzi, G. Savona, *Phytochemistry*, **25** (10), 2385 (1986).
32. M. C. Garcia-Alvarez, G. Lukacs, A. Neszmelyi, F. Piozzi, B. Rodriguez, G. Savona, *J. Org. Chem.*, **48**, 5123 (1983).
33. I. V. Boneva, P. Y. Malakov, G. Y. Papanov, *Phytochemistry*, **27**, 295 (1988).
34. G. Savona, M. P. Paternostro, F. Piotzi, J. R. Hanson, P. B. Hitchcock, S. A. Thomas, *J. Chem. Soc. Perkin Trans. I*, **6**, 1915 (1979).
35. G. Savona, M. Paternostro, F. Piozzi, B. Rodriguez, *Tetrahedron Letters*, **4**, 379 (1979).
36. P. Y. Malakov, G. Y. Papanov, I. M. Boneva, M. C. De La Torre, B. Rodriguez, *Phytochemistry*, **34** (4), 1095 (1993).
37. G. Savona, M. Paternostro, F. Piozzi, B. Rodriguez, *Heterocycles*, **14**, 193 (1980).
38. J. Fayos, F. Fernandez-Gadea, C. Pascual, A. Perales, F. Piozzi, M. Rico, B. Rodriguez, G. Savona, *J. Org. Chem.*, **49**, 1789 (1984).
39. E. Gacs-Baitz, G. Y. Papanov, P. Y. Malakov, L. Szilagy, *Phytochemistry*, **26** (7), 2110 (1987).
40. P. Y. Malakov, G. Y. Papanov, B. Rodriguez, M. C. De La Torre, M. S. J. Simmonds, W. M. Blaney, I. M. Boneva, *Phytochemistry*, **37** (1), 147 (1994).

Stability analysis and multiple solutions of a hydromagnetic dissipative flow over a stretching/shrinking sheet

M. R. Mishra¹, S. M. Hussain^{2*}, O. D. Makinde³, G. S. Seth⁴

¹Department of Mathematics, OP Jindal University, Raigarh, 496109, India

^{1,2}Department of Mathematics, Faculty of Science, Islamic University of Madinah, 42351, Saudi Arabia

³Faculty of Military Science, Stellenbosch University, Private Bag X2, Saldanha, 7395, South Africa

⁴Department of Applied Mathematics, Indian Institute of Technology (ISM), Dhanbad, 826004, India

Received: June 18, 2019; Revised: February 18, 2020

The steady hydromagnetic two-dimensional flow of a viscous, incompressible, optically thick radiative and electrically conducting fluid past a permeable stretching/shrinking sheet is studied. The effects of heat absorption, chemical reaction, viscous and Joule dissipations are taken into consideration. The governing mathematical equations comprising the partial differential equations are changed to the form of nonlinear ordinary differential equations by making use of the suitable similarity variables. Further, fourth order Runge-Kutta scheme along with a shooting technique is implemented to analyze the numerical solution. Moreover, the consequence of relatable physical parameters on the fluid velocity, temperature distribution and fluid concentration are quantified through different graphs whereas, from engineering viewpoint, the numerical findings of wall velocity gradient, Sherwood numbers and wall temperature gradient are provided in tabular form. Our results reveal that the stretching/shrinking parameter range is widened due to magnetic field and suction for which there is a solution. Meanwhile, the presence of dual solutions is observed in the range of prevailing parameters. The results obtained in the present study are compared and verified with the existing numerical results.

Keywords: Stability analysis; Dual solution; Viscous dissipation; Joule dissipation.

NOMENCLATURE

B_0	uniform magnetic field (T)	M	magnetic parameter ($\sigma B_0^2 / a\rho$)
C_p	specific heat at constant pressure ($J/(kg K)$)	Pr	Prandtl number (ν / α)
D_B	mass diffusivity (m^2/s)	Q	heat absorption parameter ($Q_0 / a\rho C_p$)
Ec	Eckert number ($\bar{u}_w^2 / C_p(T_w' - T_\infty')$)	Q_0	heat absorption coefficient ($W/(m^2K)$)
K	chemical reaction parameter (k_0 / a)	q_r	radiative heat flux ($W m^{-2}$)
k	thermal conductivity ($W m^{-1}$)	R	radiation parameter ($4\sigma^* T_\infty'^3 / k k^*$)
k^*	mean absorption coefficient (cm^{-1})	S	suction/injection parameter ($-v_0 / \sqrt{av}$)
k_0	constant rate of chemical reaction	Sc	Schmidt number (ν / D_B)
\bar{T}	fluid temperature ($^{\circ}K$)	\bar{v}	velocity along y axis ($m s^{-1}$)
\bar{u}	velocity along x axis ($m s^{-1}$)		

GREEK SYMBOLS

α	fluid thermal diffusivity (m^2/s)	σ^*	Stefan Boltzmann constant ($W / m^2 K^4$)
$\bar{\beta}$	species concentration ($kg m^{-3}$)	σ	fluid electrical conductivity ($s^3 A^2 m^{-3} kg^{-1}$)
ϕ	dimensionless species concentration	μ	fluid dynamic viscosity ($kg m^{-1} s^{-1}$)
θ	dimensionless fluid temperature	ν	fluid kinematic viscosity (m^2/s)
ρ	density of fluid ($kg m^{-3}$)		

* To whom all correspondence should be sent:
E-mail: hussain.modassir@yahoo.com

SIGNIFICANCE STATEMENT

Analysis of a boundary layer hydromagnetic flow of a dissipative fluid over a stretching/shrinking sheet is noteworthy owing to its enormous significance in industry which includes electrical power generation, plastic substances manufacturing, solar power technology, extrusion of polymers, metallurgical process, etc. Influence of various physical parameters like magnetic field, stretching/shrinking, heat absorption, suction/injection, thermal radiation, chemical reaction, etc. is quantified. Additionally, flow stability analysis is executed to analyze the physically reliable and stable solutions of the problem. Finally, validation of the numerical results is done in the limiting conditions with the previously published research paper of Yasin *et al.* [37].

INTRODUCTION

Substantial attention has been paid to the study of a hydrodynamic fluid flow over the past decades because of its enormous relevance, for instance, in heat storage systems, geophysics, oil recovery techniques, chemical processing equipment, thermal insulations, cosmic fluid dynamics, etc. Moreover, the imposition of exerted magnetic field onto the flow regime driven by non-permeable and permeable stretching sheets has engrossed the curiosity of researchers due to its significance in industry and public enterprise. The pioneering research on the magnetohydrodynamic fluid flow due to plane surface's deformation was executed by Pavlov [1]. Moreover, Chakrabarti and Gupta [2] explored this investigation considering temperature distribution. Al-Odat *et al.* [3] discussed the influence of exerted magnetic field on a boundary layer fluid flow permeated by a stretched sheet. Also, the hydromagnetic problems driven by a stretched sheet have been investigated in [4-7], etc.

Heat generation/absorption models of a fluid flow driven by a permeable stretched sheet have been investigated by many authors because of its numerous industrial applications, *viz.* hot rolling, chemical reaction that discharges heat, endothermic reactions, heat exchange from nuclear fuel wastage, glass fiber production, paper production, etc. Following this, Elbashareshy [8] numerically analyzed the solution of a quiescent fluid flow over an exponentially stretched sheet amid the significance of heat source/sink. This study illustrates that the suction can be employed to cool down the moving continuous surface. Further, this problem was extended by Elbashareshy and Bazid [9] considering an unsteady state condition. Subsequently, Eldahab and Aziz [10] considered the

suction/blowing influence on a magnetohydrodynamic flow considering heat generation and absorption over the obliquely aligned stretched surface. Makinde *et al.* [11, 12] investigated the flow of a mixed convective magnetohydrodynamic nanofluid along a permeable stretched sheet.

The vital characteristics of thermal radiation for surface heat transfer cannot be ignored while considering industrial processes like electrical power generation, designing of furnace, production of glass, missiles devices, solar power technology, etc., wherein high temperature occurs. At the present industrial scenario, due to decrease of conventional energy resources, the attention is focused on sustainable and renewable energy sources. The solar energy is the main fountain of renewable energy and thermal radiation has a noteworthy role in transforming the solar energy to the appropriate form for various applications in industry. Owing to this reason, many authors [13-17], etc. have illustrated the significance of thermal radiation on the laminar fluid flow over a plate/stretching sheet.

In the above studies, the viscous dissipation effect has been ignored as the same is supposed to be low but its relevance in food processing, instrumentations, lubrications, polymer manufacturing, etc., is considered as very significant as it enhances the characteristics of temperature distribution which induce the heat transfer rate. Some important studies dealing with the viscous dissipative flow problem induced by stretched sheet are reported [18-21]. Further, Joule dissipation behaves like a volumetric heat source in magnetohydrodynamic fluid flows and the collective influence of viscous and Joule dissipations is imperative in context of the heat-treated materials. Following this, Anjali and Ganga [22], Pal [23], Seth and Singh [24] and Seth *et al.* [25, 26] modeled their problem considering the impacts of Joule and viscous dissipations. Seth *et al.* [27] explored the Joule dissipation effects on the flow of a magnetohydrodynamic (MHD) thin film Casson fluid over a flat stretched sheet.

The relevance of a chemical reaction on a hydromagnetic fluid flow has been a matter of excessive attention in the past few decades because of its large scientific and technological impacts like polymer and ceramics production, manufacturing of insulated cables and glassware, chemical processing of materials and many more. Some relevant studies reporting the effects of a chemical reaction are presented in [28-36]. Moreover, Yasin *et al.* [37] studied two-dimensional steady hydromagnetic flows driven by a permeable stretched or shrinking

sheet, taking into account heat absorption and thermal radiation.

The present paper has the objective to unfold the combined impacts of Joule and viscous dissipations on a two-dimensional MHD fluid, as well as the mass transfer of a heat absorbing, incompressible, thick radiative, electrically conducting viscous fluid permeated by a stretching/shrinking sheet in the presence of a homogeneous chemical reaction. Numerical solutions of the governing mathematical equations are obtained employing a 4th order Runge-Kutta scheme along with a shooting technique. Additionally, flow stability analysis is executed to examine the physically reliable and stable solutions of the problem. Finally, validation of the numerical results is done in the limiting conditions with a previously published research paper. The meticulous review of research papers reported in the literature revealed that none of the authors has earlier attempted this problem although the thoughts and methodology explained in this paper can be anticipated to lead to enormously prolific connections across the disciplines.

MATHEMATICAL ANALYSIS

Mathematical problem formulation

We consider the steady 2-dimensional dissipative hydromagnetic flow of a heat absorbing, incompressible, optically thick radiative, electrically conducting, viscous fluid, as well as mass transfer fluid driven by a stretched or shrinking sheet. The fluid is induced over the stretched or shrunk sheet owing to the velocity $\lambda \bar{u}_w(x)$ where $\lambda > \text{or} < 0$ is considered for a stretched or a shrunk sheet. The transverse magnetic field B_0 is exerted along y direction (Fig. 1). For considering this fluid flow model, we have taken the x -axis along the stretched

sheet surface whilst y -axis is normal to it, the flow being limited to $y > 0$. Further, the mass flux velocity of the stretching sheet is presumed as v_0 where $v_0 < 0$ and $v_0 > 0$ are, considered for suction and injection, respectively, as the surface is considered to be permeable. At a stretched/shrunk sheet surface, the temperature \bar{T}_w and concentration $\bar{\beta}_w$ are supposed to be constant whilst ambient fluid is considered as \bar{T}_∞ and $\bar{\beta}_\infty$. Moreover, a first-order homogeneous chemical reaction k_0 having constant rate is supposed to take place among the fluid and the diffusive species.

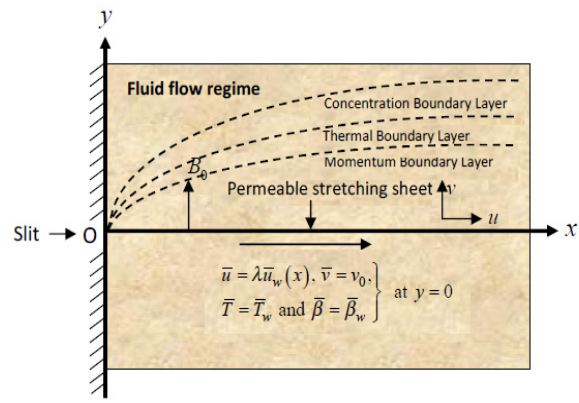


Figure 1. Physical model of the problem

The mathematical model for the fluid flow is represented as:

$$\frac{\partial \bar{u}}{\partial x} + \frac{\partial \bar{v}}{\partial y} = 0, \quad (1)$$

$$\bar{u} \frac{\partial \bar{u}}{\partial x} + \bar{v} \frac{\partial \bar{u}}{\partial y} = \nu \frac{\partial^2 \bar{u}}{\partial y^2} - \frac{\sigma B_0^2}{\rho} \bar{u}, \quad (2)$$

$$\bar{u} \frac{\partial \bar{T}}{\partial x} + \bar{v} \frac{\partial \bar{T}}{\partial y} = \alpha \frac{\partial^2 \bar{T}}{\partial y^2} + \frac{\nu}{C_p} \left(\frac{\partial \bar{u}}{\partial y} \right)^2 - \frac{1}{\rho C_p} \frac{\partial q_r}{\partial y} - \frac{Q_0}{\rho C_p} (\bar{T} - \bar{T}_\infty) + \frac{\sigma}{\rho C_p} B_0^2 \bar{u}^2, \quad (3)$$

$$\bar{u} \frac{\partial \bar{\beta}}{\partial x} + \bar{v} \frac{\partial \bar{\beta}}{\partial y} = D_B \frac{\partial^2 \bar{\beta}}{\partial y^2} - k_0 (\bar{\beta} - \bar{\beta}_\infty). \quad (4)$$

The associated boundary conditions are:

$$\left. \begin{aligned} \bar{u} = \lambda \bar{u}_w(x), \quad \bar{v} = v_0, \quad \bar{T} = \bar{T}_w, \quad \bar{\beta} = \bar{\beta}_w \quad \text{when } y = 0, \\ \bar{u} \rightarrow 0, \quad \bar{\beta} \rightarrow \bar{\beta}_\infty \quad \text{and} \quad \bar{T} \rightarrow \bar{T}_\infty \quad \text{for } y \rightarrow \infty, \end{aligned} \right\} \quad (5)$$

where $\bar{u}_w(x) = ax$ such that the constant $a > 0$.

The Rosseland approximation [38] for an optically thick radiative fluid is used to transform the radiative heat flux q_r as:

$$q_r = -\frac{4\sigma^*}{3k^*} \frac{\partial \bar{T}^4}{\partial y}. \quad (6)$$

Moreover, \bar{T}^4 is linearized by means of the Taylor's series expansion about \bar{T}_∞ (free stream

$$\bar{u} \frac{\partial \bar{T}}{\partial x} + \bar{v} \frac{\partial \bar{T}}{\partial y} = \alpha \left[1 + \frac{16\sigma^* \bar{T}_\infty^3}{3k k^*} \right] \frac{\partial^2 \bar{T}}{\partial y^2} + \frac{\nu}{C_p} \left(\frac{\partial \bar{u}}{\partial y} \right)^2 - \frac{Q_0}{\rho C_p} (\bar{T} - \bar{T}_\infty) + \frac{\sigma}{\rho C_p} B_0^2 \bar{u}^2. \quad (8)$$

Numerical solution

In order to determine the numerical solution of the aforementioned problem the following

temperature) and then higher order terms are neglected. The linearized form is given by:

$$\bar{T}^4 \cong -3\bar{T}_\infty^4 + 4\bar{T}_\infty^3 \bar{T}. \quad (7)$$

Eqs. (6) and (7) transform the energy Eq. (3) in the following form:

similarity transforms [37] were introduced:

$$\eta = y(a/\nu)^{1/2}, \psi(x, y) = x(a\nu)^{1/2} f(\eta), \theta(\eta) = \frac{\bar{T} - \bar{T}_\infty}{\bar{T}_w - \bar{T}_\infty} \text{ and } \phi(\eta) = \frac{\bar{\beta} - \bar{\beta}_\infty}{\bar{\beta}_w - \bar{\beta}_\infty}, \quad (9)$$

$$\text{where } \psi \text{ is stream function expressed as: } \bar{u} = \frac{\partial \psi}{\partial y} \text{ and } \bar{v} = -\frac{\partial \psi}{\partial x}. \quad (10)$$

$$\text{Using Eq. (9) in (10), we obtain: } \bar{u}/xa = f'(\eta) \text{ and } (a\nu)^{-1/2} \bar{v} = -f(\eta), \quad (11)$$

here primes indicate the differentiation with respect to η .

Eqs. (9) and (11) transform Eqs. (2), (8) and (4) in the form of three ordinary differential equations given as:

$$f'''(\eta) + f(\eta)f''(\eta) - Mf'(\eta) - f'(\eta)^2 = 0, \quad (12)$$

$$\frac{1}{Pr} \left[\frac{3+4R}{3} \right] \theta''(\eta) - Q\theta(\eta) + f(\eta)\theta'(\eta) + Ec \left[\{f''(\eta)\}^2 + Mf'(\eta)^2 \right] = 0, \quad (13)$$

$$\phi''(\eta) + Sc f(\eta)\phi'(\eta) - ScK\phi(\eta) = 0, \quad (14)$$

subject to the associated conditions:

$$\left. \begin{aligned} f = S, f' = \lambda, \theta = 1 \text{ and } \phi = 1 \text{ when } \eta = 0, \\ f' \rightarrow 0, \theta \rightarrow 0 \text{ and } \phi \rightarrow 0 \text{ for } \eta \rightarrow \infty. \end{aligned} \right\} \quad (15)$$

where

$$\left. \begin{aligned} Pr = \frac{\nu}{\alpha}, R = \frac{4\sigma^* T_\infty^3}{k k^*}, Q = \frac{Q_0}{a \rho C_p}, Ec = \frac{\bar{u}_w^2}{C_p (\bar{T}_w - \bar{T}_\infty)}, \\ M = \frac{\sigma B_0^2}{a \rho}, Sc = \frac{\nu}{D_B}, K = \frac{k_0}{a} \text{ and } S = -\frac{v_0}{\sqrt{a\nu}}. \end{aligned} \right\} \quad (16)$$

It may be noted that the positive and negative values of S correspond to suction and injection, respectively, whereas $Q < 0$ signifies the sink and $Q > 0$ indicates the source.

Skin friction, local Nusselt and local Sherwood numbers

From engineering aspects, skin friction coefficient S_f , local Nusselt number Nu_x and local Sherwood number Sh_x are, respectively, given by:

$$S_f = \tau_w (\rho \bar{u}_w^2(x))^{-1}, Nu_x = (k(\bar{T}_w - \bar{T}_\infty))^{-1} x q_w \text{ and } Sh_x = (D_B(\bar{\beta}_w - \bar{\beta}_\infty))^{-1} x q_m, \quad (17)$$

where $\tau_w = \mu(\partial \bar{u} / \partial y)_{y=0}$ is used for wall shear stress, $q_w = (q_r)_{y=0} - (\partial \bar{T} / \partial y)_{y=0}$ indicates the wall heat flux and $q_m = -D_B(\partial \bar{\beta} / \partial y)_{y=0}$ signifies the

wall shear mass flux. The dimensionless forms of S_f , Nu_x and Sh_x are represented as:

$$S_f = f''(0) / Re_x^{1/2}, Nu_x = -\left\{ (3+4R) / 3Re_x^{1/2} \right\} \theta'(0) \text{ and } Sh_x = -\phi'(0) / Re_x^{1/2}, \quad (18)$$

where $Re_x = x\bar{u}_w / \nu$ represents the local Reynolds number.

Flow stability analysis

To analyze the physically reliable and stable solutions, flow stability analysis was done corresponding to the solutions of Eqs. (1) to (5) by considering their unsteady forms. The continuity Eq.

(1) remains unchanged while Eqs. (2) to (4) are replaced by:

$$\frac{\partial \bar{u}}{\partial t} + \bar{u} \frac{\partial \bar{u}}{\partial x} + \bar{v} \frac{\partial \bar{v}}{\partial y} = \nu \frac{\partial^2 \bar{u}}{\partial y^2} - \frac{\sigma B_0^2}{\rho} \bar{u}, \quad (19)$$

$$\frac{\partial \bar{T}}{\partial t} + \bar{u} \frac{\partial \bar{T}}{\partial x} + \bar{v} \frac{\partial \bar{T}}{\partial y} = \alpha \frac{\partial^2 \bar{T}}{\partial y^2} + \frac{\nu}{C_p} \left(\frac{\partial \bar{u}}{\partial y} \right)^2 - \frac{1}{\rho C_p} \frac{\partial q_r}{\partial y} - \frac{Q_0}{\rho C_p} (\bar{T} - \bar{T}_\infty) + \frac{\sigma}{\rho C_p} B_0^2 \bar{u}^2, \quad (20)$$

$$\frac{\partial \bar{\beta}}{\partial t} + \bar{u} \frac{\partial \bar{\beta}}{\partial x} + \bar{v} \frac{\partial \bar{\beta}}{\partial y} = D_B \frac{\partial^2 \bar{\beta}}{\partial y^2} - k_0 (\bar{\beta} - \bar{\beta}_\infty), \quad (21)$$

where t represents the time.

For the above unsteady problem, new similarity transforms were introduced:

$$\left. \begin{aligned} \eta = y \sqrt{\frac{a}{\nu}}, \quad v = -(a\nu)^{1/2} f(\eta, \tau), \quad u = ax \partial f(\eta, \tau) / \partial \eta, \\ \theta(\eta, \tau) = (\bar{T}_w - \bar{T}_\infty)^{-1} (\bar{T} - \bar{T}_\infty), \quad \phi(\eta, \tau) = (\bar{\beta}_w - \bar{\beta}_\infty)^{-1} (\bar{\beta} - \bar{\beta}_\infty), \quad \tau = at. \end{aligned} \right\} \quad (22)$$

Now, the Eqs. (19), (20) and (21) reduce to:

$$\frac{\partial^3 f}{\partial \eta^3} + f \frac{\partial^2 f}{\partial \eta^2} - \left(\frac{\partial f}{\partial \eta} \right)^2 - M \frac{\partial f}{\partial \eta} - \frac{\partial^2 f}{\partial \eta \partial \tau} = 0, \quad (23)$$

$$\frac{1}{Pr} \left[\frac{3+4R}{3} \right] \frac{\partial^2 \theta}{\partial \eta^2} + f \frac{\partial \theta}{\partial \eta} - Q\theta + Ec \left[\left(\frac{\partial^2 f}{\partial \eta^2} \right)^2 + M \left(\frac{\partial f}{\partial \eta} \right)^2 \right] - \frac{\partial \theta}{\partial \tau} = 0, \quad (24)$$

$$\frac{\partial^2 \phi}{\partial \eta^2} + Sc f \frac{\partial \phi}{\partial \eta} - Sc K \phi - Sc \frac{\partial \phi}{\partial \tau} = 0, \quad (25)$$

and the boundary conditions are converted to:

$$\left. \begin{aligned} \partial f(\eta, \tau) / \partial \eta = \lambda, \quad f(\eta, \tau) = S, \quad \theta(\eta, \tau) = 1, \quad \phi(\eta, \tau) = 1 \quad \text{when } \eta = 0, \\ \partial f(\eta, \tau) / \partial \eta \rightarrow 0, \quad \phi(\eta, \tau) \rightarrow 0, \quad \theta(\eta, \tau) \rightarrow 0, \quad \text{for } \eta \rightarrow \infty. \end{aligned} \right\} \quad (26)$$

To analyze the stability of the solution for the case of a steady flow $\theta(\eta) = \theta_0(\eta)$, $\phi_0(\eta) = \phi(\eta)$ and $f(\eta) = f_0(\eta)$ satisfying the problem mentioned above, the following expressions were considered [39, 40]:

$$\left. \begin{aligned} f(\eta, \tau) = f_0(\eta) + e^{-\xi \tau} X(\eta, \tau), \\ \theta(\eta, \tau) = \theta_0(\eta) + e^{-\xi \tau} Y(\eta, \tau), \\ \phi(\eta, \tau) = \phi_0(\eta) + e^{-\xi \tau} Z(\eta, \tau), \end{aligned} \right\} \quad (27)$$

where ξ is an unknown eigenvalue, and the

functions $X(\eta, \tau), Y(\eta, \tau)$ and $Z(\eta, \tau)$ are relatively very small as compared to the functions $f_0(\eta), \theta_0(\eta)$ and $\phi_0(\eta)$. The solutions of the above Eqs. (23) to (26) provide a set of an infinite number of eigenvalues $\xi_1 < \xi_2 < \xi_3 < \dots$. The initial growth of disturbance is found for a negative value of ξ_1 and the fluid flow becomes unstable whereas initial decay is observed for the positive value of ξ_1 and as a result the flow becomes stable. By making use of (27) in Eqs. (23) to (25), the following linearized equations were obtained:

$$\frac{\partial^3 X}{\partial \eta^3} + f_0 \frac{\partial^2 X}{\partial \eta^2} + X \frac{\partial^2 f_0}{\partial \eta^2} - \left(2 \frac{\partial f_0}{\partial \eta} + M - \xi \right) \frac{\partial X}{\partial \eta} - \frac{\partial^2 X}{\partial \eta \partial \tau} = 0, \quad (28)$$

$$\frac{1}{Pr} \left[1 + \frac{4R}{3} \right] \frac{\partial^2 Y}{\partial \eta^2} + f_0 \frac{\partial Y}{\partial \eta} + X \frac{\partial \theta_0}{\partial \eta} + 2Ec \left(\frac{\partial^2 f_0}{\partial \eta^2} \frac{\partial^2 X}{\partial \eta^2} + M \frac{\partial f_0}{\partial \eta} \frac{\partial X}{\partial \eta} \right) - (Q - \xi)Y - \frac{\partial Y}{\partial \tau} = 0, \tag{29}$$

$$\frac{\partial^2 Z}{\partial \eta^2} + Scf_0 \frac{\partial Z}{\partial \eta} + ScX \frac{\partial \phi_0}{\partial \eta} - (K - \xi)ScZ - Sc \frac{\partial Z}{\partial \tau} = 0. \tag{30}$$

The associated boundary conditions are:

$$\left. \begin{aligned} \frac{\partial X(\eta, \tau)}{\partial \eta} = 0, X(\eta, \tau) = 0, Z(\eta, \tau) = 0, Y(\eta, \tau) = 0, \quad \text{at } \eta = 0, \\ \frac{\partial X(\eta, \tau)}{\partial \eta} \rightarrow 0, Z(\eta, \tau) \rightarrow 0, Y(\eta, \tau) \rightarrow 0, \quad \text{as } \eta \rightarrow \infty. \end{aligned} \right\} \tag{31}$$

By putting $\tau = 0$, the solutions $f(\eta) = f_0(\eta)$, $\theta(\eta) = \theta_0(\eta)$ and $\phi(\eta) = \phi_0(\eta)$ of the above mentioned problem were obtained. Here, $X(\eta) = X_0(\eta)$, $Y(\eta) = Y_0(\eta)$ and $Z(\eta) = Z_0(\eta)$ in

Eqs. (28) to (31) classify the initial growth or decay of solution. For this, the below mentioned eigenvalue problem is required to be solved:

$$X_0''' + f_0 X_0'' + X_0 f_0'' - (2f_0' + M - \xi) X_0' = 0, \tag{32}$$

$$\frac{1}{Pr} \left[1 + \frac{4R}{3} \right] Y_0'' + f_0 Y_0' + X_0 \theta_0' + 2Ec (f_0'' X_0' + M f_0' X_0') - (Q - \xi) Y_0 = 0, \tag{33}$$

$$Z_0'' + Scf_0 Z_0' + X_0 \phi_0' - (K - \xi) Sc Z_0 = 0, \tag{34}$$

together with the associated boundary conditions:

$$\left. \begin{aligned} X_0'(0) = 0, Y_0(0) = 0, X_0(0) = 0, Z_0(0) = 0, \\ Y_0(\eta) \rightarrow 0, X_0'(\eta) \rightarrow 0, Y_0(\eta) \rightarrow 0 \text{ as } \eta \rightarrow \infty. \end{aligned} \right\} \tag{35}$$

It is observed that the stability of solution $f_0(\eta)$, $\theta_0(\eta)$ and $\phi_0(\eta)$ corresponding to the steady flow can be analyzed by the least eigenvalue ξ for the pertinent flow parameters. Moreover, the possible eigenvalues range can be evaluated by relaxing the boundary condition on $X_0'(\eta)$, $Y_0(\eta)$ and $Z_0(\eta)$ as mentioned by Harris *et al.* [41]. In this problem, the condition $X_0'(\eta) \rightarrow 0$ as $\eta \rightarrow \infty$ has been relaxed and we imposed a new boundary condition $X_0''(\eta) = 1$ in order to obtain the solution of Eqs. (32) to (34).

Analytical solution

The exact solution of Eq. (12) satisfying the conditions (15) can be determined as shown below:

$$f_0(\eta) = S + \frac{\lambda(1 - e^{-\delta\eta})}{\delta}, \tag{36}$$

where

$$\delta = \frac{S \pm \sqrt{S^2 + 4(\lambda + M)}}{2}. \tag{37}$$

From Eqs. (36) and (37) it may be noted that dual solutions exist for $f_0(\eta)$ provided $S^2 + 4(\lambda + M) > 0$,

one real solution occurs if $S^2 + 4(\lambda + M) = 0$ and the problem has no real solution whenever $S^2 + 4(\lambda + M) < 0$. The critical value λ_c at which no real solution occurs can be easily determined as:

$$\lambda_c = -\frac{(S^2 + 4M)}{4} < 0. \tag{38}$$

From the above exact analysis, the value of wall velocity gradient was obtained as:

$$f_0''(0) = -\delta\lambda. \tag{39}$$

NUMERICAL METHOD IMPLEMENTATIONS

To obtain the solutions of the mentioned governing equations the 4th order Runge-Kutta scheme along with a shooting technique was employed. Foremost, the prevailing equations were converted using the suitable similarity variables into a set of five differential equations of first order. Then, the Runge-Kutta method of 4th order was applied to solve the resulting equations, wherein the initial guess for $f''(0)$, $\theta'(0)$ and $\phi'(0)$ was analyzed employing a shooting technique. The initial guess was corrected by means of the Secant method. Throughout the study, the tolerance error was considered as 10^{-6} to gain more precise results.

RESULTS AND DISCUSSION

The numerical computation was executed and the results were reported to demonstrate a comparative study showing the impacts of various parameters such as S (suction/injection), M (magnetic field), λ (stretching/shrinking), Ec (Eckert number), R (thermal radiation), Q (heat absorption), Pr (Prandtl number), Sc (Schmidt number) and K (chemical reaction) on the flow field. Figs. 2-16 represent the profiles of fluid velocity, temperature distribution and concentration for the varying relevant flow parameters which portray that the boundary layer thickness in the case of a lower branch solution is wider compared to that of an upper branch solution. Further, the existence of profiles of two types was noticed for a specific value of the flow parameter which supports the dual solutions existence. Also, these profiles satisfy the outlying boundary conditions mentioned in (15) asymptotically which validates the computational results of the solution. Figs. 2 to 7 demonstrate that due to the rise of suction and magnetic parameters, i.e. S and M , the fluid velocity $|f'(\eta)|$ and fluid temperature $\theta(\eta)$ get decreased in the regime of boundary layer for an upper branch solution. $|f'(\eta)|$ and $\theta(\eta)$ get increased in case of a lower branch solution while the shrinking parameter $\lambda(<0)$ increases $|f'(\eta)|$ and $\theta(\eta)$ in case of an upper branch solution and reduces in a lower branch solution. Enhancement of fluid temperature was observed in the cases of both upper and lower branch solutions due to the augmenting values of R and Ec as is depicted in Figs. 8 and 9. Physically Ec represents the ratio of kinetic energy and enthalpy, which converts the kinetic energy to the form of internal energy in opposition to viscous fluid stresses. For that reason, the viscous dissipation tends to enhance fluid temperature. Figs. 10 and 11 depict that for both upper and lower branch solutions the fluid temperature $\theta(\eta)$ diminishes due to the rising values of Q and Pr which implies that heat absorption has impeding impact on fluid temperature while thermal diffusion has overturn impact on it in the regime of flow. The variations in species concentration $\phi(\eta)$ for varying M , S , λ , Sc and K are presented in Figs. 12 to 16. In these figures, dual concentration profiles $\phi(\eta)$ depict that rising values of M and S result in a net reduction in $\phi(\eta)$ in case of an upper branch solution and augment in a lower branch solution whereas the shrinking parameter $\lambda(<0)$ has a reverse impact on it. But for both

branches of solutions, $\phi(\eta)$ decreases on increasing the values of Sc and K , which demonstrates that the chemical reaction reduces the fluid concentration while mass diffusion has a reverse impact on it. Moreover, the wall velocity gradient $f''(0)$ profiles displayed in Figs. 17 and 18 quantify the impacts of suction parameter $S (>0)$ and magnetic parameter M taking into consideration the shrinking sheet ($\lambda < 0$).

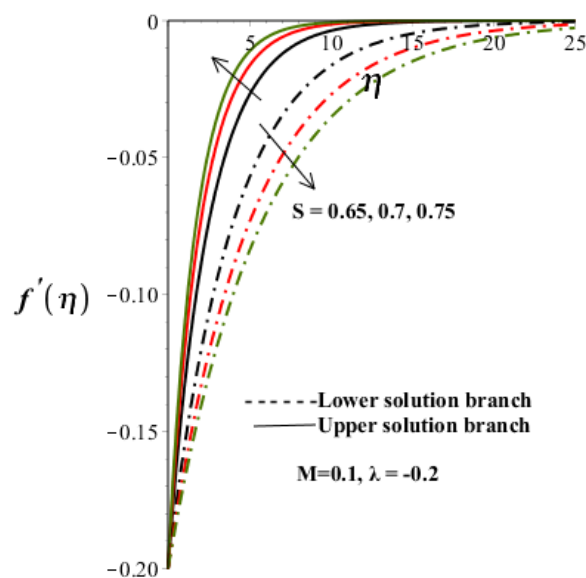


Fig. 2. Velocity profiles with increasing S .

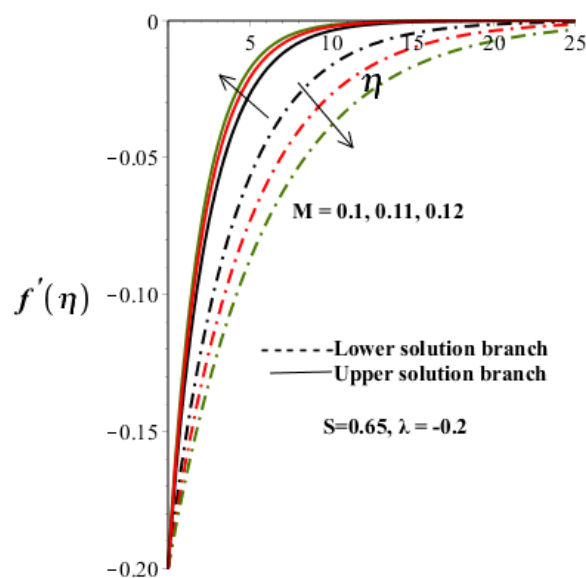


Fig. 3. Velocity profiles with increasing M .

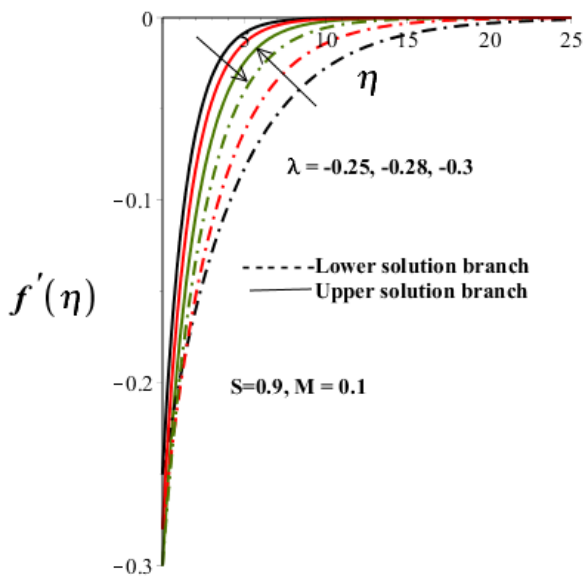


Fig. 4. Velocity profiles with increasing shrinking parameter $\lambda < 0$.

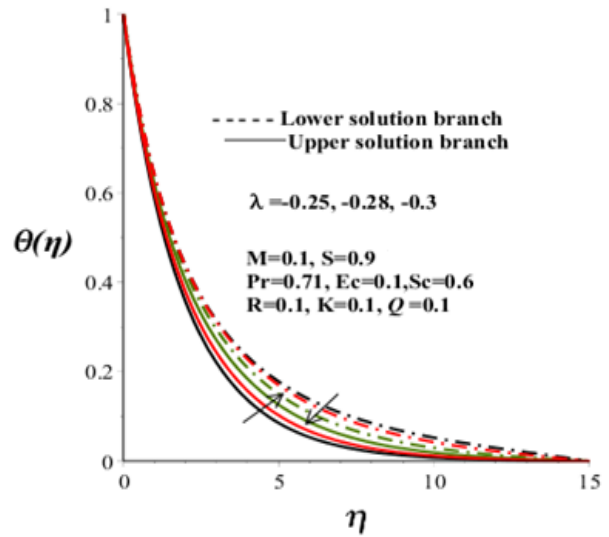


Fig. 7. Temperature profiles with increasing shrinking parameter $\lambda < 0$.

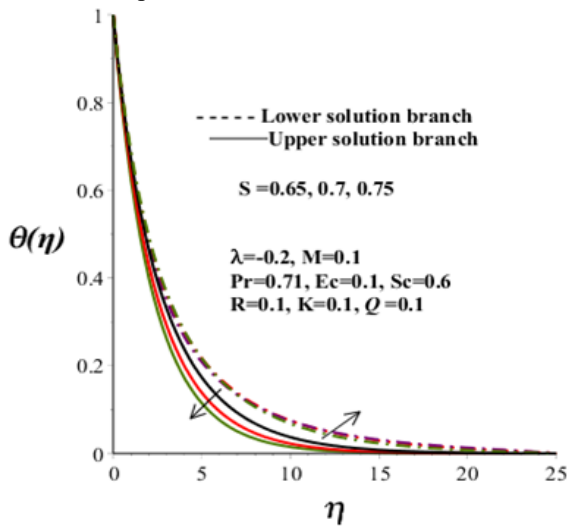


Fig. 5. Temperature profiles with increasing S.

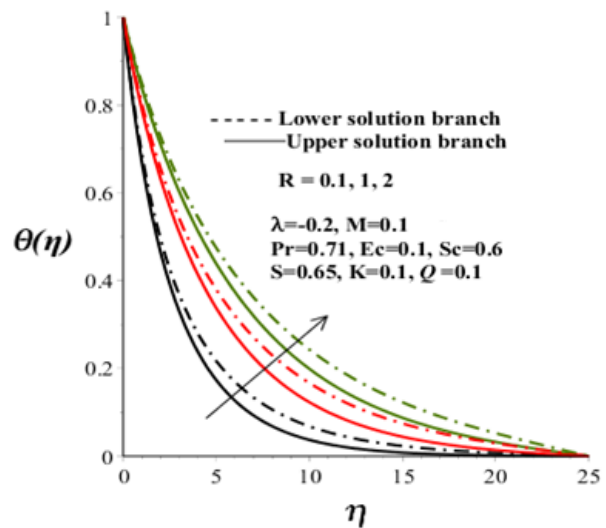


Fig. 8. Temperature profiles with increasing R.

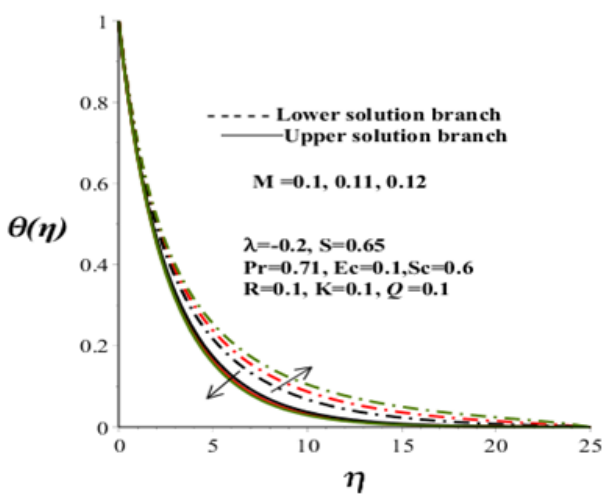


Fig. 6. Temperature profiles with increasing M.

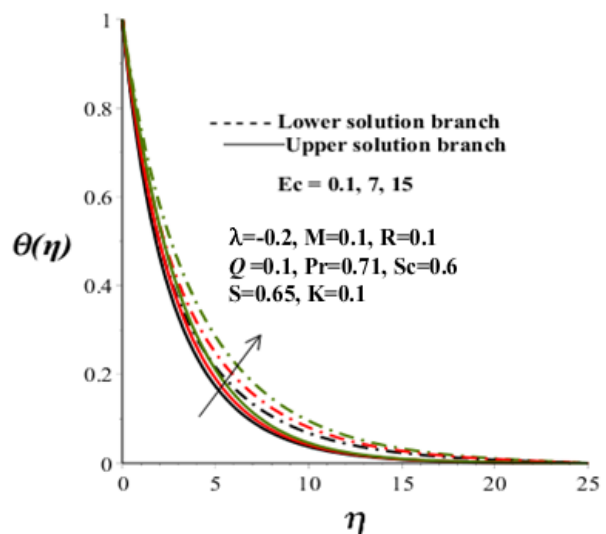


Fig. 9. Temperature profiles with increasing Ec.

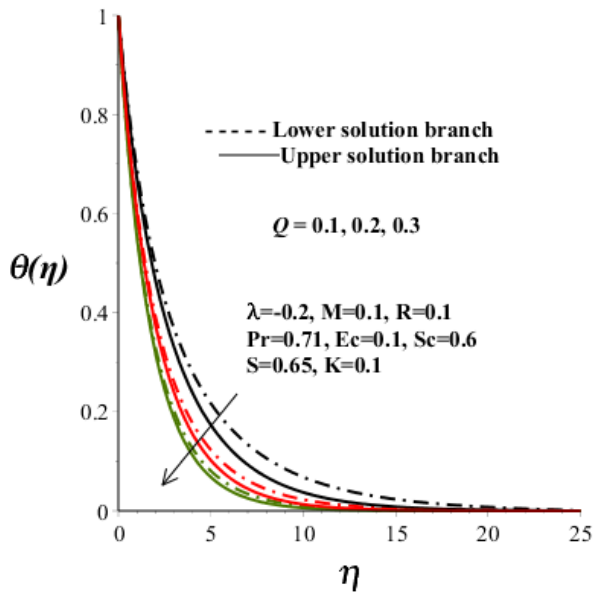


Fig. 10. Temperature profiles with increasing Q .

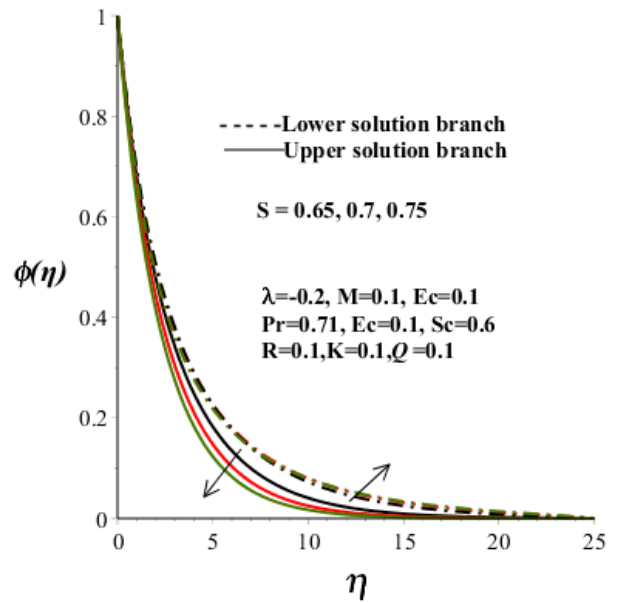


Fig. 13 Concentration profiles with increasing S .

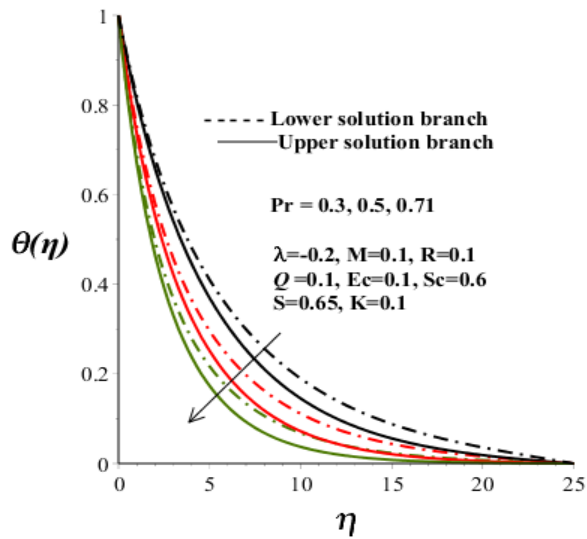


Fig. 11. Temperature profiles with increasing Pr .

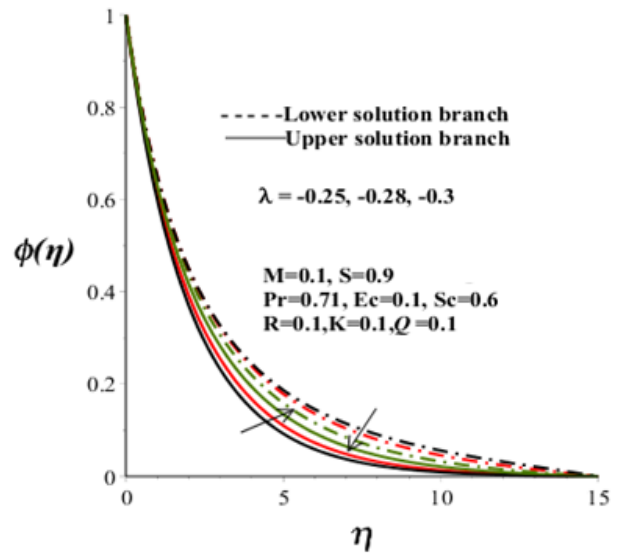


Fig. 14. Concentration profiles with increasing shrinking parameter $\lambda < 0$.

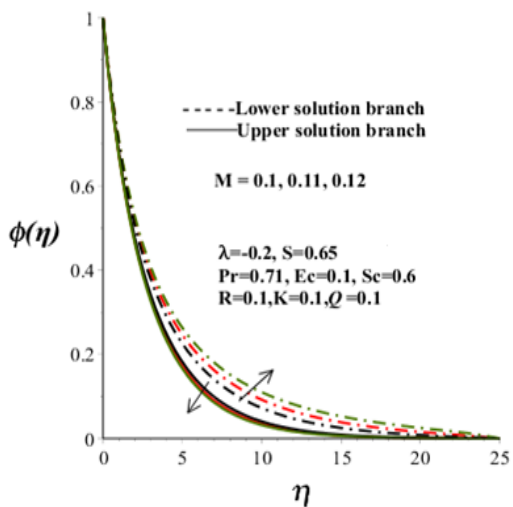


Fig. 12. Concentration profiles with increasing M .

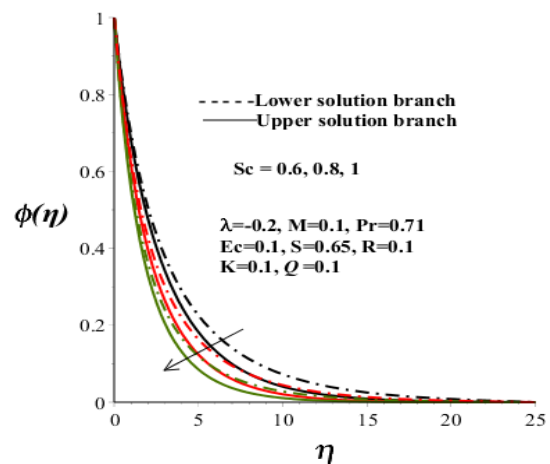


Fig. 15. Concentration profiles with increasing Sc .

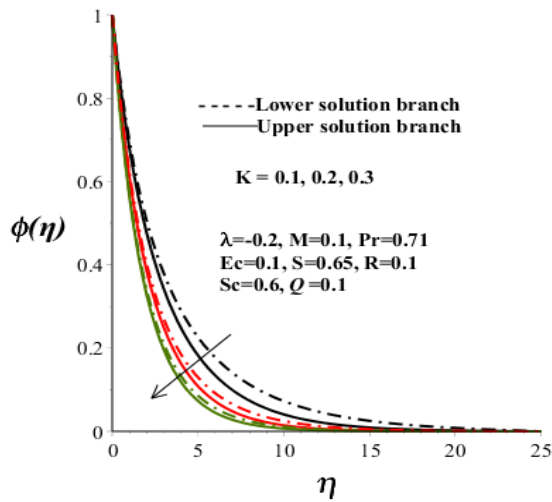


Fig. 16. Concentration profiles with increasing K .

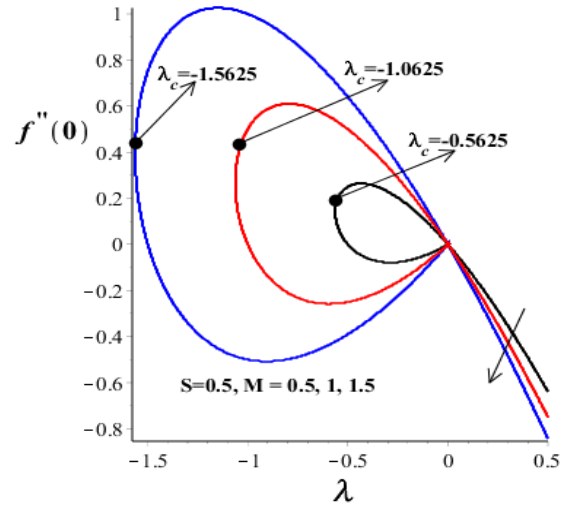


Fig. 18. Variation of $f''(0)$ with increasing M and λ .

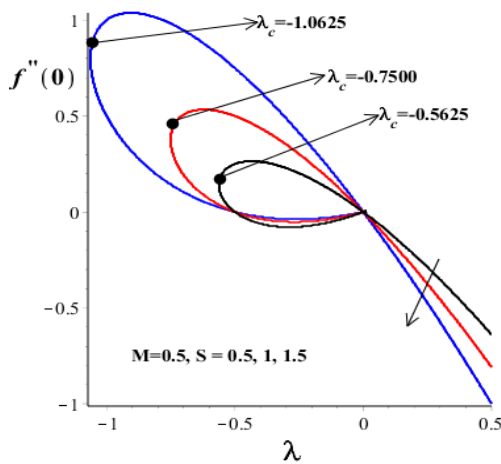


Fig. 17. Variation of $f''(0)$ with increasing S and λ .

Table 1. Computations showing the critical values of the shrinking parameter λ_c for different values of M and S .

M	S	λ_c
0.5	0.1	-0.5025
0.5	0.5	-0.5625
0.5	1	-0.7500
0.5	2	-1.5000
1	0.1	-1.0025
1	0.5	-1.0625
1	1	-1.2500
1	2	-2.0000

Table 2. Computations showing the smallest eigenvalues ξ_1 at various values of the shrinking sheet parameter ($\lambda < 0$)

M	S	λ	ξ_1 (Upper branch)	ξ_1 (Lower branch)
0.7	1	-0.4	0.8738795538	-0.442442016
0.7	1	-0.5	0.8168841346	-0.485765277
0.7	1	-0.6	0.7468719153	-0.500942232
0.7	1.2	-0.4	0.9804155402	-0.444083502
0.7	1.2	-0.5	0.9266000714	-0.500599337
0.7	1.2	-0.6	0.8647294919	-0.533302779
0.72	1	-0.4	0.8962607582	-0.448818328
0.72	1	-0.5	0.8406711179	-0.494098385
0.72	1	-0.6	0.7729698714	-0.512498179
0.72	1.2	-0.4	1.0022753340	-0.448862076
0.72	1.2	-0.5	0.9494123019	-0.507306837
0.72	1.2	-0.6	0.8889867027	-0.542405698

These figures reveal the existence of a unique solution of the reported problem when $\lambda > 0$, dual (lower and upper branch) solutions when $\lambda_c < \lambda \leq 0$ and no solution for the case of $\lambda < \lambda_c$, where $\lambda_c < 0$ represents the critical value of the shrinking parameter λ beyond which no solution of the problem exists. In addition to it, the wall velocity gradient $f''(0)$ gets increased in magnitude for rising values of S and M which shows that the shear stress gets augmented at the shrinking sheet due to suction and magnetic field. The critical values of the shrinking parameter λ_c for varying values of M and S are provided in Table 1.

In order to determine the physically reliable and stable solutions, the reported eigenvalue problem was solved to obtain the smallest eigenvalue ξ_1 . The initial growth of disturbance was found for negative values of ξ_1 and the fluid flow becomes unstable whereas initial decay is observed for positive values of ξ_1 and as a result the flow becomes stable. The computations showing the smallest eigenvalue ξ_1 at numerous values of the shrinking sheet parameter ($\lambda < 0$) are shown in Table 2. The computational results of the table indicate that ξ_1 is positive for the upper branch solution whereas it is negative in the case of lower branch solution. Hence, the upper branch solution is physically reliable and stable whilst the lower branch solution is not.

From an engineering aspect, the numerical values of S_f , Nu_x and Sh_x are obtained for the different flow parameters, which are presented in Tables 3 to 5. These tables reveal that the wall velocity gradient $f''(0)$ gets increased in magnitude for increasing values of M, λ and S while the wall temperature gradient $\theta'(0)$ decreases in magnitude with the increase in either M or λ or R or Ec and it increases on increasing either S or Q or Pr .

Physically it is construed that a shear stress at the stretched sheet gets augmented due to intensification of suction, magnetic field, and velocity slip factor whereas heat transfer rate at the stretched sheet gets reduced due to velocity slip factor, magnetic field, thermal radiation, viscous and thermal diffusions where there is a reverse impact of suction and heat absorption. The mass transfer rate at the surface of a stretched sheet is enhanced due to the chemical reaction whereas it gets reduced due to the mass diffusion.

Table 3. Numerical values of the velocity wall gradient.

M	λ	S	$-f''(0)$
0.05			4.416576
0.2			4.467439
0.6			4.598301
	-1.1		3.722558
	-1.3		4.467439
	-1.5		5.231191
		2.5	3.899999
		3.0	4.467439
		3.5	5.051801

VALIDATION OF THE NUMERICAL ALGORITHM

To justify the numerical algorithm used in the present study, we have presented a comparison of Nusselt number in the limiting sense with those of Yasin *et al.* [37]. This comparison portrays an excellent agreement of our results, as is evident from Table 6. This validates the implemented numerical algorithm of the present study along with the correctness of the obtained results.

Table 4. Numerical values of the temperature wall gradient.

M	λ	S	R	Ec	Q	Pr	$-\theta'(0)$
0.05							2.044389
0.2							2.043783
0.6							2.042221
	-1.5						2.062335
	-1.3						2.043783
	-1.1						2.024837
		2.5					1.753439
		3.0					2.043783
		3.5					2.338760
			0.1				2.043783
			0.3				1.668829
			0.5				1.412152
				0.1			2.043783
				0.3			2.018168
				0.5			1.992553
					0.1		2.043783
					1.1		2.301413
					2.1		2.516904
						0.3	0.896613
						0.5	1.460278
						0.71	2.043783

Table 5. Numerical values of the concentration wall gradient.

Sc	K	$-\phi'(0)$
0.6		2.081344
0.8		2.711802
1.0		3.336434
	0.25	3.266926
	0.5	3.336434
	0.75	3.403398

Table 6. Numerical values of Nusselt number when $M = 0.2$, $\lambda = -1.3$, $S = 3$, $Q = 0.1$, $Pr = 0.71$ and $Ec = 0$

R	Present work	Yasin <i>et al.</i> [37]
0	-2.319237	-2.31923
0.1	-2.056590	-2.05659
0.5	-1.420937	-1.42093

CONCLUSIONS

The numerical computations of a two-dimensional steady MHD heat and mass transfer boundary layer flow of an incompressible, optically thick radiative, heat absorbing, electrically conducting viscous fluid driven by a stretched/shrinking sheet in the presence of a homogeneous chemical reaction were performed to quantify the impacts of relevant flow parameters. The results revealed the existence of dual solutions. For the stretching sheet a unique solution was found whilst a dual solution was accounted for the shrinking sheet. The stability analysis conferred that an upper branch solution is physically reliable and stable whereas a lower branch solution is not. The stretching/shrinking parameter range is widened due to suction and magnetic field for which the solution exists. For a physically reliable solution, the shear stress at a stretched/shrinking sheet gets augmented owing to suction and magnetic field.

Conflict of interest: *There is no conflict of interest of authors with any researcher doing research in this area.*

REFERENCES

1. K. B. Pavlov, *Magnetohydrodynamics*, **10**, 507 (1974).
2. A. Chakrabarti, A. S. Gupta, *Quart. Appl. Math.*, **37**, 73 (1979).
3. M. Q. Al-Odat, R. A. Damseh, T A Al-Azab, *Int. J. Appl. Mech. Eng.*, **11**, 289 (2006).
4. A. Ishak, R. Nazar, I. Pop, *Nonlinear Anal.: Real World Applications*, **10**, 2909 (2009).
5. O. D. Makinde, W. A. Khan, Z. H. Khan, *Int. J. Heat Mass Transfer*, **62**, 526 (2013).
6. T. Hayat, S. A. Shehzad, A. Alsaedi, *J. Aerospace Eng.*, **27**, 1 (2014).
7. Y. Khan, *Sci. Iran. B*, **24**, 2466 (2017).
8. E. M. A. Elbashbeshy, *Arch. Mech.*, **53**, 643 (2001).
9. E. M. A. Elbashbeshy, M. A. A. Bazid, *Appl. Math. Comp.*, **138**, 239 (2003).
10. E. M. A. Eldahab, M. A. E. Aziz, *Int. J. Thermal Sci.*, **43**, 709 (2004).
11. O. D. Makinde, W. A. Khan, J. R. Culham, *Int. J. Heat Mass Transfer*, **93**, 595 (2016).
12. O. D. Makinde, F. Mabood, W. A. Khan, M. S. Tshela, *J. Molecular Liquids*, **219**, 624 (2016).
13. O. D. Makinde, K. G. Kumar, S. Manjunatha, B. J. Gireesha, *Defect Diff. Forum*, **378**, 125 (2017).
14. O. D. Makinde, I. L. Animasaun, *Int. J. Ther. Sci.*, **109**, 159 (2016).
15. O. D. Makinde, *Z. Naturforsch.*, **67**, 239 (2012).
16. O. D. Makinde, *Meccanica*, **47**, 1173 (2012).
17. N. Ali, S. U. Khan, Z. Abbas, M. Sazid, *J. Braz. Soc. Mech. Sci. & Eng.*, **38**, 2533 (2017).
18. K. Vajravelu, A. Hadjinicolaou, *Int. Comm. Heat Mass Transfer*, **20**, 417 (1993).
19. M. K. Partha, P. V. S. N. Murthy, G. P. Rajasekhar, *Heat Mass Transfer*, **41**, 360 (2005).
20. R. Cortell, *Phys. Letters A*, **372**, 631 (2008).
21. E. M. A. Aziz, *Canadian J. Phys.*, **87**, 359 (2009).
22. D. S. P. Anjali, B. Ganga, *Nonlinear Anal: Mod. Control*, **14**, 303 (2009).
23. D. Pal, *Appl. Math. Comp.*, **217**, 2356 (2010).
24. G. S. Seth, J. K. Singh, *Appl. Math. Mod.*, **40**, 2783 (2016).
25. G. S. Seth, S. Sarkar, O. D. Makinde, *J. Mech.*, **32**, 613 (2016).
26. G. S. Seth, R. Sharma, M. K. Mishra, A. J. Chamkha, *Eng. Comp.*, **34**, 603 (2017).
27. G. S. Seth, R. Tripathi, M. K. Mishra, *Appl. Math. Mech. –Eng. Ed.*, **38**, 1613 (2017).
28. J. Zucco, S. Ahmed, *Appl. Math. Mech. –Eng. Ed.*, **31**, 1217 (2010).
29. R. Nandkeoylyar, M. Das, P. Sibanda, *Math. Prob. Eng.*, **2013**, 1 (2013).
30. A. O. Ajibade, A. M. Umar, *Int. J. Energy Tech.*, **6**, 1 (2014).
31. M. M. Rashidi, E. Momoniat, M. Ferdows, A. Basiriparsa, *Math. Prob. Eng.*, **2014**, 1 (2014).
32. M. Ganapathirao, R. Ravindran, E. Momoniat, *Heat Mass Transfer*, **51**, 289 (2015).
33. M. Sheikh, Z. Abbas, *J. Magn. Magn. Mater.*, **396**, 204 (2015).
34. N. Freidoonimehr, M. M. Rashidi, B. Jalilpour, *J. Braz. Soc. Mech. Sci. & Eng.*, **38**, 1999 (2016).
35. S. M. Hussain, J. Jain, G. S. Seth, *Bul. Chem. Comm.*, **48**, 659 (2016).
36. S. M. Hussain, J. Jain, G. S. Seth, M. M. Rashidi, *J. Magn. Magn. Mater.*, **422**, 112 (2017).
37. M. H. Yasin, A. Ishak, I. Pop, *J. Magn. Magn. Mater.*, **407**, 235 (2016).
38. A. Raptis, *Thermal Sci.*, **15**, 849 (2011).
39. P. D. Weidman, A. M. J. Davis, *Int. J. Eng. Sci.*, **44**, 730 (2006).
40. A. Postelnicu, I. Pop, *Appl. Math. Comp.*, **217**, 4359 (2011).
41. S. D. Harris, D. B. Ingham, I. Pop, *Trans. Porous Media*, **77**, 267 (2009).

Effect of oxidative stress on angiotensin II-induced smooth muscle contractile activity of urinary bladder from fructose fed rats

T. K. Georgiev^{1*}, P. V. Hadzhibozheva¹, Y. D. Karamalakova², G. D. Nikolova², G. A. Krastev³, I. Nedevska³, R. Stojanov³, A. N. Tolekova¹, V. G. Gadjeva²

¹Department of Physiology, Pathophysiology and Pharmacology, Medical Faculty, Trakia University, 11 Armeiska Str., Stara Zagora 6000, Bulgaria

²Department of Chemistry and Biochemistry, Medical Faculty, Trakia University, 11 Armeiska Str., Stara Zagora 6000, Bulgaria

³Medical Faculty, Trakia University, 11 Armeiska Str., Stara Zagora 6000, Bulgaria

Received: July 07, 2019; Revised: August 30, 2019

The persistent hyperglycemia in the diabetes and metabolic syndrome causes a generation of reactive oxygen species (ROS) and can seriously violate the oxidative homeostasis. This could affect the oxidative sensitive signal transduction pathways, thus contributing to the pathogenesis of some later complications as is the smooth muscle dysfunction. The purpose of this study was to examine the effects of fructose intake on the oxidative homeostasis and on Angiotensin II (AngII) – induced motility of the urinary bladder. Mature Wistar rats were randomly divided into two groups (9 rats per group): control group (drinking tap water) and fructose-drinking group (15% fructose, dissolved in tap water). The duration of the experiment was 12 weeks. In the end of the experimental period, strips from urinary bladder were prepared and influenced by AngII. The curves of contractions were analyzed and the parameters of the contractile process were calculated. Detection of the oxidative status was performed by the evaluation of ascorbate radicals, ROS production and lipid peroxidation in tissue homogenates from liver, kidneys and blood. The plasma glucose and some parameters of lipid metabolism were registered. The developed metabolic disturbances decreased force parameters, changed the time profile characteristics, and reduced the speed of AngII-stimulated urinary bladder contraction. The oxidative imbalance was clearly demonstrated by the elevated levels of NO• and reactive oxygen radicals. Metabolic and oxidative disturbances as a result of fructose-fed diet modified the smooth muscle contractile activity and led to a smooth muscle dysfunction.

Keywords: Angiotensin II, fructose, oxidative imbalance, urinary bladder

INTRODUCTION

The metabolic syndrome (MetS) is a cluster of clinical and biochemical features that include abdominal obesity, insulin resistance and dyslipidemia. It is well known that MetS is associated with the increased risk of developing type 2 diabetes (T2D) [1]. Nowadays, the growing incidence of disorders in many smooth muscle organs is frequently observed in patients suffering from T2D and MetS. The lower urinary tract symptoms (LUTS) are among the first significant complications connected with the progression of the mentioned diseases [2]. LUTS are found to be common and chronic, with over 50% of the patients suffering from some form of urinary bladder dysfunction (urinary incontinence, detrusor underactivity or detrusor overactivity, etc.) [2, 3]. The changes in the bladder contractility during T2D may be due to a variety of factors, including alterations in innervation, changes in signaling between urothelium and smooth muscle or within the smooth muscle itself [2]. Interestingly, MetS is considered as an independent risk factor of bladder

dysfunction.

According to Lee [3], LUTS are positively associated with MetS with or without diabetes. This raises the question for the role of the persistent hyperglycemia and the other biochemical features as the underlying factors for the development of LUTS even before the actual manifestation of the diabetes. The persistent hyperglycemia causes a generation of reactive oxygen species (ROS) and can seriously violate the oxidative homeostasis. Oxidative stress (OS) is defined as an imbalance between ROS production and the antioxidant activity in cell and plasma, resulting in accumulation of oxidative products. The role of OS in many pathological conditions such as MetS and diabetes is well-recognized [4, 5]. The excess accumulation of oxidative products could affect the oxidative sensitive signal transduction pathways, thus contributing to the pathogenesis of the metabolic disorders as is the smooth muscle dysfunction. On the other hand, the metabolic disturbances are connected with the activity of circulated and local rennin–angiotensin systems (RAS) which are one of the main regulators of

* To whom all correspondence should be sent:

E-mail: phript@gmail.com

smooth muscle tone and contractility. As a main effector of RAS, Angiotensin II (AngII) has various actions, many of them affecting the activity of the visceral smooth muscles of the urogenital tract [6]. Moreover, a crosstalk between AngII and the insulin resistance [1, 7], as well as RAS and the lipid metabolism [8] has been reported. The established role of RAS in diabetes and its interaction with insulin signaling and some other aspects of metabolism [9], focused our interest towards the effects of AngII on diabetic visceral smooth muscles. Despite the observed development of diabetic smooth muscle dysfunction in a number of organs, the information about how MetS and T2D change urinary bladder response to Ang II is still insufficient.

The purpose of this study was to examine the effects of the fructose diet on the oxidative metabolic homeostasis and on Ang II – induced motility of the urinary bladder of Wistar rats.

EXPERIMENTAL

Animals and sample preparation

All of the experiments were carried out according to the Guide for the Care and Use of Laboratory Animals and the guidelines of the Council Directive 2010/63/EU of September 22, 2010 on the protection of animals used for scientific purposes. The animal experiments were approved by the Commission of Ethics at the Medical Faculty of Trakia University, Stara Zagora.

Mature male Wistar rats, weighing 250-300 g, housed in polycarbonate wire floor cages in controlled conditions (12 h light/dark cycles), temperature of 18–23°C and humidity of 40–60%, were divided into two groups (9 rats per group): control group (healthy animals) and fructose group (animals drinking 15% fructose dissolved in tap water and injected after 14 days with streptozotocin 20 mg/kg i.p.). The duration of the experiment was 12 weeks. At the end of the experimental period the animals were anesthetized with Nembutal 50 mg/kg i.p. and exsanguinated. Fresh blood (8-10 ml) was collected directly from the heart in cold EDTA-containers (5 ml Monovette, Germany). After centrifugation of the blood (4000 rpm at 4°C for 10 min), several samples of plasma (200 µl) from each animal were stored at 4°C until further assay was done. The liver and kidneys were immediately isolated and washed in cold saline (4°C). After homogenization and addition of solvents the samples were centrifuged at 4000 rpm at 4°C for 10 min and 300 µl of supernatant from each sample were stored at -4°C until further assay was done. The urinary bladder was dissected out and

transferred immediately in cold Krebs solution (3°C). The composition of Krebs solution, the preparation of the urinary bladder strips and the recording of mechanical activity were as it was previously described [10].

Chemicals and drugs

AngII (Sigma-Aldrich, Germany) was solubilized in bidistilled water. Streptozotocin (Sigma-Aldrich, Germany) was dissolved in cold 0.1 M citrate buffer, pH 4.5. Dimethyl sulfoxide (DMSO), N-tert-butyl-alpha-phenylnitron (PBN), 2-(4-carboxyphenyl)-4,4,5,5-tetra-methylimidazole-1-oxyl-3-oxide (Carboxy-PTIO.K), PBS and all reagents for the preparation of Krebs solution were purchased from Sigma-Aldrich Chemie GmbH, Germany. All other chemicals used in this study were of analytical grade.

Biochemical and EPR analyses

The biochemical analyses were performed on a UV-VIS spectrophotometer-400 (THERMO Sci., RS232C, Stratagene, USA). Total cholesterol and triglycerides were estimated using a commercially available diagnostic kit (AM- 2035- KA, 2017). Blood glucose levels were measured by Medisign mm 810 glucometer (Empecs Medical Device Co. Ltd., China). The electron paramagnetic (EPR) measurements were performed on an X-band EMXmicro spectrometer (Bruker, Germany) with settings: 3505 g centerfield, 6.42 mW microwave power, 5 g modulated amplitude, 1-5 scans. All experiments were made in triplicate.

Estimation of plasma lipid peroxidation

The method of estimation of lipid peroxidation of thiobarbituric acid (TBA), which measures malondialdehyde (MDA)-reactive products, was used [11]. In brief, 0.5 mg of fresh spleen-tissues, 1 ml of physiological solution, and 1 ml of 25% trichloroacetic acid were mixed and centrifuged at 7,000 rpm for 20 min. 2 ml of protein-free supernatant with 0.5 ml of 1% TBA (prepared in 0.025 M NaOH) were added to the reaction mixture. The resultant mixture was then subjected to 95°C in a water bath for 1 h. A pink-coloured chromogen complex was formed, readable at 532 nm.

Estimation of plasma antioxidant enzymes

The activities of superoxide dismutase (SOD) and catalase (CAT) were determined using the method described by Sun *et al.* [12] and by Aebi [13], respectively.

Estimation of plasma EPR ex vivo evaluation of nitric (NO•) radicals

Plasma NO• radicals were studied by the methods of Yoshioka *et al.* [14] and Yokoyama *et al.* [15], adapted for EPR estimation of the spin-adduct formed between carboxy-Ptio.K and generated radicals. EPR settings were as follows: 3505 G centerfield, 6.42 mW microwave power, 5G modulation amplitude, 75G sweep width, 2.5×10² gain, 40.96 ms time constant, 60.42 s sweep time, 1 scan per sample.

Estimation of plasma EPR ex vivo evaluation of ascorbate radicals (Asc•)

The Asc• levels in organ homogenates were studied according to Buettner and Jurkiewicz [16] with slight modifications, adapted for EPR estimation. EPR settings were as follows: center field 3505 G; sweep width 30 G; microwave power 12.70 mW; receiver gain 1×10⁴; modulation amplitude 5.00 G; time constant 327.68 ms; sweep time 82.94 s; 1 scan per sample.

Estimation of cellular ex vivo evaluation of ROS production

Liver and kidneys tissue homogenates (100 mg) and 100 µl of plasma were homogenized with 900 µl of 50 mM spin-trap PBN dissolved in DMSO using sonication at one cycle for 2 min. After 5 min of ice incubation, the suspension was centrifuged at 4000 rpm at 4°C for 10 min. Supernatants were transferred into cold Eppendorf tubes and immediately analysed. The real-time formation of ROS production in the supernatant was estimated according to methods described earlier [17] with some modifications [18]. EPR settings were as follows: center field 3503 G; sweep width 10.0 G; microwave power 12.83 mW; receiver gain 1×10⁶; modulation amplitude 5.00 G; time constant 327.68 ms; sweep time 81.92 s, 5 scans per sample.

Analysis of the contractile activity

After the equilibration, the preparations from urinary bladder (n=9 for each group) were influenced by AngII (1 µmol). The mechanical activity was digitized and recorded using ISOSYS-Advanced 1.0 software (Experimetria, Ltd., Hungary). The conversion of the data for later analysis was performed with KORELIA-Processing and KORELIA-Dynamics programs [19, 20]. The duration of the interval for analysis of the tonic contraction was defined from the beginning of the contraction, until the amplitude fell to 50%. The amplitude of contraction, the integrated force of contraction (AUC) and following time-parameters [21]: half-contraction time (T_{hc}); contraction time (T_c); half-relaxation time (T_{hc}); contraction plus half-relaxation time (T_{chr}), were examined.

Statistical analysis

EPR spectral processing was performed using Bruker Win-EPR and SimFonia Software. Statistical analysis was performed with Statistica 8.0, Stasoft, Inc., one-way ANOVA, Student *t*-test to determine significant differences among data groups. The results were expressed as mean ± standard error (SE). A value of *P* < 0.05 was considered to be statistically significant.

RESULTS

Biochemical analysis

As it can be seen from Table 1, the levels of blood glucose were significantly increased in the experimental group compared to the controls. The same tendency was observed about the levels of plasma lipids. There were significant differences between the two groups with exception of the levels of total cholesterol. The most significant difference was observed in the levels of triglycerides in the fructose group, which concentration was twice as high compared to controls (Table 1).

Table 1. Plasma glucose and lipids concentration.

Parameter	Control group (n=9)	Fructose group (n=9)
Glucose (mmol/l)	9.84±0.91	12.59±0.62*
Total Cholesterol (mmol/l)	1.33±0.04	1.24±0.08
LDL (mmol/l)	0.43±0.04	0.28±0.05*
HDL (mmol/l)	0.54±0.02	0.43±0.04*
Triglycerides (mmol/l)	0.81±0.06	1.73±0.36*
Total Cholesterol/ HDL ratio	2.51±0.08	2.92±0.14*
Triglycerides/ HDL ratio	1.54±0.13	3.74±0.6*

*vs controls, *p* < 0.05

Estimation of the oxidative stress

The levels of oxidative stress (Table 2) were measured by investigation of the antioxidant activity of SOD and CAT, the concentration of MDA and EPR analysis of free radicals. In regard to the antioxidant activity of SOD and CAT there were observed no statistically significant differences between the two investigated groups. On the other hand, there was a significant decrease in the levels of MDA in the plasma, liver and kidneys in the experimental group compared to the control one. The EPR analysis of free radicals demonstrated big differences in both plasma and tissue homogenates. Measured Asc• in all samples were significantly decreased in the experimental group compared to control. Exactly the opposite statistically significant differences were observed in the levels of NO•. Concerning the levels of ROS in plasma, there were no statistical differences between both groups. The levels of ROS were significantly decreased in the livers from the experimental group, while in kidneys there was a significant increase compared to the control group.

Smooth muscle contraction

Fig.1 represents a graphical visualization of the contractile process of AngII-induced urinary bladder activity in the different groups. The amplitude of the contractions of the bladders from the fructose group was significantly lower than that of the control one (0.98±0.08 g vs. 1.74±0.22 g).

There was no significant difference between both investigated groups regarding AUC (106.53±10.7 gs vs. 121.13±13.7gs). The investigation of time parameters demonstrated a significant delay in developing urinary bladder contraction of the animals from the fructose group (T_{hc} – 24.9±4.6 s vs. 13.3±1.7 s; T_c – 60.6±10.4 s vs. 33±3.2 s; T_{chr} – 134.3±23.4 s vs. 83±7 s).

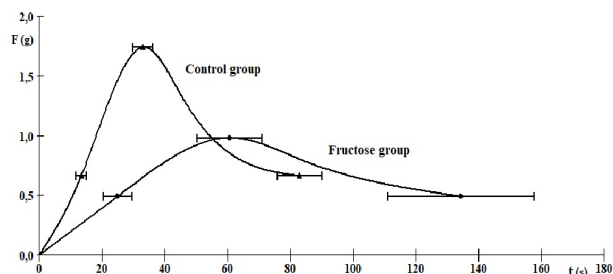


Fig. 1. Graphical visualization of the contractile process of Ang II-induced urinary bladder activity in the different groups (control and fructose, n=9).

DISCUSSION

The goal of the present study was to examine the effects of the fructose diet on the oxidative metabolic homeostasis and on AngII – induced urinary bladder motility. In our experiment, the fructose drinking rats showed a statistically significant worsening of both glucose and lipid profile.

Table 2. Levels of oxidative stress in plasma and tissue homogenates.

\		Controls (n=9)	Fructose group(n=9)
SOD (IU/gHb)	Plasma	467.1±32	392.3±56
	Liver	660.8±48	603.5±20
	Kidneys	479.7±28	507.8±18
CAT (IU/gHb)	Plasma	63845±4852	72364±6123
	Liver	53775±4823	63840±5982
	Kidneys	74849±5584	67977±5122
MDA (µmol/l)	Plasma	3.06±0.52	1.41±0.2*
	Liver	2.76±0.35	1.58±0.18*
	Kidneys	3.32±0.46	1.00±0.12*
ROS (Arb. Units)	Plasma	18.12±2.05	17.19±1.98
	Liver	18.43±1.82	11.64±1.3*
	Kidneys	17.96±1.96	28.59±3.2*
NO• (Arb. Units)	Plasma	7.01±0.8	9.17±0.95*
	Liver	6.66±1.1	13.74±2.1*
	Kidneys	12.28±2.3	16.1±2.5
Asc• (Arb. Units)	Plasma	0.74±0.08	0.07±0.01*
	Liver	0.61±0.08	0.05±0.01*
	Kidneys	2.62±0.18	0.12±0.01*

*vs controls, p < 0.05

SOD – superoxide dismutase; CAT – catalase; MDA – malondialdehyde; ROS – reactive oxygen species; NO• – nitric radicals; Asc• – ascorbate radicals.

In this regard, particularly indicative were the total cholesterol/HDL-ratio and triglycerides/HDL-ratio, which are recently considered to be more significant markers for metabolic risk than the absolute values themselves [22]. At the same time, the low levels of MDA in the fructose group are impressive, and are not in accordance with the classical conception for the oxidative stress constellation (high levels of lipid peroxidation and ROS). In the studies of some authors [23, 24], although not statistically significant, inversely proportional relationship between the high triglyceride levels and the low MDA concentration was reported. In our study, the lower MDA levels in the plasma and tissue homogenates of fructose drinking rats are probably associated with the 2-fold higher triglyceride levels in the experimental group, rather than directly indicating the lipid peroxidation level. As more specific and more accurate, EPR methods reliably reveal the levels of oxidative stress. In these tests, the levels of Asc• radicals were statistically lower in all of the samples from the experimental group, thus clearly showing the depletion of the stores for ascorbic acid. On the other hand, ROS and NO• were significantly increased in most of the samples, which indicates the presence of oxidative stress in the experimental group. These results are in agreement with the majority of the authors describing the primary role of OS in the development of MetS and T2D [4, 5].

OS causes alterations on proteins, lipids and DNA, thus leading to organ dysfunction. Regarding the smooth musculature, there are controversial data about the contractility (enhanced or decreased) of the urinary bladder in diabetic animals, depending on the different design of the studies (diabetes induction methodology, used species, etc.), but the registered reduced contractility to muscarinic agonists is reported as a common result [2]. The observed and described by us reduced contractile responses to AngII are also in support to the stated above. Obviously, the metabolic disturbances and OS seriously affect the reaction of the urinary bladder to contractile agents. The excessive formation of ROS, which leads to OS and disrupted cell calcium signaling machinery, is probably the main etiological factor for this disturbance [3]. According to Wang *et al.* [25], the accumulation of glycation end products is likely to play a central role in the development of the bladder dysfunction. Moreover, many diabetic patients with bladder dysfunction have suffered from metabolic perturbations [3]. Many authors conclude that there is a relationship between the

duration of diabetes and the bladder dysfunction [3, 25, 26]. With longer periods of diabetes-induced hyperglycemia the bladder characteristics progress toward decompensation and underactivity. This decompensated phase is probably a result from the polyuria and the hyperglycemic-induced metabolic disturbances and OS [25, 27].

In a conclusion, in our study the oxidative imbalance was clearly demonstrated by the elevated levels of NO• and reactive oxygen radicals. Metabolic and oxidative disturbances as a result of fructose diet modified the smooth muscle contractile activity and led to a urinary bladder dysfunction.

Disclosure of interest: The authors declare that they have no conflict of interest.

REFERENCES

1. L. Tran, V. Yuen, J. McNeill, *Mol. Cell Biochem.*, **332** (1-2), 145 (2009).
2. D. Kendig, H. Ets, R. Moreland, *Am. J. Physiol. Renal Physiol.*, **310**, 909 (2016).
3. W. Lee, *JTUA*, **20**, 155 (2009).
4. E. Henriksen, M. Diamond-Stanic, E. Marchionne, *Free Radic. Biol. Med.*, **51** (5), 993 (2011).
5. I. Lozano, R. Van der Werf, W. Bietiger, E. Seyfritz, C. Peronet, M. Pinget, N. Jeandidier, E. Maillard, E. Marchioni, S. Sigrist, S. Dal, *Nutr. Metab. Lond.*, **13**, 15 (2016).
6. H. Phull, M. Salkini, C. Escobar, T. Purves, C. Comiter, *Neurourol. Urodyn.*, **26** (1), 81 (2007).
7. F. Andreozzi, E. Laratta, A. Sciacqua, F. Perticone, G. Sesti, *Circ. Res.*, **94** (9), 1211 (2004).
8. X. Yang, H. Zhao, Y. Sui, R. Ma, W. So, G. Ko, A. Kong, R. Ozaki, C. Yeung, G. Xu, P. Tong, J. Chan, *Diabetes*, **58** (7), 1518 (2009).
9. A. Ribeiro-Oliveira, A. Nogueira, R. Pereira, W. Boas, R. Dos Santos, A. Simões e Silva, *Vasc. Health Risk Manag.*, **4** (4), 787 (2008).
10. P. Hadzhibozheva, T. Georgiev, R. Kalfin, A. Tolekova, *Bulg. Chem. Comm.*, **44** (3), 252 (2012).
11. Z. Plaser, L. Cushman, B. Jonson, *Anal. Biochem.*, **16** (2), 359 (1966).
12. Y. Sun, L. Oberley, Y. Li, *Clin. Chem.*, **34** (3), 497 (1988).
13. H. Aebi, *Meth. Enzymol.*, **105**, 121 (1984).
14. T. Yoshioka, N. Iwamoto, K. Ito, *J. Am. Soc. Nephrol.*, **7** (6), 961 (1996).
15. K. Yokoyama, K. Hashiba, H. Wakabayashi, K. Hashimoto, K. Satoh, T. Kurihara, N. Motohashi, H. Sakagami, *Anticancer Res.*, **24** (6), 3917 (2004).
16. G. Buettner, B. Jurkiewicz, *Free Radic. Biol. Med.*, **14** (1), 49 (1993).
17. H. Shi, Y. Sui, X. Wang, Y. Luo, L. Ji, *Comp. Biochem. Physiol. C Toxicol. Pharmacol.*, **140** (1), 115 (2005).
18. A. Zheleva, Y. Karamalakova, G. Nikolova, R. Kumar, R. Sharma, V. Gadjeva, *Biotechnol. & Biotechnolog. Equipm.*, **26** (1), 146 (2012).

19. K. Yankov, *Trakia J. Sci.*, **8** (3), 41 (2010).
20. K. Yankov, in: Proceedings of the International Conference on Information Technologies (InfoTech-2012), R. Romanski (ed.), Technical University, Sofia, 2012, p. 114.
21. K. Yankov, in: Proceedings of the International Conference on Information Technologies (InfoTech-2011), R. Romanski (ed.), Technical University, Sofia, 2011, p. 225.
22. G. Cai, G. Shi, S. Xue, W. Lu, *Medicine*, **96** (37), E:8058 (2017).
23. O. Ogunrinola, *MOJ Toxicol.*, **1** (5), 149 (2015).
24. V. Rao, R. Kiran, *J. Cardiovasc. Dis. Res.*, **2** (1), 57 (2011).
25. Y. Wang, G. G. Deng, K. P. Davies, *Am. J. Physiol. Endocrinol. Metab.*, **311** (2), 471 (2016).
26. G. Liu, F. Daneshgari, *Chin. Med. J. (Engl.)*, **127** (7), 1357 (2014).
27. N. Xiao, Z. Wang, Y. Huang, F. Daneshgari, G. Liu, *J. Urol.*, **189** (3), 1130 (2013).

Fast-growing tree species as sugars sources

N. Yavorov*, I. Valchev

Department of Pulp, Paper and Printing Arts, University of Chemical Technology and Metallurgy, 8 St. Kliment Ohridski Blvd., 1756 Sofia, Bulgaria

Received: September 13, 2019; Accepted: October 02, 2019

The use of lignocellulosic biomass for the production of bio-based products is a worldwide tendency. The present study examines steam explosion pretreatment and subsequent enzymatic hydrolysis of different fast-growing tree species (poplar, willow, black locust, paulownia and ailanthus) to obtain sugars that can be substrate in various fermentation processes. Experimental results showed that the pretreatment of species with low wood density can be carried out under milder conditions compared to those with higher density. It was established that the efficiency of hydrolysis by a commercial cellulase complex also depends on the wood density, and the highest yield of glucose is reached from paulownia. The topochemical kinetic mechanism of cellulase hydrolysis of fast-growing tree species was established, and it was found that the activation energy and the pre-exponential factor increase with wood density decrease. The determinant for the process rate is the pre-exponential factor.

Keywords: Fast-growing tree, Lignocellulosic biomass, Steam explosion, Enzymatic hydrolysis, Fermentable sugars

INTRODUCTION

The rapid increase in energy demand and the unsustainable use of natural resources are among the major global concerns. The excessive dependency on petroleum fuel leads to various concerns regarding economics, environment and energy security. In this context, use of plant biomass is the favourable substitute to the conventional sources of energy production [1]. Lignocellulosic biomass is the most abundant source of renewable biopolymers on Earth and a promising cheap raw material for the production of fuels, chemicals and materials [2–4]. The major polymeric components in lignocellulosic biomass are: cellulose, hemicelluloses and lignin. Compositions vary for different types of biomass [5]. The conversion of lignocellulosic materials into bioproducts enables to avoid competition between their manufacturing and food production [6]. Lignocellulosic biomass broadly includes agricultural residues, forest-based plants, food wastes, agricultural by-products and purpose-grown energy crops, such as switch grass, fast-growing tree species, etc. [7]. The production of biomass from fast-growing trees for energy purposes has become a new line of agricultural production, which is defined as the agro power industry [8]. The wood biomass from plantations of fast-growing tree species, such as paulownia, poplar, black locust, eucalyptus and willow, can be an attractive alternative for bioethanol production. Fast-growing tree species grown in short-rotation plantations are a promising source of lignocellulosic biomass because of high

yield, opportunities for use on lower-quality lands and biodiversity support at the landscape level [9, 10]. Biochemical conversion of lignocellulosic biomass involves a pretreatment step to depolymerise its lignin-carbohydrates complex and subsequent enzymatic hydrolysis for releasing fermentable sugars [11]. The effective pretreatment plays a key role, since it critically influences the subsequent enzymatic hydrolysis [12]. A large number of pretreatment technologies have been developed on a wide variety of lignocellulosic materials, since individual raw materials have different physicochemical characteristics. The pretreatment methods can be classified into physical, chemical, physicochemical, biological methods and by some combinations of these processes [4, 13]. Among these methods, steam explosion (SE) is one of the most commonly used physicochemical methods for pretreatment of wood-based raw materials relying on recovering partially-degraded hemicelluloses from wood tissue by an attractive hydrolysing medium that enables a wide variety of reactions without catalyst [12, 14]. SE is a combination of physical and chemical effects, and involves exposing lignocellulosic biomass to high-pressure saturated steam at temperatures typically between 160 and 260°C for several seconds to a few minutes and then quickly reducing pressure to atmospheric condition [15–17]. This leads to disruption of the lignocellulosic complex, removal of hemicelluloses, partial removal and/or redistribution of lignin and considerable enhancement of the accessibility of the enzymes to the cellulose fibrils [18].

* To whom all correspondence should be sent:
E-mail: nyavorof@gmail.com

Several wood-based raw materials have shown positive effects on pretreatment with SE, such as poplar wood [17, 19–21], eucalyptus wood [22, 23] and spruce wood [24]. The present study aims to evaluate the processes and the potential for obtaining sugars from fast-growing tree species (poplar, willow, black locust, paulownia and ailanthus) by SE pretreatment and enzymatic hydrolysis. In order to clarify the influence of the pretreatment on enzymatic hydrolysis, the relationship between structural features and sugars yield was investigated. Additionally, the dependence of the kinetic parameters of cellulase hydrolysis on wood density of the species concerned is reported.

EXPERIMENTAL

Materials

The following fast-growing tree species were investigated: paulownia (*Paulownia elongata* S.Y. Hu (PE) and *Paulownia tomentosa* Thunb. (PT)), poplar (*Populus alba* L. (PA) and *Populus ×euramericana* (Dode) Guinier (PEA), cultivars (cvs.) 'I 214' and 'I 45 51'), willow (*Salix viminalis rubra* L. cv. 'X/3' (SVR)), black locust (*Robinia pseudoacacia* L. (RPA), cvs. 'Jáskiséri', 'Pordim' and 'Tsarevets') and ailanthus (*Ailanthus altissima* (Mill.) Swingle (AA)). The tree species were harvested and collected from the Experimental Station for Fast-growing Forest Tree Species, Svishtov, Bulgaria (43°37'N 25°21'E). Initially, they were chipped to a particle size of 20–25 mm. Chemical analyses were based on the following methods: for cellulose according to Kürschner and Hoffer [25], pentosans (TAPPI standard T 223 cm-10), lignin (TAPPI standard T 222 om-11), hot water solubility (TAPPI standard T 207 cm-08) and ash (TAPPI standard T 211 om-12). The results are reported as percentages of oven-dry weight. The wood density was determined according to DIN EN 52182 standard.

Methods

Steam explosion pretreatment. The SE pretreatment of wood chips was carried out in a 2 L stainless steel laboratory-scale system at a solid-to-liquid ratio of 1:10 (w/v). The raw materials were steamed at the desired temperature (190 and 200°C, respectively) under pressure for 10 min. Defibration of the pretreated materials was achieved by a rapid decompression. After the pretreatment, the solid and liquid fractions were separated in a cyclone. The solid fraction was washed with distilled water to remove the dissolved components. The separated

prehydrolysates were analysed for sugar composition. The effects of temperature and time on the pretreatment process were calculated based on the severity factor (Eq. 1) defined by Overend *et al.* [26].

$$\log(R_0) = \log(t \cdot \exp^{(T-100)/14.75}) \quad (1)$$

where R_0 is the severity parameter, T is the reaction temperature (°C), 100 is a reference temperature (°C), t is time (min) and 14.75 is an empirical parameter related to temperature and activation energy.

Enzymatic hydrolysis. Pretreated solids of various severity factors were enzymatically hydrolysed by the commercial complex Cellic CTec2 (produced by *Trichoderma reesei*) containing 125 FPU/g of cellulase (filter paper activity). All hydrolysis runs were carried out in polyethylene bags in a water bath at 10% solids loading (g of dry solids/volume of the hydrolysis mixture) and enzyme loading – 5% of Cellic CTec2 per g of dry pretreated substrate (approximately 6.3 FPU/g). The process was conducted at a temperature of 50°C, pH of 5.0 (according to the manufacturer's recommendations) and reaction time of 2880 min. The treatment was stopped by heating the samples at 100°C for 10 min.

HPLC analysis. The sugars (glucose, xylose and cellobiose) and furan compounds (5-hydroxymethylfurfural (5-HMF) and furfural) contents were measured on a Dionex HPLC system (Dionex Inc., CA, USA) equipped with a Shodex RI-101 RI detector (Showa Denko KK, Kawasaki, Japan), according to the National Renewable Energy Laboratory (NREL) analytical methods for biomass [27]. The separation was performed in a Hi-Plex H column, 7.7 mm × 300 mm (Agilent Technologies, USA) at 65°C with ultrapure water produced by a Simplicity® water purification system (Merck KGaA, Darmstadt, Germany) as eluent at a flow rate of 0.5 mL/min. Injected volume: 20 µL. The results were evaluated by the Chromeleon 6.80 software. The amount of sugars was calculated as a percentage (%) on a dry matter basis.

RESULTS AND DISCUSSION

Chemical composition. The broad-leaved tree species studied differ considerably in their density (Table 1). The results obtained show that the black locusts are characterized with the highest density, it being 773 kg/m³ in the case of the wood of RPA cv. 'Pordim'. Lowest is the density of the wood of PT – 240 kg/m³.

Table 1. Chemical composition and wood density

Tree species	ρ_0 (kg/m ³)	Lignin (%)	Cellulose (%)	Pentosans (%)	Ash (%)	Hot water solubility (%)
PE	311	22.03	46.42	22.47	0.42	5.86
PT	240	20.73	47.78	22.29	0.84	8.35
AA	592	20.85	48.07	25.75	0.83	5.21
SVR	420	25.38	45.05	22.25	1.38	6.15
PEA cv. 'I 214'	418	24.81	49.85	23.23	0.53	2.18
PEA cv. 'I 45 51'	400	23.93	49.24	22.03	0.57	2.39
PA	325	21.23	48.79	24.62	0.65	2.56
RPA cv. 'Pordim'	773	26.56	48.25	21.92	0.35	6.51
RPA cv. 'Jáskiséri'	720	23.41	45.78	21.90	0.52	6.85
RPA cv. 'Tsarevets'	661	23.05	48.89	22.73	0.41	4.03

The density is relatively low in the case of poplars and willows, whereas the wood of ailanthus takes an intermediate position with respect to this indicator. PEA cvs. 'I 214' and 'I 45 51', which also have the lowest percentage of substances soluble in hot water, are characterized with the highest cellulose content (49.85% and 49.24%, respectively). The presence of these substances is most often connected with the content of some low-molecular, extractive and pectic substances capable of being hydrolysed and dissolved at a temperature of up to 100°C. From Table 1 it is seen that their amount predominates in PT (8.35%). Similar results have been also reported by Balatinecz and Kretschmann [28], where holocellulose amounts in poplar wood were found to be approximately 80%, made up of 50% cellulose and 30% hemicelluloses. The total content of cellulose and pentosans in case of the fast-growing tree species studied is within 67.30% – 73.82%, it being highest in the case of ailanthus and poplars, and lowest in the case of willow that is characterised with high lignin content. The wood with highest density of RPA cv. 'Pordim' contains the highest lignin amount, and that with lowest density of PT is characterised with very low lignin content. Other visible dependences between the wood chemical composition and density cannot be found.

It is known that the chemical composition of the wood of the individual tree species varies considerably. With respect to one tree species only, there is a difference in the chemical composition which is related to a number of factors, some of which are: time of harvesting, growth conditions, tree part from which the sample for analysis is taken, etc. [29, 30].

It can be noted that the chemical composition of the wheat straw, which is the main raw material in

the production of sugars for bioethanol, is characterised with a similar cellulose (44%) and lignin (24.3%) content whereas the content of pentosans (33.5%), ash (4.6%) and substances soluble in hot water (20.7%) is considerably higher [31].

Steam explosion pretreatment. To facilitate the enzyme action into the complex lignocellulosic structure of wood biomass, a SE pretreatment was carried out. The effect of structural differences between the tree species was evaluated by applying the same pretreatment conditions. Different steam pretreatment severities ($\log R_0 = 3.65$ and 3.94 , respectively) were applied to compare the degree of hemicelluloses dissolution and recovery in a monomeric form with limited degradation of solubilised sugars to furan derivatives.

The SE pretreatment of wood chips of broad-leaved fast-growing tree species showed that the wood density has a determining effect on the pretreatment conditions. It was established that in the case of the tree species with density below 350 kg/m³, the process may be carried out at $\log R_0 = 3.65$ or lower. In the case of the tree species with higher density it is necessary to apply higher severity in order to defibre the wood in the explosion process.

The amount of the dissolved wood components in the SE pretreatment carried out at $\log R_0 = 3.94$ is lowest in the case of black locusts that are also characterized with the highest density.

The analysis of the prehydrolysates generated during the SE pretreatment showed that the monosaccharides content increases along with concomitant increase in severity of the pretreatment (Table 2).

Table 2. Yield and amount of dissolved substances after SE pretreatment

Tree species	Severity factor (R_0)	Solid recovery (%)	Glucose (%)	Xylose (%)	Cellobiose (%)	5-HMF (%)	Furfural (%)
PE	3.65	67.51	1.08	2.19	0.56	0.12	0.22
	3.94	63.02	1.95	2.86	1.02	0.29	0.35
PT	3.65	67.12	1.12	2.0	0.89	0.11	0.26
	3.94	62.74	1.98	2.81	1.16	0.33	0.37
PA	3.65	67.72	1.62	2.98	1.12	0.22	0.35
	3.94	62.31	1.87	3.65	1.31	0.36	0.49
SVR	3.65	68.81	0.71	0.97	0.13	0.09	0.17
	3.94	62.34	0.91	1.55	0.43	0.11	0.19
PEA cv. 'I 214'	3.94	63.27	1.04	2.68	0.68	0.19	0.34
PEA cv. 'I 45 51'	3.94	63.71	0.62	1.32	0.70	0.15	0.35
AA	3.94	63.33	0.93	1.85	0.66	0.08	0.18
RPA cv. 'Pordim'	3.94	66.81	1.14	2.28	0.98	0.03	0.24
RPA cv. 'Jászakiséri'	3.94	66.76	1.26	2.09	1.56	0.11	0.18
RPA cv. 'Tsarevets'	3.94	65.14	1.13	2.11	0.68	0.03	0.17

The results of HPLC also indicated the presence of a significant content of soluble oligomeric sugars. 5-HMF and furfural derived from glucose and xylose degradation, respectively, were also detected in the prehydrolysates.

The data obtained during the SE pretreatment of the wood showed that the low wood density favours the process and allows its implementation under milder conditions. In general, pretreatments at high severity $R_0 \geq 4$) showed a produced higher xylose recovery but also higher sugars degradation and inhibitors production [20].

Enzymatic hydrolysis. The effect of the pretreatment in the case of the examined fast-growing tree species on the efficiency of the subsequent enzymatic hydrolysis was studied. The generated hydrolysates were analysed by means of HPLC analysis to establish their composition. The obtained results about the yield of monosaccharides – glucose and xylose, are summarized and presented in Table 3. The results showed that the highest yield of glucose is reached after 2880 min in the case of PT that is characterized with the lowest density. Relatively good results were also obtained in the

Table 3. Yield of sugars after enzymatic hydrolysis of SE pretreated wood

Tree species	Severity factor (R_0)	Glucose (%)	Xylose (%)
PE	3.65	38.98	2.57
	3.94	39.31	2.99
PT	3.65	44.13	2.61
	3.94	44.63	2.86
PA	3.65	35.92	2.34
	3.94	36.94	2.42
SVR	3.65	26.45	2.84
	3.94	30.06	3.19
PEA cv. 'I 214'	3.94	33.78	1.92
PEA cv. 'I 45 51'	3.94	33.16	2.92
AA	3.94	33.52	3.26
RPA cv. 'Pordim'	3.94	27.51	3.66
RPA cv. 'Jászakiséri'	3.94	32.34	3.29
RPA cv. 'Tsarevets'	3.94	34.91	3.08

case of the tree species PE and PA and RPA cv. 'Tsarevets'. The glucose yield in the case of these tree species is comparable with and higher than that after enzymatic hydrolysis of wheat straw [32]. It was established that the efficiency of the enzymatic hydrolysis is lower in RPA cv. 'Pordim' that is characterized with the highest density and lignin content. The remaining tree species take an intermediate position, not yielding considerably to wheat straw. The xylose yield after the enzymatic hydrolysis is within 1.92% to 3.66% and practically does not depend on the density of the tree species. It was also established that the severity of the SE pretreatment does not exercise considerable effect on the efficiency of the enzymatic hydrolysis in the case of the tree species with low density Paulownia and PA, which is yet another confirmation of the possibility for implementation of the process under milder conditions. The results obtained are an indicator of the high potential of the fast-growing tree species with low density as a raw material for production of sugars.

It was established that the kinetics of the cellulosic action in all fast-growing tree species is most exactly described by the Prout-Tompkins topochemical equation [33]. The applicability of a topochemical kinetic mechanism is an indicator of the zonal course of the process that is characterized with opening of new active centres in case of diffusion limitations. The fibrous structure of the wood biomass is determining for the applicability of the topochemical kinetic mechanism observed. Unlike wood, the kinetics of the cellulosic action in wheat straw is most exactly described by the exponential kinetic equation [31]. The predominant content of non-fibrous structures in wheat straw is probably determining for the observed difference and for the applicability of the exponential kinetic model valid for processes taking place at heterogeneous surfaces [34]. During the study of the effect of the properties of the fast-growing tree species on the kinetics of the enzymatic action, well expressed linear dependences (Eqs. 2 and 3) between the wood density, on the one hand, and the activation energy and the pre-exponential factor, on the other hand, were established (Fig. 1).

$$E = E^0 - m \cdot \rho \quad (2)$$

$$\ln \lambda = \ln \lambda^0 - n \cdot \rho \quad (3)$$

where: E^0 , m , $\ln \lambda^0$ and n are empirical constants.

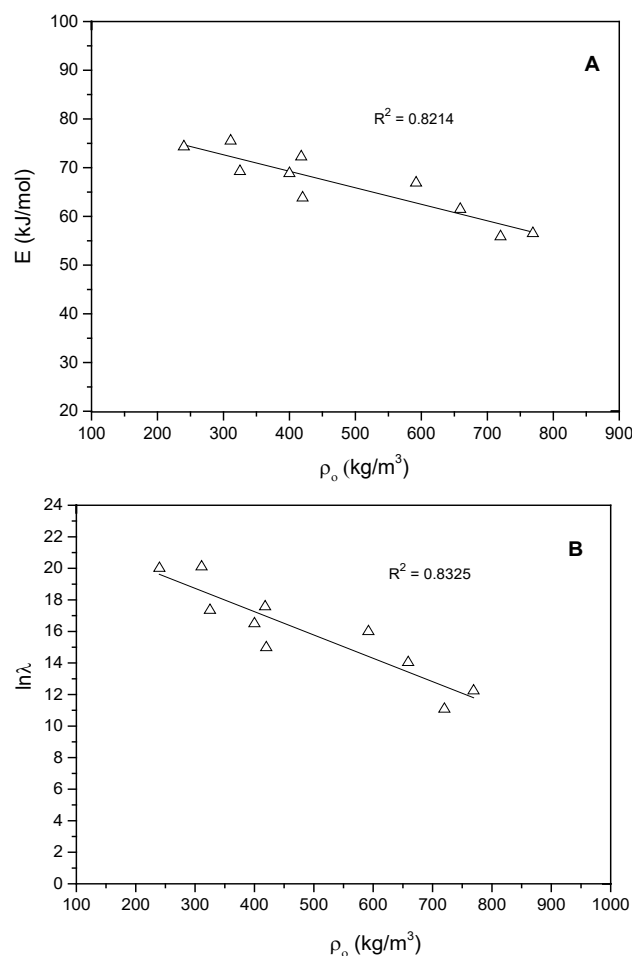


Fig. 1. Dependence of A: activation energy, B: pre-exponential factor on the wood density.

Both kinetic parameters increase with the decrease of the wood density, but determining is the effect of the pre-exponential factor. The combination of chemical interaction and diffusion processes affects the rate of the process of enzymatic hydrolysis of the examined fast-growing tree species with various density. The process of hydrolysis is limited by the diffusion of the large enzyme molecules in the capillary system of the fibrous matrix, which also determines the observed regularity of rate decrease with the increase of the steric difficulties with the increase of the wood density.

CONCLUSIONS

When studying the composition of the fast-growing tree species, no expressed dependences between the chemical composition and the density were observed, but it was established that the wood with the highest density is characterized with the highest lignin content, and that with the lowest density has the lowest lignin content. It was established that the low wood density favours the implementation of the SE pretreatment at lower

severity and ensures the necessary efficiency of the enzymatic hydrolysis. The results of the enzymatic hydrolysis showed that the highest glucose yield is obtained in the case of PT that is also characterized with the lowest density. The efficiency of the enzymatic hydrolysis of the tree species with low density is comparable and higher than that of enzymatic hydrolysis of wheat straw. A common feature of the kinetics of enzymatic hydrolysis of the pretreated fast-growing tree species is the topochemical mechanism that is characterized with a zonal course of the process with diffusion limitations. It was established that by the decrease of the wood density, the pre-exponential factor, that has a determining effect on the process rate, increases.

REFERENCES

1. S. Nanda, A. K. Dalai, J. A. Kozinski, *J-FOR*, **3**, 15 (2013).
2. F. H. Isikgor, C. R. Becer, *Polym. Chem.*, **6**, 4497 (2015).
3. M. Bilal, M. Asgher, H. M. N. Iqbal, H. Hu, X. Zhang, *Int. J. Biol. Macromol.*, **98**, 447 (2017).
4. A. K. Kumar, S. Sharma, *Bioresour. Bioprocess.*, **4**, 7 (2017).
5. M. Zhou, J. Yang, H. Wang, T. Jin, D. J. Hassett, T. Gu, in: *Bioenergy Research: Advances and Applications*, V. K. Gupta, M. G. Tuohy, C. P. Kubicek, J. Saddler, F. Xu (eds.), Elsevier BV, Oxford, 2014, p. 131.
6. K. Buzala, P. Przybysz, J. Rosicka-Kaczmarek, H. Kalinowska, *Cellulose*, **22**, 663 (2015).
7. K. Ullah, V. K. Sharma, S. Dhingra, G. Braccio, M. Ahmad, S. Sofia, *Renew. Sust. Energ. Rev.*, **51**, 682 (2015).
8. A. Szostak, G. Bidzinska, E. Ratajczak, M. Herbec, *Drewno*, **56**, 85 (2013).
9. S. González-García, M. T. Moreira, G. Feijoo, R. J. Murphy, *Biomass Bioenergy*, **39**, 378 (2012).
10. A. Procentese, F. Raganati, G. Olivieri, M. E. Russo, M. de la Feld, A. Marzocchella, *N. Biotechnol.*, **39**, 135 (2017).
11. J. Xu, Z. Wang, J. J. Cheng, *Bioresour. Technol.*, **102**, 7613 (2011).
12. E. Domínguez, A. Romani, L. Domingues, G. Garrote, *Appl. Energy*, **187**, 777 (2017).
13. P. Alvira, E. Tomás-Pejó, M. Ballesteros, M. J. Negro, *Bioresour. Technol.*, **101**, 4851 (2010).
14. F. Cotana, C. Buratti, M. Barbanera, E. Lascaro, *Bioresour. Technol.*, **198**, 470 (2015).
15. Y. Sun, J. Cheng, *Bioresour. Technol.*, **83**, 1 (2002).
16. H. Rabemanolontsoa, S. Saka, *Bioresour. Technol.*, **199**, 83 (2016).
17. T. Auxenfans, D. Crônier, B. Chabbert, G. Paës, *Biotechnol. Biofuels*, **10**, 36 (2017).
18. N. Mosier, C. Wyman, B. Dale, R. Elander, Y. Y. Lee, M. Holtzapple, M. Ladisch, *Bioresour. Technol.*, **96**, 673 (2005).
19. W. R. Grous, A. O. Converse, H. E. Grethlein, *Enzyme Microb. Technol.*, **8**, 274 (1986).
20. M. Cantarella, L. Cantarella, A. Gallifuoco, A. Spera, F. Alfani, *Biotechnol. Prog.*, **20**, 200 (2004).
21. J. S. Martín-Davison, M. Ballesteros, P. Manzanares, X. P. B. Sepúlveda, A. Vergara-Fernández, *Int. J. Green Energy*, **12**, 832 (2015).
22. A. P. Nunes, J. Pourquie, *Bioresour. Technol.*, **57**, 107 (1996).
23. R. Martín-Sampedro, M. E. Eugenio, J. C. García, F. Lopez, J. C. Villar, M. J. Diaz, *Biomass Bioenergy*, **42**, 97 (2012).
24. M. Muzamal, K. Jedvert, H. Theliander, A. Rasmuson, *Holzforchung*, **69**, 61 (2015).
25. K. Kürschner, A. Hoffer, *Techn. Chem. Papier und Zellstoff Fabr.*, **26**, 125 (1929).
26. R. P. Overend, E. Chornet, J.A. Gascoigne, *Phil. Trans. R. Soc. Lond. A*, **321**, 523 (1987).
27. A. Sluiter, B. Hames, R. Ruiz, C. Scarlata, J. Sluiter, D. Templeton, NREL, Golden, 2008.
28. J. J. Balatinez, D. E. Kretschmann, in: *Poplar Culture in North America*, D.I. Dickmann, J. G. Isebrands, J. E. Eckenwalder, J. Richardson (eds.), NRC Research Press, Ottawa, 2001, p. 227.
29. F. Pitre, F. Lafarguette, B. Boyle, N. Pavy, S. Caron, N. Dallaire, P. Poulin, M. Ouellet, M. Morency, N. Wiebe, E. Lim, A. Urbain, G. Mouille, J. Cooke, J. Mackay, *Tree Physiol.*, **30**, 1273 (2010).
30. M. Stolarski, M. Krzyżaniak, M. Łuczyński, D. Załuski, S. Szczukowski, J. Tworkowski, J. Gołaszewski, *Ind. Crops Prod.*, **75**, 66 (2015).
31. G. Radeva, I. Valchev, S. Petrin, E. Valcheva, P. Tsekova, *Cellulose Chem. Technol.*, **46**, 61 (2012).
32. I. Valchev, S. Petrin, in: *R&D on Processes for Solid, Liquid and Gaseous Fuels from Biomass* (Proc. 21st EU BC and E, Copenhagen, 2013), A. Eldrup, D. Baxter, A. Grassi, P. Helm (eds.), ETA-Florence Renewable Energies, Italy, 2013.
33. I. Valchev, N. Yavorov, S. Petrin, *Holzforchung*, **70**, 1147 (2016).
34. S. Singh, D. Dutt, C. H. Tyagi, *BioResources*, **6**, 154 (2010).

Synthesis and hydrolytic stability of new analogues of Bactenecin 2A

A. Hristova¹, S. Valcheva-Kuzmanova², T. Pajpanova^{3*}

¹Medical College, Medical University "Prof. Dr. Paraskev Stoyanov", 84 Tsar Osvoboditel Blvd., 9002 Varna, Bulgaria

²Department of Pharmacology and Clinical Pharmacology and Therapeutics, Faculty of Medicine, Medical University "Prof. Dr. Paraskev Stoyanov", 55 Marin Drinov str., 9002 Varna, Bulgaria

³Institute of Molecular Biology "Roumen Tsanev", Bulgarian Academy of Sciences, Acad. G. Bonchev str., block 21, Sofia 1113, Bulgaria

Received: August 20, 2019; Revised: April 03, 2020

The hydrolytic stability of peptides is one of the most important properties in terms of their application in practice. Pre-information on stability is essential for the pharmacokinetic behavior in the body, the storage conditions, the occurrence of toxic effects associated with their degradation products, and others. We synthesized a series of short linear Bactenecin 2A mimetics containing cationic unnatural amino acids and examined their hydrolytic stability under physiological conditions. The five newly synthesized analogues showed high hydrolytic stability in the acidic region and only some of them were stable in neutral and alkaline environment.

Keywords: antimicrobial peptides, Bactenecin, unnatural amino acids, solid-phase synthesis, hydrolytic stability

INTRODUCTION

Drug resistance of microorganisms is among the serious threats to human health, and in the last few years an incremental trend in the incidence of diseases caused by resistant microorganisms has been observed. That determines the necessity to search for new antibiotics, and to look for substances which are capable of enhancing antibiotic effects, or of reversing microbial resistance, even if they themselves have no antimicrobial effect. Some peptides have been shown to have antimicrobial activity, and/or ability to enhance the effects of antimicrobial agents. Thus, the antimicrobial peptides (AMPs) are some of the most promising candidates for a novel class of antibiotics [1-4].

Cationic antimicrobial peptides (CAMPs), also called cationic host defense peptides, are present in virtually every form of life, from bacteria and fungi to plants, invertebrates, and vertebrates [5]. An under-studied representative of this group is the cyclic cationic peptide Bactenecin isolated from bovine neutrophils. This short peptide ((R¹L²C³R⁴I⁵V⁶V⁷I⁸R⁹V¹⁰C¹¹R¹²)) is composed of 12 amino acid residues including four arginines and two cysteines, and is shown to form a β -turn structure consisting of one disulfide bond [6].

Bactenecin is active against *Escherichia coli* and *Staphylococcus aureus* as it was previously found [7, 8]. Compared to other β -structural natural AMPs, Bactenecin has less pronounced antimicrobial activity, but because of its small size it is used as the basis for creating more effective AMPs [8-11].

The **Bac2A** peptide (Fig. 1) is a linear variant of Bactenecin. In **Bac2A**, two cysteine residues are replaced by two alanine residues. They have an average activity with MICs between 2 and 32 $\mu\text{g/ml}$ for Gram-negative bacteria and between 0.25 and 16 $\mu\text{g/ml}$ for Gram-positive bacteria. Based on the substitution analysis of **Bac2A** (RLARIVVIRVAR-NH₂), different 12mer peptides with superior activity against different human pathogens were developed [12].

On the other hand, there are several limitations to the clinical application of AMPs as therapeutic agents, especially their low bioavailability under physiological conditions due to proteolytic degradation. To overcome this problem and improve their antimicrobial potential, several studies have focused on chemical modification of naturally occurring sequences [13, 14], such as the use of unnatural amino acids, D-form amino acids, fatty acids, or conjugation with antibiotics [15]. A peptidomimetic approach that was applied in our recent studies with significant potential is the use of unnatural amino canavanine, a structural analogue of arginine [16].

In this context, our first objective was to synthesize short model peptide fragments of **Bac2A** (Fig. 1) containing non-protein amino acids canavanine (Cav), as well as S-cysteine sulfonamide (Cys(SO₂NH₂)) and D-amino acid S-homocysteine sulfonamide (hcys(SO₂NH₂)),

* To whom all correspondence should be sent:

E-mail: tamara@bio21.bas.bg

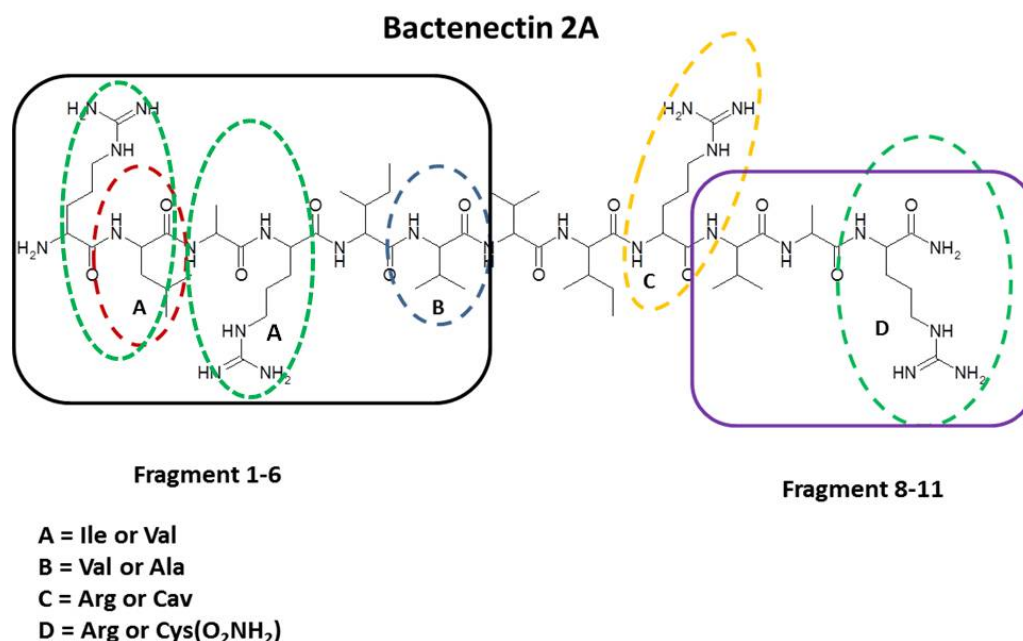


Figure 1. Bac2A and its structural analogues.

for which there is evidence of antimicrobial activity [17-19].

The second aim of this study was to evaluate the hydrolytic stability of newly synthesized Bac2A analogues under physiological conditions such as body temperature of 37° C and pH values of 1.2 (stomach), 7.4 (blood plasma) and 8.5 – 9.0 (small intestine).

EXPERIMENTAL

Peptide synthesis

For the preparation of the desired model peptides, we have referred to the solid phase peptide synthesis method. Reagents, resins and Fmoc-amino acids used in peptide synthesis were purchased from Merck (Darmstadt, Germany) and Iris Biotech GMBH (Germany). Solvents dimethylformamide (DMF) and dichloromethane (DCM) were purchased from Merck (Darmstadt, Germany).

Fmoc-Cav(Boc)-OH, Z-Cys(SO₂NH₂)-OH and Fmoc-hcys(SO₂NH₂)-OH were prepared according to previously reported methods [19, 20].

Synthesis of all peptides was performed by the conventional manual stepwise Fmoc solid-phase synthesis on 2-chlorotrityl chloride resin with substitution, 1.4 mmol/g. The coupling of each amino acid was performed in the presence of 3 mol excess of Fmoc-amino acid, 3 mol excess of N-hydroxybenzotriazole (HOBt), 3 mol excess of diisopropylcarbodiimide (DIC), and 5 mol excess of diisopropylamine (DIPEA) in DMF. The completion of coupling reactions was monitored by the Kaiser test and the Fmoc groups were removed by adding

25% piperidine in DMF. The peptides were cleaved from the resin and the final deprotection was done in a cocktail containing trifluoroacetic acid (TFA), triisopropylsilane (TIPS), thioanisole, and water (92.5 : 2.5 : 2.5 : 2.5). The crude peptides were precipitated into cold petroleum ether/diisopropyl ether (50:50). Then, the precipitate was dissolved in 10% CH₃COOH and desalted by gel filtration on a Sephadex G25.

Peptide purity

HPLC analysis was performed with LKB Bromma (Sweden) and Waters Alliance® (Waters Corporation, USA) instruments and a variable detector using column: XTerra® MS C18, 3,5µm, 3.0 × 150 mm; eluent: ACN/0.05%TFA 5/95 (v/v), flow 0.4 ml/min, 25°C, 220 nm, injected volume 20 µL.

Peptide stability

The hydrolytic stability of the peptides was determined by UV spectroscopy. For stability testing, the concentration 0.5·10⁻⁴ mol/l of each of the peptides (P1 – P5), respectively, was dissolved in 10 ml of buffers: pH=1.2 (0.063 mol/l HClO₄); pH=7.4 (0.1 mol/l Na₂HPO₄ + 0.1 mol/l NaH₂PO₄); pH=9.0 (0.1 mol/l Na₂B₄O₇). The obtained solution of the peptides was tempered in the incubator ES-20 LKB (Sweden) at 37°C. The test samples were placed in a Beckman DU 650 spectrophotometer (Beckman Instruments, USA) equipped with a temperature-controlled cell changer; 1 ml quartz cuvettes were used. The decrease in the absorbance

at 220 nm (UV maximum of the peptide) was monitored.

RESULTS AND DISCUSSION

In order to design short model peptide fragments of Bac2A, literature data have been taken into account indicating that the most important structural requirement for high antimicrobial activity is the presence of basic amino acids such as arginine and lysine, at least 3 net charge in each peptide.

It was also shown that changes in any single position of the peptide may affect other residues at all other positions in the parent peptide. Therefore, each single modified peptide variant may lead to different activity and stability [21].

In our study, a substantial difference in obtaining the corresponding **Bac2A** analogue was found primarily in the non-protein amino acid used. Arg at positions **1** and **4**, as well as Val at position **6** were successively or simultaneously replaced with Arg(NO₂) and non-protein amino acids – Cav, Cys(SO₂NH₂) and hcys(SO₂NH₂).

All linear shortened analogues (**P1-P5**) of **Bac2A**, modified at the N-terminus (fragment 1-6) were obtained using essentially the same experimental set-up outlined in Scheme 1.

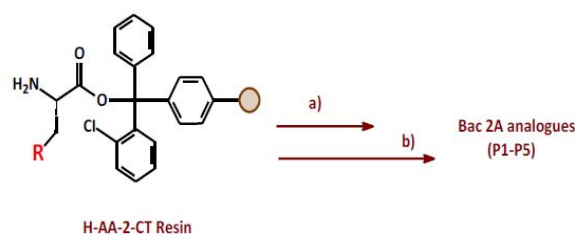
The yields of each peptide were over 60%. HPLC analysis revealed a purity of >95% for all obtained analogues (Fig. 2). The net charge, yield, RP-HPLC purity and molecular weight of Bac 2A linear analogues synthesized in this study are summarized in Table 1.

The hydrolytic stability of peptides is one of the most important properties in terms of their application in practice. Pre-information on stability is essential for the pharmacokinetic behavior in the body, the storage conditions, the occurrence of toxic effects associated with their degradation products, and others.

We examined the hydrolytic stability of the resulting peptide analogues under physiological conditions such as: body temperature of 37° C and physiological pH value of 1.2 (stomach), 7.4 (blood plasma) and 8.5–9.0 (small intestine) using UV-spectrophotometry and RP-HPLC. At defined intervals of time we measured the absorbance at 220 nm. For each of the studied peptides, a plotted time/concentration graph was constructed.

As shown on Fig. 3, at acidic pH, the peptide Cav-Leu-Ala-Arg(NO₂) (**P1**) retained stability for six hours and its concentration was about 95%. By the third hour of the test, the peptide remained stable at both acidic and alkaline pH of nearly 100 %. At alkaline pH, at the end of the sixth hour the concentration of the peptide was about 90 %.

At pH7.4, **P1** retained significantly higher stability within one hour of the test, after which its concentration decreased to 80% at the end of the sixth hour.



P1 - Cav-Leu-Ala-Arg(NO₂); **P2** - Arg(NO₂)-Leu-Ala-Cav;
P3 - Cys(SO₂NH₂)-Ile-Arg-Val-Ala;
P4 - Cys(SO₂NH₂)-Ile-Arg-Val-Val;
P5 - Arg(NO₂)-Leu-Ala-Arg(NO₂)-Ile-hcys(SO₂NH₂)

Scheme 1. Reagents and conditions: a) 1/ Fmoc-AA-OH, DIC, DIPEA, HOBt, DMF; 2/ 25% piperidine/DMF; b) TFA/ TIPS /H₂O/thioanisol, RT, 1-2 h.

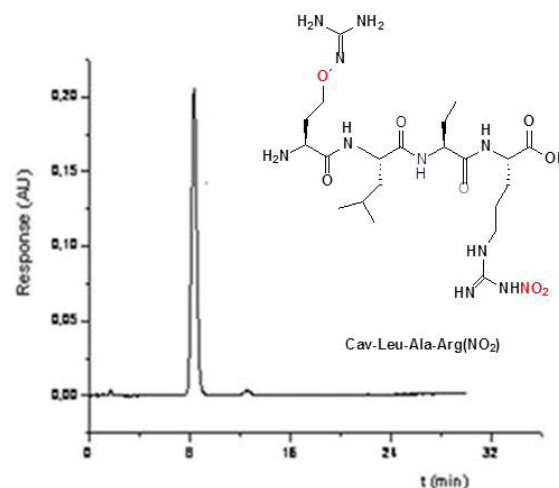


Figure 2. Analytical HPLC of H-Cav-Leu-Ala-Arg(NO₂)-OH (**P1**); Column: AtlantisTMdC18 (Beckman Ultrasphere®) 4.6 × 150 mm; mobile phase: acetonitrile / deionized water 40/60 (v/v); 25°C, flow rate: 1 ml/min, UV detection – 206 nm.

Table 1. Analytical data on synthesized analogues of Bactenecin 2A.

Code	Net charge	Yield %	Purity %	Molecular formula	MW calculated	MW [M + H ⁺]
P1	2+	86	99	C ₂₀ H ₃₉ N ₁₁ O ₈	561.591	562.597
P2	2+	87	99	C ₂₀ H ₃₉ N ₁₁ O ₈	561.591	562.593
P3	2+	46	96	C ₂₃ H ₄₅ N ₉ O ₈ S	607.720	608.207
P4	2+	77	98	C ₂₅ H ₄₉ N ₉ O ₈ S	635.780	636.805
P5	3+	71	95	C ₃₁ H ₆₀ N ₁₅ O ₁₃ S	882.960	868.937

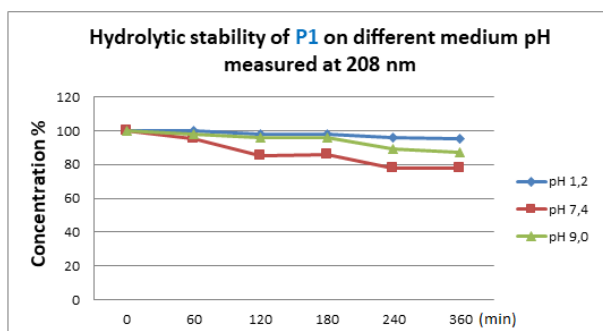


Figure 3. Hydrolytic stability of P1 at different pH measured at 220 nm by UV-spectroscopy.

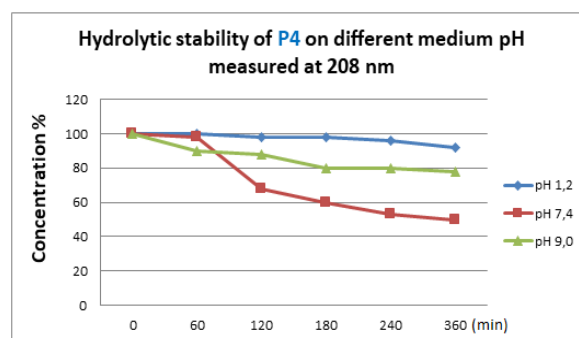


Figure 6. Hydrolytic stability of P4 at different pH measured at 220 nm by UV-spectroscopy.

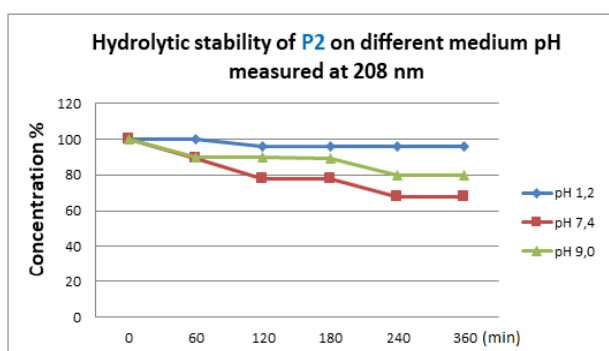


Figure 4. Hydrolytic stability of P2 at different pH measured at 220 nm by UV-spectroscopy.

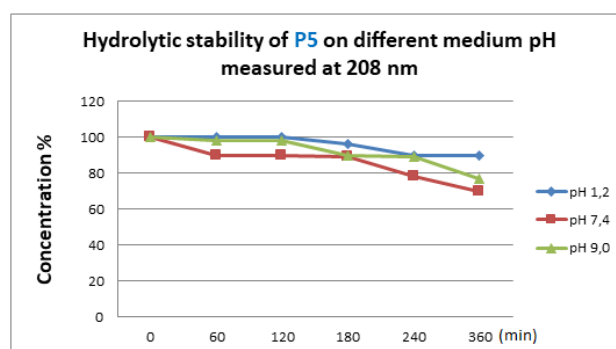


Figure 7. Hydrolytic stability of P5 at different pH measured at 220 nm by UV-spectroscopy.

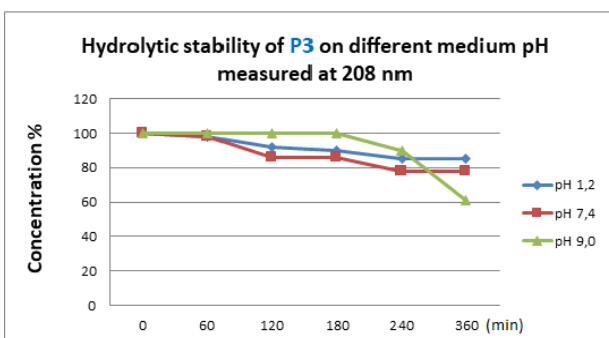


Figure 5. Hydrolytic stability of P3 at different pH measured at 220 nm by UV-spectroscopy.

On Fig. 4, the hydrolytic stability of the Arg(NO₂)-Leu-Ala-Cav (**P2**) peptide is presented. It is evident from the graph that **P2** retained its stability in acidic medium till the end of the sixth hour to a significant extent (98%), even higher than that of **P1** (95%). As opposed to **P1**, the concentration of **P2** in alkaline and neutral pH began to decrease within the first hour (90%). The concentration till the end of the sixth hour in neutral medium decreased to 80% and in alkaline environment to 70%.

The peptide Cys(SO₂NH₂)-Ile-Arg-Val-Ala (**P3**) (Fig. 5) retained 100% stability in the three physiological media within the first hour of the assay. In an alkaline environment, it retained its stability by the end of the third hour, then at the fourth hour its concentration was about 84% and at the end of the sixth hour it was 60%. At acidic pH, at the end of the test the concentration was 83% and at pH 7.4 it was 79%.

Fig. 6 presents the graph showing the stability of the peptide Cys(SO₂NH₂)-Ile-Arg-Val-Val (**P4**). The concentration it retained in acidic medium (93%) till the end of the test was very close to those of **P1** and **P2**. The stability in a neutral buffer medium remained unchanged within the first hour, then sharply dropped and at the end of the sixth hour hardly reached 50%. At pH 9.0, the concentration gradually decreased, being 79% at the end of the study.

The stability of the peptide Arg(NO₂)-Leu-Ala-Arg(NO₂)-Ile-hcys(SO₂NH₂) (**P5**) is presented on Fig. 7.

Like the other four peptides (**P1-P4**), in acidic medium **P5** retained the highest levels of concentration (90%) for a long time. At pH 9.0 the peptide remained unchanged for three hours, after which the concentration was reduced to 79% at the end of the sixth hour. At neutral pH, on the first hour

the concentration of the peptide was 90% and it was maintained until the end of the third hour. At the end of the test the concentration was 75%.

As it was expected, all newly synthesized peptides containing unnatural amino acids exhibited a remarkably high hydrolytic stability. It is noticeable that after six hours of incubation in acidic medium, > 95% of the initial concentration of **P1** and **P2** was still present. The stability profile of all peptides in basic and neutral medium looks similar for the first three hours, even 90% of the initial concentration of **P1** is still present after six hours of incubation. The concentrations of **P4** and **P5** sharply dropped at the end of the six hours and hardly reached 50%. We might note that among all modifications made, introduction of the canavanine residue at position **1** (**P1**) and at position **4** (**P2**) is the most favorable for the hydrolytic stability.

CONCLUSION

In summary, we successfully synthesized 5 novel shortened analogues of Bactenecin 2A that exhibited a high hydrolytic stability in the acidic region. Our results indicated that they were more sensitive to hydrolytic degradation in neutral and alkaline environment in which **P1** showed the highest stability. The incorporation of the unnatural amino acid canavanine into the N-terminal region of Bac 2A may be a useful tool to improve the stability of the shortened linear analogues without a great loss of the activity.

Acknowledgement: The work was supported by Science Fund, Medical University, Varna, Bulgaria; Project: 17010/2017.

REFERENCES

1. H. B. Koo, J. Seo, *PeptSci.*, **111**, 1 (2019).
2. M. Mahlapuu, J. Håkansson, L. Ringstad, C. Björn, *Front. Cell. Infect. Microbiol.*, **6**, 1 (2016).
3. N. Molchanova, P. R. Hansen, H. Franzyk, *Molecules*, **22**, 1430 (2017).
4. N. K. Brogden, K.A. Brogden, *Int. J. Antimicrob. Agents*, **38**, 217 (2011).
5. R. E. W. Hancock, R. Lehrer, *Trends Biotechnol.*, **16**, 82 (1998).
6. D. Romeo, B. Skerlavaj, M. Bolognesi, R. Gennaro, *J. Biol. Chem.*, **263**, 9573 (1988).
7. S. W. Radermacher, V. M. Schoop, H. J. Schluesener, *J. Neurosci. Res.*, **36**, 657 (1993).
8. M. Wu, R. E. Hancock, *Antimicrob. Agents Chemother.*, **43**, 1274 (1999).
9. Ji-Y. Sim, S. Kim, J. Lee, H. Lim, H. H. Kim, Ze-Y. Park, J. I. Kim, *Biochem. Biophys. Res. Commun.*, **514**, 497 (2019).
10. H. Choi, J. S. Hwang, H. Kim, D. G. Lee, *Biochem. Biophys. Res. Commun.*, **440**, 94 (2013).
11. Y. H. Nan, B. Jacob, Y. Kim, S. Y. Shin, *J. Pept. Sci.*, **18**, 740 (2012).
12. K. Hilpert, R. Volkmer-Engert, T. Walter, R. E. W. Hancock, *Nat. Biotechnol.*, **23**, 1008 (2005).
13. K. Hilpert, C. D. Fjell, A. Cherkasov, in: Peptide-Based Drug Design. Methods in Molecular Biology™, L. Otvos (ed.), vol. 494, Humana Press, 2008.
14. H. Choi, J. S. Hwang, H. Kim, D. G. Lee, *Biochem. Biophys. Res. Commun.*, **440**, 94 (2013).
15. A. Reinhardt, I. Neundorff, *Int. J. Mol. Sci.*, **17**, 701 (2016).
16. S. Michailova, T. Dzimbova, K. Kalikova, E. Tesařová, T. Pajpanova, *Bulg. Chem. Commun.*, **49**, (E), 113 (2017).
17. T. Dzimbova, T. Pajpanova, S. Tabakova, E. Golovinsky, in: 5th Hellenic Forum on Bioactive Peptides, Patras, P. Cordopatis (ed.), Typorama, Patras, 2007, p. 223.
18. J. Miersh, K. Grancharov, T. Pajpanova, D. Neumann, S. Tabakova, S. Stoev, G.-J. Krauss, E. Golovinsky, *Amino Acids*, **18**, 41 (2000).
19. G. Videnov, B. Aleksiev, M. Stoev, T. Pajpanova, G. Jung, *Liebigs Ann. Chem.*, 941 (1993).
20. T. Pajpanova, S. Stoev, E. Golovinsky, G.-J. Krauss, J. Miersch, *Amino Acids*, **12**, 191 (1997).
21. K. Hilpert, M. R. Elliott, R. Volkmer-Engert, P. Henklein, O. Donini, Q. Zhou, D. F. H. Winkler, R. E. W. Hancock, *Chem. Biol.*, **13**, 1101 (2006).

*Selected papers presented at the 16th National Conference on Catalysis organized by
Bulgarian Catalysis Society, Sofia, June 27, 2019.
This event was dedicated to the 150th anniversary of the Bulgarian Academy of Sciences and the
80th anniversary of Professor Lachezar Petrov.*

Kinetics and mechanism of the ozone reaction with cyclohexanol in solution

M. P. Anachkov*, P. A. Karakashkova, V. F. Georgiev, S. K. Rakovsky, L. S. Minchev,
T. T. Batakliiev

Institute of Catalysis, Bulgarian Academy of Sciences, Acad. G. Bonchev St., Bl. 11, 1113 Sofia, Bulgaria

Dedicated to the 80th anniversary of Professor Lachezar Petrov, DSc,
Corresponding Member of the Bulgarian Academy of Sciences

Received: November 11, 2019; Revised: December 11, 2019

Ozone absorption by cyclohexanol solution during ozonolysis in a bubbling reactor has been studied by continuous monitoring of the ozone concentration at the reactor outlet under conditions of constant values of the initial ozone concentration at the reactor inlet. It was found that the values of the rate constant (at 25 °C) and the activation energy of the reaction were $3.1 \text{ M}^{-1}\cdot\text{s}^{-1}$ and 10.2 kcal/mol, respectively. Infrared spectroscopy and GC/MSD were employed to determine the products obtained at 24% conversion degree of the substrate by oxidation of a 1% solution of cyclohexanol in CCl_4 at room temperature. Three bands at 1710, 1724, and 1776 cm^{-1} were observed in the IR spectra of the ozonized solutions, which are characteristic of acidic, ketone, and ester functional groups, respectively. Based on the obtained IR and GC data it was established that cyclohexanone is the main reaction product of the cyclohexanol ozonolysis. Cyclohexanone and 2-chlorocyclohexanone to ester quantitative ratio determined by GC/MSD analysis was found to be 53/47. The amount of the main ester product, hexanedioic acid, dicyclohexyl ester, was 37% of the total ester yield.

Keywords: ozone, ozonolysis, cyclohexanol, solution, oxidation

INTRODUCTION

It is well known that ozonolysis of alcohols could be used for selective preparation of ketones and aldehydes that have various applications in the chemical and pharmaceuticals industries, fine chemicals synthesis, etc. [1, 2]. These reactions proceed under mild conditions and are characterized by high yields of the respective carbonylic compounds [3]. In some cases of oxidation of open chain (simple) and cyclic secondary alcohols the yield of corresponding ketones lies in the range of 57–83% [4].

On the other hand, alcohols have been considered the first oxidation step during ozonolysis of alkanes and cycloalkanes [1, 5]. A characteristic feature of the alcohols is their significantly higher reactivity with respect to ozone in comparison with that of the corresponding alkanes [3, 6]. For this reason, it could be expected that some of the compounds identified in the model reaction of cyclohexane ozonolysis, are products of cyclohexanol ozonolysis [5]. In this connection, there are theoretical and experimental works dealing mainly with reaction kinetics studies [6, 7].

Except for cyclohexanone, there is a problem with the identification of other reaction products related to the reaction mechanism [8, 9].

The aim of the present paper is the precise determination of the kinetic parameters of the cyclohexanol ozonolysis, identification, and

quantitative characterization of the main reaction products.

EXPERIMENTAL

Ozone was obtained by passing a dried oxygen flow (99.99%) through a 4–9 kV discharge in a self-made design of tubular type of ozone generator.

The ozonation experimental runs were performed in a bubbling reactor containing 10–15 ml of 1% solution of p.a. grade cyclohexanol in CCl_4 . An ozone-oxygen mixture with ozone concentration within the range of 1000–25000 ppm (4.5×10^{-5} – $1.2 \times 10^{-3} \text{ mol}\cdot\text{l}^{-1}$) was passed through the reactor at a flow rate of about $(1.3 \pm 0.3) \times 10^{-3} \text{ l}\cdot\text{s}^{-1}$ at room temperature. Ozone concentrations in the gas phase at the reactor inlet ($[\text{O}_3]_0$) and outlet ($[\text{O}_3]_g$) were measured spectrophotometrically by a BMT model 964 ozone analyser.

IR spectra of the samples were recorded on a Nicolet 6700 FTIR spectrometer (Thermo Electron Corporation, USA). The spectra were collected in the middle IR region using 100 scans at a resolution of 4 (data spacing 1.928 cm^{-1}).

GC-MSD analyses were performed on an Agilent Technologies model 890A instrument equipped with mass-selective detector model 5975C. A DB-WAXETR capillary column of 30-m length and 0.25-mm i.d., coated with polyethylene glycol (0.25 μm), was used in the experiments. The temperature settings were as follows: injector temperature 200 °C; column temperature program from 40 to 260 °C;

* To whom all correspondence should be sent:
E-mail: anachkov@ic.bas.bg

transfer line temperature 230 °C; detector temperature 150 °C; electronic source 230 °C, carrier gas He (5.0) at a rate of 0.7 ml/min, volume of the injected samples 0.2 µl; split 20:1. The quantitative ratios among reaction products were determined by the Internal Standard (ISTD) method.

Thermal treatment of the ozonized solutions was applied. Samples of ozonized solutions sealed in glass ampoules were heated for 2 hours at 100 °C. After the treatment, the samples were examined by IR spectroscopy and GC-MS analysis under the same conditions as those for the unheated samples.

RESULTS AND DISCUSSION

The ozone absorption process was studied by continuous monitoring of the ozone concentration at the reactor outlet under constant initial ozone concentration at the reactor inlet. The $[O_3]_g = f(\tau)$ dependence was recorded on a computer connected to the ozone analyser (Fig. 1).

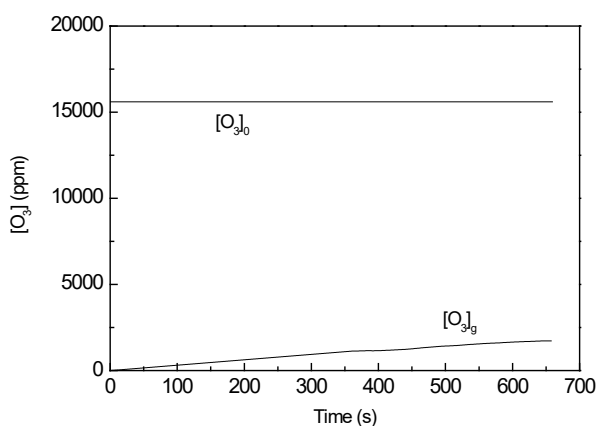


Fig. 1. Dependence of the ozone gas phase concentration ($[O_3]$) in the ozone-oxygen mixture on bubbling time: 1% solution of cyclohexanol in CCl_4 , gas feeding rate – $1.3 \times 10^{-3} \text{ l.s}^{-1}$, temperature – 24°C, $[O_3]_0$ – ozone concentration in the reactor inlet, $[O_3]_g$ – ozone concentration in the reactor outlet.

Considerable differences between $[O_3]_0$ and $[O_3]_g$ were observed, which indicate that a significant amount of bubbling ozone in the reactor is consumed during the reaction. The area enclosed between the $[O_3]_g = f(\tau)$ and $y = [O_3]_0$ curves is proportional to the amount of ozone consumed in the reaction. This amount was calculated by using the coefficient of ozone extinction at 254-nm UV-C wavelength, $3000 \text{ l.cm}^{-1} \cdot \text{mol}^{-1}$ [5], and the respective inlet flow rate of the ozone-oxygen mixture. In this way, it was determined that the amount of consumed ozone corresponds to 20% of the initial amount of cyclohexanol in the reactor.

As a rule, the low values of the $[O_3]_g/[O_3]_0$ ratio, which are characteristic of cyclohexanol ozonolysis (Fig. 1), if compared with those during ozone reaction with cyclohexane, could be explained by a significantly higher rate constant of the alcohol. One of the most often used methods for determination of the rate constants of ozonolysis of organic compounds is based on the approach proposed by Razumovskii *et al.* [3], which is a relationship between the balance of consumed ozone and the rate of the chemical reaction, Eq. (1):

$$\omega([O_3]_0 - [O_3]_g) = k[O_3]_l[RH], \quad (1)$$

where ω is the relative flow rate of the ozone-oxygen gas mixture (as litres per litre of solution per sec); $[O_3]_0$ and $[O_3]_g$ are ozone concentrations at the reactor inlet and outlet, respectively, $[O_3]_l$ is the concentration of ozone dissolved in the liquid phase; $[RH]$ is the concentration of the reagent. This model is valid in all cases when the rate of ozone absorption is considerably higher than the rate of the chemical reaction. In accordance with Henry's law for a bimolecular reaction, if $[O_3]_l$ is replaced by $[O_3]_g$, where α is Henry's coefficient (as mol.l^{-1} in liquid/ mol^{-1} in the gas phase), then Eq. (1) can be transformed into Eq. (2):

$$k = \omega \Delta[O_3] / ([RH] \cdot \alpha [O_3]_g) \quad (2)$$

Kinetic parameters of cyclohexanol ozonolysis were determined according to Eq. (2) in special experiments, which were carried out in accordance with the requirements for complete elimination of the diffusion limitation during the reaction [6]. It was found that the values of the rate constant (at 25 °C) and of the activation energy of the reaction were $3.1 \text{ M}^{-1} \cdot \text{s}^{-1}$ and 10.2 kcal/mol , respectively. These values are close to some other reported in the literature [6]. It is interesting to note that the k value of the cyclohexanol ozonolysis is more than two orders of magnitude higher than that of cyclohexane ozonolysis.

Infrared spectroscopy was employed to determine the different functional groups obtained at 24% ozone conversion of a 1% solution of cyclohexanol in CCl_4 at room temperature. The IR spectrum of the ozonized solution is presented in Fig. 2. The main peculiarity of the spectrum is the appearance of three bands at 1710, 1724, and 1776 cm^{-1} . According to literature data, these bands could be ascribed to acidic, ketone, and ester functional groups, respectively [10]. It is seen that the most intense band is observed at 1724 cm^{-1} , which is characteristic of cyclohexanone absorption.

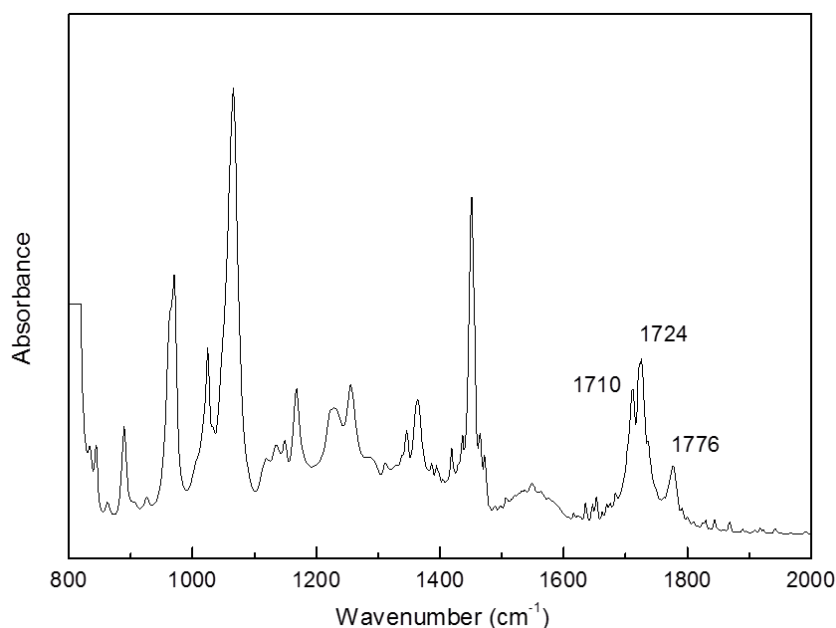


Fig. 2. IR spectrum of ozonized 1% solution of cyclohexanol in CCl_4 (24% conversion, NaCl cuvette 0.61 mm)

In contrast to infrared spectroscopy, the GC/MSD method provides a possibility of identification of individual reaction products. It should be noted that cyclohexanol conversion determined by chromatography was about 24%, while the amount of consumed ozone in the reactor reached 20% with respect to cyclohexanol initial content. Results of the identification and quantitative characterization of the organic compounds with a noticeable contribution among the mixture of reaction products are displayed in Table 1. It is seen that the basic products are ketones and esters. Also, small amounts of lactones, caprolactone and δ -valerolactone, and cyclohexane, 1,1'-[methylenebis(oxy)]bis- were detected.

Table 1. GC/MSD-determined content of the reaction products after ozonolysis of 1% solutions of cyclohexanol in CCl_4 under conditions of 24% conversion.

	Compound	Content, %
1	Cyclohexanone	39.68
2	Cyclohexyl formate	5.03
3	Cyclohexanone, 2-chloro	13.08
4	Pentanoic acid, cyclohexyl ester	3.50
5	5-Chloropentanoic acid, cyclohexyl ester	4.17
6	Hexanoic acid, 2-hexenyl ester, (E)-	2.37
7	Hexanoic acid, cyclohexyl ester	5.35
8	Cyclopentanecarboxylic acid, pentyl ester	9.42
9	Hexanedioic acid, dicyclohexyl ester	17.44

According to Table 1, the ketone/ester ratio is 53/47. The acidic components of the esters are pentanoic acid, 5-chloropentanoic acid, hexanoic acid, cyclopentanecarboxylic acid, and hexanedioic acid. The amount of the main ester product, hexanedioic acid dicyclohexyl ester, is about 37% of the total ester yield.

Significant amounts of identified cyclohexanone, 2-chloro- and 5-chloropentanoic acid, cyclohexyl ester could be regarded as a piece of evidence for ongoing radical processes with the participation of CCl_4 .

It is important to note that the results, discussed above, differ significantly from those published in Ref. [9]. Owing to ozonolysis of pure cyclohexanol, the cyclohexanone/ester ratio determined by Korotkova *et al.* under comparable conditions of reagent conversion (27.7%) and reaction temperature (40 °C) is 47.8/22.9. In this case, however, 'esters' refer to a mixture of cyclic esters (lactones) and classic esters. Furthermore, according to their analysis of the reaction products, the amount of caprolactone is about 70%, whereas the major acidic component of the classic esters is acetic acid. In our opinion, these differences can be explained by the formation of HCl due to solvent participation in the reaction. It is well known that mineral acids are capable of catalysing the interaction between organic acids and alcohols (cyclohexanol), which leads to the formation of the respective esters.

Although the IR spectra indicate presence of acidic groups among the reaction products, chromatographic identification of individual acids is

not possible within the limits of the available experimental equipment. Assuming that the main amounts of the esters having cyclohexanol as alcohol component are mostly obtained by the classical esterification reaction, it follows that formic, pentanoic, 5-chloropentanoic, hexanoic, and hexanedioic acids are present in the reaction mixture. Reported data in Table 1 show that the largest amount is concerned with hexanedioic (adipic) acid. According to literature data, cyclohexanone to acid ratio is 47.8/16.3, while that of monocarboxylic to dicarboxylic acids is about 0.20–0.22. Acetic, butyric, valeric, and caproic acids have been identified as monocarboxylic acids, whereas adipic acid is dominating among the dicarboxylic acids (77–94%) [9].

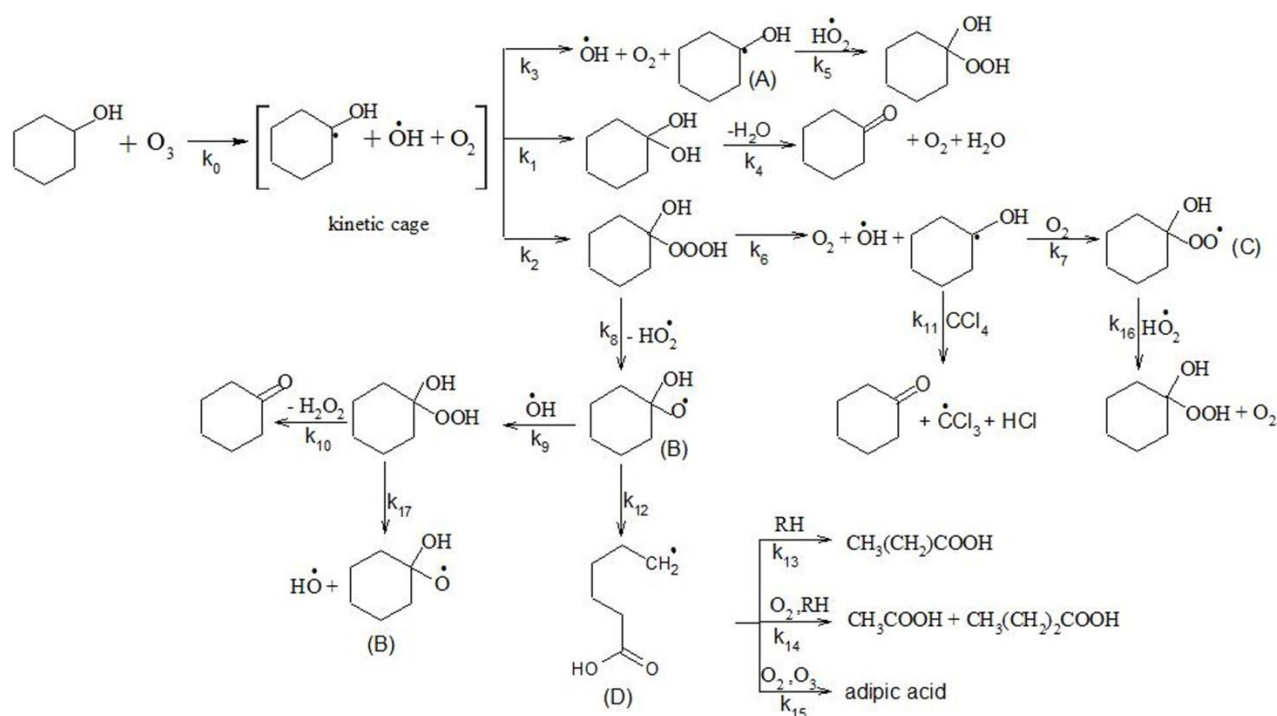
Different types of compounds containing peroxide-bonded oxygen are known to be among the major reaction products of cyclohexanol ozonolysis [6, 8, 9]. However, IR spectroscopy and gas chromatography are not suitable methods to identify and quantify individual hydroperoxide and peroxide compounds. Moreover, they are thermally unstable and practically inseparable from the reaction mixture. Bearing in mind reference data on iodometric titration, the ratio of cyclohexanone to the total amount of organic compounds containing O-O bonds is 47.8/9.7 [9]. Hydrogen peroxide formation has also been determined. The following products containing peroxide-bonded oxygen have been identified by thin layer chromatography: 1,1-

hydroxy-cyclohexyl hydroperoxide; 1-oxy-1'-hydroperoxi-dicyclohexyl peroxide; 1,1'-dioxy-dicyclohexyl peroxide [8, 9].

An attempt to incorporate different reaction routes, which lead to the formation of basic type of ozonolysis products, is presented in Scheme 1.

Ozone attacks the α -H atom to form a linear complex, which further undergoes decomposition into a radical pair in one kinetic cage. Being unstable, the α -hydroxy alcohol leaves the cage and rapidly decomposes to the corresponding ketone by liberating water and oxygen (reactions 1, 2). This scheme shows that the cyclohexanone is also formed as a result of decomposition of the 1,1-hydroxycyclohexyl hydroperoxide (reaction 10). Korotkova *et al.* proposed interaction between α -hydroxycyclohexyl radical and CCl_4 , which leads to the formation of respective ketone and hydrochloric acid (reaction 11) [9]. Significant amounts of cyclohexanone, 2-chloro- and 5-chloropentanoic acid, cyclohexyl ester among the reaction products are also indicative of solvent participation in various radical reactions.

It is accepted that the classical route to prepare various acids begins with the isomerization of α -hydroxyalkoxycyclohexyl radicals (Scheme 1, reaction 12) [9, 11]. The scheme displays the formation of caproic, butyric, acetic, and adipic acids (reactions 13, 14 and 15).



Scheme 1. Ozonolysis of cyclohexanol

Another route to prepare adipic acid could be the ozonation of cyclohexanone (cyclohexanone \rightarrow ϵ -caprolactone \rightarrow adipic acid).

One of the directions of hydroxytrioxy alcohol decomposition is the formation of hydroxyl radical, oxygen, and hydroxycyclohexyl radical (reaction 6). Interaction of the latter with oxygen from the air gives rise to α -hydroxyperoxidecyclohexyl radical (reaction 7). The 1,1-hydroxy-cyclohexyl hydroperoxide is obtained during a recombination process between the matching peroxide and hydroperoxide radicals (reaction 15). Reactions between the α -hydroxyalkoxycyclohexyl and hydroxyl radicals on the one hand (reaction 9), and between the hydroxycyclohexyl and hydroperoxyl radicals on the other hand (reaction 5), may also cause the formation of the discussed 1,1-hydroxy-cyclohexyl hydroperoxide. Contribution of reaction 5 is supposed to be small due to the high reactivity of the hydroxycyclohexyl radical with respect to oxygen [8, 9]. In the literature sources, the hydroxyl-cyclohexyl hydroperoxide is considered a main peroxide product, which is also the source for preparation of the other two peroxide compounds [8].

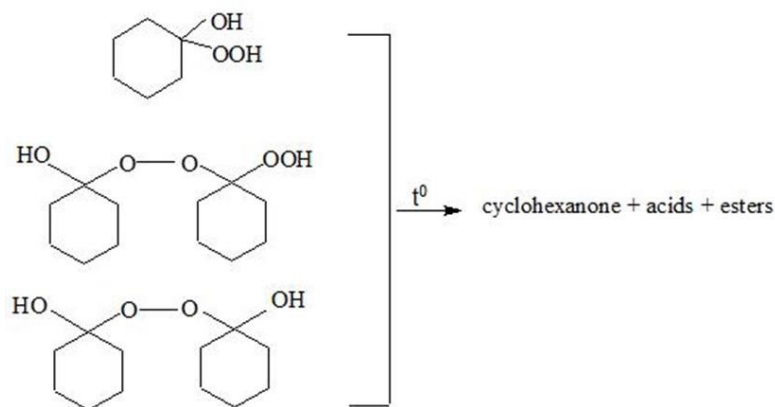
Reaction between organic acid and alcohol in the presence of Lewis or Brønsted acid sites is regarded as the most common route to prepare corresponding esters. The reaction mechanism of the so-called 'Fischer esterification' includes proton addition to the respective acidic groups to become electrophiles that are more reactive. A nucleophilic attack of the alcohol produces a tetrahedral intermediate with two equivalent hydroxyl groups. One of these groups is eliminated after a proton shift (tautomerism) to give water and ester [12]. In our case, it could be assumed that this reaction is the main source for the formation of hexanedioic acid dicyclohexyl ester, hexanoic acid cyclohexyl ester, pentanoic acid cyclohexyl ester, possibly 5-chloropentanoic acid cyclohexyl ester, and cyclohexyl formate. Most likely, this type

of esterification is catalysed by hydrochloric acid, which is the product of various radical reactions involving carbon tetrachloride participation [9].

The presence of hexanoic acid 2-hexenyl ester (E)-, and cyclopentanecarboxylic acid pentyl ester shows that there should be some alternative reaction pathways for the formation of the considered reaction products, because 2-hexen-1-ol and pentanol are not identified among the reaction products. It is seen in Table 1 that there are some esters, formed from acidic and alcoholic components, which have less than six carbon atoms. Changes in the carbon skeleton of cyclohexanol during ozonolysis are most likely related to transformation of various radical intermediates, such as hydroxycyclohexyl (A), α -hydroxy-alkoxy-cyclohexyl (B), α -hydroxyperoxidecyclohexyl (C), and isomerized α -hydroxyalkoxycyclohexyl (D) radicals. The degradation reactions of the mentioned radicals are known from literature sources [11, 13] and are not discussed in detail in the present work.

Since peroxide type products are thermally unstable, their decomposition could also be considered a source for ester formation [14]. It has been established that thermal treatment of various organic peroxides and hydroperoxides causes the formation of acids, carbonyl compounds, and esters (Scheme 2) [15–17]. Furthermore, it could be expected that heating of the reaction mixture during chromatographic analysis could lead to partial or complete decomposition of some of the products containing peroxide-bonded oxygen.

It is generally accepted that the first step on decomposing peroxide-type products is scission of the O-O bond that precedes formation of the corresponding radicals [14, 15]. Further, radical intermediates undergo various transformations and interactions, depending on chemical structure and reaction conditions (temperature and presence of oxygen), resulting in a wide range of ketones, acids, and esters [14, 18].



Scheme 2. Thermal decomposition of peroxide-type products.

In the process of thermal degradation, various gases such as CO₂, CO, and H₂ have also been detected [17, 18]. In this study, a mixture of three different peroxide-type compounds was thermally degraded in the presence of cyclohexanol, cyclohexanone, and a few acids. Under these conditions, differentiation of individual routes that are responsible for the preparation of specific compounds (ketones, acids, and esters) is practically impossible.

In order to study the chromatographically identified contents of the reaction products, samples from the reaction mixture after thermal degradation of peroxide-type compounds were further thermally treated under conditions that according to literature reports provide complete decomposition of all types of peroxides. [14, 18]. It was found that after thermal treatment of the ozonized samples the intensity of the bands at 1724 cm⁻¹ (cyclohexanone) and 1776 cm⁻¹ (esters) was increased by 29 and by about 53%, respectively. In addition, it is important to note that the band at 1710 cm⁻¹ was not changed while the intensity of the peak at 3344 cm⁻¹ due to the cyclohexanol hydroxyl group was reduced.

The chromatographic analysis did not indicate any formation of new products after thermal degradation of the peroxide-type compounds. A significant difference is an increase in share of hexanedioic acid dicyclohexyl ester with respect to the total ester amount from 37% in the initial sample to 66% after thermal treatment. In our opinion, thermal treatment of the ozonated samples creates favourable conditions for esterification between the cyclohexanol and the dominating adipic acid. The intensity of the peak at 1710 cm⁻¹ is not changed, since the amount of acidic groups consumed in the esterification reaction is compensated by that gained because of thermal degradation.

CONCLUSIONS

Upon cyclohexanol ozonolysis the values of the rate constant (at 25 °C) and of the activation energy of the reaction were found to be 3.1 M⁻¹.s⁻¹ and 10.2 kcal/mol, respectively.

Cyclohexanone and 2-chlorocyclohexanone to ester quantitative ratio determined by GC/MSD analysis was 53/47. The amount of the main ester product (hexanedioic acid, dicyclohexyl ester) was 37% of the total ester yield.

REFERENCES

1. P. S. Bailey, Ozonation, in: Organic Chemistry, Vol. 2: Nonolefinic Compounds, Academic Press, NY, USA, 1982.
2. E. T. Denisov, N. I. Mitskevich, V. E. Agabekov, Mechanism of Liquid-Phase Oxidation of Oxygen Containing Compounds, Science and Technique Publishing House, Minsk, 1975.
3. S. D. Razumovskii, S. K. Rakovski, D. M. Shopov, G. E. Zaikov, Ozone and Its Reactions with Organic Compounds, Publ. House Bulg. Acad. Sci., Sofia, 1983 (in Russian).
4. W. L. Waters, A. J. Rollin, C. M. Bardwell, J. A. Schneider, T. W. Aanerud, *J. Org. Chem.*, **41**, 889 (1976).
5. M. Anachkov, P. Karakashkova, V. Georgiev, S. Rakovsky, L. Minchev, T. Batakliiev, *Bulg. Chem. Commun.*, **49**, Special Issue L, 38 (2017).
6. S. K. Rakovsky, M. P. Anachkov, V. I. Iliev, A. E. Eliyas, *J. Adv. Oxid. Technol.*, **16**, 31 (2013).
7. G. E. Zaikov, S. K. Rakovsky, Ozonation of Organic & Polymer Compounds, Smithers, Shrewsbury, UK, 2009.
8. I. V. Berezin, E. T. Denisov, N. M. Emanuel, Intermediate Reactions of Cyclohexanol, in: Sequence of Intermediate Product Conversion During Cyclohexane Oxidation. The Oxidation of cyclohexane, Ch. VI, Pergamon Press Ltd., London, 1966.
9. N. P. Korotkova, A. M. Syroezhko, V. A. Proskuryakov, *Zh. Prikl. Khim.*, **54**, 3, 660 (1981) (in Russian).
10. A. L. Smith, Applied Infrared Spectroscopy, Moscow, Mir, 1982 (in Russian).
11. R. Atkinson, *Atmospheric Environ.*, **41**, 8468 (2007).
12. J. D. Roberts, M. S. Caserio, Basic Principles of Organic Chemistry, Vol. 2, Mir, Moscow, 1978 (in Russian).
13. N. M. Emanuel, D. Gal, Ethylbenzene oxidation (model reaction), Nauka, Moscow, 1984 (in Russian).
14. E. G. E. Hawkins, Organic Peroxides. Their Formation and Reactions, Khimia, Moscow, 1964 (in Russian).
15. N. E. Frankel, Hydroperoxide decomposition, in: Lipid Oxidation (Second edn.), Ch. 4, Woodhead Publishing Ltd, UK, 2012.
16. X. R. Li, H. Koseki, *J. Loss Prev. Process Ind.*, **18**, 460 (2005).
17. I. B. Talouba, N. Bensahlam, H. Medjkoune, N. Mouhab, L. Balland, M. A. Abdelghani-Idrissi, *Thermochim. Acta*, **589**, 270 (2014).
18. S. D. Razumovskii, Ju. N. Juryev, *Neftehimia*, **6**, 737 (1966).

Preparation and electromagnetic properties of epoxy/organoclay/MWCNT/gold nanocomposites

V. A. Angelov^{1*}, T. T. Batakliiev^{1,2}, V. F. Georgiev², E. H. Ivanov¹, R. K. Kotsilkova¹

¹ Open Laboratory for Experimental Mechanics of Micro and Nanomaterials, Institute of Mechanics, Bulgarian Academy of Sciences, Acad. G. Bonchev St., Bldg. 4, 1113 Sofia, Bulgaria

² Institute of Catalysis, Bulgarian Academy of Sciences, Acad. G. Bonchev St., Bldg. 11, 1113 Sofia, Bulgaria

Dedicated to the 80th anniversary of Professor Lachezar Petrov, DSc,
Corresponding Member of the Bulgarian Academy of Sciences

Received: November 19, 2019; Revised: March 8, 2020

This study is concerned with preparation methods and electromagnetic properties of epoxy/organoclay/MWCNT/Au nanocomposites. Nanofillers were prepared by using an impregnation method and characterized through TEM. The nanocomposites were prepared using *in-situ* polymerization technique. Results of this research show a synergistic effect between MWCNTs and AuNPs and improved electromagnetic shield properties of the nanocomposites.

Keywords: preparation, gold nanoparticles, organoclay, MWCNT, electromagnetic properties

INTRODUCTION

A typical gold nanoparticle synthesis involves chemical reduction of gold chloride using sodium borohydride and sodium citrate to produce particles of 2–10 and 12–100 nm size, respectively [1]. To support gold nanoparticles on a stable inorganic or organic matrix is a prime requirement for applications such as catalysis. Varieties of supports as SiO₂, TiO₂, Al₂O₃, Fe₂O₃, carbon, clay, and polymer for stabilizing gold nanoparticles have been reported [2–5]. Zhang *et al.* [6] have reported decoration of gold nanoparticles on layered silicates. They suggest a simple wet chemical method to synthesize clay-APTES-Au nanocomposites where 3-aminopropyl-triethoxysilane (APTES) acts as the linkage. APTES silane terminal forms bonds with the clay surface, while the –NH₂ terminal bonds interact with gold nanoparticles. Patel *et al.* [7] suggest a method for preparation of gold nanoparticles anchored on surfactant-intercalated montmorillonite (MMT). They have used two approaches to synthesize gold nanoparticles. One of the methods involves gold nanoparticle synthesis by reduction of gold salt in hexadecyl trimethyl ammonium bromide (HDTA) and dioctadecyl dimethyl ammonium chloride (DODA) followed by exchange of HDTA and DODA solution containing gold nanoparticles into MMT. In the second approach, HDTA and DODA with gold salt is exchanged with MMT and then reduced to obtain gold nanoparticles.

In the last years, most of the studies of Au-CNT nanocomposites are focused on sensors applications [8–11]. Carbon nanofillers show high wave

absorption properties, however, addition of carbon nanotubes (CNT) to polymer nanocomposites decreases the absorption effect [12, 13]. A combination of carbon nanotubes with gold nanoparticles in nanocomposite materials may lead to synergistic effects between the two nanofillers.

EXPERIMENTAL

Materials

Clay Cloisite 30B (Southern Clay Products, Inc.), organically modified with methyltallow bis-2-hydroxyethyl quaternary ammonium chloride (MT2EtOH) was used as a substrate for gold nanoparticle synthesis. Tetrachloroaurate trihydrate (HAuCl₄·3H₂O) from Sigma-Aldrich was the precursor for the synthesis of gold nanoparticles. Epoxy resin prepolymer Epilox T 19-38/500 (liquid oligomer, $\eta = 450\text{--}550$ mPa.s at 25 °C) and amine hardener Epilox H 10-30 ($\eta = 200\text{--}300$ mPa.s at 25 °C) were purchased from Leuna-Harze GmbH (Germany) and used as received.

Preparation methods for nanofillers, nanodispersions, and nanocomposites

A variation of the wet impregnation method for ‘decoration’ of clay with gold nanoparticles is proposed using an aqueous solution of HAuCl₄ as a precursor. Quaternary alkylammonium MT2EtOH as the organoclay intercalate was used both to attach gold nanoparticles onto organoclay and as a reducing agent. A HAuCl₄ solution in distilled water (3.35 g, 0.00017 mol HAuCl₄) was prepared with a concentration of 1.73 wt%. After that the HAuCl₄ aqueous solution was mixed with 1.71 g clay for 30 min. The resulting mixture was further dried in an

* To whom all correspondence should be sent:
E-mail: v.angelov@imbm.bas.bg

oven at 80 °C for 8 h and then irradiated for several hours using UV light until the color of the treated clay turned to dark gray. Thus, both the organoclay modifier and the UV treatment promoted the subsequent reduction of the gold cations to neutral gold atoms forming gold nanoparticles on the clay platelets. The result of this synthesis was clay decorated with 1.92 wt% of gold nanoparticles with an average size ranged from 5 to 150 nm as described in detail in our previous work [14].

For preparation of ternary nanodispersions an appropriate amount of AuNPs/clay was added to the liquid epoxy resin oligomer and the mixture was homogenized for 30 min by mechanical mixing at 9000 rpm followed by a 30-min ultrasonication treatment at 250 W. The obtained gold/clay/epoxy nanodispersions were then degassed in a vacuum oven for 1 h at 90 °C and cooled to 20 °C. The respective amount of MWCNT nanofiller was added to the three-component nanodispersions.

Solid gold/clay/epoxy/MWCNT nanocomposites were prepared from the nanodispersions using an *in situ* polymerization method. A proper amount of amine hardener was added to the respective dispersion at a molar ratio of epoxy resin to hardener of 100:49. The mixture was poured into a cylindrical mold and cured for 24 h at room temperature followed by postcuring at 100 °C for 4 h. The nanocomposites contained 2 wt% organoclay, 0.5 wt% MWCNT, and the gold nanoparticle content varied from 0.04 to 1 wt% AuNPs.

Characterization methods

Transmission electron microscope JEOL JEM 2100 with selected area electron diffraction (SAED) was used for local area characterization of sample morphology and element analysis. Powder samples were deposited on the TEM holders. High magnification TEM has been provided with magnification from 50 to 1 500 000 times.

Microwave measurements were conducted with RS-408R (ELMIKA) analyzer. IEC 62431:2008(E) standard was used to select the method for measuring the reflective properties of electromagnetic materials during normal radiation. The electromagnetic response of the samples represented as a ratio of transmitted through signal (S21) to reflected signal (S11) was measured in the high frequency spectrum from 0.1 to 1 THz. This spectrum is important due to limited number of materials that can provide protection against such radiation. The measurements were conducted at Institute for Nuclear Research, Belarusian State

University, Minsk, Belarus as part of FP7 FET Flagship-ICT- 604391 Graphene project.

RESULTS AND DISCUSSION

Figure 1 shows a TEM image of the synthesized gold nanoparticles using wet impregnation method on the surface of organoclay before and after UV treatment of the powder. The size and the shape of the gold nanoparticles shown in the TEM image could be further analyzed using PEBBLES software, namely a user-friendly tool, which implements an accurate, unbiased, reproducible, and fast method to measure morphological parameters of nanoparticle (NP) populations from TEM micrographs [15].

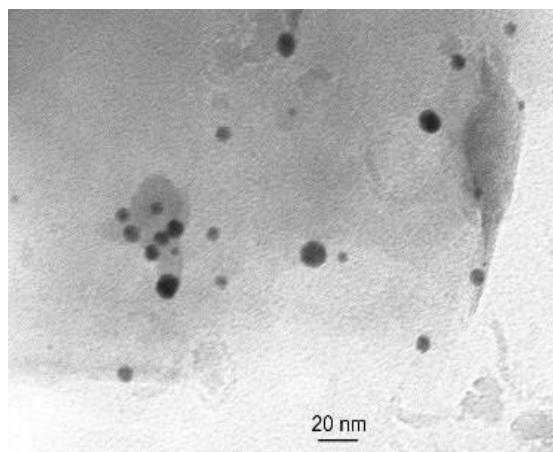


Fig. 1. TEM image with 200 000 times magnification of a sample obtained using wet impregnation method.

Figure 2 shows a TEM image of the sample shown in Fig. 1 using a smaller magnification of 50 000 times. The observed nanoparticles have various shapes, mostly spherical, but also ellipsoid, cylindrical, triangular, or pentagonal.

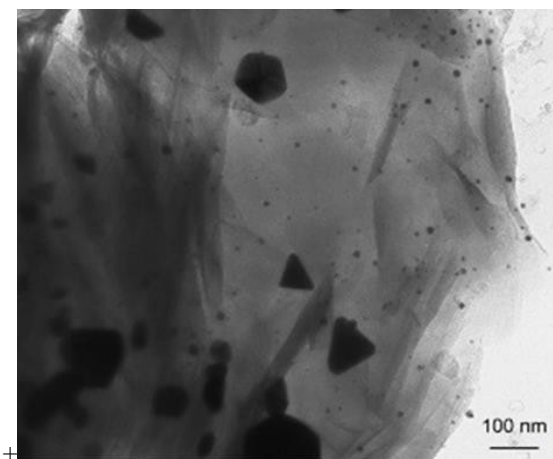


Fig. 2. TEM image with 50 000 times magnification of a sample obtained using wet impregnation method.

Table 1. Statistical analysis of gold nanoparticle size

Statistical analysis of gold nanoparticle size (nm)					
Method	Mean	Standard Deviation	Minimum	Medium	Maximum
Wet impregnation	35.63	34.31	10.30	16.86	146.69

The agglomeration effect can be attributed to the UV treatment that induces further aggregation of the gold nanoparticles [16]. Results from the statistical analysis of the TEM images are shown in Table 1. To investigate the electromagnetic transmittance of nanocomposites in the high frequency spectrum of 0.1–1 THz, the samples were prepared as thin squares with thickness of 1 mm. Figure 3 shows the electromagnetic transmittance of the nanocomposites for the various frequencies.

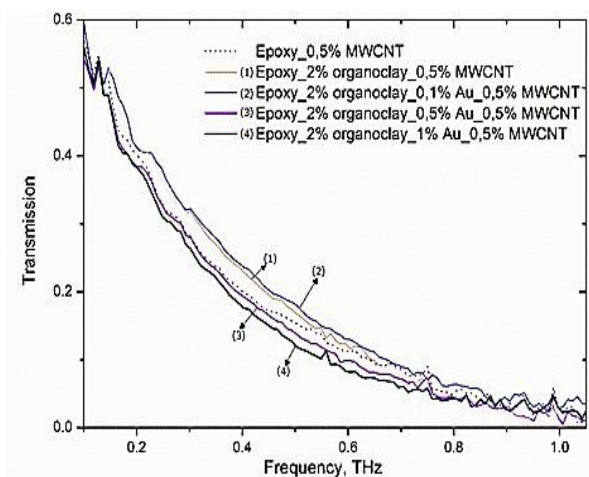


Fig. 3. Electromagnetic properties of epoxy/organoclay/MWCNT/Au nanocomposites measured in the high frequency spectrum.

Lower transmittance values of 0.1–1 THz were observed in the high frequency zone for a high amount of gold nanoparticles (1 wt.% AuNPs). Inserted gold nanoparticles increased the MWCNT effect and improved the electromagnetic shielding behavior of the nanocomposites.

CONCLUSIONS

In the present study, gold nanoparticles over organoclay were prepared using wet impregnation method with distilled water as solvent. The prepared gold nanoparticles were characterized by TEM. The electromagnetic properties of the nanocomposites were studied by applying a microwave measurement

analyzer. Results from the electromagnetic study show that epoxy/organoclay/gold/MWCNT nanocomposites with concentration of 0.5 wt% MWCNTs and 1 wt% AuNPs are promising materials for high-frequency electromagnetic wave absorbers.

Acknowledgements: This study was supported by the COST Action MP1202 and FP7-SME-NanoXCT.

REFERENCES

1. G. Frens, *Nat. Phys. Science*, **241**, 20 (1973).
2. H. Miyamura, R. Matsubara, Y. Miyazaki, S. Kobayashi, *Angew. Chem. Int. Ed.*, **46**, 4151 (2007).
3. W. Yan, S. M. Mahurin, B. Chen, S. H. Overbury, S. Dai, *J. Phys. Chem. B*, **109**, 15489 (2005).
4. S. Carrettin, P. McMorn, P. Johnston, K. Griffin, C. J. Kiely, G. Hutchings, *J. Phys. Chem. Chem. Phys.*, **5**, 1329 (2003).
5. N. Aihara, K. Torigoe, K. Esumi, *Langmuir*, **14**, 4945 (1998).
6. R. Zhang, M. Hummelgard, H. Olin, *Langmuir*, **26**, 5823 (2010).
7. H. Patel, H. Bajaj, R. Jasra, *J. Nanosci. Nanotechnol.*, **9**, 5946 (2009).
8. R. Y. Zhang, H. Olin, *Int. J. Biomed. Nanosci. Nanotechnol.*, **2**, 112 (2011).
9. M. L. Yolaa, N. Atarb, *Electrochim. Acta*, **119**, 24 (2014).
10. J. Jia, Z. Zhou, X. Zhaob, J. Suna, X. Sun, *Biosens. Bioelectron.*, **66**, 590 (2015).
11. C. Tasaltin, F. Basarir, *Sens. Actuators B Chem.*, **194**, 173 (2014).
12. D. Polley, A. Barman, R. K. Mitra, *Opt. Lett.*, **39**, 1541 (2014).
13. A. V. Okotrub, V. V. Kubarev, M. A. Kanygin, O. V. Sedelnikova, L. G. Bulusheva, *Phys. Status Solidi B*, **248**, 2568 (2011).
14. V. Angelov, E. Ivanov, R. Kotsilkova, *Bulg. Chem. Commun.*, **48**, Sp. Issue G, 142 (2016).
15. S. Mondini, A. M. Ferretti, A. Puglisi, A. Ponti, *Nanoscale*, **4**, 5356 (2012).
16. S. Yang, Y. Wang, Q. Wang, R. Zhang, B. Ding, *Colloid. Surf. A Physicochem. Eng. Asp.*, **301**, 174 (2007).

Ozone decomposition on the surface of a novel Mn-Al catalyst in gas phase

T. Batakliiev*, V. Georgiev, M. Gabrovska, D. Nikolova, S. Rakovsky

Institute of Catalysis, Bulgarian Academy of Sciences, Acad. G. Bonchev Str. Bl. 11, 1113 Sofia, Bulgaria

Dedicated to the 80th anniversary of Professor Lachezar Petrov, DSc,
Corresponding Member of the Bulgarian Academy of Sciences

Received: November 13, 2019; Revised: January 07, 2020

Ozone is widely used in some industrial and environmental processes as semiconductor manufacturing, deodorization, disinfection, and water treatment. It is a highly toxic gas being harmful regarding human health at concentrations over 0.1 mg/m^3 . An effective method to purge waste gases containing ozone is the catalytic process of heterogeneous decomposition of the latter. The catalytic activity of alumina-supported manganese oxide samples prepared by incipient wetness impregnation was determined by using a specific experimental set-up. Inlet and outlet ozone concentrations were monitored by means of a BMT 964 UV absorption-type ozone analyzer. The catalysts were activated by calcination and their structure characteristics were studied applying physical techniques as BET and TEM. The catalytic properties of the samples were estimated by conversion of a high quantity of dry ozone ($\sim 10000 \text{ ppm}$) to molecular oxygen. It was found that all tested Mn-Al catalysts are active in the ozone decomposition reaction as over 60% conversion was registered for the sample having 15 wt% manganese oxide on the alumina support. The 15-wt% $\text{MnO}_x/\text{Al}_2\text{O}_3$ catalyst exhibited moderate catalytic activity even under humid gas flow conditions measured by the γ coefficient of ozone decomposition. A reaction mechanism of the catalytic ozone decomposition on Mn-Al catalyst was suggested.

Keywords: Ozone decomposition, Manganese catalyst, Impregnation method, Alumina

INTRODUCTION

Ozone is a major air pollutant because of short-term and long-term harm to the human body. Weschler [1] has estimated that ozone exposure of 43–76% occurs indoors and therefore techniques for ozone decomposition need to be developed. The major source of indoor ozone is coming from outdoor ozone [2], while various indoor ozone sources also exist, such as laser printers, photocopiers, and electrostatic precipitators [3–6]. Studies by United States Environmental Protection Agency (US-EPA) on human exposure to air pollutants indicate that the level of many pollutants in indoor air may be two to five times, and occasionally more than 100 times, higher than the level in outdoor air [7]. Commonly used active catalysts for ozone decomposition include noble metals as Au, Pt, and Pd, economically not likable, and transition metal oxides, which are much more cost-effective [8–13]. Manganese oxide catalysts are of great interest due to their excellent redox properties [14] and applicability to many catalytic reactions such as electro-catalytic water oxidation [15], selective oxidation of olefins in the liquid phase [16], and highly effective removal of toluene [17].

Aluminium oxide is well known as catalyst support [18, 19] and recently it has been used in a

manganese oxide containing catalyst system for gas phase decomposition of ozone and nitrogen dioxide in humid indoor air treatment [20]. In another recent study, nitric acid treated birnessite-type MnO_2 has been designed for humid ozone (O_3) decomposition [21]. A sample treated by nitric acid (H-MnO_2) was reported to exhibit a stable O_3 conversion of $\sim 50\%$ within 24 h under 50% of relative humidity and 115-ppm inlet O_3 concentration. The mechanism of ozone destruction process on the surface of alumina-supported silver catalyst has disclosed the important role of the dissociative adsorption of O_3 producing surface chemisorbed atomic oxygen in sufficiently high concentrations to promote oxidation [22]. Silver ability to provide electrons during the reaction and its high concentration on the catalytic surface was reported to initiate the redox chemical reactions thus increasing ozone conversion to molecular oxygen.

The aim of the present study is to investigate the activity of an alumina-supported manganese oxide system during heterogeneously catalyzed ozone decomposition, and to analyze the influence of humidity in the O_3/O_2 gas flow on catalyst efficiency. Finally, an attempt will be made to suggest a catalytic cycle of the ozone decomposition process on the catalyst surface.

* To whom all correspondence should be sent:
E-mail: todor@ic.bas.bg

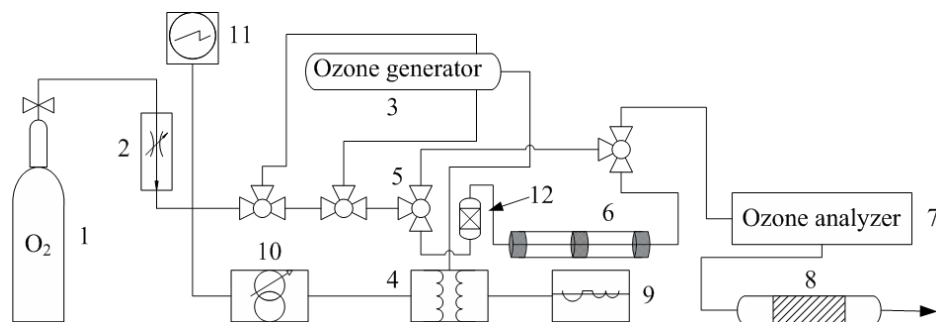


Fig. 1. Experimental set-up for catalytic decomposition of ozone: 1 - oxygen; 2 - flow controller; 3 - ozone generator; 4 - transformer; 5 - three-way stopcock; 6 - reactor charged with catalyst sample; 7 - ozone analyzer; 8 - reactor for decomposition of residual ozone; 9 - current stabilizer; 10 - autotransformer; 11 - voltmeter; 12 - moisturizer.

EXPERIMENTAL

Manganese oxide catalysts (5, 10, and 15 wt%) were synthesized by the incipient wetness impregnation method using aqueous solutions of manganese acetate ($\text{Mn}(\text{CH}_3\text{COO})_2 \cdot 4\text{H}_2\text{O}$, BDH Chemicals >99.99%). Pellet-shaped alumina (Al_2O_3 , BASF, Germany) was employed for catalyst support. After impregnation, the samples were dried at 373 K for 6 h and then calcined at 723 K for 2.5 h to prepare the $\text{MnO}_x/\text{Al}_2\text{O}_3$ catalyst.

Ozone conversion measurements were carried out at room temperature in a tubular glass reactor (10×125 mm) loaded with 0.25 g of catalyst. Figure 1 shows the experimental set-up used for the catalytic tests.

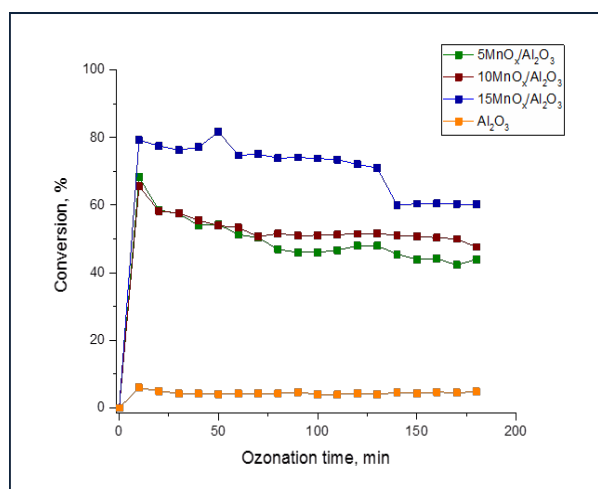


Fig. 2. Ozone conversion as a function of ozonation time for varying manganese oxide contents in the catalyst samples.

Kinetic experiments for determining the catalytic activity in decomposition of dry and humid ozone were performed at O_3/O_2 flow rates ranging from 6.0 to 24 l h^{-1} and inlet ozone concentration of 10000 ppm. The ozone was generated by passing dry oxygen through a high-voltage silent-discharge ozone generator. The inlet and outlet ozone

concentrations were monitored using a BMT 964 UV absorption-type ozone analyzer.

Catalyst textural characteristics were determined by BET (Brunauer-Emmett-Teller) method at a temperature of 77 K using Quantachrome Instruments NOVA 1200, USA. Prior to measurements, the samples were pretreated under vacuum at 200 °C for 2 h. Specific surface area values (S_{BET}) were found by applying BET equation. Pore size (D_{av}) and pore volume (V_{t}) distributions were calculated from the adsorption branches of the nitrogen physisorption isotherms through BJH method.

Catalyst particle morphology and images of the catalyst crystal lattice were observed by means of high-resolution transmission electron microscopy (HRTEM, JEOL 2100, Japan).

RESULTS AND DISCUSSION

The catalytic activities of titania-supported 5, 10, and 15 wt% manganese oxide samples were compared in the decomposition reaction of ozone produced from pure oxygen under dry conditions (Fig. 2).

The 15-wt% MnO_x catalyst exhibited the highest ozone conversion of almost 80%, in spite of the observed decrease of catalytic activity up to 60% during the last 50 min of reaction time. The catalytic behaviour of the other two samples was very similar showing nearly 50% decomposition of the initial ozone. This was found to be far above the catalytic activity of the unmodified pure alumina used as a support.

As the potential application of the prepared catalysts could be for indoor air treatment, the influence of humid conditions is unavoidable, since a relative humidity between 40 and 65% is mostly encountered in indoor premises [20]. The performance of the Mn-Al catalyst in humid reaction environment was duly compared to the work of a catalyst under dry reaction conditions and was estimated by the γ coefficient of ozone

decomposition (Fig. 3). This coefficient depends on the rate constant of the ozone destruction process and shows catalyst efficiency in the reaction as a count of active interactions (leading to decomposition) of the ozone molecules with the catalyst surface [23]. The definition of γ as an essential ozone decomposition parameter is an important issue of the reaction characterizing the kinetic processes on the interface between solid catalyst surface and O₃/O₂ gas stream. It should be mentioned that studies of materials catalytic activity using the coefficient of ozone decomposition, γ , are applicable when the gas phase reactor has a tubular form. The γ coefficient can be calculated through the following kinetic equation:

$$\gamma = \frac{4\omega}{S_{VT}} \ln \frac{[O_3]_0}{[O_3]}$$

where ω is the O₃/O₂ gas flow rate (l h⁻¹); S - catalyst geometric surface area (cm²); v_T - specific heat rate of ozone molecules (m s⁻¹); [O₃]₀ and [O₃] - inlet and outlet ozone concentrations (ppm), respectively.

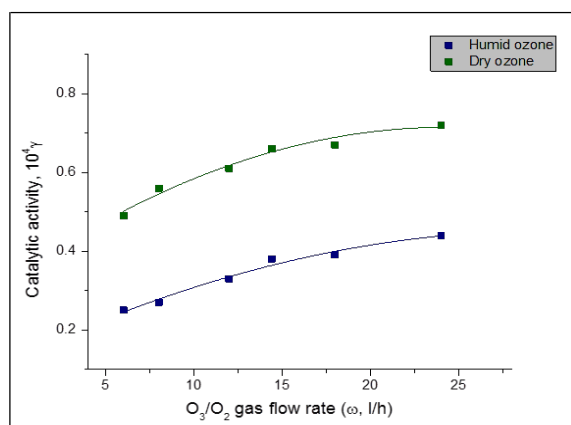
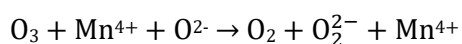


Fig. 3. Flow rate dependence on catalytic activity in dry and humid reaction environment.

As seen in Figure 3, ozone removal efficiency significantly decreases under humid flow conditions but the catalytic performance remains stable and no deactivation was observed. The negative effect of water vapor could be a result of thin film formation on the catalyst surface thus making the ozone diffusion to the active sites more difficult.

An alleged reaction scheme of ozone decomposition consisting of electron transfer from Mn²⁺ catalyst site to ozone molecule is described in Figure 4. The mechanism involves formation of higher oxidation Mn⁴⁺ species generating O₂²⁻ peroxide particles through the redox reaction:



Finally, reduction of the Mn⁴⁺ catalyst site to Mn²⁺ oxidation state occurs upon desorption of a peroxide entity releasing an oxygen molecule (O₂²⁻ → O₂ + 2e⁻). BET specific surface area, pore volume distribution, and average pore size of the catalyst samples are summarized in Table 1. Catalyst textural properties indicate presence of a typical mesoporous structure that can be deduced as well from the nitrogen adsorption-desorption isotherms being of type IV by IUPAC classification. Besides, the hysteresis loop of all catalysts is H2 type, showing a combined mesoporous structure of various size and shape.

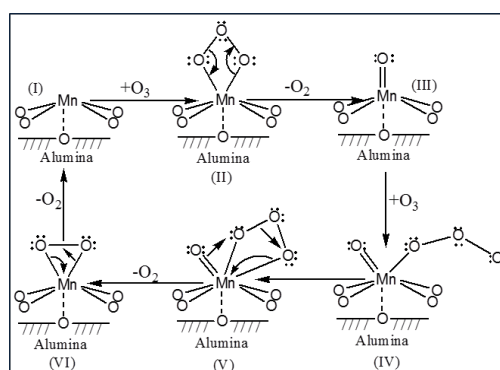


Fig. 4. Mechanism of ozone decomposition on MnO_x/Al₂O₃ catalyst.

Table 1. Textural characteristics of manganese oxide catalysts.

Sample	S _{BET} , m ² /g	V _T , cm ³ /g	D _{av} , nm
Al ₂ O ₃ BASF	253	0.54	8.6
5 wt% MnO _x /Al ₂ O ₃	243	0.52	8.5
15 wt% MnO _x /Al ₂ O ₃	213	0.44	8.3

Isotherm and hysteresis type did not change after modification of the γ-Al₂O₃ support with manganese oxide (Figs. 5a and 5b). The use of incipient wetness impregnation usually leads to catalyst pores filled up by the precursors. Therefore, on comparing the pore structure characteristics of the MnO_x/Al₂O₃ catalyst to the neat γ-Al₂O₃ support one can see a decrease in specific surface area and adsorbed pore volume with increment of manganese content in the samples.

MnO_x/Al₂O₃ catalyst morphology was characterized by HRTEM. Figure 6a is an image of the pure alumina whereas Figure 6b displays well noticeable MnO_x nanocrystalline clusters over the surface of the alumina support. The interplanar spacing of the manganese oxide sample is presented in Figure 6b inset. HRTEM inset image demonstrates catalyst excellent crystallinity suggesting the presence of a tetragonal α-MnO₂ phase with lattice fringe spacing of 0.316 nm corresponding to (310) plane of manganese oxide [9].

Selected area electron diffraction (SAED) patterns are shown in Figures 6c and 6d revealing an improved nanocrystalline state of the manganese

oxide catalyst regarding the unmodified alumina support.

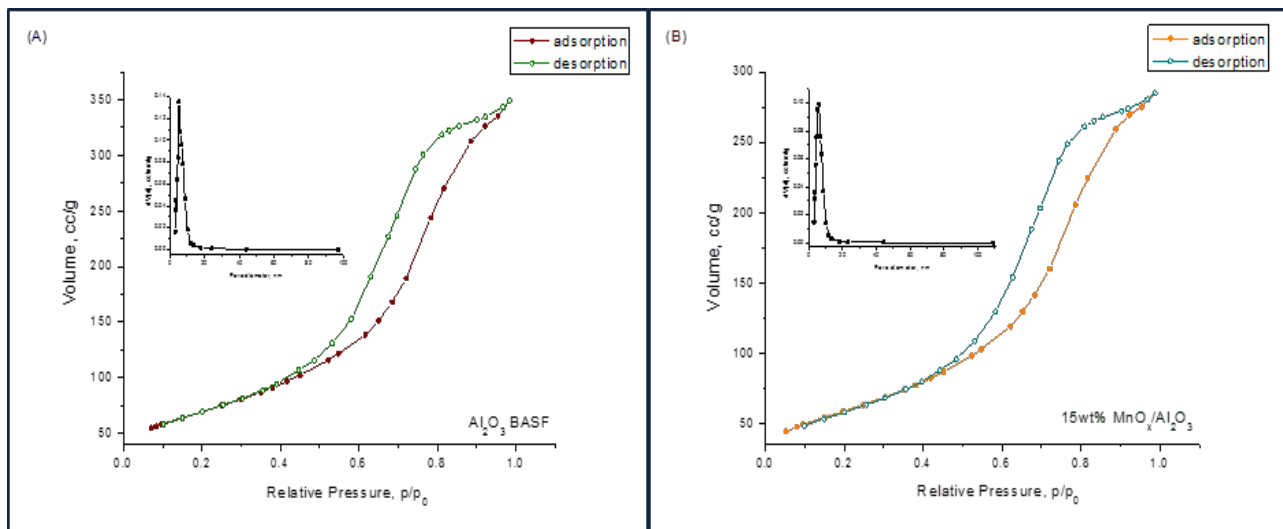


Fig. 5. Nitrogen adsorption-desorption isotherms of pure Al_2O_3 (a) and 15 wt% $\text{MnO}_x/\text{Al}_2\text{O}_3$ catalyst (b)

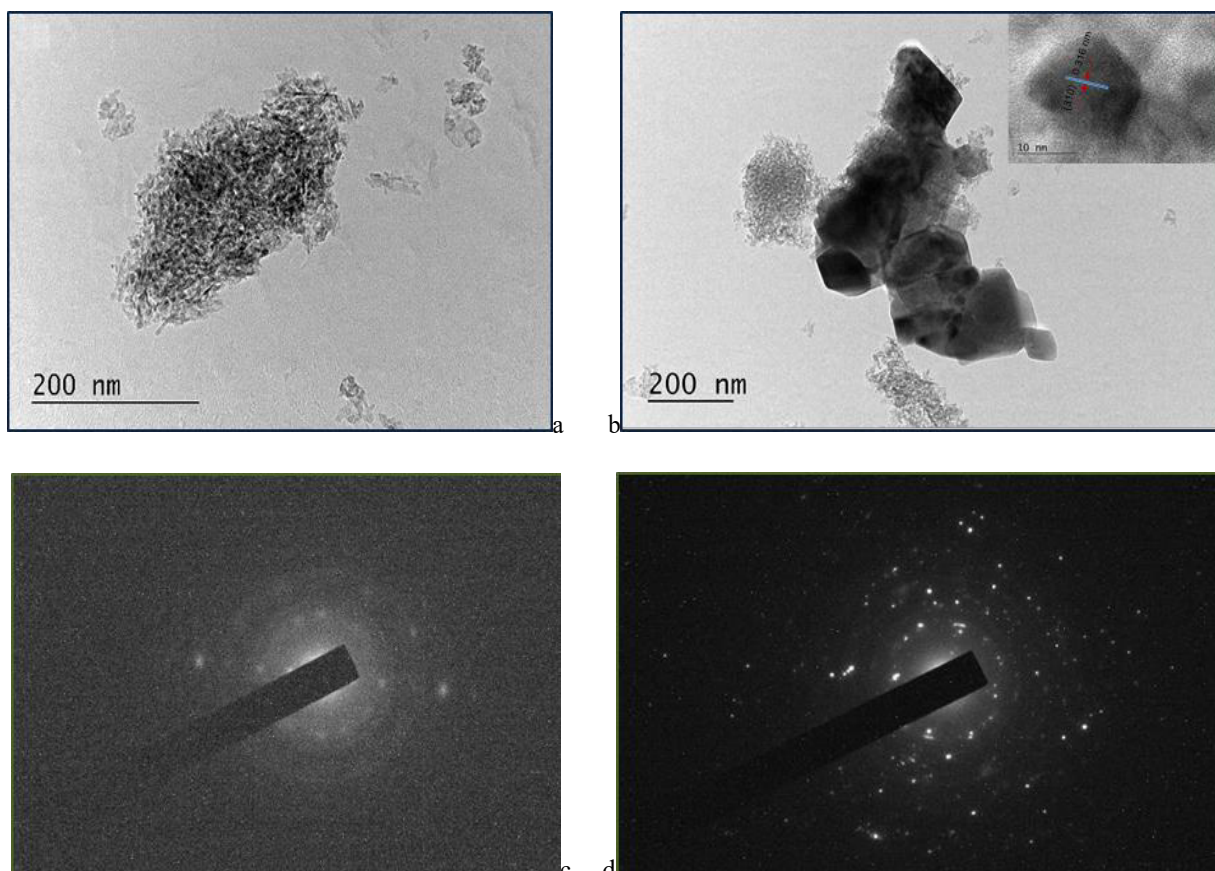


Fig. 6. HRTEM images of Al_2O_3 (a) and $\text{MnO}_x/\text{Al}_2\text{O}_3$ catalyst (b); SAED patterns of Al_2O_3 (c) and $\text{MnO}_x/\text{Al}_2\text{O}_3$ catalyst (d).

CONCLUSIONS

It was found that all analyzed Mn-Al samples show catalytic activity in ozone decomposition reaction as maximum conversion (over 70%) was established for the catalyst having 15 wt% MnO_x. Calculation of γ ozone destruction coefficient at room temperature even under humid reaction environment disclosed that the catalyst keeps moderate performance and did not deactivate under O₃/O₂ gas flow in the range of 6–24 l h⁻¹. The nitrogen adsorption-desorption isotherm of pure alumina is described as typical of mesoporous structure. H₂ hysteresis type did not change after manganese impregnation. TEM images of the catalyst depict excellent nanocrystalline surface morphology of the MnO_x/Al₂O₃ sample.

REFERENCES

1. C. J. Weschler, *Environ. Health Perspect.*, **114**, 1489 (2006).
2. C. J. Weschler, *Indoor Air*, **10**, 269 (2000).
3. T. Tuomi, B. Engström, R. Niemelä, J. Svinhufvud, K. Reijula, *Appl. Occup. Environ. Hyg.*, **15**, 629 (2000).
4. N. Britigan, A. Alshawa, S. A. Nizkorodov, *J. Air Waste Manage.*, **56**, 601 (2006).
5. D. A. Kunkel, E. T. Gall, J. A. Siegel, A. Novoselac, G. C. Morrison, R. L. Corsi, *Build. Environ.*, **45**, 445 (2010).
6. E. Barrese, A. Gioffrè, M. Scarpelli, D. Turbante, R. Trovato, S. Iavicoli, *Occup. Dis. Environ. Med.*, **2**, 49 (2014).
7. R. M. Carver, J. S. Zhang, Z. Wang, Air cleaning technologies for indoor air quality (ACT-IAQ): growing fresh and clean air, New York State Energy Research and Development Authority, 2010, p. 1.
8. Z. P. Hao, D. Y. Cheng, Y. Guo, Y. H. Liang, *Appl. Catal. B: Environ.*, **33**, 217 (2001).
9. G. X. Zhu, J. G. Zhu, W. J. Jiang, Z. J. Zhang, J. Wang, Y. F. Zhu, Q. F. Zhang, *Appl. Catal. B: Environ.*, **209**, 729 (2017).
10. Z. Lian, J. Ma, H. He, *Catal. Commun.*, **59**, 156 (2015).
11. Y. Xiao, X. Wang, W. Wang, D. Zhao, M. H. Qiao, *ACS Appl. Mater. Interfaces*, **6**, 2051 (2014).
12. C. B. Zhang, H. He, K. Tanaka, *Appl. Catal. B Environ.*, **65**, 37 (2006).
13. M. Kobayashi, S. Motonobu, M. Mitsui, K. Kiichiro, *Jap. Pat., CA*, **110**, 120511d (1989).
14. Z. Wu, G. Zhang, R. Zhang, F. Yang, *Ind. Eng. Chem. Res.*, **57**, 1943 (2018).
15. A. C. Thenuwara, E. B. Cerkez, S. L. Shumlas, N. H. Attanayake, I. G. McKendry, L. Frazer, E. Borguet, Q. Kang, R. C. Remsing, M. L. Klein, M. J. Zdilla, D. R. Strongin, *Angew. Chem. Int. Ed.*, **55**, 10381 (2016).
16. R. Ghosh, Y.-C. Son, V. D. Makwana, S. L. Suib, *J. Catal.*, **224**, 288 (2004).
17. F. Wang, H. X. Dai, J. G. Deng, G. M. Bai, K. M. Ji, Y. X. Liu, *Environ. Sci. Technol.*, **46**, 4034 (2012).
18. H. Einaga, S. Futamura, *J. Catal.*, **243**, 446 (2006).
19. F. Lin, Z. Wang, Q. Ma, Y. Yang, R. Whiddon, Y. Zhu, K. Cen, *Appl. Catal. B Environ.*, **198**, 111 (2016).
20. L. Chen, M. Ondarts, J. Outin, Y. Gonthier, E. Gonze, *J. Environ. Sci.*, **74**, 58 (2018).
21. Y. Liu, W. Yang, P. Zhang, J. Zhang, *Appl. Surf. Sci.*, **442**, 640 (2018).
22. T. Batakliiev, G. Tyuliev, V. Georgiev, A. Eliyas, M. Anachkov, S. Rakovsky, *Ozone Sci. Eng.*, **37**, 216 (2015).
23. V. V. Lunin, M. P. Popovich, S. N. Tkachenko, Physical chemistry of ozone, Moscow State University Publisher, 1998 (in Russian).

Parameter optimization of photocatalytic reactors using Taguchi-Grey technique

A. E. Eliyas^{1*}, G. Munteanu², P. Karakashkova¹, M. Fabian³

¹ Institute of Catalysis, Bulgarian Academy of Sciences, Acad. G. Bonchev St., Bl. 11, 1113 Sofia, Bulgaria

² Ilie Murgulescu Institute of Physical Chemistry, Romanian Academy, 202 Splaiul Independentei St., 060021 Bucharest, Romania

³ Institute of Geotechnics, Slovak Academy of Sciences, Watsonova 45, 040 01 Košice, Slovak Republic

Dedicated to the 80th anniversary of Professor Lachezar Petrov, DSc,
Corresponding Member of the Bulgarian Academy of Sciences

Received November 27, 2019; Revised December 28, 2019

The aim of the present study is to optimize the input parameters and the operation of a flat-plate gas-phase continuous flow photocatalytic reactor for air purification in order to achieve maximum efficiency, i.e. maximum conversion degree of ethylene as model air pollutant. The optimization procedure is based on the application of a combined methodology – an experimental plan, which is designed using Taguchi L32 Orthogonal Array and Grey Relational Analysis. The highest conversion degree is achieved at the highest ethylene feed concentration of 10000 ppm, the highest ethylene contact time of 6 min, and the maximal UV-C illumination intensity of 15 mW/cm², achieved at zero distance of illumination and five TiO₂ thin film coatings on the flat plate. Relative humidity has a small effect on the photocatalytic oxidation reaction.

Keywords: photocatalytic reactor, air purification, Taguchi-Grey methodology

INTRODUCTION

Different types and design configurations of photocatalytic reactors are used for air decontamination from volatile organic compounds (VOCs) originating from the industry, presenting a serious environmental problem [1]. One specific type of these photocatalytic reactors is the flat-plate continuous flow reactor [2]. All these types of reactors require operational input parameters optimization in order to achieve maximum efficiency. One possible approach is the procedure, which is based on Design of Experiments (DoE) proposed by different authors, applying different approaches: from complete factorial design to Taguchi's method, which is time-saving and lowering expenses for experimental runs [3–5]. It is a statistical technique used to study many factors simultaneously and most economically. By studying the effects of individual input parameters on the response function the optimal factor combination can be determined. When applied to a design Taguchi's technique helps to seek out the best design among the many alternatives, it is a powerful tool in optimization of experimental setup configuration, including catalytic reactors configuration and operational conditions.

Taguchi is implying orthogonal arrays (OAs), and in our case, five input parameters were selected considering five levels for each input parameter. Most often, it is L25 or L32 orthogonal arrays that are applied for evaluation of the measured output

response; here, the conversion degree of photocatalytic oxidation of ethylene over TiO₂ on single layer or multilayer thin film coatings under UV-light irradiation.

The aim of the study is to improve the efficiency of the photocatalytic oxidation of ethylene in a recently designed and constructed gas-phase flat-plate continuous flow photocatalytic reactor (Fig. 1a, 1b) over commercial TiO₂ semiconductor material Degussa P25, upon varying the photooxidation process parameters. The parameters were feed concentration of ethylene: 1000 to 10 000 ppm (P1), ethylene contact time 120–360 s (P2), under different UV-C illumination intensities of 1.3–15 mW/cm² (P3) at illumination distances from 40 cm to 0 cm, relative humidity RH of the feed of 10–30% (P4) and number of TiO₂ coats from 1 to 5 (P5). Then Grey Relational Analysis (GRA) [6, 7] was applied to find out which ones of the input parameters are significant and what is the percentage of their contribution to the conversion degree and what is the optimal set of the operational conditions to achieve a maximum of the ethylene conversion based on Analysis of Variance statistical tool (ANOVA).

EXPERIMENTAL METHODS

In order to develop a statistical model to analyse the effect of input parameters P1-P5 a first-order mathematical model and ANOVA technique were used to verify model competency. The investigation was focused on the direct effect of the input process parameters on the single response function: degree

* To whom all correspondence should be sent:
E-mail: alel@ic.bas.bg

of complete oxidation of ethylene (conversion degree).

The significant input parameters are: intensity of illumination, ethylene contact time, and humidity. The Taguchi L32 orthogonal array was used for the design of the experiments and to optimize the parameters. Regression coefficients were calculated using five factors on five levels central composite design with 95% confidence level. The central composite first-order design is the most efficient tool in response with a minimal number of experimental runs without significant loss of accuracy. The ANOVA comprises the sum of values and degrees of freedom. The sum is transformed into contributions from the regression model, as well as residual error. A first-order model was developed to predict the resultant response function F (conversion degree): $F = f(C_e, \tau_e, I, RH, N_c)$; the regression coefficients were calculated using a five-factor on a five-level central composite design. If the calculated value of F is greater than the standard tabulated value for 95% confidence level, then the model is considered to be adequate inside the confidence limit. This validates

the significance of the model – the testing was done using the ANOVA. The value of probability 95% means that model deviation is less than 0.05, which proves the significance of the model. The determination coefficient R^2 exhibits the goodness of fit of the model.

In the gas-phase experimental runs a continuous flow flat-plate steady-state reactor for air purification (Fig. 1a, Fig. 1b) was applied and the degree of conversion of ethylene was evaluated using LANCOM III gas analyzer (UK) at different flow rates of ethylene or nitrogen flow rates through the water vapor saturator (different contact times).

The relative humidity of the feed mixture as an important reaction parameter was varied without any variation of the O_2/C_2H_4 feed ratio. Different light intensities were achieved by varying the distance between the lamp and the flat plate quartz glass illumination window. The illumination intensity was 1.3 to 15 mW/cm^2 for the UV-C light. Ethylene was selected as contaminant; its feed concentration was varied by changing the Matheson settings.

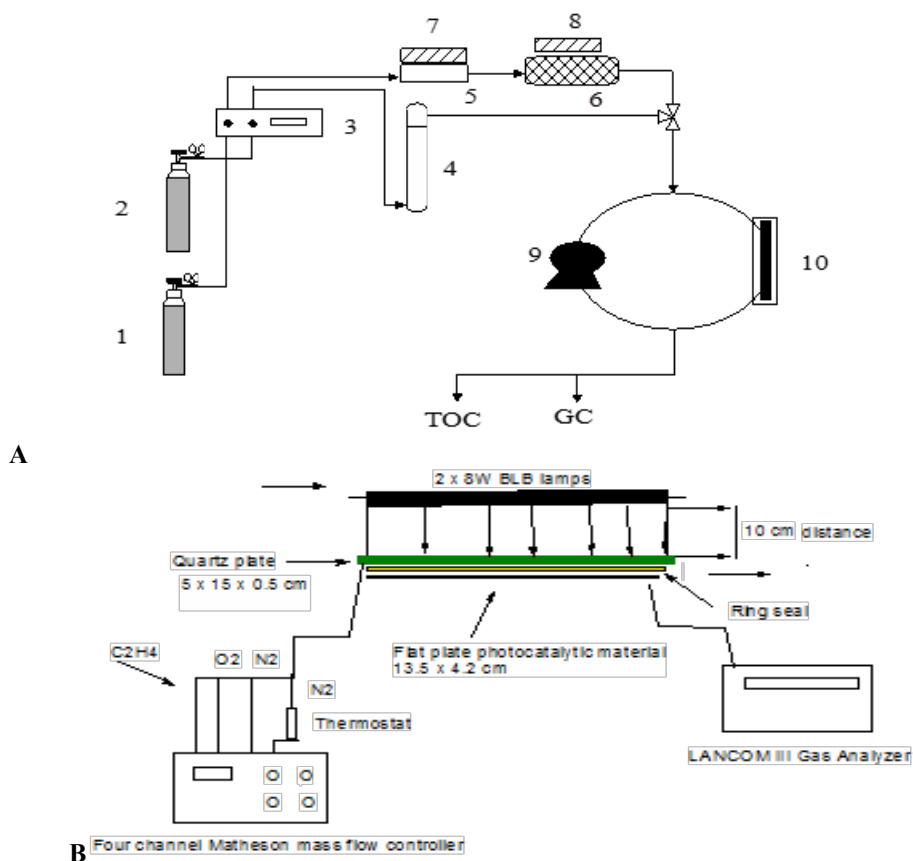


Fig. 1. A. Gas-phase flow-circulation photocatalytic reactor equipped with GC and TOC: 1&2 – O_2 and C_2H_4 gas cylinders, 3 – Matheson mass flow controller; 4 – water vapor saturator; 5 – zeolite dehumidifier; 6 – flat plate reactor; 7 – heating tape; 8 – light source; 9 – gas circulation pump; 10 – cylindrical thin film reactor with built in lamp. B. Flat-plate reactor with quartz glass illumination window: Matheson mass flow controller for the feed gaseous mixture and LANCOM III gas analyzer for the converted mixture.

Prior to layered deposition of the photocatalytic material as powder form on a TLC sheet (Al foil, Merck, pre-coated with a 0.2 μm SiO_2 film) it was dispersed in H_2O by sonication to obtain a stable slurry (UP200S Hielscher ultrasonic processor 24 kHz, Germany). The regime of operation of this photocatalytic reactor has already been described in a previous work [2]. The authors have specified the optimal experimental conditions to achieve maximal conversion degree, namely, optimal coating thickness to guarantee kinetic region of operation avoiding any diffusion limitations, as well as the time interval on stream to achieve steady state operation for a such size of photocatalytic reactor.

RESULTS AND DISCUSSION

We paid special attention to the preparation of TiO_2 layers. The commercially available photocatalyst Degussa P25 TiO_2 (75% anatase and 25% rutile) was used as standard material. The single-point BET method (30% N_2 + 70% He mixture at inlet flow rate of 15 ml/min – adsorption of N_2 as a monolayer at the boiling temperature of liquid nitrogen 77 K) showed that the Degussa P25 TiO_2 specific surface area was 50 m^2/g .

The suspension of nanosized particles was sonicated for 30 min in impulse regime: 24 kHz, 100% amplitude, cycle 0.5, which turned out to be more efficient than the continuous cycle 1.0. Thereafter it was deposited on thin layer chromatography sheets (SiO_2 coated) by the capillary technique with directing air stream until obtaining the optimal coating thickness of 1 mg/cm^2 [2]. This is a standard reference coating for making comparison between different photocatalytic materials. TiO_2 over-layer is located on the sub-layer of large angular micrometer-sized SiO_2 crystals (SEM) on the TLC sheet. Anatase (A) is generally accepted to be the better photocatalyst under UV-illumination than rutile (R) whose crystals are more compact and therefore the specific surface area is smaller. However, there exists a synergistic effect between anatase and rutile since their band gaps are different (3.0 eV for rutile corresponding to an absorption edge $\lambda_{\text{max}} = 413$ nm). The positions of the conduction and the valence bands of these two semiconductors allow charge carrier separation as the valence bands merge and therefore the holes are migrating freely. However, the conduction bands of A and R are separated and the photoexcited electrons remain localized. The Degussa company has made use of this synergistic effect and produces the best commercially available photocatalyst having an A/R ratio of 3:1. If this charge separation model is correct then the best A/R ratio would be 1:1; however, in this

specific case the surface area would be too low because of the high content of rutile. So, Degussa have found an optimal combination between synergism and specific surface area at 3:1.

The measure of the photocatalytic activity was taken to be the ethylene degree of conversion (single response function) as a result of varying the five input parameters (Table 1). The O_2 feed flow rate created a large excess of oxygen with respect to the stoichiometrically required amount for the oxidation reaction. This allowed us to disregard the difference between the inlet and outlet oxygen concentrations under illumination. Thus, the sixth variable P6 was not included in the consideration, which simplifies the reaction picture. So, the bimolecular reaction of Langmuir-Hinshelwood type of mechanism is reduced to a pseudo first-order kinetic equation following only the pollutant concentration decrease with the time. In the case of the air purification photocatalytic reactor (continuous air flow mode or flow-circulation regime of operation) the conversion degree of the pollutant (ethylene flow) is measured as a function of the pollutant contact time.

Feeding C_2H_4 and O_2 by two independently regulated channels allows varying the feed ethylene concentration (P1) but at the same time also the ethylene contact time (P2). In all the experimental runs the oxygen concentration is in large excess with respect to the stoichiometrically required oxygen amount to achieve 100% conversion of ethylene. So, this parameter can be disregarded in our analysis as we can accept that the outlet concentration of oxygen remains practically unchanged, i.e. it is practically the same as the inlet concentration in the photocatalytic reactor and, therefore, it can be included in the value of the effective kinetic constant in the kinetic equation.

The illumination intensity parameter can be varied by changing the UV-C lamp distance to the TiO_2 thin film coating. The use of two independently regulated channels for feeding N_2 enables the variation of the humidity of the gaseous mixture (parameter P4). This is a very important operational parameter [8] during photocatalytic oxidation processes as the water vapour is the source of the hydroxyl radicals formed under UV-light irradiation [9], being the main active particles oxidizing practically all classes of organic compounds. The number of TiO_2 thin film coatings deposited on the TLC sheet was also varied (P5). All these considerations make a set of 5 parameters on 5 levels (Table 1), which is described by an orthogonal array L32 (5^5) of the central composite design matrix (Table 2).

Table 1. Five input parameters on five levels under UV-C light illumination

Symbol	Input parameter	Level 1 -2	Level 2 -1	Level 3 0	Level 4 1	Level 5 2
P1	C ₂ H ₄ inlet concentration	1 000 ppm	3 000 ppm	5 000 ppm	7 000 ppm	10 000 ppm
P2	C ₂ H ₄ contact time	2 min	3 min	4 min	5 min	6 min
P3	Illumination distance	0 cm	10 cm	20 cm	30 cm	40 cm
	Intensity	15 mW/cm ²	11.5 mW/cm ²	8.1 mW/cm ²	4.7 mW/cm ²	1.3 mW/cm ²
P4	Relative humidity	10%	15%	20%	25%	30%
P5	Number of TiO ₂ coats	1	2	3	4	5

Table 2. Experimental design based on the central composite plan matrix.

Trial No	P1	P2	P3	P4	P5	Response conversion
1	-1	-1	-1	-1	1	26.1
2	1	-1	-1	-1	-1	37.8
3	-1	1	-1	-1	-1	30.4
4	1	1	-1	-1	1	53.0
5	-1	-1	1	-1	-1	10.3
6	1	-1	1	-1	1	22.4
7	-1	1	1	-1	1	31.8
8	1	1	1	-1	-1	26.4
9	-1	-1	-1	1	-1	20.5
10	1	-1	-1	1	1	18.3
11	-1	1	-1	1	1	20.6
12	1	1	-1	1	-1	50.0
13	-1	-1	1	1	1	26.8
14	1	-1	1	1	-1	25.4
15	-1	1	1	1	-1	46.9
16	1	1	1	1	1	39.3
17	-2	0	0	0	0	22.8
18	2	0	0	0	0	37.5
19	0	-2	0	0	0	28.9
20	0	2	0	0	0	49.5
21	0	0	-2	0	0	42.6
22	0	0	2	0	0	38.9
23	0	0	0	-2	0	31.42
24	0	0	0	2	0	27.7
25	0	0	0	0	-2	33.9
26	0	0	0	0	2	53.3
27	0	0	0	0	0	44.0
28	0	0	0	0	0	45.1
29	0	0	0	0	0	43.8
30	0	0	0	0	0	44.1
31	0	0	0	0	0	46.4
32	0	0	0	0	0	44.7

The main task of the study was the development of a mathematical function (statistical model), based on five input parameters on five levels, to predict the values of the single response function, which have already been measured experimentally (Table 2) with possibly small model deviation. This function linearly depends on all the five input parameters; its expression being determined by multilinear regression. In the regression procedure, the real values of the input parameters are replaced with the corresponding Taguchi parameters (Table 2). The model should describe the relation between the input process parameters and the response. This would

enable to determine the optimal process variable levels that could produce a desirable output (the highest conversion degree). Therefore, in the current investigation a first-order mathematic model consistent with first-order kinetics [10] was developed to predict the resultant conversion degree.

The response function F can be expressed as follows:

$$F = f(C_e^0, \tau_e, I_{uv}, RH, N_c) \equiv C_1P_1 + C_2P_2 + C_3P_3 + C_4P_4 + C_5P_5 + b,$$

where C_e^0 is the inlet concentration of ethylene, τ_e is the ethylene contact time, I_{uv} is the intensity of UV-C light irradiation, RH is the relative humidity, N_c is the number of TiO₂ coatings on the TLC flat plate and P_1, P_2, \dots, P_5 are the corresponding Taguchi working parameters (Table 2). The regression coefficients C_1, C_2, \dots, C_5 , and b were calculated by multilinear regression using a five-factor five-level central composite design in MINITAB 15 BASICS statistical software with 95% confidence level.

The mathematical model developed using the evaluated regression coefficients for calculating the resultant conversion degree is given by the following expression:

$$F = 33.18 + 3.69P_1 + 6.33P_2 - 1.45P_3 + 0.09P_4 + 1.22P_5.$$

According to the above expression the optimal maximum conversion is obtained when $P_1 = 2, P_2 = 2, P_3 = -2, P_4 = 2$ and $P_5 = 2$, i.e. when $C_e^0 = 10000$ ppm C₂H₄, the contact time $\tau_e = 6$ min, $I_{uv} = 15$ mW/cm², $RH = 30\%$ and $N_c = 5$. In Table 2 no trial is characterized by these Taguchi parameters: 2, 2, -2, 2, 2 and, consequently, it is not possible to check whether this mathematical prediction is in agreement or not with experimental data. In spite of this fact, we have to mention that the results obtained in trials 4, 12, 18, 20, 21, and 26 are in accord with the expression above.

Another item that could be concluded taking into account the values of the coefficients from this expression, is whether a hierarchy between the input parameters can be established: the higher the value of a coefficient, the greater is the importance of the corresponding parameter. Consequently, the order of

the importance of the parameters is the following: contact time, ethylene concentration, illumination intensity, and number of coats. According to the obtained expression the conversion is only slightly sensitive to the change of the relative humidity.

Table 3. Comparison of the observed values and the predicted values of ethylene conversion degree (response function) and the resulting percentage of error.

Trial No	Observed conversion	Predicted conversion	Error, %
1	26.1	25.74	1.38
2	37.8	30.68	18.84
3	30.4	35.96	15.46
4	53.0	45.78	13.62
5	10.3	20.40	49.51
6	22.4	30.22	25.88
7	31.8	35.50	10.42
8	26.4	40.44	34.72
9	20.5	23.48	12.69
10	18.3	33.30	45.05
11	20.6	38.58	46.60
12	50.0	43.52	12.96
13	26.8	23.02	14.10
14	25.4	27.96	9.16
15	46.9	33.24	29.13
16	39.3	43.06	8.73
17	22.8	25.80	11.63
18	37.5	40.56	7.54
19	28.9	20.52	29.00
20	49.5	45.84	7.39
21	42.6	36.08	15.31
22	38.9	30.28	22.16
23	31.42	33.00	4.85
24	27.7	33.36	16.97
25	33.9	30.74	9.32
26	53.3	35.62	33.17
27	44.0	33.18	24.59
28	45.1	33.18	26.43
29	43.8	33.18	24.25
30	44.1	33.18	24.76
31	46.4	33.18	28.49
32	44.7	33.18	25.77

Validating the adequacy of the model, ANOVA was used to assess the relationship between the response variable and one or more predictor variables. Thus, the significance of each process variable is evaluated for determining the quality characteristic. Table 3 compares the observed and predicted values and the resulting percentage of error.

CONCLUSION

The highest conversion degree was achieved at the highest concentration of 10000 ppm C₂H₄, the maximal illumination intensity at 0 distance of illumination, the highest contact time of 6 min, and five TiO₂ thin film coatings, whatever the relative humidity.

Acknowledgement: The authors are grateful for the sponsorship by the Bulgarian National Science Fund under Contract DNTS/Slovakia/01/2.

REFERENCES

1. I. Grcic, G. LiPuma, *Appl. Catal. B: Environ.*, **211**, 222 (2017).
2. A. Eliyas, K. Kumbilieva, L. Petrov, *Nanosci. & Nanotech.*, **9**, 50 (2009).
3. R. K. Roy, *Design of Experiments Using the Taguchi Approach: 16 Steps to Process Improvement*, Wiley Intersc. Publ., New York, 2001.
4. D. S. Sivia, *Data Analysis. A Bayesian Tutorial for Scientists and Engineers*, Oxford Sci. Publ., Clarendon Press, Oxford, 1996.
5. A. L. Horvath, *Calculations in Industrial Chemistry. A Series of Solved Problems*, Wiley & Sons, 1996.
6. M. Kumar Das, K. Kumar, T. K. Barman, P. Sahoo, *Procedia Mater. Sci.*, **6**, 729 (2014)
7. M. Sankar, A. Gnanavelbabu, K. Rajkumar, *J. Balk. Tribol. Assoc.*, **23**, 431 (2017)
8. T. N. Obee, S. O. Hay, *Environ. Sci. Technol.*, **31**, 2034 (1997)
9. K.-L. Chang, K. Sekiguchi, Q. Wang, F. Zhao, *Aerosol Air Qual. Res.*, **13**, 618 (2013)
10. K. V. Kumar, K. Porkodi, F. Rocha, *Catal. Commun.*, **9**, 82 (2008).

Efficient squaraine dye photosensitized TiO₂/rGO catalyst with enhanced catalytic activity for degradation of Methylene Blue

V. F. Georgiev*, S. I. Minkovska, T. T. Batakliiev, P. A. Karakashkova, M. P. Anachkov

Institute of Catalysis, Bulgarian Academy of Sciences, 1113 Sofia, Bulgaria

Dedicated to the 80th anniversary of Professor Lachezar Petrov, DSc,
Corresponding Member of the Bulgarian Academy of Sciences

Received: November 11, 2019; Revised: December 19, 2019

Synergistic effect of coupling a squaraine dye (SQ) as a photosensitizer with a composite catalyst containing titania and reduced graphene oxide (TiO₂/rGO) has been investigated. A three-component TiO₂/rGO/SQ catalyst was synthesized and its ability to improve Methylene Blue discoloration in aqueous solution under visible light irradiation has been tested. XRD, SEM, TEM, and VIS spectroscopy were employed for sample characterization. A squaraine dye excited by visible light is capable of transferring electrons to TiO₂/rGO material, which contributes to increasing the apparent discoloration rate constant up to 0.028 mol/l.s., which is 18 times higher than that of bare titania.

Keywords: Photocatalysis; Squaraine; Photosensitizer; TiO₂; Graphene

INTRODUCTION

Water pollution caused by textile industry is a matter of great concern these days. Dye effluent contains given substances, which can be toxic, carcinogenic or mutagenic to living organisms [1]. Treatment of dye effluent is a significant challenge because wastewater can be complex containing different types of chemicals. The use of semiconductor-photocatalyzed degradation of organics in the wastewater pollutants is a promising method [2, 3]. Several semiconductors such as TiO₂, ZnO, Fe₂O₃, WO₃, SnO₂, ZrO₂, CdS, SrTiO₃, and ZnS have band gap energies sufficient for catalyzing a wide range of chemical reactions [4, 5]. Considerable efforts have been devoted to the design of long-term operating photocatalytic systems exhibiting high efficiency and stability for transforming light into chemical energy. Fenton and photo-Fenton catalytic processes, where Fe³⁺ cations have a beneficial effect because of the ability of Fenton reactants to consume H₂O₂ in the aqueous phase [6–9] have been studied under various experimental conditions for organic pollutants removal from wastewaters. The overall efficiency of the photocatalysts is strongly dependent on the lifetime of the separated electron-hole charge carriers generated under UV light irradiation. In chemically effective semiconductor photocatalysts, electron-hole pair recombination could be suppressed by trapping the photogenerated electron and hole or both of them near the surface.

Further, these charges are transferred across the interphase boundary and upon reaching the adsorbed substances they can become involved in oxidation-

reduction reactions [10]. Heterogeneous photocatalysis using TiO₂ as a photocatalyst appears to be the most widely deployed purification approach because of the strong oxidizing potential of the titania positively charged holes providing the best combination between catalytic performance and stability in aqueous media [11, 12]. Doping the TiO₂ nanoparticles with noble metals has been proven an efficient approach for increasing their photocatalytic activity. Photogenerated electrons, being injected in the conduction band of the titania, might be transferred to the dopant lowest unoccupied molecular orbital (LUMO) and subsequently further to the absorbed species, which are being reduced. Coupling the titania with gold, platinum, palladium, and silver has been widely applied for improving the destructive power of the photocatalysts acting as traps of electrons by transferring them to the outer system [13–15]. These photocatalysts can be activated only under ultraviolet (UV) light irradiation, under which they work efficiently. However, their activity is limited as ozone in the stratosphere absorbs UV light and only 4–6% can reach the earth surface. In order to overcome this disadvantage and extend photocatalyst efficiency to the visible area, titania is being doped with metal ions including Fe, Au, Gd, and Ag, or non-metallic ions such as C, N, and S [16–18].

Graphene oxide (GO) can be easily mixed with different polymers and other materials, thereby improving the mechanical and electromagnetic properties [19, 20]. Moreover, the surface properties of the graphene make it suitable for the production of composite material in combination with TiO₂ having excellent adsorption which can facilitate the

* To whom all correspondence should be sent:
E-mail: vlado@ic.bas.bg

efficacy in photodegradation of pollutants.

Thanks to the unique properties of graphene, the composite simultaneously combines three excellent properties, i.e., increasing the adsorption of pollutants, expanding the absorption range of light, and separation of charges by efficiently transferring electrons from titania to the graphene. On the other hand, some transition metal-based dyes can be used as titania sensitizers in the visible spectrum because of their high molar absorption coefficient, as well as broad absorption band [21–24]. Due to the exceptionally rigid, planar and zwitterionic structures, squaraines have strong absorption (molar absorptivity, ϵ , equal or more than $10^5 \text{ l}\cdot\text{mol}^{-1}\cdot\text{cm}^{-1}$) in the visible to the near-IR region. Squaraines intense absorption properties are suitable for applications related to the photosensitization phenomenon [25]. Sensitizing a TiO₂ semiconductor with squaraine may produce a highly effective photocatalytic system due to the electron transfer from the excited dye to the titania conduction band or pre-adsorbed molecular oxygen. Effective photocatalytic decomposition of different types of pollutants through dye-sensitized TiO₂ systems is due to a simultaneous effect of both semiconductor and dye. The critical factor in this cooperation is the charge transfer ($e^- - h^+$) as the mechanism and the type of active oxidizers produced are affected by the nature of the irradiation source. Typically, these photocatalysts are activated by irradiation with visible or sunlight, but the best efficiency for contaminant degradation is generally obtained under solar light [26].

The purpose of this work is to investigate the synergistic effect resulting from combination of a squaraine dye acting as a photosensitizer and a TiO₂/GO composite. The photocatalytic experiments were carried out under visible light irradiation in order to examine squaraine dye ability for enhancing the photoactivity of the TiO₂/rGO nanocomposite in discoloration of Methylene Blue (MB).

EXPERIMENTAL

Preparation of photocatalyst

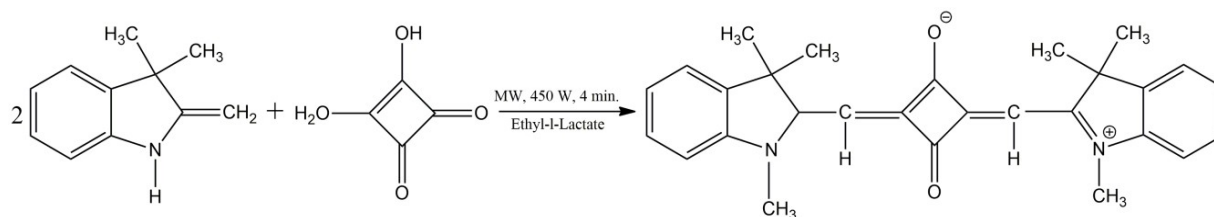
Graphite powder ($\geq 150 \mu\text{m}$, $\geq 99.99\%$ trace metals basis; Sigma-Aldrich), sulfuric acid (98%, Merck), sodium nitrate, potassium permanganate, and hydrogen peroxide solution (30 wt.% in H₂O) were used for the synthesis of graphene oxide. TiO₂ (Degussa, P25) and Methylene Blue (MB) were employed as ingredient for preparation of the catalyst and as substrate, respectively. The following Sigma-Aldrich chemicals were used as commercial products of analytical grade without further purification for the synthesis of squaraine dye: 1,3,3-

trimethyl-2-methyleneindoline, squaric acid, and ethyl *L*-lactate.

Graphene oxide was synthesized using modified Hamer's method. The latter can be divided into three stages. The first 'cold stage' involved 5 g of graphite, 115 ml of sulfuric acid, and 2.5 g of sodium nitrate mixed in an ice bath for 30 min. Then 15 g of KMnO₄ were slowly added while stirring over 2 h and keeping the temperature below 5 °C since upon the reaction $\text{KMnO}_4 + \text{H}_2\text{SO}_4 = \text{K}_2\text{SO}_4 + \text{Mn}_2\text{O}_7 + \text{H}_2\text{O}$ the resulting Mn₂O₇ decomposes explosively at a temperature about 50 °C. During the second 'mid-stage', the temperature was raised to 45 °C under stirring for 1 h. Finally, 230 ml of distilled water were added, and the temperature was raised to 95 °C while stirring for 30 min. In the third 'high-temperature stage', reduction of the residual permanganate and manganese dioxide to colorless soluble manganese sulfate was achieved by adding 600 ml of distilled water and 150 ml of H₂O₂ (9%) to the mixture. The suspension was filtered, washed in 5% HCl and then in distilled water to reach neutral pH, and dried at 60 °C. The dried cake was added to 50 ml of water under stirring and then sonicated for 6 h. The dry form of graphene oxide was obtained by centrifugation, followed by drying at 60 °C [27].

TiO₂/rGO composite containing 5 wt% rGO was prepared by dissolving 10 ml of concentrated GO solution (~150 mg GO) in 500 ml of deionized (DI) water and then put under ultrasonic dispersion for about 5 h. Then 0.5 g of titania powder were gradually added into the solution to anchor the TiO₂ particles onto GO surfaces. In order to turn GO into graphene 3 g of sodium hydroxide were further added as well. After 10 h of vigorous stirring the resulting solution was transferred to a Teflon-sealed autoclave and kept under 120 °C for 24 h. Then the resulting suspension was washed with DI water, filtered, and dried at 60 °C. A reference rGO sample was prepared similarly without adding TiO₂ into the hydrothermal vessel.

For squaraine dye synthesis (Scheme 1) 1,3,3-trimethyl-2-methyleneindoline (10 mmol, 1.73 g, ~1.77 ml), squaric acid (5 mmol, 0.57 g), and ethyl *L*-lactate (10 ml) were placed into a 100-ml Erlenmeyer flask. The reaction mixture was heated in a microwave oven at 450 W to 140 °C. After 1 min, the reagents were dissolved and the liquid turned blue. The reaction was kept at 140 °C for 4 min. The mixture was allowed to cool down to room temperature, then diluted with ethanol (10 ml), and placed in water (200 ml) with ice (50 g). The resulting precipitate was filtered, washed with 200 ml of hot water until colorless filtrate, and finally air-dried.



Scheme 1. Preparation of squaraine dye.

Ternary composite catalyst, TiO₂/rGO/SQ, was prepared by adding 20 mg of SQ into a 70-ml water suspension containing 60 mg of TiO₂/rGO. After continuous ultrasonication for 3 h and subsequent stirring for 2 h the resulting product was filtered and dried at 60 °C until reaching a constant mass.

Methods and experimental setup

X-ray diffraction (XRD) measurements were carried out at room temperature using a Bruker D8 Advance powder diffractometer with Cu K α radiation source and SolX detector. The samples were scanned at 2θ angles ranging from 10° to 80° at a scanning rate of 0.04° s⁻¹.

Photocatalyst morphology was examined by a transmission electron microscope (JEOL 2100). Visible light spectra of the samples were recorded on a Shimadzu UV-2700 Vis scanning spectrophotometer.

Studies on MB photocatalytic discoloration were performed in a self-constructed cylindrical reactor (150 mm outer diameter, 130 mm high) at 25 °C, maintained by recirculating water through the reactor jacket. Photocatalytic efficiency of the catalyst was evaluated based on the degradation rate of MB (10 mg/l) in water under visible light irradiation employing a halogen lamp. A 400-ml reaction suspension containing 10 mg/l MB and 0.1 g/l catalyst was stirred for 30 min in the dark to achieve a possible adsorption-desorption equilibrium on the catalyst surface. Samples were collected at every 20 min and filtered (Whatman, Grade 42) prior to measuring absorption in the visible spectrum.

RESULTS AND DISCUSSION

Catalysts characterization

Crystalline phase composition of the prepared catalyst samples was analyzed by XRD. Fig. 1 shows the XRD patterns of the samples used in this study. The main peaks in the spectrum of the TiO₂/rGO/SQ composite catalyst correspond to tetragonal TiO₂ (anatase, 73%) dominating over rutile (23%) which was also observed in the spectrum. Comparing the XRD spectra of the individual samples presented in Fig. 1 one can see that during hydrothermal treatment as a stage of the synthesis, GO has been

successfully turned into rGO. A proof of this is the disappearance of the diffraction peak at $2\theta = 10.18^\circ$ in the TiO₂/rGO/SQ spectrum, which is indicative of GO and its shift to $2\theta = 25^\circ$ characteristic of rGO [28].

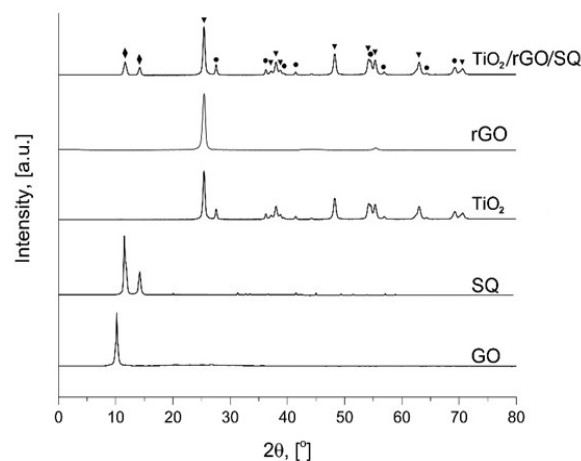


Fig. 1. XRD patterns of TiO₂, GO, SQ, rGO, and TiO₂/rGO/SQ samples (▼ - anatase, • - rutile, ◆ - SQ).

Peaks characteristic of graphene are not visible on the TiO₂/rGO/SQ composite catalyst spectrum since the main peak of rGO is at about $2\theta = 25^\circ$ and overlaps with that of anatase at $2\theta = 25.54^\circ$. The peaks that appear on the spectrum of the ternary sample at $2\theta = 11.5^\circ$ and 14.2° which are specific for SQ confirmed the successful SQ attachment to the TiO₂/rGO during the catalyst synthesis. Sample morphology prior to SQ attaching was studied by high-resolution transmission electron microscopy (HRTEM) and scanning electron microscopy (SEM). Figures 2 and 3 display SEM and TEM images, respectively, of a TiO₂/rGO sample. It is seen that titania clusters are allocated on rGO sheets. Titania individual particles sizes measured from TEM images were in the range of 15–20 nm.

Photocatalytic activity testing

Titanium dioxide supported on SQ-sensitized rGO was tested for photocatalytic discoloration of MB in aqueous solution. Batch reactor experimental results were assessed in terms of maximum absorption of MB at 665 nm in the converted mixture with time under illumination. Blank experiments to evaluate MB self-destruction were also conducted.

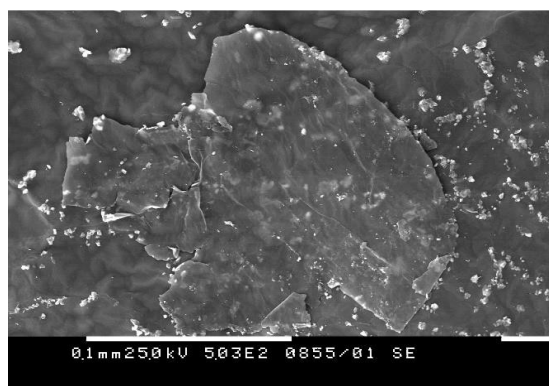


Fig. 2. SEM micrograph of TiO₂/rGO/SQ sample.

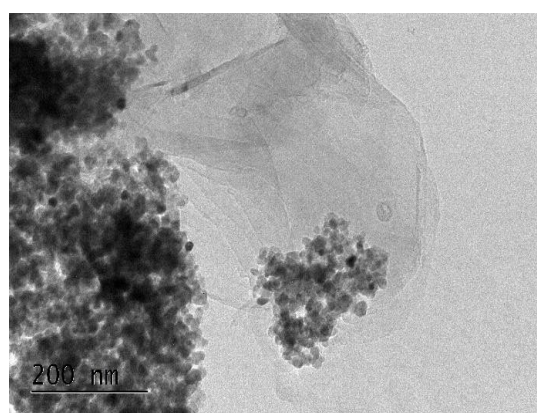


Fig. 3. TEM image of TiO₂/rGO/SQ sample.

MB concentration was calculated at equal intervals according to the absorption spectra during process applying Beer-Lambert law. The results showed that self-conversion was within the frame of 4% for 120 min of irradiation. A higher degradation efficiency concerning MB was observed using pure titania reaching ~16% conversion under the same conditions. Figure 4 discloses the absorption of the reaction solution in the course of the experiment in the presence of TiO₂/rGO/SQ sample under visible light irradiation.

Discoloration efficiency (D) was evaluated applying eq. (1) to the data from Figure 5 that indicates the MB decay during illumination:

$$D \% = \frac{C_0 - C_t}{C_0} \times 100, \quad (1)$$

where C_0 is the initial concentration of dye solution in mol/l and C_t is the concentration of dye solution after irradiation for a selected time interval in mol/l.

It was found that the nanocomposite showed a much higher degradation rate than pure titania reaching conversion over 90%, which is a remarkable photocatalytic activity under visible light illumination.

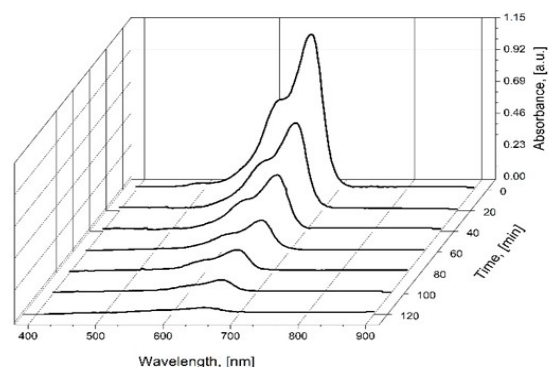


Fig. 4. Absorption spectra of MB solution during visible light irradiation.

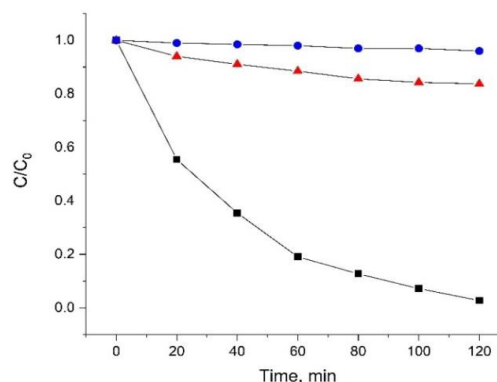


Fig. 5. Normalized discoloration curves of MB degradation under visible light in presence of: ● - self-destruction; ▲ - TiO₂; ■ - TiO₂/rGO/SQ.

A plot of $\ln[\text{MB}]$ versus t gives a straight line with coefficient of determination of 0.996 so the reaction can be considered of first order in MB. Further, using the first order kinetics we were able to calculate the apparent rate constants of MB destruction according to eq. (2):

$$\ln\left(\frac{C_0}{C}\right) = k_{app}t \quad (2)$$

or $C_t = C_0 e^{-k_{app}t}$, where C_0 is the concentration of MB at the moment of turning on the vis-lamp and C_t is MB concentration at time t .

The corresponding apparent rate constants were calculated according to the plot of $\ln(C_0/C)$ versus time (Fig. 6). The highest rate constant reaching a value of 0.028 mol/l.s was exhibited in the presence of TiO₂/rGO/SQ composite catalyst that was 18 times higher than that over bare titania.

As titania has a wide energy band gap of 3.2 eV and remains transparent to the visible light, its photonic efficiency is close to zero because of the insufficient photon energy needed for excitation of the electrons from the valence to the conduction band.

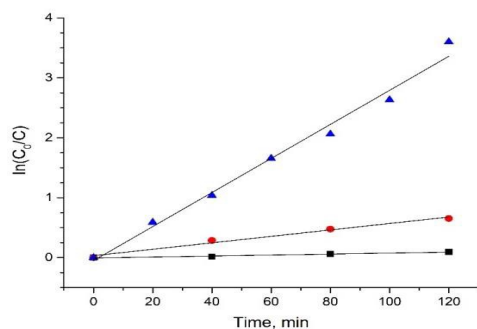


Fig. 6. Apparent rate constants of MB degradation under Vis-light (▲ - TiO₂/rGO/SQ; ● - TiO₂; ■ - self-destruction).

In this case, photodegradation of the dye is realized by a photosensitization procedure as the light is almost exclusively absorbed by the dye with subsequent transfer of the excited electron into the conduction band of the semiconductor leaving behind a hole localized on the dye. Then the atmospheric molecular oxygen acts as a scavenger for the separated electron so that the recombination of the e^-/h^+ is being prevented and the dye is destroyed by the remaining hole [29]. Photodegradation by direct excitation of titania is not excluded but it is very limited. Having investigated TiO₂ and graphene as photocatalysts for MB degradation, Markad *et al.* [30] confirmed that there is an insignificant change in concentration of MB after illumination for sufficiently long time indicating inability of these materials to act as a photocatalyst individually in visible light. The self-destruction rate could be neglected because it takes place at a much lower rate constant estimated to be 8.24×10^{-4} mol/l.s. Further, the MB discoloration was studied by incorporating graphene and SQ in the titania to investigate the synergic effect of coupling these materials.

The combination of rGO and SQ together with TiO₂ was found to be the most effective MB destroyer, having an apparent rate constant of 0.028 mol/l.s as mentioned above. This result was achieved as each of these three components gives its contribution to the overall decomposition process shown in Figure 7.

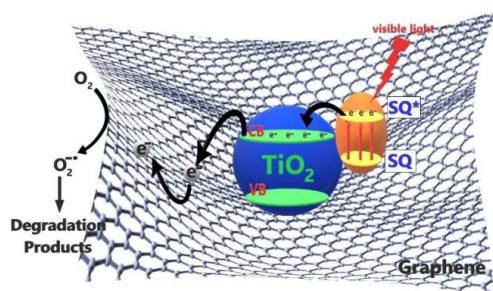


Fig. 7. Schematic illustration of the MB destruction

mechanism.

CONCLUSION

A ternary squaraine photosensitized titania catalyst containing 5 wt% reduced graphene oxide was synthesized. The novel TiO₂/rGO/SQ catalyst exhibited a remarkable activity with respect to MB photodiscoloration in aqueous solution under visible light irradiation leading to increasing the apparent rate constant of the process by 18 times compared to that of bare titania.

Acknowledgement: The authors gratefully acknowledge financial support by Bulgarian National Science Fund, Ministry of Education and Science of Bulgaria (Project DFNI 239/28.02.2019).

REFERENCES

1. T. Suzuki, S. Tinolei, L. Kurunczi, U. Dietze, G. Schuuirmann, *Chemosphere*, **45**, 1 (2001).
2. F. D. Ollis, E. Pelizzetti, N. Serpone, in: *Photocatalysis: Fundamentals and Applications*, N. Serpone and E. Pelizzetti (eds.), Wiley Interscience, New York, 1989, p. 603.
3. R. M. Hoffmann, S. T. Martin, W. Choi, D. W. Bahnemannt, *Chem. Rev.*, **95**, 69 (1995).
4. C. M. Yeber, J. Rodríguez, J. Freer, N. D. Durán, H. Mansilla, *Chemosphere*, **41**, 1193 (2000).
5. J. M. Herrmann, *Topics Catal.*, **34**, 49 (2005)
6. G. P. Anipsitakis, D. D. Dionysiou., *Appl. Catal. B: Environ.*, **54**, 155 (2004).
7. A. Matilainen, M. Sillanpää., *Chemosphere*, **80**, 351 (2010).
8. J. M. Monteagudo, A. Durán, I. San Martín, *J. Environ. Manage.*, **141**, 61 (2014).
9. X. Huang, B. Feng, Y. Niu, *Catal. Lett.*, **148**, 1 (2018).
10. S. Anandan, Y. Ikuma, K. Niwa., *Solid State Phenom.*, **162**, 239 (2010).
11. H. Lin, C. P. Huang, W. Li, C. Ni, I. Shah, Y.-H. Tseng, *Appl. Catal. B: Environ.*, **68**, 1 (2006).
12. K. Rajeshwar, M. E. Osugi, W. Chanmanee, C. R. Chenthamarakshan, *J. Photochem. Photobiol. C: Photochem. Rev.*, **9**, 172 (2008).
13. V. Subramanian, E. Wolf, P. V. Kamat, *J. Phys. Chem. B*, **105**, 11439 (2001).
14. A. Scelafania, J. Herrmann, *J. Photochem. Photobiol.*, **113**, 181 (1998).
15. K. Venkata, S. Rao, B. Lavédrine, P. Boule, *J. Photochem. Photobiol. A: Chem.*, **154**, 189 (2003).
16. B. Yao, C. Peng, W. Zhang, Q. Zhang, J. Niu, J. Zhao, *Appl. Catal. B: Environ.*, **174-175**, 77 (2015).
17. C. Wang, J. Li, G. Mele, G. M. Yang, F. X. Zhang, L. Palmisano, G. Vasapollo, *Appl. Catal. B: Environ.*, **76**, 218 (2007).
18. K. Assaker, C. Carteret, T. Roques-Carmes, J. Ghanbaja, M. J. Stébéa, J. L. Blin, *New J. Chem.*, **38**, 208 (2014).
19. T. Batakliiev, I. Petrova-Doycheva, V. Angelov, V. Georgiev, E. Ivanov, R. Kotsilkova, M. Casa, C.

- Cirillo, R. Adami, M. Sarno, P. Ciambelli, *Appl. Sci.*, **9**, 469 (2019).
20. G. Spinelli, P. Lamberti, V. Tucci, R. Kotsilkova, S. Tabakova, R. Ivanova, P. Angelova, V. Angelov, E. Ivanov, R. D. Maio, C. Silvestre, D. Meisak, A. Paddubskaya, P. Kushir, *Materials*, **11**, 2256 (2018).
21. A. Kruth, S. Peglow, N. Rockstroh, H. Junge, V. Brüser, K. D. Weltmann, *J. Photochem. Photobiol. A: Chem.*, **290**, 31 (2014).
22. Z. S. Seddigi, S. A. Ahmed, S. Sardar, S. K. Pal, *Photochem. Photobiol. Sci.*, **15**, 920 (2016).
23. D. J. Wasylenko, R. D. Palmer, E. Schott, C. P. Berlinguette, *Chem. Commun.*, **48**, 2107 (2012).
24. E. Regulska, D. Rivera-Nazario, J. Karpinska, M. Planska-Brzezinska, L. Echevoyen, *Molecules*, **24**, 1118 (2019).
25. S. Minkovska, N. Burdzhiev, A. Alexiev, T. Deligeorgiev, *Chem. Papers*, **72**, 1549 (2018).
26. Z. Youssef, L. Colombeau, N. Yesmurzayeva, F. Baros, R. Vanderesse, T. Hamieh, J. Toufaily, C. Frochot, T. Roques-Carmes, S. Acherar, *Dyes Pigm.*, **159**, 49 (2018).
27. S. Alam, N. Sharma, L. Kumar, *Graphene*, **6**, 1 (2017).
28. L. Stobinski, B. Lesiak, A. Malolepszy, M. Mazurkiewicz, B. Mierzwa, J. Zemek, P. Jiricek, I. Bieloshapka, *J. Electron Spectrosc. Relat. Phenom.*, **195**, 145 (2014).
29. E. Stathatos, T. Petrova, P. Lianos, *Langmuir*, **17**, 5025 (2001).
30. G. Markad, S. Kapoor, S. Haram, P. Thakur, *Solar Energy*, **144**, 127 (2017).

Biomass-based nanoporous carbon as catalyst support for production of hydrogen by methanol degradation

I. Stoycheva¹, T. Tsoncheva¹, B. Tsyntsarski^{1*}, B. Petrova¹, G. Georgiev¹,
A. Sarbu², A. Radu², T. Sandu²

¹ Institute of Organic Chemistry with Centre of Phytochemistry, Bulgarian Academy of Sciences, Acad. G. Bonchev St., Bldg. 9, 1113 Sofia, Bulgaria

² National Research-Development Institute for Chemistry and Petrochemistry INCDCP-ICECHIM Bucharest, 202 Splaiul Independentei, 060021 Bucharest, Romania

Dedicated to the 80th anniversary of Professor Lachezar Petrov, DSc,
Corresponding Member of the Bulgarian Academy of Sciences

Received: November 19, 2019; Revised: December 22, 2019

The present investigation deals with preparation of porous carbons based on of agricultural wastes as peach stones. The carbons obtained were modified with manganese and tested as catalysts in methanol decomposition for hydrogen production. Various physicochemical techniques, such as XRD, nitrogen physisorption, TPR, FTIR, and UV-Vis spectroscopy were used for characterization. Porous carbons produced from peach stones exposed a high surface area and well-developed porous structure with high amount of micropores and mesopores. Decomposition of added Mn salts caused reduction of the micropore and mesopore volume due to Mn particles located in the carbon pores. The resulting catalysts exhibited high catalytic activity and selectivity.

Keywords: biomass, nanoporous carbon, hydrogen, methanol, decomposition, catalysts

INTRODUCTION

In the last years, various alternative power sources have been developed and studied due to fast depletion of fossil fuel resources. Hydrogen is considered the fuel of the future; however, there are some problems related to production, storage, and application that have to be solved.

Being a steam reforming catalytic process, methanol decomposition is a reliable way to produce high purity hydrogen. The aim of the present investigation is by using agricultural waste such as peach stones to prepare nanoporous carbon with suitable texture and chemical surface properties as catalyst support for methanol degradation.

Porous carbons are appropriate for use in heterogeneous catalysis because they satisfy most of desirable properties required for a proper support [1]. Porous carbon supports stable to chemicals and temperature can be prepared with different physical forms: granules, pellets, extrudates, cloth, and fibers. A significant advantage is the possibility to design largely porous carbon structure and internal surface by various methods[2].

Activated carbon (AC) exhibits a wide range of pore size, thus facilitating the access of the active phase during catalyst preparation and making possible high catalyst dispersions. Catalytic activity and adsorption capacity of carbons depend on porous

structure and chemical nature of the surface.

Active site distribution normally as edges of carbon sheets is also important. Catalytic activity can be changed by the presence of heteroatoms. Nitrogen increases activity whereas sulphur inhibits activity. Activity can also be influenced by the presence of acid or base surface oxide species.

Carbon-based catalysts are applied to many processes like oxidative dehydrogenation of hydrocarbons [3], dehydration and dehydrogenation of alcohols [4], NO_x reduction [5, 6], SO_x oxidation [7,8], ozonation [9], catalytic wet air oxidation [10,11], etc.

The aim of the current paper is the preparation of porous carbon using different agricultural wastes and preparation conditions. The materials obtained were modified with Mn active phase and tested as catalysts in methanol decomposition for hydrogen production.

EXPERIMENTAL

Peach stone based activated carbon (AC) was produced by carbonization (10 deg/min) at 450 °C for 1 h and hydrolysis (10 deg/min) at 750 °C for 45 min. Both carbonization and hydrolysis were performed using a stainless steel reactor placed in a tube furnace with 3 SiC heaters. Mn (8 wt%) was added as manganese nitrate to activated carbon by incipient wetness impregnation. 0.5 g of activated carbon were heated at 60 °C under vacuum for 30

* To whom all correspondence should be sent:
E-mail: btsintsarski@orgchm.bas.bg

min.

The impregnation was performed with manganese nitrate dissolved in 0.1 ml of methanol.

Nitrate decomposition was carried out in a flow of N₂ at 500 °C for 2 h at a heating rate of 5 deg/min.

Texture characteristics were determined by N₂ adsorption at -196 °C by a Quantachrome NOVA 1200 apparatus. The amount of various acidic oxygen-containing functional groups was determined by Boehm's method using aqueous solutions of NaHCO₃, Na₂CO₃, NaOH, and C₂H₅ONa [12].

The amount of basic sites was verified by 0.05 N HCl [13]. Determination of pH values was made by boiling for 5 min in 100 ml H₂O, decantation, and cooling the solution to ambient temperature. XRD analysis was performed on a Bruker D8 Advance diffractometer with Cu K_α radiation and LynxEye detector. The average crystallite size was evaluated according to Scherrer equation. Temperature-programmed reduction/thermo-gravimetric (TPR/TG) analysis was performed on a Setaram TG92 instrument in a flow of 50 vol % H₂ in Ar (100 cm³/min) at a heating rate of 5 deg/min.

Methanol conversion was carried out in a fixed bed flow reactor (0.055 g of catalyst), argon being used as a carrier gas (50 cm³/min). The methanol partial pressure was 1.57 kPa. The catalysts were tested under conditions of a temperature-programmed regime within the range of 80–500 °C at a heating rate of 1 deg/min. On-line gas chromatographic analysis was performed on an HP apparatus equipped with flame ionization and thermal conductivity detector, using a PLOT Q column, an absolute calibration method, and a carbon-based material balance.

RESULTS AND DISCUSSION

The nitrogen isotherms (-196 °C) of nanoporous carbon and Mn catalyst are shown in Fig. 1. The studied carbon sample shows a relatively narrow pore size distribution within the micropore range with a maximum at 1–2 nm, thus indicating that microporosity in this case is composed of pores of large dimensions. The ratio of calculated micropore to mesopore volumes also confirmed that the carbon obtained was highly microporous. Detailed porosity characteristics of the prepared samples are summarized in Table 1. Data show that after steam activation the sample displays an open structure of interconnected pores in a micro/mesoporous network. Isotherm similarity between parent and manganese loaded carbons clearly indicate absence of significant structural collapse of the supports during the modification procedure.

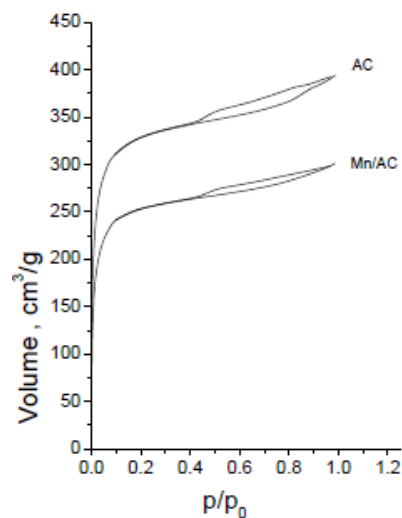


Fig. 1. Nitrogen physisorption (-196 °C) isotherms of the activated carbon and manganese catalyst.

Table 1. Nitrogen physisorption data for parent AC and their manganese modifications

Sample	S _{BET} , m ² /g	S _{mi} , m ² /g	S _{ext} , m ² /g	V _t , cm ³ /g	V _{mi} , cm ³ /g	V _{meso} , cm ³ /g
ACP	1258	1116	143	0.610	0.448	0.105
Mn/ACP	941	830	111	0.463	0.341	0.050

A decrease in BET surface area and pore volume after modification clearly reveals the deposition of the active phase into the porous structure of the support. A significant decrease observed in the microporous volume implies location of Mn particles exclusively into the micropores of the carbon supports.

Table 2 presents some chemical characteristics of the produced porous carbon. Presence of acidic (mainly carbonyl and hydroxyl) and basic groups was detected. The amount of carbonyl and lactonic groups is below detection limit obviously due to the high temperature treatment during preparation. The pH values indicate that the AC sample is characterized by relatively high basicity. This fact can be explained with the presence of basic groups on the carbon surface and considerably low amount of acidic surface groups.

Table 2. Chemical characteristics of the porous carbon.

Sample	pH	Acidic surface functional groups, mmol/g				Basic groups, mmol/g
		Carboxyl	Lactonic	Hydroxyl	Carbonyl	
AC	9.4	BDL	BDL	0.29	1.07	1.04

The FTIR spectra contain bands at 2925 and 1390 cm⁻¹, attributed to C-H stretching vibrations [5]. A broad band at 2835 cm⁻¹ indicates vibrations of CH₃-O group. The band at 1690 cm⁻¹ corresponds to C=O vibrations of lactonic, carboxyl, or ether groups [5].

The broad bands around 1525 and 1090 cm^{-1} are assigned to ring vibrations in a large aromatic skeleton typical of carbons [5]. The region of 1200–700 cm^{-1} contains various bands related to aromatic out-of-plane C-H bending [5]. The band at 1094 cm^{-1} could also be due to vibrations in ether C-O-C groups [5]. The observed changes in the bands at around 1690, 1525, and 1090 cm^{-1} for the Mn catalyst could be ascribed to interaction between Mn species with oxygen containing groups and aromatic ring. Increased absorption at around 800–500 cm^{-1} is probably due to δ -modes in Mn-O and Mn-O-C structures.

Fig. 2 displays the TPR-TG and TPR-DTG profiles for the manganese modified activated carbon. Generally, the reduction of MnO_2 and Mn_2O_3 in hydrogen takes place as a stepwise process with the formation of Mn_3O_4 in the inter-mediate step and further reduction to MnO [14] as follows: $\text{MnO}_2 \rightarrow \text{Mn}_2\text{O}_3 \rightarrow \text{Mn}_3\text{O}_4 \rightarrow \text{MnO}$.

In these three steps, the theoretical hydrogen consumption ratio is 3:1:2, respectively. Here, the main reduction effects with the manganese catalyst occur in the range 200–330 $^\circ\text{C}$ and above 380 $^\circ\text{C}$. According to the literature [14], the low-temperature effect corresponds to manganese reduction in $\text{Mn}^{3+}/\text{Mn}^{4+}$ state, while the high temperature effect is due to further reduction of Mn_3O_4 to MnO. TPR profile variations support data from the physicochemical analysis on differences in the state (phase composition, dispersion, location into the pores) of the loaded manganese species. XRD and UV-Vis data provide evidence for presence of MnO.

Fig. 3a shows the temperature dependence of methanol conversion over the Mn catalyst. CO, methane, and CO_2 were the only registered carbon-containing products, and the CO selectivity, which is directly related to the hydrogen release from methanol, is presented in Fig. 3b.

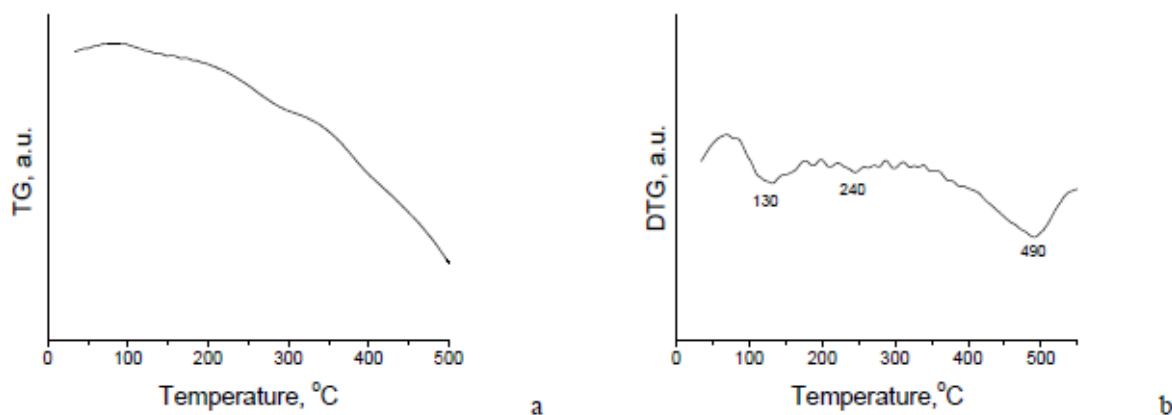


Fig. 2. TPR-TG (a) and TPR-DTG (b) profiles of manganese-modified activated carbon.

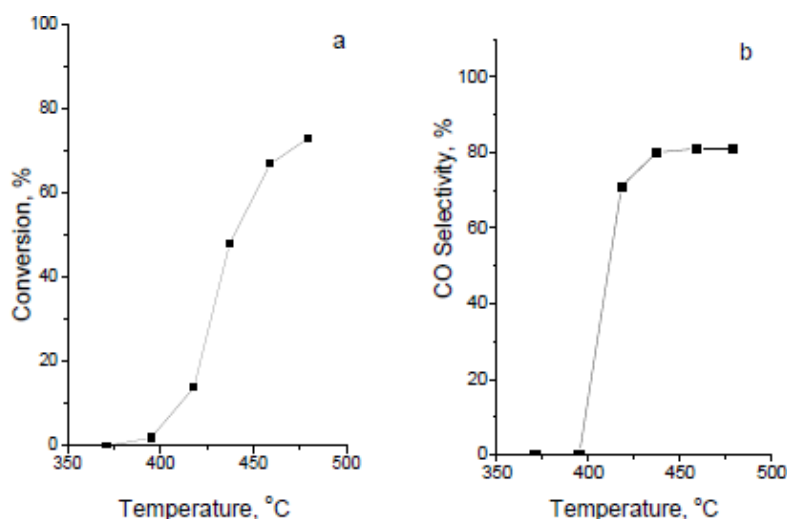


Fig. 3. Methanol conversion (a) and selectivity (b) towards CO of Mn catalyst.

The Mn catalyst was active above 400 °C with a steep increase in the conversion up to 70% at 460°C. The selectivity to the main product (CO) remained high within 420–480 °C.

CONCLUSIONS

Nanoporous carbons from peach stones possess a high surface area and well-developed porous structure with a high amount of micropores and mesopores. Modification treatment reduced the micropore and mesopore volumes due to the formation of Mn species into the pores. The catalyst based on biomass carbon exhibited a high catalytic activity and selectivity. The state of the manganese phase and its catalytic behavior is related to carbon structure and surface functionality.

Taking into account N₂ physisorption, XRD, IR spectral and TPR results, we can assume that the catalytic activity is facilitated by the location of the manganese species into the mesopores of the carbon support. It seems that the catalytic selectivity is also influenced by the Mn oxidation state and the presence of Mn³⁺/Mn⁴⁺ ions increases the ability for methanol decomposition to hydrogen and CO. It is not excluded that these species could be stabilized by some effects related to surface acidic groups.

Depending on composition and treatment conditions, the selected raw material allowed preparation of porous carbon with desired texture and chemical nature of the surface. This allowed us to study the characteristics of the porous carbon as a potential catalyst support. Mn catalyst samples were active over 400 °C showing a steep increase in the conversion up to 70% at 460 °C. Data show that the catalytic activity is favored by manganese species located into the mesopores of the carbon support.

*

Acknowledgements: The authors gratefully acknowledge the funding by Project KP-06-N29/2 and Romanian-Bulgarian POMCAME Project.

REFERENCES

1. F. R. Rodriguez-Reinoso, *Carbon* **36**, 159 (1998).
2. H. Juntgen, *Fuel*, **65**, 1436 (1986).
3. A. Malaika, M. Kozłowski, *Int. J. Hydrogen Energ.*, **35**, 10302 (2010).
4. A. Moreno-Castilla, F. Carrasco-Marin, C. Parejo-Pérez, M. López Ramón, *Carbon*, **39**, 869(2001).
5. J. Zawadzki, M. Wisniewski, K. Skowronska, *Carbon*, **41**, 235 (2003),
6. G. S. Szymanski, T. Grzybek, H. Papp, *Catal.Today*, **90**, 51 (2004).
7. E. Raymundo-Pinero, D. Cazorla-Amorós, A. Linares-Solano, *Carbon* **41**, 1925(2003).
8. K. Li, L. Ling, C. Lu, W. Qiao, Z. Liu, L. Liu, I. Mochida, *Carbon*, **39** 1803(2001).
9. P. C. C. Faria, J. J. M. Órfão, M. F. R. Pereira, *Ind. Eng. Chem. Res.* **45**, 2715 (2006).
10. H. T. Gomes, B. F. Machado, A. Ribeiro, I. Moreira, M. Rosário, A. M. T. Silva, J. L. Figueiredo, J. L. Faria, *J. Hazard. Mater.* **159**, 420 (2008).
11. A. Santos, P. Yustos, S. Rodriguez, F. Garcia-Ochoa, *Appl. Catal. B Environ.* **65**, 269 (2006).
12. H. P. Boehm, *Adv. Catal.*, **16**, 179 (1966).
13. E. Papirer, S. Li, J.-B. Donnet, *Carbon*, **25**, 243 (1987).
14. A. Kaddouri, S. Ifrah, P. Gelin, *Catal. Lett.*, **119**, 237 (2007).

Activity and selectivity of Co-Pd/TiO₂ catalysts in CO hydrogenation

M. G. Shopska*, I. Zh. Shtereva, H. G. Kolev, K. I. Aleksieva, S. Zh. Todorova, G. B. Kadinov

Institute of Catalysis, Bulgarian Academy of Sciences, Acad. G. Bonchev St., Bldg. 11, 1113 Sofia, Bulgaria

Dedicated to the 80th anniversary of Professor Lachezar Petrov, DSc,
Corresponding Member of the Bulgarian Academy of Sciences

Received: November 29, 2019; Revised: December 27, 2019

Activity and selectivity of the (10%Co+0.5%Pd)/TiO₂ system in CO hydrogenation were studied in dependence of pretreatment mode and reduction and reaction temperature. The investigation was directed to evaluate information about influence of surface species and sites on catalyst performance. Samples were preliminary treated in air, hydrogen, or argon and studied by chemisorption of H₂ and CO, TPR, XPS, EPR, *in situ* DRIFTS, and catalytic measurements. Dependences of pretreatment mode and reduction temperature on catalyst activity in CO conversion and selectivity to CH₄ were found. Pretreatment in hydrogen resulted in an active catalyst characterized by bridged CO species on the metal surface with weakened C-O bonds that facilitated cleavage at lower temperatures and sites of medium strength on the support where bidentate carbonate species was formed. This catalyst produced methane at a lower temperature but the selectivity was low due to high CO₂ formation. A selective catalyst was prepared by pretreatment in air and distinguished by dominance of formate and monodentate carbonate species formed on strong adsorption sites of the support. Thus, methane production started at higher temperatures but at a higher CH₄/CO₂ ratio. Being a reducible support of weak Lewis acidity TiO₂ contributed to CO₂ formation because of its intrinsic activity in the water-gas shift reaction. Contribution of the support depended on preliminary treatment mode and the effect of the latter was supposed stronger in the case of active catalyst preparation.

Keywords: CO hydrogenation, Co-Pd catalysts, TiO₂ carrier, DRIFTS, selectivity, H₂ and CO chemisorption

INTRODUCTION

Catalysis is an instrument of the so-called green chemistry to overcome disadvantages and challenges in chemical production. A diversity of chemical processes poses different tasks to catalysis in order to achieve the green chemistry requirements to become ecology friendly. Catalysts meeting the green chemistry 12 postulates should be highly selective, characterized by a decreased variety of intermediates to avoid unnecessary by-product synthesis and thus allowing reagent complete inclusion into target products [1].

The CO hydrogenation process takes place in presence of cobalt and cobalt-palladium supported catalysts. Their surface may be composed by various compounds. The adsorption sites on the surface of metal particles differ in property and vary in concentration ratio: Co and Pd sites with modified properties exist parallel to typical Co and Pd adsorption sites. The influence of the latter on hydrogen and CO adsorption is of great significance determining the heterogeneous catalytic process mechanism.

Main reactions of the CO hydrogenation process are synthesis of CH₄/hydrocarbons (HCs) and water-gas shift reaction (WGSR).

In the related literature the explanation of reaction mechanism, products formation, and catalyst selectivity during the CO hydrogenation process are not generally accepted because of contradiction among obtained data in many cases. Methanation (HCs synthesis) takes part on Co and Pd atoms. There are different ideas about CH₄ formation on cobalt and they have developed in two directions [2, 3]: (i) CO adsorption (CO_{ads}), C-O bond cleavage with formation of surface carbon (C_{ads}) that is distinguished from metal carbide, and C_{ads} hydrogenation; (ii) CO adsorption and hydrogenation of CO_{ads} species to CH_xO_{ads}. It has been established that C_{ads} hydrogenation occurs very easily while that of CO_{ads} requires an increased temperature, which indicates a lower reaction rate. HCs synthesis, i.e. formation of C-C bonds, is explained by creation of CH_x intermediates, condensation of CH_xO entities, and CO insertion. Different surface species of CO have been registered on the catalyst surface. However, another type of O-containing intermediates, different from the aforementioned, has not been found. In spite of that there are investigations reporting results about CH_xO species on Co [4] and Pd [5, 6]. In a great number of studies, it is supposed that a predominant pathway for CH₄ formation is through CO dissociation.

* To whom all correspondence should be sent:

E-mail: shopska@ic.bas.bg

WGS proceeds in presence of eighth-group metals independent of whether they are in reduced or oxidized state, however, in the latter case the rate is much higher [7]. There are different hypotheses about the reaction mechanism: (i) formate; (ii) redox; and (iii) carboxylate [8]. Carboxyl species is shorter-lived than formate one. It has been established that the reaction goes through formation of surface formic acid intermediate [CO-OH] and the rate-determining step is assigned to decomposition into hydrogen and CO₂ [9, 10]. A reaction intermediate for the redox route has not been proved experimentally [8]. Amongst alumina supported catalysts based on eighth-group metals, a reduced Co/Al₂O₃ sample has been characterized by the highest activity [7].

The present paper deals with the activity and selectivity of (10%Co+0.5%Pd)/TiO₂ catalysts depending on factors like pretreatment, reduction temperature, and reaction temperature. The paper is also aimed at putting forward some additional information about how the variety of surface species and sites affects the performance of obtained bimetallic systems. Variance of the above-mentioned factors may lead to an increase in activity. However, activity is not an isolated property of the catalyst since it is accompanied by kind of selectivity in work. It is necessary to vary purposefully the factors and regulate the effect of their influence at creation of catalysts so that a higher activity is accompanied by improved selectivity.

EXPERIMENTAL

Bimetallic Co-Pd catalysts were prepared by depositing metal nitrate salts from aqueous solution on non-porous TiO₂ (Degussa P-25, 50 m²/g) support. The suspension was dried in a vacuum rotary desiccator at 60 °C for 24 h. The procedure was aimed at preparing ~10% cobalt and ~0.5% palladium loading.

Preliminary treatment of the precursors comprised consecutive heating in a gas flow at 100, 200, and 300 °C for 1 h at each level (heating rate of 100 deg/h). Air, hydrogen, and argon were used for oxidative, reductive, and inert gas pretreatment atmosphere, respectively. Selected pretreatment mode was carried out *in situ* in the measuring cell of the respective device before each kind of study. The prepared samples were denoted as 'ox', 'red', and 'inert' in order to distinguish used pretreatment medium.

Chemisorption of hydrogen and carbon monoxide was measured by the volumetric method in a glass device. The experiments were performed with samples successively reduced in hydrogen flow

at 300 °C for 1 h, at 400 °C for 1 h, and at 450 °C for 2 h. After reduction, as well as after each hydrogen adsorption measurement the samples were evacuated to $P < 1.33 \times 10^{-3}$ Pa at the temperature of reduction. Adsorption isotherms of hydrogen were obtained in the pressure range 0–13.3 kPa at a temperature of ca. 100 °C in order to minimize absorption in the bulk of palladium [11] and to activate hydrogen adsorption on cobalt [12, 13]. Monolayer coverage was determined by extrapolation of the linear part of the isotherm to zero pressure.

Carbon monoxide chemisorption was measured at room temperature. The term 'total adsorption' is used to designate the amount of all kinds of adsorbed CO species on various sites. Strongly (irreversibly) adsorbed CO species determine the reaction mechanism in the CO hydrogenation process. For a quantitative analysis of the metal surface, it is necessary to measure and eliminate the share of weakly bonded CO to Co and Pd ions and other sites on the support.

Experimentally, the strongly adsorbed species of CO (CO_s) was determined in the following sequence: (i) total CO adsorption measurement; (ii) evacuation of the sample at room temperature to $P < 1.33 \times 10^{-3}$ Pa; (iii) second measurement of isotherm to determine weak (reversible) adsorption (CO_w). Strongly bonded CO was estimated as a difference between 'total' and 'weak' adsorption [14].

Catalytic activity measurements in the process of CO hydrogenation were carried out in a flow-type glass reactor at atmospheric pressure in the temperature range of 150–360 °C. Catalyst loading was 140 mg (fraction 0.63–0.8 mm). The measurements were carried out with reduced samples at three temperatures following the procedure mentioned above. Before each test, the catalyst was cooled in a hydrogen flow to the selected initial reaction temperature. A H₂/CO reaction mixture of 4/1 at a flow rate of 25 ml/min was used. At reactor outlet the mixture was analyzed by gas chromatography (Varian 3700 with thermal conductivity detector, 2 m Porapak Q column working at room temperature, hydrogen carrier gas 20 ml/min).

In situ diffuse-reflectance IR spectroscopy (DRIFTS) was used to monitor the catalytic measurements of CO hydrogenation (H₂/CO = 4/1, 8 ml/min, T ≤ 250°C). Spectra were recorded on a Nicolet 6700 FTIR spectrometer (Thermo Electron Corporation, USA) equipped with Collector II accessory where a High Temperature/Vacuum Chamber (Thermo Spectra-Tech, USA) was mounted. CaF₂ windows limited the working

spectral range to 1111–4000 cm⁻¹, and the spectra were collected at 100 scans, 1.928 cm⁻¹ date spacing. Temperature-programmed reduction (TPR) was carried out in a quartz reactor with 150 mg of sample charge. 10% H₂ in Ar at a total flow rate of 25 ml/min was used as reducing agent. The temperature was raised by 10 deg/min up to 900 °C. Recorded TPR profiles were used for graphical calculation of the peak area at temperatures higher than the applied T_{red}. This area is proportional to the amount of unreduced metal (URM) and could help in determining metal dispersion of the studied samples.

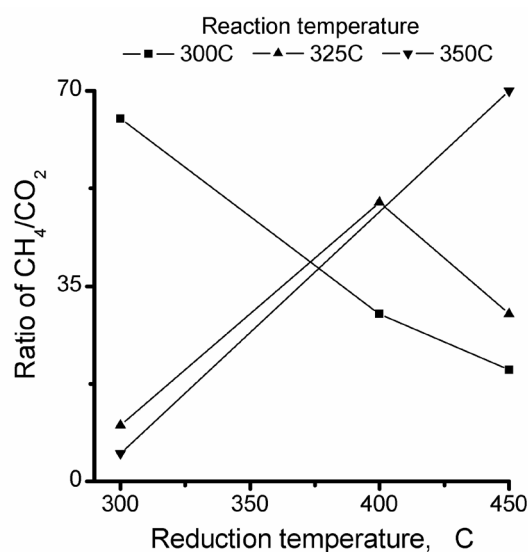


Fig. 1. Selectivity ratio dependence on reduction and reaction temperature for (10%Co+0.5%Pd)/TiO₂(ox) sample.

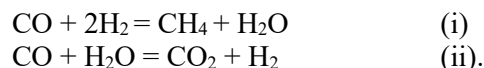
X-ray photoelectron spectroscopy (XPS) was used for *ex-situ* study of sample surface after the catalytic measurements. The analyses were carried out by an ESCALAB MkII (VG Scientific) electron spectrometer at a base pressure in the analysis chamber of 5×10⁻¹⁰ mbar (during measurements 1×10⁻⁸ mbar) using AlK α X-ray source (excitation energy $h\nu = 1486.6$ eV). The pass energy of the hemispherical analyzer was 20 eV, 6 mm slit widths (entrance/exit). The instrumental resolution measured as the full width at a half maximum (FWHM) of the Ag3d_{5/2} photoelectron peak was 1 eV. The energy scale was corrected depending on the Ti2p peak maximum at 458.8 eV. Processing of the measured spectra included subtraction of X-ray satellites and Shirley-type background [15]. The peak positions and areas were evaluated by a symmetrical Gaussian-Lorentzian curve fitting. The relative concentrations of the different chemical species were determined based on normalization of the peak areas to their photoionization cross-sections as calculated by Scofield [16].

Ex-situ spectra based on electron paramagnetic resonance (EPR) phenomenon were recorded on a JEOL JES-FA 100 EPR spectrometer operating in X-band with standard TE011 cylindrical resonator. An ES-DVT4 Varied Temperature Controller provided spectra detection at a temperature of -150 °C. The desired low temperature was achieved by a cooling gas (liquid nitrogen) system, which was controlled by the spectrometer computer.

RESULTS AND DISCUSSION

Metal dispersion was determined based on hydrogen chemisorption experiments for all studied samples. An average value of about 3.4% was obtained after reduction at 300 °C, which decreased to ~1.8% after reduction at the higher temperature (400/450 °C) studied.

All catalysts were tested in the CO hydrogenation process at atmospheric pressure. Under the selected reaction condition, CH₄ was produced as the sole hydrocarbon [17]. Two main reactions were running in this investigation:



The results showed a different type of change of CO conversion and of hydrocarbon production with reaction temperature.

The CH₄/CO₂ ratio was low and almost constant independent of reduction and reaction temperature for a hydrogen-pretreated (prereduced) sample and for a sample pretreated in an inert gas flow. The change of reduction temperature from 300 to 450 °C affected the behaviour of these samples by decreasing both conversion and selectivity. There was not a clear dependence of the CH₄/CO₂ ratio on reduction or reaction temperature in the case of (10%Co+0.5%Pd)/TiO₂(ox). However, a somewhat similar effect was found on the selectivity ratio upon combination between reduction and reaction temperature in the region of 300 – 450 °C (Fig. 1).

Comparative analysis showed that depending on precursor treatment mode (oxidative, inert, or reductive medium) and reduction temperature the catalysts ranged in different rows of activity in CO conversion and selectivity to CH₄ formation. Information, parameters, and properties derived using different methods are shown in Table 1 featuring the most active sample in CO conversion and that of the highest selectivity to CH₄ amongst all studied samples. For comparative purpose, data collected at a reaction temperature of 300 °C are taken as reference. Figures 4 – 7 illustrate some of the discussed sample properties.

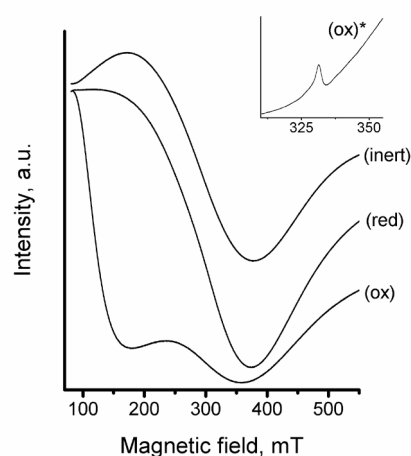
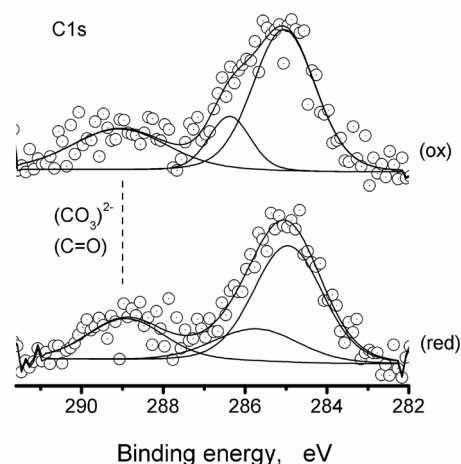
Table 1. Data derived from TPR, XPS, chemisorption and catalytic measurements about the catalyst system (10%Co+0.5%Pd)/TiO₂.

Parameter	Active	Selective
Pretreatment	(red)	(ox)
T _{red} , (°C)	300	300
Co states (TPR)	Co ⁰ , Co ⁿ⁺	Co ⁰ , Co ⁿ⁺
R _{URM}	0.2	
Total carbon, (at.%)	9.53	8.71
CO ₃ , (%)	20	26
CH ₄ /CO ₂	3	65
D _{H100C} , (%)	3.6	3.7
H _{100C} /CO _s	2.9	2
CO _s /CO _w	0.8	1
	(22/28)	(32.8/31.8)

Legend: CO₃ – percentage of deposited surface carbon corresponding to carbonate(s); R_{URM} - unreduced metal ratio ($R_{URM} = URM_a:URM_s$), H_{100C} – sample capacity for monolayer hydrogen adsorption measured at 100 °C after reduction at a respective T_{red}; CO_w - sample capacity for weak (reversible) CO adsorption measured at room temperature after reduction at a respective T_{red}; Co_s – calculated sample capacity for strong (irreversible) CO adsorption; D_{H100C} - metal dispersion based on H_{100C} and determined after reduction at a respective temperature.

After performing the catalytic tests, all the samples were investigated by XPS and EPR. Results obtained by EPR spectroscopy (Fig. 2) show that at room temperature a broad singlet line with a g factor of 2.2551 ± 0.005 was detected in samples pretreated in reductive and inert flow, which is due to tetrahedrally coupled Co²⁺ ions [18]. It can be supposed that the line is significantly broadened due to additional deformation of the Co²⁺ tetrahedra or superposition of metallic Pd because the studied catalysts were bimetallic [19]. Another possible reason for this line broadening is dipole-dipole interaction between the particles, since cobalt concentration is 10%, high enough for EPR measurements. Preliminary treated catalyst in air (denoted as ‘ox’) has a signal of g factor 5.4552, which can be assigned to isolated octahedrally coordinated Co²⁺ ions with some tetragonal and trigonal distortions [20]. In addition, a weak signal with a g factor of 1.9751 due to Ti³⁺ was recorded at a temperature of –150 °C (Fig. 2, inset) [21]. Co²⁺ and Co³⁺ on the surface of the tested samples were also registered by XPS measurements, as well as metallic Pd and Pd²⁺ [22]. The presence of these ions in the used (already reduced) samples is due to available unreduced oxide phase(s) and/or to the ‘*ex-situ*’ measurements where oxygen adsorption and oxidation of the particle surface layer proceeds without penetration into the bulk during exposition to air [23, 24]. Additionally, 8.71–10.06 at. % carbon

were registered by XPS (Table 1, Fig. 3).

**Fig. 2.** EPR spectra of samples measured at room temperature and –150 °C (inset) after catalytic test.**Fig. 3.** C1s high-resolution XP spectra of samples from different systems tested in CO hydrogenation and classified correspondingly as selective or active catalysts.

Carbon deposition due to XPS measurement itself was not observed. So, the registered amounts of HCs were assigned to surface HCs species formed along with methane and remained adsorbed on the catalyst and/or because of contamination upon sample preparatory procedure of grinding. The shape of the C1s peak exhibited a shoulder corresponding to carbon in a typical surrounding of carbonates [22]. Deconvolution of the high-resolution C1s peaks revealed that about 20–26% of the surface carbon was in the form of carbonates.

The TiO₂ support is not entirely inert. A strong metal-support interaction (SMSI) phenomenon is frequently observed after reduction of the catalysts and during reactions under reductive conditions. This phenomenon includes several features: Ti⁴⁺→Ti³⁺ reduction; anatase→rutile transition; acceleration of both transformations in presence of metals capable of hydrogen dissociative adsorption

(e.g. Co, Pd); metal surface decoration by partially reduced titania; and CoTiO₃ formation [14, 25–29]. Temperature-programmed desorption from TiO₂ revealed the CO₂ origin from bidentate carbonate species on sites of medium strength in the interval 190–230 °C and from monodentate species on strong adsorption sites at about 320 °C [30]. Evidence for SMSI in the studied samples was proved by a sharp decrease of metal dispersion found through hydrogen chemisorption, while presence of Ti³⁺ ions was confirmed by EPR.

XPS data about carbonate species retained on the surface are consistent with presence of adsorption sites of significant strength.

The amount of unreduced Co in the samples was evaluated by the area under the TPR profile above the reduction temperature of the respective sample (Fig. 4, grey area).

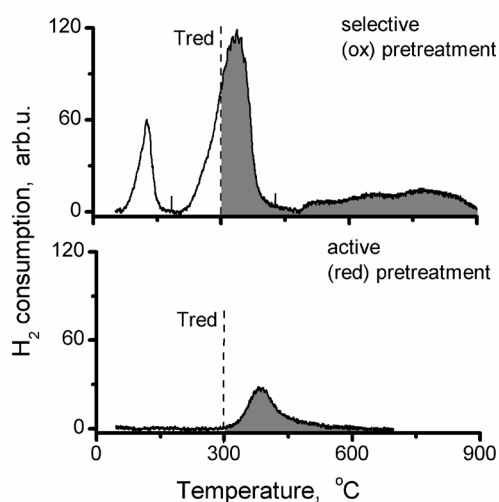
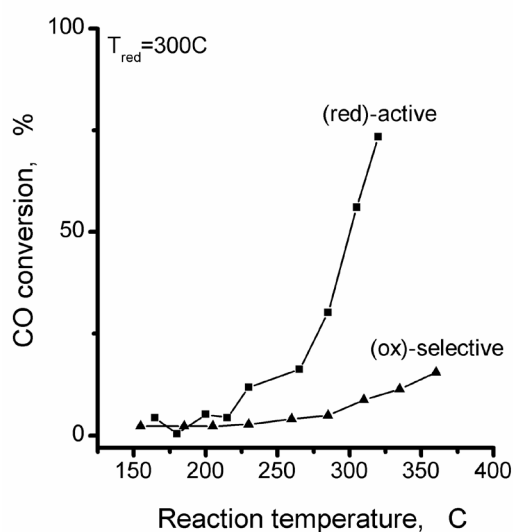
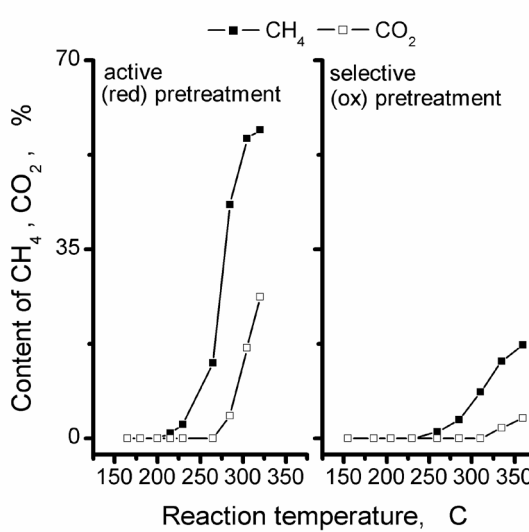


Fig. 4. TPR profiles of differently pretreated (10%Co+0.5%Pd)/TiO₂ samples.



A



B

Fig. 5. Catalytic behaviour in CO hydrogenation of differently pretreated (10%Co+0.5%Pd)/TiO₂ catalysts: A - CO conversion, B - products distribution.

The ratio of active sample area (URM_a) to selective sample (URM_s) area (R_{URM}, Table 1) was regarded as an additional feature to evaluate the role of unreduced metal.

The TPR study showed that cobalt occurred in metallic and ionic state in both samples independent of T_{red} and preliminary treatment. The amount of Coⁿ⁺ predominated in the selective (10% Co + 0.5% Pd)/TiO₂(ox) sample (R_{URM} = 0.2). These results imply that most probably after ‘oxidative’ pretreatment unreduced cobalt is in the form of Co₃O₄ and CoTiO₃, whereas after ‘reductive’ pretreatment it is, presumably, in the form of unreduced CoO [31–37].

The catalytic activity measurements revealed that the more active catalyst was prepared by ‘reductive’ pretreatment and final reduction at 300 °C, both procedures being carried out by pure hydrogen (Fig. 5). Such a pretreatment implies the appearance of Ti³⁺ sites and O²⁻ vacancies [14, 25, 26].

The measurements of CO and hydrogen chemisorption indicated: (i) nearly the same metal dispersion of both samples; (ii) a higher H/CO_s ratio of 2.9 for the catalyst after ‘reductive’ pretreatment; (iii) the CO_s/CO_w ratio was almost the same for both catalysts (0.8 and 1), however, CO amount adsorbed on the surface was higher with the selective (10% Co+0.5% Pd)/TiO₂(ox) catalyst. Acquired data can be assigned to a large quota of CO adsorbed on metal ions, a larger share of bridge-bonded CO, a lot of separate Co and Pd particles in the active catalyst. Accordingly, the active sample was also characterized by bimetallic particles, Ti⁴⁺, Coⁿ⁺, and lack or lower level SMSI.

The selective catalyst was prepared by pretreatment in air and TiO₂ was stabilized in relation to phase transformations. Thus, on the surface of this sample there existed sites of different nature/character and strength for CO adsorption. The latter include Co, Pd and highly diluted Pd atoms on the surface of bimetallic particles, Ti³⁺ ions and O²⁻ vacancies of relatively lower amount, Ti⁴⁺ ions, many unreduced Co⁰ ions (very low R_{URM} = 0.2). At the same time, the surface of the metal particles is partially covered by reduced titania due to SMSI. The low activity of this sample could be assigned to SMSI since the metal dispersion was almost preserved (Table 1).

Formation of carbonate species on the samples/support could proceed by two distinct mechanisms: (i) a contact of CO with surface defects followed by interaction with OH groups or (ii) direct interaction between CO and surface hydroxyls [30]. The probability to realize these ways is different depending on the preliminary treatment of the catalyst. Both mechanisms could be equally operative in the case of an active sample, because of surface site diversity characterized by more ions capable of CO adsorption and conversion. The latter mechanism is most probable in the case of selective catalyst taking into account a narrower site distribution.

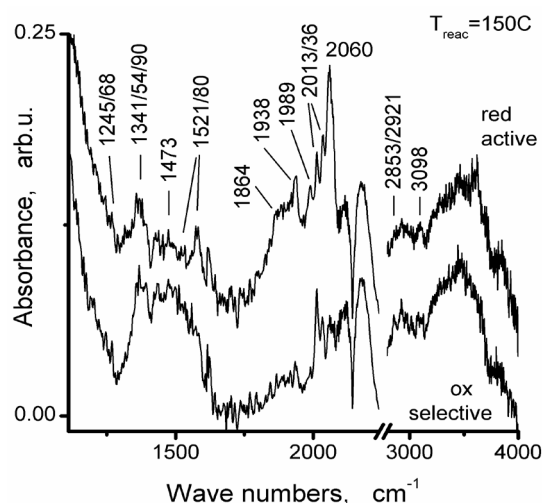


Fig. 6. *In situ* DRIFTS during CO hydrogenation.

Figure 6 shows the results obtained by *in situ* DRIFTS during CO hydrogenation. The doublet centered at 2142 cm⁻¹ is characteristic of gaseous CO. Bands of CO species adsorbed on the metal surface appeared at 2013, 2036, and 2060 cm⁻¹ for linearly adsorbed CO on cobalt particles; 1936 and 1989 cm⁻¹ for bridge-bonded CO on Pd; 1864 cm⁻¹ for multicenter bonded CO on Pd (Pd (111) facets on the surface of palladium particles) [32, 38].

Bidentate (1245/68, 1580, 1618, 1640 cm⁻¹) and

monodentate (1341/54, 1472, 1521 cm⁻¹) carbonate and formate species (1341/54/90, 1580, 1618 cm⁻¹) were registered on the catalyst surface [38]. Bands of monodentate carbonate and formate species were of higher intensity in the spectrum of the selective sample. This observation allows to state that the selective catalyst had larger amounts of the aforementioned surface species. They were relatively stable since reaction temperatures over 150 °C were necessary to initiate their transformation compared to the spectra of active sample. In addition, the bands were clearly visible to exhibit higher intensity even at 250 °C. Bands characteristic of hydrocarbon species (1390, 2853, 2921 cm⁻¹) were better resolved in the spectrum of the selective catalyst [38]. A band of the CH₄ reaction product at 3098 cm⁻¹ was recorded in both cases [38]. These observations concerning carbonate and hydrocarbon species retained on the selective sample surface are in agreement with XPS findings.

Figure 7 presents the changes of 2013 and 2036 cm⁻¹ band intensities in dependence of the reaction temperature. A general feature of the changes is concerned with decreasing band intensity. However, in the case of active sample (open symbols), some increase in intensity appeared in the interval of 150–225 °C.

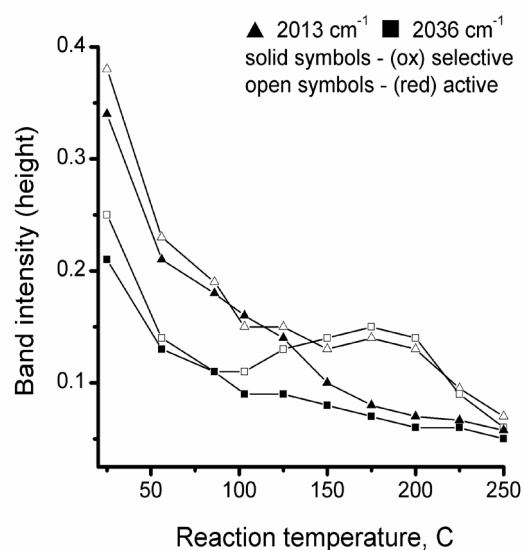


Fig. 7. Dependence of some infrared band intensities on reaction temperature.

The latter was accompanied by appearance and increasing intensity of bands characteristic of CO adsorbed as different species on palladium atoms. The observed feature could be attributed to synergism mode, surface reorganization, and a decrease in SMSI effect. The CH₄/CO₂ product ratio at the reaction temperature of 300 °C for the active and the selective catalysts was 3 and 65, respectively (Table 1). The XPS study revealed higher carbon

deposition on the surface of the active sample but a larger amount of carbonates on the surface of the selective sample. The results could be explained by (i) domination of sites for strong CO adsorption on the metal surface and for monodentate carbonates on the support in the selective catalyst that determine CO₂ formation at higher temperatures during the catalytic process; (ii) adsorption sites of medium strength for bidentate carbonate species, which prevail on the surface of the active catalyst; (iii) possibility for a varying ratio of linear to bridged CO species on the surface of metal particles in the active catalyst where weakened C-O bonding in bridge-bonded species facilitate cleavage at lower reaction temperatures. It is known that carriers with acid surface and those, which can be partially reduced, are suitable for WGS catalysts [39]. TiO₂ meets both requirements, namely, it is a weak acid support mainly with Lewis acid properties and in presence of metals (like Co and Pd) can be partially reduced to form oxygen vacancies. Even more, it has been found that Pd/TiO₂ (so as Pt, Rh, or Ru on TiO₂) is very effective in WGS and the catalytic activity is in proportion with SMSI [39]. Therefore, such a property should be taken into account together with the other factors mentioned above on discussing catalytic performance of the active catalyst.

CONCLUSIONS

Comparative analysis showed that the synthesis of (10%Co+0.5%Pd)/TiO₂ catalysts by applying different pretreatment and reduction sets could result in an active catalyst in the process of CO conversion to CH₄ and CO₂ or a selective one to higher yields of CH₄ and hydrocarbons. Since CO hydrogenation on bimetallic catalysts is dependent on Co state, amount of unreduced metal, bimetallic Pd-Co particle formation, and support features for CO and CO₂ adsorption, then the H_{100C}/CO_s and CO_s/CO_w ratios become apparent as important criteria for catalyst performance.

Acknowledgement: The financial support by the Bulgarian National Science Fund through contract KP-06-H29-9/14.12.2018 is gratefully acknowledged.

REFERENCES

1. P. T. Anastas, M. M. Kirchhoff, T. C. Williamson, *Appl. Catal. A-Gen.*, **221**, 3 (2001).
2. J. A. Rabo, A. P. Risch, M. L. Poutsma, *J. Catal.*, **53**, 295 (1978).
3. P. Biloen, J. N. Helle, W. M. H. Sachtler, *J. Catal.*, **58**, 95 (1979).
4. G. Blyholder, D. Shihabi, W. V. Wyatt, R. Bartlett, *J. Catal.*, **43**, 122 (1976).
5. M. L. Poutsma, L. F. Elek, P. A. Ibarbia, A. P. Risch, J. A. Rabo, *J. Catal.*, **52**, 157 (1978).
6. M. A. Vannice, R. L. Garten, *Ind. Eng. Chem. Prod. Res. Dev.*, **18**, 186 (1979).
7. D. C. Grenoble, M. M. Estadt, D. F. Ollis, *J. Catal.*, **67**, 90 (1981).
8. C. Ratnasamy, J. P. Wagner, *Catal. Rev.*, **51**, 325 (2009).
9. M. Masuda, K. Miyahara, *Bull. Chem. Soc. Japan*, **47**, 1058 (1974).
10. M. Masuda, *J. Res. Inst. Catal., Hokkaido Univ.*, **24**, 83 (1976).
11. P. C. Aben, *J. Catal.*, **10**, 224 (1968).
12. R. C. Reuel, C. H. Bartholomew, *J. Catal.*, **85**, 63 (1984).
13. J. M. Zowtiak, C. H. Bartholomew, *J. Catal.*, **83**, 107 (1983).
14. J. R. Anderson, Structure of metallic catalysts, Mir, Moscow, 1978 (in Russian).
15. D. Shirley, *Phys. Rev. B*, **5**, 4709 (1972).
16. J. H. Scofield, *J. Electron Spectrosc.*, **8**, 129 (1976).
17. S. Zheng, Y. Liu, J. Li, B. Shi, *Appl. Catal. A-Gen.*, **330**, 63 (2007).
18. N. Guskos, J. Typek, M. Maryniak, G. Żolnierkiewicz, M. Podsiadly, W. Arabczyk, Z. Lendzion-Bielun, U. Narkiewicz, *Mater. Sci. Poland*, **24**, 4 (2006).
19. P. Stefanov, S. Todorova, A. Naydenov, B. Tzaneva, H. Kolev, G. Atanasova, D. Stoyanova, Y. Karakirova, K. Aleksieva, *Chem. Eng. J.*, **266**, 329 (2015).
20. E. V. Makshina, N. S. Nesterenko, S. Siffert, E. A. Zhilinskaya, A. Aboukais, B. V. Romanovsky, *Catal. Today*, **131**, 427 (2008).
21. P. Claus, S. Schimpf, R. Schodel, P. Kraak, W. Morke, D. Honicke, *Appl. Catal. A-Gen.*, **165**, 429 (1997).
22. J. F. Moulder, W. F. Stickle, P. E. Sobol, K. D. Bomben, Handbook of X-ray Photoelectron Spectroscopy, Perkin-Elmer Corp., Minnesota, 1992.
23. N. M. Popova, L. V. Babenkova, G. A. Saveleva, Adsorption and interaction of simple gases with VIII group metals, Nauka, KazSSR, Alma-Ata, 1979 (in Russian).
24. D. Potoczna-Petru, J. M. Jablonski, J. Okal, L. Krajczyk, *Appl. Catal. A-Gen.*, **175**, 113 (1998).
25. C. N. Satterfield, Heterogeneous Catalysis in Industrial Practice, 2nd edn., McGraw-Hill Inc., 1980 (© 1991).
26. A. Nobile, Jr., M. W. Davis, Jr., *J. Catal.*, **116**, 383 (1989).
27. K. I. Hadjiivanov, D. G. Klissurski, *Chem. Soc. Rev.*, **25**, 61 (1996).
28. R. Riva, H. Miessner, G. Del Piero, D. Rebours, M. Roy, *Stud. Surf. Sci. Catal. (Natural gas conversion V)*, **119**, 203 (1998).
29. M. Voß, D. Borgmann, G. Wedler, *J. Catal.*, **212**, 10 (2002).
30. C. Weilach, C. Spiel, K. Föttinger, G. Rupprechter, *Surf. Sci.*, **605**, 1503 (2011).
31. S. Zh. Todorova, G. B. Kadinov, *Bulg. Chem. Commun.*, **34**, 232 (2002).
32. G. B. Kadinov, Ch. Bonev, S. Todorova, A. Palazov,

- J. Chem. Soc. Faraday Trans.*, **94**, 3027 (1998).
33. M. G. Shopska, I. Zh. Shtereva, G. B. Kadinov, *Bulg. Chem. Commun.*, **34**, 476 (2002).
34. M. G. Shopska, G. B. Kadinov, *Asian Chem. Lett.*, **14**, 111 (2010).
35. M. G. Shopska, G. B. Kadinov, I. Zh. Stereva, *Oxid. Commun.*, **34**, 85 (2011).
36. M. Shopska, G. Kadinov, I. Shtereva, *Rev. Roum. Chim.*, **59**, 219 (2014).
37. S. Todorova, A. Ganguly, A. Naydenov, H. Kolev, I. Yordanova, M. Shopska, S. Mondal, G. Kadinov, S. Saha, A. K. Ganguli, *Bulg. Chem. Commun.*, **47(C)**, 42 (2015).
38. L. H. Little, *Infrared spectra of adsorbed species*. Academic Press Inc., London, New York, 1966.
39. L. E. Oi, M.-Y. Choo, H. V. Lee, H. C. Ong, S. B. A. Hamid, J. C. Juan, *RSC Adv.*, **6**, 108741 (2016).

Instructions about Preparation of Manuscripts

General remarks: Manuscripts are submitted in English by e-mail. The text must be typed on A4 format paper using Times New Roman font size 11, normal character spacing. The manuscript should not exceed 15 pages (about 3500 words), including photographs, tables, drawings, formulae, etc. Authors are requested to use margins of 2 cm on all sides.

Manuscripts should be subdivided into labelled sections, e.g. **Introduction, Experimental, Results and Discussion, etc.** The **title page** comprises headline, author's names and affiliations, abstract and key words. Attention is drawn to the following:

a) **The title** of the manuscript should reflect concisely the purpose and findings of the work. Abbreviations, symbols, chemical formulas, references and footnotes should be avoided. If indispensable, abbreviations and formulas should be given in parentheses immediately after the respective full form.

b) **The author's** first and middle name initials and family name in full should be given, followed by the address (or addresses) of the contributing laboratory (laboratories). **The affiliation** of the author(s) should be listed in detail by numbers (no abbreviations!). The author to whom correspondence and/or inquiries should be sent should be indicated by asterisk (*) with e-mail address.

The abstract should be self-explanatory and intelligible without any references to the text and containing not more than 250 words. It should be followed by key words (not more than six).

References should be numbered sequentially in the order, in which they are cited in the text. The numbers in the text should be enclosed in brackets [2], [5, 6], [9–12], etc., set on the text line. References are to be listed in numerical order on a separate sheet. All references are to be given in Latin letters. The names of the authors are given without inversion. Titles of journals must be abbreviated according to Chemical Abstracts and given in italics, the volume is typed in bold, the initial page is given and the year in parentheses. Attention is drawn to the following conventions: a) The names of all authors of a certain publication should be given. The use of "*et al.*" in the list of references is not acceptable. b) Only the initials of the first and middle names should be given. In the manuscripts, the reference to author(s) of cited works should be made without giving initials, e.g. "Bush and Smith [7] pioneered...". If the reference carries the names of three or more authors it should be quoted as "Bush *et al.* [7]", if Bush is the first author, or as "Bush and co-workers [7]", if Bush is the senior author.

Footnotes should be reduced to a minimum. Each footnote should be typed double-spaced at the bottom of the page, on which its subject is first mentioned. **Tables** are numbered with Arabic numerals on the left-hand top. Each table should be referred to in the text. Column headings should be as short as possible but they must define units unambiguously. The units are to be separated from the preceding symbols by a comma or brackets. Note: The following format should be used when figures, equations, etc. are referred to the text (followed by the respective numbers): Fig., Eqns., Table, Scheme.

Schemes and figures. Each manuscript should contain or be accompanied by the respective illustrative material as well as by the respective figure captions in a separate file (sheet). As far as presentation of units is concerned, SI units are to be used. However, some non-SI units are also acceptable, such as °C, ml, l, etc. The author(s) name(s), the title of the manuscript, the number of drawings, photographs, diagrams, etc., should be written in black pencil on the back of the illustrative material (hard copies) in accordance with the list enclosed. Avoid using more than 6 (12 for reviews, respectively) figures in the manuscript. Since most of the illustrative materials are to be presented as 8-cm wide pictures, attention should be paid that all axis titles, numerals, legend(s) and texts are legible.

The authors are required to submit the text with a list of three individuals and their e-mail addresses that can be considered by the Editors as potential reviewers. Please, note that the reviewers should be outside the authors' own institution or organization. The Editorial Board of the journal is not obliged to accept these proposals.

The authors are asked to submit **the final text** (after the manuscript has been accepted for publication) in electronic form by e-mail. The main text, list of references, tables and figure captions should be saved in separate files (as *.rtf or *.doc) with clearly identifiable file names. It is essential that the name and version of the word-processing program and the format of the text files is clearly indicated. It is recommended that the pictures are presented in *.tif, *.jpg, *.cdr or *.bmp format.

The equations are written using “Equation Editor” and chemical reaction schemes are written using ISIS Draw or ChemDraw programme.

EXAMPLES FOR PRESENTATION OF REFERENCES

REFERENCES

1. D. S. Newsome, *Catal. Rev.–Sci. Eng.*, **21**, 275 (1980).
2. C.-H. Lin, C.-Y. Hsu, *J. Chem. Soc. Chem. Commun.*, 1479 (1992).
3. R. G. Parr, W. Yang, *Density Functional Theory of Atoms and Molecules*, Oxford Univ. Press, New York, 1989.
4. V. Ponec, G. C. Bond, *Catalysis by Metals and Alloys (Stud. Surf. Sci. Catal., vol. 95)*, Elsevier, Amsterdam, 1995.
5. G. Kadinov, S. Todorova, A. Palazov, in: *New Frontiers in Catalysis (Proc. 10th Int. Congr. Catal., Budapest, (1992)*, L. Guzzi, F. Solymosi, P. Tetenyi (eds.), Akademiai Kiado, Budapest, 1993, Part C, p. 2817.
6. G. L. C. Maire, F. Garin, in: *Catalysis. Science and Technology*, J. R. Anderson, M. Boudart (eds), vol. 6, SpringerVerlag, Berlin, 1984, p. 161.
7. D. Pocknell, *GB Patent 2 207 355* (1949).
8. G. Angelov, PhD Thesis, UCTM, Sofia, 2001, pp. 121-126.
- 9 JCPDS International Center for Diffraction Data, Power Diffraction File, Swarthmore, PA, 1991.
10. CA **127**, 184 762q (1998).
11. P. Hou, H. Wise, *J. Catal.*, in press.
12. M. Sinev, private communication.
13. <http://www.chemweb.com/alchem/articles/1051611477211.html>.

Texts with references which do not match these requirements will not be considered for publication!!!

K. Mehmood, M. Shakeel, M. Siddiq, Solutions and thermodynamic properties of three pharmacologically important drugs in ethanol.....	179
G. Mohammadi Ziarani, Z. Hassanzadeh, A. Badii, S. Asadi, A. Abolhassani Soorki, Microwave-assisted synthesis of 2,2'-(2-oxindoline-3,3'-diyl)-bis(1 <i>H</i> -inden-1,3(2 <i>H</i>)-dione) derivatives using SBA-Pr-SO ₃ H and their antibacterial activities study.....	184
S. Svilović, D. Rušić, R. Stipišić, N. Kuzmanić, Process optimization for copper sorption onto synthetic zeolite NaX.....	189
J. M. Velicković, E. J. Kostić, Comparative analysis of phenolic and mineral composition of traditionally used wild medicinal plants from Southeast Serbia.....	197
L. Dospatliev, M. Ivanova, Comparison of selenium determination in bone tissue samples from lambs, piglets and calves by spectrophotometry and inductively coupled plasma – tandem mass spectrometry.....	203
G. Chinnasamy, S. Kaliannan, P. M. Jeganathan, Development of a novel agitated vessel for gas-induction to improve the gas-liquid mass transfer.....	208
A. Ullah, A. Mushtaq, R. Ahmed Qamar, Z. Uddin Ali, Optimization of an organic waste biogas reactor.....	214
O. Ağyar, A. S. Ertürk, A. Özkaya, M. G. Sucak, Y. Şahin, Estimation of mineral, trace element and fatty acid profile of Anatolian water buffalo milk.....	230
M. N. Joy, Y. D. Bodke, S. Telkar, 4-Methyl-7-alkynyl coumarin derivatives as potent antimicrobials and antioxidants.....	237
B. Abrashev, D. Uzun, A. Kube, N. Wagner, K. Petrov, Optimization of the bi-functional oxygen electrode (BOE) structure for application in a Zn-air accumulator.....	245
P. I. Bozov, Clerodane diterpenoids isolated from Bulgarian species of genus <i>Teucrium</i> (Lamiaceae).....	250
M. R. Mishra, S. M. Hussain, O. D. Makinde, G. S. Seth, Stability analysis and multiple solutions of a hydromagnetic dissipative flow over a stretching/shrinking sheet.....	259
T. K. Georgiev, P. V. Hadzhibozheva, Y. D. Karamalakova, G. D. Nikolova, G. A. Krastev, I. Nedevska, R. Stojanov, A. N. Tolekova, V. G. Gadjeva, Effect of oxidative stress on angiotensin II-induced smooth muscle contractile activity of urinary bladder from fructose fed rats.....	272
N. Yavorov, I. Valchev, Fast-growing tree species as sugar sources.....	278
A. Hristova, S. Valcheva-Kuzmanova, T. Pajpanova, Synthesis and hydrolytic stability of new analogues of Bactenecin 2A.....	284
<i>Selected papers presented on the 16th National Catalysis Conference, Bulgarian catalysis Club, Sofia, June 27, 2019.....</i>	
M. P. Anachkov, P. A. Karakashkova, V. F. Georgiev, S. K. Rakovsky, L. S. Minchev, T. T. Batakliiev, Kinetics and mechanism of the ozone reaction with cyclohexanol in solution...	291
V. A. Angelov, T. T. Batakliiev, V. F. Georgiev, E. H. Ivanov, R. K. Kotsilkova, Preparation and electromagnetic properties of epoxy/organoclay/MWCNT/gold nanocomposites.....	297
T. Batakliiev, V. Georgiev, M. Gabrovska, D. Nikolova, S. Rakovsky, Ozone decomposition on the surface of a novel Mn-Al catalyst in gas phase.....	300
A. E. Elias, G. Munteanu, P. Karakashkova, M. Fabian, Parameter optimization of photocatalytic reactors using Taguchi-Grey technique.....	305
V. F. Georgiev, S. I. Minkovska, T. T. Batakliiev, P. A. Karakashkova, M. P. Anachkov, Efficient squaraine dye photosensitized TiO ₂ /rGO catalyst with enhanced catalytic activity for degradation of Methylene Blue.....	310
I. Stoycheva, T. Tsoncheva, B. Tsyntsarski, B. Petrova, G. Georgiev, A. Sarbu, A. Radu, T. Sandu, Biomass-based nanoporous carbon as catalyst support for production of hydrogen by methanol degradation.....	316
M. G. Shopaska, I. Zh. Shtereva, H. G. Kolev, K. I. Aleksieva, S. Zh. Todorova, G. B. Kadinov, Activity and selectivity of Co-Pd/TiO ₂ catalysts in CO hydrogenation.....	320
INSTRUCTIONS TO AUTHORS.....	328